



**HAL**  
open science

# Numerical modeling for the electromagnetic non-destructive evaluation: Application to the non-destructive evaluation of concrete.

Xisto Lucas Travassos

► **To cite this version:**

Xisto Lucas Travassos. Numerical modeling for the electromagnetic non-destructive evaluation: Application to the non-destructive evaluation of concrete.. Other. Ecole Centrale de Lyon, 2007. English. NNT: . tel-00177523

**HAL Id: tel-00177523**

**<https://theses.hal.science/tel-00177523>**

Submitted on 8 Oct 2007

**HAL** is a multi-disciplinary open access archive for the deposit and dissemination of scientific research documents, whether they are published or not. The documents may come from teaching and research institutions in France or abroad, or from public or private research centers.

L'archive ouverte pluridisciplinaire **HAL**, est destinée au dépôt et à la diffusion de documents scientifiques de niveau recherche, publiés ou non, émanant des établissements d'enseignement et de recherche français ou étrangers, des laboratoires publics ou privés.

THÈSE

présentée à

L'ÉCOLE CENTRALE DE LYON

pour l'obtention du

DIPLÔME DE DOCTORAT

Spécialité : ELECTRONIQUE, ELECTROTECHNIQUE, AUTOMATIQUE

soutenue publiquement le 22 juin 2007

par

**Lucas Travassos**

---

**Modélisation numérique pour l'évaluation non destructive électromagnétique : application au contrôle non destructif des structures en béton.**

---

Directeur de Thèse : Alain Nicolas

JURY : M Jean-Louis Coulomb, Président,  
M Nathan Ida, Rapporteur,  
M Joao Pedro Bastos, Rapporteur,  
M Dominique Lesselier, Examineur,  
M Christian Vollaire, Directeur de thèse,  
M Alain Nicolas, Directeur de thèse.



---

# Contents

<b>Remerciements</b>	<b>v</b>
<b>Introduction</b>	<b>vii</b>
0.1 Thesis objectives . . . . .	viii
0.2 Scope and contribution of the present work . . . . .	ix
<b>1 NDT techniques for concrete structures</b>	<b>1</b>
1.1 Overview . . . . .	2
1.2 Problems in concrete . . . . .	3
1.2.1 Compressive strength . . . . .	3
1.2.2 Carbonation . . . . .	3
1.2.3 Chloride content . . . . .	3
1.2.4 Voids and inhomogeneities . . . . .	3
1.3 Most commonly used NDT methods for concrete . . . . .	3
1.3.1 Visual inspection . . . . .	4
1.3.2 Liquids penetrant . . . . .	4
1.3.3 Magnetic testing . . . . .	5
1.3.4 Half-cell electrical potential method . . . . .	5
1.3.5 Impact-echo system . . . . .	5
1.3.6 Acoustic emission . . . . .	6
1.3.7 Ultrasonic reflection method . . . . .	7
1.3.8 Thermography . . . . .	7
1.3.9 Covermeter . . . . .	8
1.3.10 Electrical resistivity . . . . .	9
1.3.11 Radiography . . . . .	9
1.3.12 Ground penetrating radar . . . . .	11
1.3.13 Use of techniques in combination . . . . .	12
1.3.14 Background radar for concrete inspection . . . . .	12
1.4 Modeling needs . . . . .	15
<b>2 Numerical modeling</b>	<b>17</b>
2.1 Basic electromagnetic equations . . . . .	18
2.1.1 Maxwell's equations and constitutive relations . . . . .	18
2.1.2 Interface Conditions . . . . .	19
2.1.3 Boundary conditions . . . . .	20
2.1.4 Wave equation . . . . .	21
2.2 Numerical techniques . . . . .	21
2.2.1 Review on PDE based numerical methods . . . . .	22
2.2.2 Review on integral formula based numerical methods . . . . .	24
2.3 FDTD algorithm . . . . .	26
2.3.1 FDTD for dispersive media . . . . .	28
2.3.2 Applications: Pulsed microwave confocal system . . . . .	36
2.3.3 Optimal configurations for PML . . . . .	40

---

<b>3</b>	<b>Radar testing of concrete</b>	<b>49</b>
3.1	System design . . . . .	50
3.1.1	Range . . . . .	51
3.1.2	Clutter . . . . .	52
3.1.3	Depth resolution . . . . .	52
3.1.4	Plane resolution . . . . .	53
3.1.5	Additional considerations . . . . .	53
3.2	Concrete properties . . . . .	53
3.2.1	Theoretical models of the complex permittivity of concrete . . . . .	55
3.3	Antennas . . . . .	59
3.3.1	Basic antenna concepts . . . . .	60
3.3.2	Types of antennas . . . . .	64
3.3.3	Bowtie antenna optimization . . . . .	65
3.4	Time-domain analysis . . . . .	70
3.4.1	Summary of concrete dielectric properties . . . . .	70
3.4.2	Homogeneous model . . . . .	70
3.4.3	Heterogeneous model . . . . .	73
3.5	Signal processing . . . . .	83
3.5.1	A-scan processing . . . . .	83
3.5.2	B-scan processing . . . . .	84
3.5.3	C-scan processing . . . . .	85
3.5.4	Image processing . . . . .	85
<b>4</b>	<b>Imaging algorithms</b>	<b>91</b>
4.1	Inverse problems . . . . .	92
4.2	Reverse-time migration algorithm . . . . .	93
4.2.1	Bistatic configuration . . . . .	94
4.3	Model fitting . . . . .	95
4.4	Neural networks . . . . .	102
4.5	Inclusion characterization . . . . .	102
4.5.1	Parallel layer perceptron . . . . .	103
4.6	Compressing data for ANN training . . . . .	105
4.6.1	The curse of dimensionality . . . . .	105
4.6.2	Principal component analysis . . . . .	106
4.6.3	The expected error . . . . .	107
4.6.4	Results . . . . .	108
<b>5</b>	<b>Conclusions and scope for future research</b>	<b>111</b>
5.1	Future work . . . . .	112
<b>A</b>	<b>Implementation of CPML in FDTD</b>	<b>113</b>
A.1	Derivation of the finite-difference expressions . . . . .	113
<b>B</b>	<b>Transmission line matrix method</b>	<b>117</b>
B.1	PML derivation for the TLM SCN node . . . . .	117
	<b>Bibliography</b>	<b>125</b>
	<b>Vita</b>	<b>133</b>

---

# Remerciements

Les travaux de recherche développés dans ce mémoire ont été réalisés au sein de l'Ecole Centrale de Lyon et The University of Akron.

Je remercie vivement Monsieur Laurent Nicolas, directeur du laboratoire Ampère, de m'avoir accueilli au sein de son équipe.

Je tiens à remercier les personnes qui m'ont orienté :

- Monsieur A. Nicolas pour la qualité de l'encadrement dont j'ai pu bénéficier tout au long de ce travail et pour toute sa confiance et son soutien inconditionnel dans mes décisions.
- Monsieur Christian Vollaire pour la qualité de ses relations humaines durant ces années me faisant grandement bénéficier de son expérience et de ses compétences.
- Monsieur Nathan Ida pour m'avoir accueilli pendant mon séjour a The University of Akron. Qu'il trouve ici l'expression de ma profonde reconnaissance par ses qualités humaines, scientifiques et pour son extrême disponibilité.

Que Monsieur J-L. Coulomb et Monsieur D. Lesselier, soient ici remerciés de l'honneur qu'ils me font en jugeant ce travail. Monsieur J. P. Bastos, de la même manière, mérite une mention spéciale pour avoir accepte sans hésiter d'être rapporteur de mon travail de thèse de doctorat.

Je tiens à remercier aussi les professeurs, élèves et personnel du ECL et UA, pour m'avoir accueilli dans la plénitude de mes attentes pendant mon séjour en France et aux Etats-Unis. Je voudrais remercier tout particulièrement Monsieur Philippe Billoux, assistant de direction, pour son aide, patience et conseils pour la vie quotidienne en France.

Je ne saurais oublier Monsieur Ronan Perrussel pour toutes ses précieuses contributions pour ce travail pendant presque trois années. Qu'il sache que je serais toujours reconnaissant pour la qualité remarquable de ses commentaires dont il m'a fait bénéficier mais aussi pour sa patience, sa disponibilité et sa bonne humeur.

Finalement, je tiens à remercier vivement mes parents qui ont su m'apporter tout leur soutien, leurs pensées, leurs prières et leur amour à distance mais à tout instant.

---



# Introduction

The ability of any industrialized nation to produce and sustain economic growth is directly related to its infrastructure. Concrete is the most common building material and accounts for a large part of the systems that are necessary for a country to operate smoothly including buildings, roads, and bridges. In particular, structural reinforced and pre-stressed concrete has been used extensively in the construction of nuclear facilities since the birth of the civil nuclear industry in the late 1940s.

Today [1], France counts 58 pressurized water reactors (Figure 1). Fessenheim, which started in Alsace in 1977, was the first of the 34 units of the 900 megawatt class. The last of the 4 units of the 1450 megawatt class was brought into service at the end of 1999 at Civaux. In twenty years of operation, the nuclear industry proved its reliability. Thanks to its nuclear reactors, with a 63200 megawatts installed working capacity, France ensures a rate of energy independence close to 50%.

CARTE DES UNITÉS ÉLECTRONUCLÉAIRES EN FRANCE (2001)

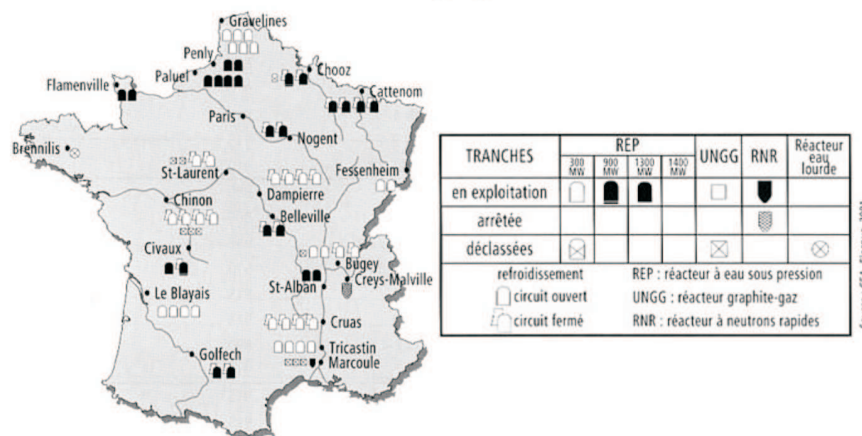


Figure 1: French nuclear plan [1].

The electricity produced in France is currently one of most competitive in Europe. Under normal conditions, the nuclear power, with a production cost of 28,4 euros per MWh including all taxes, appears more competitive than gas (35 euros/MWh) and coal (32 to 33,7 euros/MWh).

Moreover, the cost of nuclear power is stable, because it is not very dependant on the prices of uranium, while the kWh cost of gas based energy is strongly related to the price of oil that, in the long term, is uncertain because of the strongly anticipated growth in demand.

Despite the many years of maintenance-free operation, this infrastructure in France is currently deteriorating at an alarming rate putting pressure on maintenance authorities in a world where public safety is paramount and the financial and other consequences of failure are great. To maintain a sure state of operation during its planned lifespan (40 years envisaged at construction [2]), the maintenance function holds a major role in the life-cycle of a nuclear thermal power station.

Before any repairs can be undertaken on a concrete structure, its condition needs to be evaluated to determine the existing conditions and understand the mechanisms of deterioration. Nondestructive testing (NDT) is one of the techniques that can be used to assess the structural condition.

In the last decade, the concept of using Ground Penetrating Radar (GPR) for the NDT of concrete structures has grown, involving researchers from many different disciplines. The interest in this technique can be explained, basically, by its advantages compared to other techniques such as portability, relative low cost and weight, the ease of application to different surfaces (military and space applications).

The idea of *seeing* into the subsurface started in the late 1950s. However, only in the late 1970s this method started to become common in the assessment of concrete structures. This can be explained by the space race in the cold war and the consequent miniaturisation and integration of electronic circuits.

The main goal of simulating the GPR analysis of concrete structures is to predict the behavior of the system and its capability to detect faults and inclusions in many different configurations.

The study of this kind of assessment is complex due to the concrete inhomogeneity, boundary conditions, and the variety of antenna configurations. Analytical solutions of the governing partial differential equations are only available for the simplest of NDT geometries and hence numerical methods must be used if reasonable solutions are to be obtained for practical electromagnetic NDT geometries. Such solutions are needed for test design purposes, for the physical understanding of the field-defect interactions and for the generation of data to aid in the inverse or defect characterization problem.

## 0.1 Thesis objectives

This thesis investigates the following three aspects of radar assessment of concrete structures:

1. Radar interferometry for subsurface detection,
2. 3D modeling of radar electromagnetic (EM) wave propagation in heterogeneous dielectric structures, and
3. Reconstruction of subsurface inclusions characteristics using radar signals.

This is the first work at the Ampère Laboratory concerning electromagnetic waves at medium and high frequency for the NDT of concrete structures. Thus far, most of the activities in NDT were developed using eddy currents to detect inclusions in conductors, an area in which this institution enjoys broad recognition. Ampère Laboratory at Ecole Centrale de Lyon is planning to pursue studies in the radar assessment for civil engineering, which will be deployed in a project constituted by the LCPC (Laboratoire Central des Ponts et Chaussées), EDF (Electricité de France), and the CNRS (Centre National de la Recherche Scientifique).

At the beginning of this research work, it seemed possible to obtain real radar data from the inspection of a characterized concrete structure for code validation of the main simulator and the imaging algorithms for subsurface inclusions. Unfortunately, during the course of the research no radar data could be obtained. Therefore, the present research is confined to simulation studies, and the developed target reconstruction techniques using inverse problems and the main code simulator has been verified by using three different techniques and antenna measured data, respectively.

The objectives of the thesis can be summarised as follows:

- To review and describe the current status of NDT methods for concrete structures.
  - To obtain a comprehensive understanding of the physical processes in the assessment of concrete structures using radar testing. In order to simulate a dielectric material close to the concrete's properties, different models are implemented to include concrete characteristics such as porosity, water, salt content, and temperature.
  - To discuss the types of radar systems available. The available types of radar vary from short pulse systems, through stepped frequency systems.
  - To discuss the relevant antenna constraints in a radar assessment. The interaction antenna/medium is outlined showing the behaviour in the radiation pattern and the air/ground field ratio.
  - To develop an optimal design concept of an antenna for radar testing. The goal is to change the radiation pattern of the antenna in order to detect closely spaced targets.
-

- To model the process of a radar testing system using numerical methods. This modeling code will be used to study the radar wave propagation in a dispersive medium using the reflected wave from different types of concrete structures and different inclusions.
- To optimize the modeling process by improvements in the absorbing boundary condition, and
- To implement imaging algorithms which should be capable to detect faults given a radar reflected signal.

## 0.2 Scope and contribution of the present work

In the present study, it is proposed to implement electromagnetic wave propagation models in concrete structures using various numerical techniques to investigate the different aspects of GPR, or simply, radar inspection of concrete. First, a 3D Finite-Difference Time-Domain (FDTD) algorithm was implemented for the simulation of concrete structures which allows modeling of characteristics such as porosity, salt content and degree of saturation of the mixture using Debye parameters. Next, a novel optimization algorithm for the improvement of bowtie antennas for closely spaced targets using Genetic Algorithms and the Moment Method (MoM) is proposed. Finally, parametric and non-parametric imaging algorithms were implemented, to obtain fast and accurate estimation of target shapes under some constraints in inhomogeneous media using a Migration Algorithm, Particle Swarm Optimization and Neural Networks. The performance of the proposed algorithms are confirmed by numerical simulations.

Chapter 1 presents a brief discussion about the most commonly used NDT techniques for concrete. Operation principles, advantages and drawbacks of each technique are outlined. This chapter ends with a discussion of the needs of numerical modeling for NDT.

Chapter 2 reviews the electromagnetic basic equations to simulate the radar assessment of concrete structures and the most commonly used numerical techniques to model the interaction field-defect. The main algorithm using the FDTD method has been verified with measurements of a microstrip antenna and a Transmission Line Matrix (TLM) algorithm implemented by the candidate. Detailed derivation has been included where necessary and references are given where material is drawn from outside sources. The implementation and coding of a radar simulator in a dispersive environment is the candidate's own original work. In addition an optimal configuration for Perfectly Matched Layers (PML) is proposed [3] using a theoretical approach and both the mono-objective genetic algorithm (GA) and multiobjective genetic algorithm (MGA), which is a novel approach.

Chapter 3 reviews the radar systems available at present and discusses the relevant antenna constraints with particular emphasis on amplitude-modulated signals. Although most of the topics discussed in this chapter are in no sense novel, this chapter provides a good overview of the fundamental aspects of radar assessment. In addition, a procedure to improve the radiation pattern of bowtie antennas is presented [4]. This procedure seeks to achieve two objectives: to minimize the metal area of the antenna (in order to reduce the size and weight) and to maximize the gain in the plane perpendicular to the antenna. This approach involves the Moment Method (MoM) in conjunction with the MGA. Finally, a study of the dispersion from heterogeneous dielectrics is shown.

Chapter 4 presents the imaging algorithms used to classify the targets. First, the Reverse-Time Migration Algorithm is implemented in order to detect buried inclusions in the presence of noise and heterogeneity. Next, a model fitting approach is shown using Particle Swarm Optimization (PSO) in order to reduce the computational cost of non-linear inverse problems. Finally, Artificial Neural Networks (ANN) are used to improve the detection of buried cylinders using the Parallel Layer Perceptron (PLP) Architecture. A new approach [5] using PLP and Principal Component Analysis (PCA) is proposed to compress the radar data in order to train ANN faster. To the candidate's best knowledge, the application of PCA to reduce the order of the data in ANN training in the context of radar assessment in concrete environment is also a novel approach.

Chapter 5 summarises the work and provides recommendations for future research.



## Chapter 1

# NDT techniques for concrete structures

NDT techniques are potentially the most useful methods for assessing the condition of in-situ concrete structures such as bridges, buildings and specially nuclear power plants. Their importance results from the noninvasive nature of the techniques, the anticipated speed of measurements, the non-disturbance to the service during data collection, and the quantitative assessment of the condition.

A general definition of NDT is an examination, test, or evaluation performed on any type of test object without changing or altering that object in any way, in order to determine the absence or presence of conditions or discontinuities that may have an effect on the usefulness or serviceability of that object [6]. In other words, the examination of an object that does not affect its future usefulness.

As existing structures age, effective inspection has become a greater issue due to environmental, economical and socio-political aspects. Virtually all concrete structures exposed to natural environments experience deterioration over time. For example, instances of ageing degradation have occurred relatively early at some US plants which threatened continued operation. Consequently, nuclear plants seeking to extend operating life to 60 years will have to demonstrate that passive structures are capable of continuing to fulfill their intended function with an adequate level of safety.

Therefore structural integrity has to be guaranteed by developing optimal maintenance strategies. However, one problem that has been prevalent within the concrete industry for years is that the true properties of an in-place specimen have never been tested without leaving a certain degree of damage on the structure.

Inspection personnel have difficulty determining the quality of in-situ concrete that has experienced decay without direct material sampling. The disadvantage to material sampling is that an inspector must remove a portion of the structure, usually by means of coring, and make repairs to the sample area. Removing cores from a concrete structure is a destructive process that can weaken the structure and usually affects the structural performance and durability.

It is believed that new, innovative NDT techniques will have to be developed and/or optimised to demonstrate their capability to examine an object by its physical characteristics (geometry, composition, temperature) without damaging its structure. Techniques that would allow engineers to detect subsurface deterioration during routine inspections can help in their efforts to prevent major defects from occurring.

Moreover, these procedures would allow engineers to optimize the life-cycle cost of a constructed facility and minimize disturbance to its users. With the many recent technological advances in NDT several methods for evaluating concrete structures have been implemented to realize this task. NDT approaches such as liquid penetrant test, stress wave transmission, impact-echo, radar, radiography, and infrared thermography are useful for qualitative condition surveys as well as identification of internal features such as voids or fracture areas.

Therefore, it is believed that NDT has potential applications in three key areas in the management of safety related concrete structures [7] :

- determination of as-built (or current) structural details;
-

- detection of inclusions (air, water...);
- characterisation and quantification of inclusions.

The latter includes the use of NDT techniques as a means for monitoring concrete ageing. A distinction has been drawn between detection, and characterisation and quantification of inclusions, as the requirements for NDT in each application differ. Detection of inclusions only requires that a given technique identify that an inclusion is present, and give an approximate indication of location and extent. Characterisation and quantification techniques should be able to measure the nature and extent of an inclusion with sufficient sensitivity to allow an engineering assessment of the impact of the flaw on safety and serviceability of the structure.

Efficient and accurate techniques are needed for a reliable evaluation of safety in concrete structures. Although, imaging is routinely used in various fields, implementation of these technologies in NDT of civil engineering systems, especially of concrete structures, offers many challenges and requires additional development due to the composite nature of concrete and the complexities of reinforced or prestressed concrete systems [8].

In all cases, the objective is likely to obtain data for use in an engineering assessment. Other destructive and semi-destructive techniques are available to carry out the above tasks. Also, in some structures extensive instrumentation is available but they will not be discussed in this research work. There are many techniques that are currently being researched for the NDT of materials. In the present research work it will be discussed only the most common methods of assessment of conditions of concrete structures will be discussed.

## 1.1 Overview

Concrete is a highly versatile construction material well suited for many applications that differ from other construction materials in that it can be made from an infinite combination of suitable materials and that its final properties are dependent on the treatment after it arrives at the job site. Strength, durability and many other factors depend on the relative amounts and properties of the individual components. It is electrically nonconductive but usually contains significant amounts of steel reinforcement. While concrete is noted for its durability, it is susceptible to a range of environmental degradation factors, which can limit its service life.

There has always been a need for test methods to measure the in-place properties of concrete for quality assurance and for evaluation of existing conditions. Ideally, these methods should be nondestructive so that they do not impair the function of the structure and permit re-testing at the same locations to evaluate changes in properties with time.

There are many NDT techniques, each based on different theoretical principles, and producing as a result, different sets of information regarding the physical properties of the structure. These properties, such as electromagnetic and ultrasonic wave velocities, electrical resistivity and so on, have to be interpreted in terms of the structure's characteristics.

While they have great potential for in-situ applications, nondestructive techniques are not perfect. Furthermore, many structural problems are best studied by a particular NDT method, depending upon which physical properties of the construction materials offer the best chance of being reliably determined. There are five major factors, which need to be considered in the design of an NDT survey, as follows [9]:

1. the required depth of penetration into the structure;
2. the vertical and lateral resolution required for the anticipated targets;
3. the contrast in physical properties between the target and its surroundings;
4. signal to noise ratio for the physical property measured at the structure under investigation;
5. historical information concerning the methods used in the construction of the structure.

Careful application of all the above factors to the design of an NDT survey should result in a specification which either achieves the desired objectives or, more importantly, recommends an alternative approach if no NDT surveying method is deemed appropriate for the solution of the problem specified.

---

## 1.2 Problems in concrete

The following material properties affect the concrete resistance and are of importance for the safety evaluation of concrete structures:

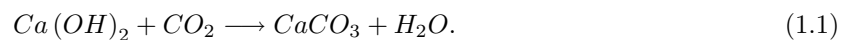
- compressive strength,
- carbonation depth,
- chloride content,
- porosity and,
- existence of voids and inhomogeneities.

### 1.2.1 Compressive strength

High strength concrete requires a low water/cement (w/c) ratio in the mixture. The selection of a w/c gives the engineer control over the final properties of the concrete. It is an important decision because it is a tradeoff between two desirable properties: strength and workability. A mixture with a high w/c will be more workable than a mixture with a low w/c. However, a high w/c will bring to the concrete the frequency-dependent characteristics of the water.

### 1.2.2 Carbonation

During the hydration of cement  $Ca(OH)_2$  is formed resulting in the pH-value of the pore water being about 12.6. To prevent corrosion of the steel reinforcement a minimum pH-value of 11.5 is required. The  $Ca(OH)_2$  reacts with carbon dioxide in air resulting in a decrease of the pH-value:



The carbonation process is also called depassivation. Carbonation penetrates below the exposed surface of concrete extremely slowly. The significance of carbonation is that the usual protection of the reinforcing steel generally is neutralized by carbonation.

### 1.2.3 Chloride content

A high chloride content in concrete accelerates the corrosion process of the reinforcement. For safety evaluation of existing concrete structures the determination of chloride content, therefore, is an important part of the evaluation. A high chloride content of the concrete in most of the cases is caused by the use of salts. This process is often seen in marine and chemical industries environments.

### 1.2.4 Voids and inhomogeneities

Of special interest to the evaluation of concrete structures are poorly compacted spots in concrete members, so called honeycombs. In most cases, these imperfections are located at the concrete surface and can be found by visual inspection. To find voids inside the concrete, NDT methods must be used.

## 1.3 Most commonly used NDT methods for concrete

The NDT techniques most commonly used to assess concrete include radiography, impact-echo, ultrasonic, infrared thermography, acoustic emission and ground penetrating radar. Most of these techniques may also be used for other purposes like assessing pavements, bridge decks and so on. Next, some of the major techniques are briefly described.

---



Figure 1.1: Robot used for visual survey at the WTC disaster site.

### 1.3.1 Visual inspection

Visual testing is probably the most important of all nondestructive tests. Visual features may be related to structural serviceability, and material deterioration and it is particularly important that the engineer be able to differentiate between the various signs of distress which may be encountered. Extensive information can be gathered from visual inspection to give a preliminary indication of the structure's condition and allow formulation of a subsequent testing program.

In order to ensure optimal collection of information, an inspection concept is needed, including:

- description of the structure,
- historical information,
- possible removal of everything that prevents good visual access.

When searching historical information of a structure special attention should be paid to all kinds of modifications the structure may have suffered. It is obvious that the research of historical information does not only concern the time of construction, but its complete lifetime. In addition, some information about the construction details can be obtained in order to facilitate the use of other techniques.

In addition, visual inspection is fast, convenient and relatively inexpensive. This technique allows inspectors to make real-time evaluations and recommendations of a given structure, which is particularly valuable in emergency or safety inspections. Figure 1.1 shows a robot used in the World Trade Center disaster where the condition of concrete is evaluated without risk to human life<sup>1</sup>. Although disaster inspection is a highly specialized and limited field of research, the technology developed and implemented for this work will become more prevalent in the visual inspection industry.

The important limitation of the visual inspection technique is sight obstructions, which can be due to lighting, access or obstruction. Another disadvantage of visual inspection is the misinterpretation.

### 1.3.2 Liquids penetrant

The liquid penetrant examination method can be used for the NDT of nonporous materials. Liquid penetrant methods are nondestructive testing methods for detecting discontinuities open to the surface, such as cracks, through leaks, or lack of fusion. These methods are applicable to in-process, final, and maintenance examinations. They can be effectively used in the examination of nonporous, metallic materials, both ferrous and nonferrous, and of nonmetallic materials such as glazed or fully densified ceramics, certain nonporous plastics, and glass.

The surface of the part under evaluation is coated with a penetrant in which a visible or fluorescent dye is dissolved or suspended. The penetrant is pulled into surface defects by capillary action. After a

---

<sup>1</sup>Five victims of the WTC disaster were successfully found by the robots.

waiting period to insure the dye has penetrated into the narrowest cracks, the excess penetrant is cleaned from the surface of the sample. A white powder, called developer, is then sprayed or dusted over the part. The developer lifts the penetrant out of the defect, and the dye stains the developer. Then by visual inspection under white or ultraviolet light, the visible or fluorescent dye indications, respectively, are identified and located, thereby defining the defect [10].

Although liquid penetrant methods have been beneficial in the location of surface defects in solids, they have several limitations. Existing liquid penetrant examination techniques are applicable to the inspection of nonporous solids and are thus not applicable to the survey and inspection of concrete structures and buildings. The majority of these are composed of concrete and masonry; both of which are porous materials.

### 1.3.3 Magnetic testing

Magnetic particle testing is an NDT technique for crack identification that relies on local or complete magnetization of the component or surface being analyzed. The idea of using magnetic techniques for nondestructive testing and evaluation of ferromagnetic materials originated in 1905.

When a crack is present on the surface, then some magnetic flux will leak out from the sides of the crack (provided that the magnetic flow is in a suitable direction relative to the crack).

A magnetic field is established in a component made from ferromagnetic material. The magnetic lines of force or flux travel through the material, and exit and reenter the material at the poles. Defects such as cracks or voids are filled with air that cannot support as much flux, and force some of the flux outside of the part. Magnetic particles distributed over the component will be attracted to areas of flux leakage and produce a visible indication.

Currently, magnetic testing have no relevant use in the NDT of concrete itself due to the fact that concrete is a nonmagnetic material. However, the use of magnetic methods for the inspection of ferromagnetic materials embedded within concrete structures has proven to be extremely valuable.

### 1.3.4 Half-cell electrical potential method

The method of half-cell potential measurements normally involves measuring the potential of an embedded reinforcing bar relative to a reference half-cell placed on the concrete surface. The half-cell is usually a copper/copper sulphate or silver/silver chloride cell but other combinations are used. The concrete functions as an electrolyte and the risk of corrosion of the reinforcement in the immediate region of the test location may be related empirically to the measured potential difference. In some circumstances, useful measurements can be obtained between two half-cells on the concrete surface.

The method and the equipment has the advantage of being simple. This allows an almost nondestructive survey to be made to produce isopotential contour maps of the surface of the concrete member. Zones of varying degrees of corrosion risk may be identified from these maps. The limitation of the method is that it cannot indicate the actual corrosion rate. It may require to drill a small hole to enable electrical contact with the reinforcement in the member under examination, and surface preparation may also be required. It is important to recognize that the use and interpretation of the results obtained from the test requires experienced operators who will be aware of other limitations such as the effect of protective or decorative coatings applied to the concrete.

This technique can also serve as a complement when applied with other techniques such as resistivity surveys to obtain a greater reliability [11] and such surveys could also be combined with radar surveys to assess the capabilities of radar in this field. For example, the electro-potential survey can identify areas of active corrosion with a reasonable degree of reliability and it may be possible to correlate these with specific signatures in radar signals.

### 1.3.5 Impact-echo system

Impact echo is a technique developed for evaluating concrete structures [12] that is normally used in structures of thickness up to 1 meter, although in principle it may be used for thicknesses of several metres.

---

The low frequency compression wave which is sent out by impact on the surface of the concrete is reflected from the boundaries of the concrete element or from internal flaws. A transducer placed in the vicinity of the impact records surface displacements caused by these reflected waves. The resulting waveform is transformed into the frequency domain using a Fast Fourier Transform.

A transfer or frequency response function is then calculated for the system and reflections or echoes of the compressional wave energy are indicated by pronounced resonant frequency peaks in the frequency spectrum. These peaks correspond to the thickness or flaw depth resonant frequencies and knowing the compressional wave velocity in concrete the depth to the corresponding flaw can be calculated.

Figure 1.2 shows a typical impact-echo system. Impact echo has been effective for testing and detecting flaws in large surface areas of concrete, although analysis of results can be complicated by complex geometries.

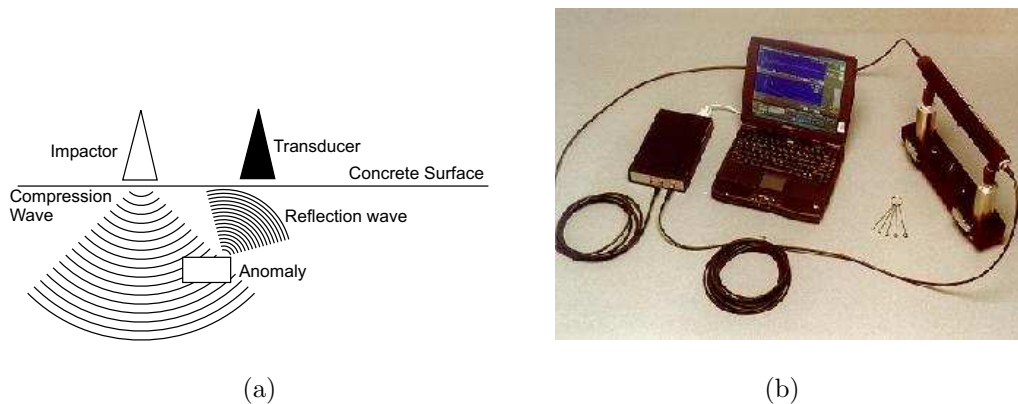


Figure 1.2: Typical impact-echo system: (a) Schematic (b) Equipment.

Impact-echo testing of bridges has focused largely on identifying voids in ducts. Finite element method (FEM) analyses of a laboratory experiment at the University of Edinburgh showed that defects can be identified provided a sufficiently high frequency ( $\lambda/2$  with respect to the defect) [13].

The major disadvantage of the technique is the limited localized information, requiring a series of point-by-point measurements to map larger regions [14].

### 1.3.6 Acoustic emission

Among the various NDT techniques, acoustic emission (AE) monitoring is arguably based on the simplest physical concepts, but is one of the most difficult techniques to implement in practice.

The AE testing process begins with forces acting on a body as seen in Fig. 1.3; the resulting stress is the stimulus that causes deformation and with it, acoustic emission. This emission is captured by a sensor (the sensor is a piezoelectric transducer) that produces an electrical signal, which is passed to electronic equipment for further processing [6].

Acoustic emission is highly dependent on the stress history of the scanned structure, which is also dependent on the material properties and the type of deformation produced during the emission.

Acoustic emission testing is usually performed in rotating equipment, some composites and other structures subject to stress or loading. Large areas can be monitored to detect deteriorating conditions. However, sensors must contact the test surface. For location of flaws, multiples sensors are required.

The main use of acoustic emission is the detection of areas of growing degradation in concrete structures. It may be possible to differentiate between different types of defects through analysis of the acoustic emissions generated as defects develop [15] [16] [17].

A further application is the detection of non-growing cracks through the weak acoustic emissions generated by relative movement of the crack walls [18]. Some structures may be suited to carrying out ultrasonic and AE investigations at the same time because of the similarities in the energy detected [19].

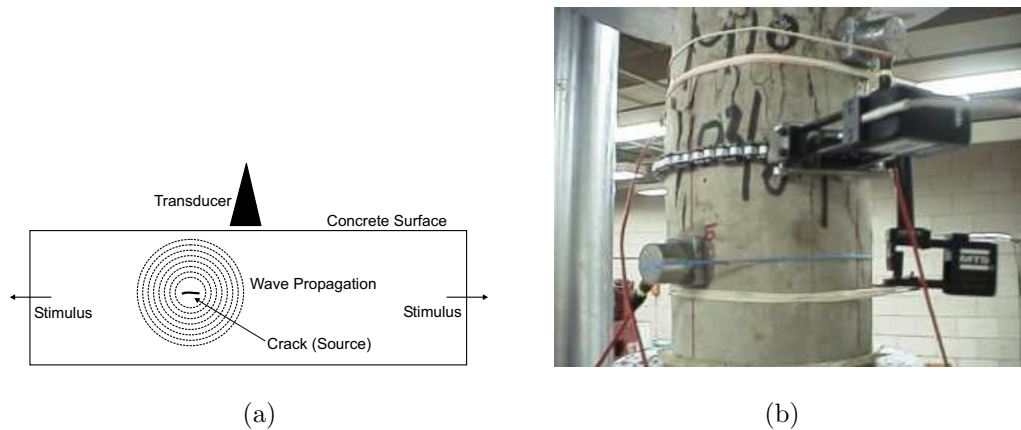


Figure 1.3: Set-up for acoustic emission test: (a) operating principles (b) Test equipment.

### 1.3.7 Ultrasonic reflection method

The ultrasonic method is a stress wave propagation method that involves measuring the travel time, over a known path length, of a pulse of ultrasonic waves. The pulses are generated into the concrete by a piezoelectric transducer, and the response of the concrete depends on its geometry and mechanical properties. The signal is either the transmitted signal to another transducer (pitch-catch method) or reflected back to the original transducer (pulse-echo method). Ultrasonic testing uses sound waves with frequencies greater than the human hearing limit (above 20 kHz) to examine materials.

The system measures the time it takes for the pulse to travel from the transmitting to the receiving transducers. The presence of low density, or cracked concrete increases the travel time which results in a lower pulse velocity. By conducting tests at various points on a structure, locations with lower quality concrete can be identified by their velocity.

The observed signal can give a detailed account of the specimen under investigation. Using this method, it is possible to determine [20]:

- the ultrasonic wave velocity or the thickness of the specimen;
- the presence of a flaw, defect, or delamination, and its size, shape, position, and composition;
- material properties, such as density and elastic constants.

This method was the first one developed for the testing of concrete [9].

In ultrasonic testing, the main factor to overcome is the coupling between the transducer and the structure's surface under test. A coupling agent should be used to smooth out surface irregularities and eliminate any air between the transducer and the surface. In general this agent is a gel-coupling material that fully wets the transducer and the surface of the tested structure, to temporarily adhere the transmitter and the receiver to the surface. In addition, ultrasonic waves typically cannot reveal planar flaws (cracks) whose length lies parallel to the direction of wave travel [20].

The availability of increasingly powerful personal computers has led to a developing interest in the use of ultrasonic tomography [21] [22] [23]. More sophisticated processing techniques may also be applied to standard ultrasonic signal data sets to improve resolution and sensitivity to defects [24].

Moreover, there is a prospect for using new or multi-element sensors, which can further improve the quality of the inspection [25] [26]. Because of similarities in the penetration, resolution and signal processing, there seems to be considerable scope for using ultrasonics and radar inspection techniques in combination.

### 1.3.8 Thermography

Thermography is a surface measurement technique with some capabilities to indicate sub-surface conditions and the presence of defects through features of the thermal image at the surface [27]. The operating



Figure 1.4: Road condition assessment using thermography.

principle consists in exposing the surface under inspection to thermal bursts coming from a thermal source (hotter or cooler). Those burst can last anything from a few milliseconds to a few seconds, depending on the experiment. During and immediately after the exposure, the temperature of the specimen is monitored using an infrared camera [28]. Figure 1.4 shows the thermography image from a deteriorated road section.

The infrared radiation varies from  $0.75$  to  $100 \mu\text{mm}$ , and it is often divided in four sub-regions near ( $0.75 - 3 \mu\text{mm}$ ), middle ( $3 - 6 \mu\text{mm}$ ), far ( $6 - 15 \mu\text{mm}$ ) and extreme infrared ( $15 - 100 \mu\text{mm}$ ). Infrared cameras can be defined as short wave (SW-middle infrared), and long wave (LW-far infrared) according to the operation wavelength range. The radiation measured by the camera is a function of the target surface temperature, but it depends also on the value of emissivity. Emissivity is the relationship between the efficiency of a radiant surface and the efficiency of a blackbody. The emissivity depends on the given material, the material temperature and the surface shape (planar, or non planar). The value of emissivity is important, because this value is the proportionality constant between the target temperature and the energy radiated by the target surface [29].

The method generally has a low spatial resolution because of the low thermal conductivity of concrete materials, but has been used to show the presence of voids, porosity, spalling or de-lamination and cracks. It may be used in a *static* mode, where steady state, in-service, temperature variations at the surface can be related to features below the surface; a *dynamic* application is also possible - transient thermography [30] that is essentially limited to surface or near surface inspections.

Both techniques have been shown capable of locating rebars in concrete structures, although the time involved is significant and their practicality is somewhat questionable. Some studies have shown that thermography can be used as a means of determining the location of delaminations on roads and pavements. This is a dynamic approach, reliant on the diurnal heating from the sun and consequently limited to outdoor usage over specific time slots (sunrise and sunset).

### 1.3.9 Covermeter

Covermeters are routinely used in inspection of nuclear structures. They measure variations in one of several possible electrical parameters of a detector as it scans over the test area [31]. Changes in the parameter being measured due to the presence of steel and other objects in the sub-surface enable an estimate of the size of the object or its depth below the surface to be determined. By using ratio measurements made with a covermeter, it may be possible to improve the accuracy of its results and obtain a measurement of rebar diameters [32].

The operating principle shown in Fig. 1.5 consists in a transmitter coil that radiates an electromagnetic field which induces currents in the subsurface. The currents, in turn, induce a secondary electromagnetic field. The secondary field is then intercepted by a receiver coil. The voltage measured in the receiver coil is related to the subsurface conductivity. These conductivity readings can then be related to subsurface

conditions.

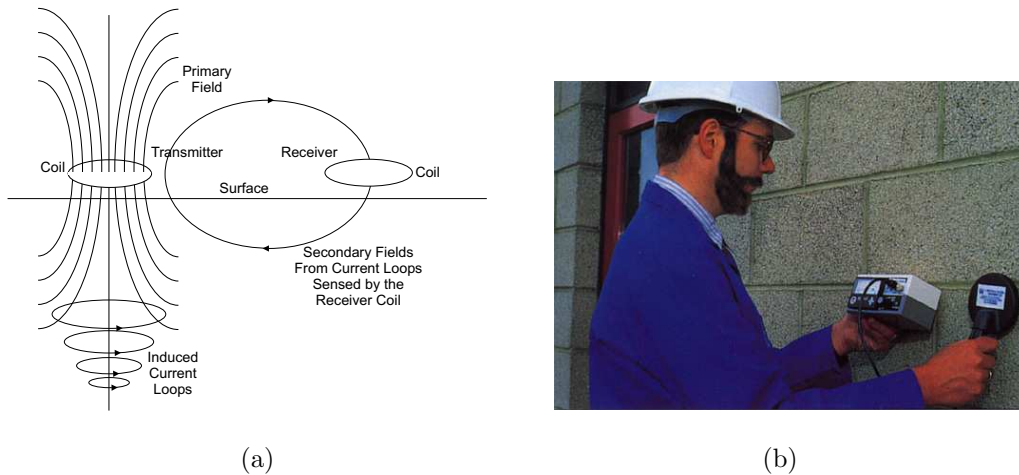


Figure 1.5: Covermeter operating principles: (a) Schematic (b) Test equipment.

The influence of steel on the induced current has a non-linear relationship with the thickness of the concrete and is also influenced by the diameter of the rod. However, modern covermeters are designed and calibrated to accommodate these effects and with a careful application excellent results can be achieved. It should be noted that if the concrete has been penetrated by saline water the increased electrical conductivity of the concrete above the reinforcing rods may affect the accuracy of the results measured on the covermeter [9].

### 1.3.10 Electrical resistivity

Measurements of resistivity can provide an indication of the presence, and possibly the amount, of moisture in a concrete structure, so clearly can have a bearing on evaluating the extent and rate of corrosion of rebars and other included steelwork [11][33][34]. However, resistivity measurements are sensitive to the disposition of steelwork within the structure, so assessment of conditions in a structure and the likelihood of corrosion occurring needs to be made with careful reference to its construction [35].

Resistivity is dependent on the moisture condition of the concrete, on the permeability and interconnectivity of the pore structure, and on the concentration of ionic species in the pore water of concrete. In general, the concrete structure can be evaluated as:

- poor quality, saturated concrete has low resistivity (e.g.  $<10 \text{ k}\Omega \cdot \text{cm}$ );
- high-quality, dry concrete has high resistivity (e.g.  $>25 \text{ k}\Omega \cdot \text{cm}$ ).

Typically, an electrical current is applied to the ground through a pair of electrodes. A second pair of electrodes is then used to measure the resulting voltage (see Fig. 1.6). The greater the distance between electrodes, the deeper the investigation.

The measurement depends upon subsurface permittivity changes. These changes can be related to the ability of corrosion currents to flow through the concrete, which is a function of the water/cement ratio, the moisture content and the salt content. The major problem associated with this method is that of achieving a good electrical contact between the electrodes and the concrete structure.

### 1.3.11 Radiography

The application of radiography methods to the inspection of concrete was developed in the 1950s. This method involves a source of electromagnetic radiation and a sensor to measure the intensity of the radiation after it has travelled through the structure. The structure is evaluated its attenuation or

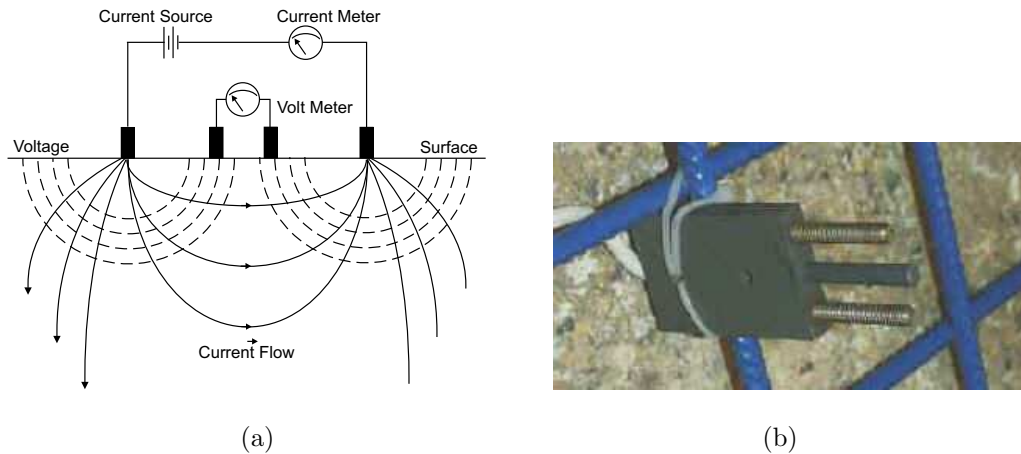


Figure 1.6: Electrical resistivity operating principles: (a) Schematic (b) Real equipment

absorption of the penetrating radioactive energy. The radiation which passes through the structure can be detected and recorded on either film or sensitised paper as shown in Fig. 1.7.

In radiography, X-rays,  $\gamma$ -rays or neutron rays can be used for concrete assessment. There are two basic methods to use X-rays and  $\gamma$ -rays in nondestructive testing of concrete. In the transmission method, the amplitude of the radiation passing through a member is measured. In the backscatter method, a radioactive source is used to supply gamma-rays and a detector close to the source is used to measure the backscattered rays [36].

Radiographic techniques are not widely used in inspection of safety related concrete structures because they are unsuited to penetration of the thick ( $>1\text{m}$ ) sections commonly encountered, require dual sided access and can present significant operational difficulties. Nevertheless, gamma radiography (together with gamma scintillation techniques) has been effective for determining internal damage in thin, lightly reinforced structures. It is of particular value for detection and measurement of reinforcement/prestressing tendons and voids but can only be used for structures less than a metre or so in thickness.

There are newly developed high-energy X-Ray accelerators which are portable and compact. These allow practical inspection of concrete up to 1.2m thick. Real time radiography is a possible area for development which could be combined with tomographic techniques to obtain improved results.

However, there are safety hazards with the use of radiation devices. Radiation cannot be seen, tasted, or felt. It has no odor and if humans are subjected to radiation exposure, the effects are not manifest for a period of time.

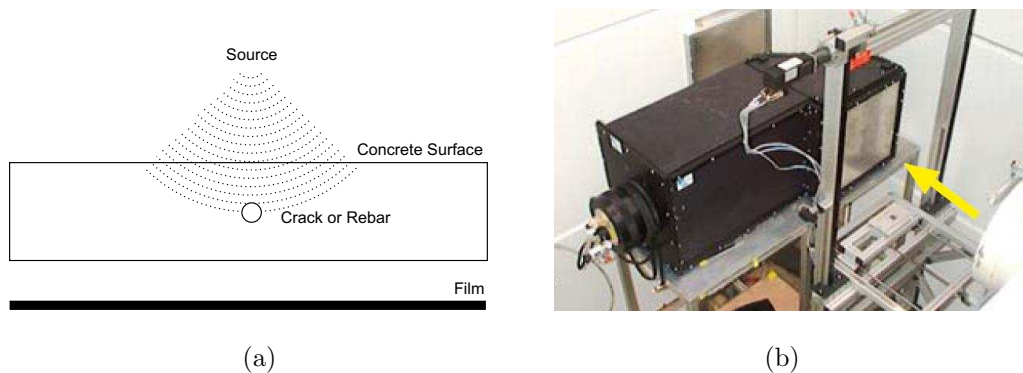


Figure 1.7: Radiography Principles: (a) Schematic (b) Test equipment.

### 1.3.12 Ground penetrating radar

In recent studies, radar technology proved to be the cheapest and easiest method for mapping reinforcements but neither characterisation of flaws by dimension and material nor crack detection could be demonstrated [37]. Nevertheless radar has significant potential for development by way of software for signal and image processing to improve resolution.

The development of specialised antennas with more appropriate beam width and other characteristics for concrete structures is considered to be useful. For application in nuclear power plants, an assessment of emission levels may be needed to permit usage within the plant to ensure electromagnetic compatibility. There is an European project on radar in the building and construction industries [38], and a completed concrete society report [7, 8] which addresses some of the needs identified.

Radar (acronym for RAdio Detection And Ranging) is analogous to the pulse-echo (or pitch-catch) technique previously discussed, except that pulses of electromagnetic waves (short radio waves or microwaves) are used instead of stress waves. Radar was developed during World War II to provide early warning of approaching enemy aircraft. During the 1960s, the need for a device to locate non-metallic land-mines<sup>2</sup> provided the impetus for the development of high resolution ground probing radar. In the 1970s, radar began to be applied in the field of civil engineering.

In civil engineering applications of radar, relatively short distances and small targets are involved, therefore, devices were developed to emit very short pulses of electromagnetic waves. For this reason the technique is often called short-pulse radar, impulse radar, or ground penetrating radar (GPR). The radar operating principle is analogous to that of the stress wave, echo methods.

An antenna emits a short duration pulse (on the order of nanoseconds) of electromagnetic (EM) waves. The pulse travels through the underlying material, and when the pulse encounters an interface between dissimilar materials, some of the energy is reflected back towards the antenna. The antenna receives the reflected portion of the pulse and generates an output signal (Fig. 1.8).

An important characteristic of the radar system is the duration of the pulse. To be able to differentiate echoes from closely spaced objects (resolution), the pulse should be short. A short pulse contains high frequency EM waves. The attenuation of the pulse as it travels through the material is a function of the frequency content: higher frequencies result in more attenuation. Thus a compromise between resolution and penetration ability must be formulated. The typical frequencies used in concrete evaluations are between 0.2 and 2GHz. For a given frequency, the penetration is affected by the conductivity of the material. Since moisture in concrete or soil increases conductivity, the penetrating ability decreases with increasing moisture content.

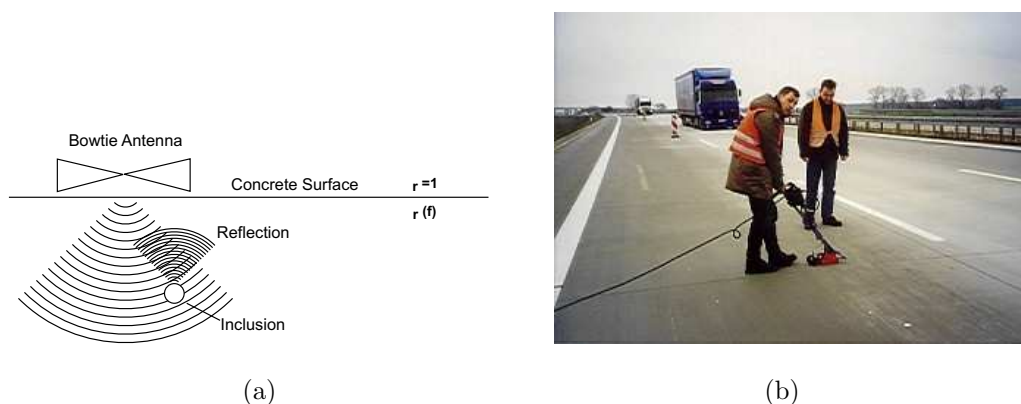


Figure 1.8: Grounding penetrating radar principles: (a) Schematic (b) Test equipment.

<sup>2</sup>Over 100 million anti-personnel mines are embedded in over 70 countries. About 24000 people are killed or injured every year by these anti-personnel mines.

### 1.3.13 Use of techniques in combination

There are two reasons for combining techniques. The first is to use a well developed technique to validate results from another that is less well developed, but which has the potential to provide greater reliability or other benefits. This is mainly applicable during the demonstration phase for a technique. The second reason is to exploit synergies between techniques, where techniques give similar coverage of a structure but are not sensitive to precisely the same parameters or features, or where information gathered by one technique can be used as input data for interpreting/calibrating the results from another technique.

Basically, the techniques can be combined according to their advantages and limitations. Table 1.1 summarizes the characteristics of the techniques described above.

### 1.3.14 Background radar for concrete inspection

Radar technology for subsurface applications was forgotten until the late 1950s when a US Air Force plane crashed into the ice in Greenland while it was trying to land; it had misread the altitude given by its radar system *seeing* through ice. This event started investigations into the ability of radar to see into the subsurface, especially for ice sounding, mapping subsoil properties, and locating water tables [39]. A new impetus was given to the subject in the early 1970s when lunar investigations<sup>3</sup> and landings were in progress.

Geophysical applications grew from that period for identifying relatively deep features such as strata changes and more recently environmental features such as contaminants or buried gas tanks and pipes in site surveys. The range of applications has been expanding steadily, and now includes archaeology, road and rail quality assessment, location of voids, tunnels and landmines, as well as remote sensing by satellite.

In the past few decades, radar has been increasingly used as a tool for testing reinforced and mass concrete structures. Since the 1980s, has been used for different applications related to the assessment of concrete structures like estimation of pavement layer thicknesses and the detection of moisture.

Radar has been employed in concrete applications such as the location of delaminations in bridge decks [40] (corrosion of reinforced steel), the detection of buried pipes [41], the determination of concrete pavement thickness [42] and the location of reinforcements [43]. Today the most common surveys are:

1. location of reinforced steel and buried pipes.
2. identification of construction details.
3. location of construction features.
4. crack detection.

The use of radar in NDT inspection of nuclear structures became common in the 1990s [44][45][46] when many significant developments in system hardware particularly in data analysis and enhancement software [47][48][49] and significant development of signal processing to improve resolution [50, 51] have been reported. The aspects that are also likely to have potential for development include assessing the degree of corrosion and the integrity of reinforcing bars [51, 52] and the detection of excess chloride in concrete [53].

Currently, research continues in many areas including sizing and antenna performances, with assessment of in-situ concrete conditions being of particular interest. This includes quantifying moisture and chloride content as well as their influence on signal velocity and hence depth estimations. Signal processing techniques and imaging algorithms are another issue of interest for improving the radar assessment.

---

<sup>3</sup>Surface electrical properties experiments were carried out on Apollo 17 with a lunar rover to sound the subsurface.

---

Table 1.1: NDT techniques characteristics

Method	Principle	Advantages	Limitations
Ground Penetrating Radar	Radio frequency waves (0.5 to 2GHz) from radar transmitter are directed into the material. The waves propagate through the material until a boundary of different electrical characteristic is encountered. Then part of the incident energy is reflected and the remainder travels across the boundary at a new velocity. The reflected (echo) wave is picked up by a receiver.	It can be used to survey large areas rapidly for location of reinforcement, voids and cracks.	Results must be correlated to test results obtained from samples. Any features screened by steel reinforcement will not be recorded. With increasing depth, low level signals from small targets are harder to detect due to signal attenuation. It is expensive to use and uneconomical for surveying small areas.
Covermeter	The basic principle is that the presence of steel affects the magnetic field. An electromagnetic search probe is swept over the surface of the concrete under test. The presence of reinforcement within the range of the instrument is shown by movement of the indicator needle. When the probe is moved until the deflection of the needle is at a maximum, the bar in question is then parallel to the alignment of the probe and directly beneath it.	The presence of closely spaced reinforcing bar, laps, transverse steel, metal tie, wires or aggregates with magnetic properties can give misleading results. The meter has several scales for different bar sizes, therefore the bar diameter must be known if a true indication of cover is to be obtained.	The maximum range of the instrument for practical purposes is about 100 mm. It does not give indication of the quality of concrete cover or the degree of protection afforded to the reinforcement.
Acoustic emission	When a material is loaded part of it may be loaded beyond its elastic limit. Kinetic energy is released, this is known as in the form of acoustic emission. Emissions are inaudible but can be detected by sensors attached to the surface of a test object.	It monitors the response of existing structures to applied loads. It is capable of detecting onset of failure and locating the source of possible failures. Since acoustical signals come from defects throughout the structures, a few transducers are sufficient to detect and locate defects over large areas.	The equipment costs are high. The method requires means of loading the structure and complex electronic equipment. As the method is not yet fully developed it is still regarded as a laboratory method.
Thermography	An infrared scanning camera is used to detect variations in the infrared radiation output of a surface. Thermal gradients arise because of difference in surface temperature between sound and unsound concrete. Hence delaminations in concrete surfaces can be detected. The temperature gradients are displayed on a TV screen in the form of colour thermal contours.	It is portable and permanent records can be made. Testing can be done without direct access to the surface and large areas can be rapidly inspected using infrared cameras.	It is an expensive technique. Reference standards are needed and a heat source to produce thermal gradient in the test specimen may also be required. It is very sensitive to thermal interference from other heat sources. Moisture on the surfaces can also mask temperature differences.

Ultrasonic pulse echo	Pulsed compressional waves are induced in materials and those reflected back are detected by a hand-held accelerometer. This is connected to a signal processor that integrates the signal and displays it on an oscilloscope.	It is portable, simple and cheap to use. Photographic records can be made. Internal discontinuities can be located and their sizes estimated.	It cannot determine net cross section of piles or its bearing capacity. Interpretation of results can be difficult and calibrating standards are required. It also requires smooth surfaces for the probe.
Radiography	A radioactive isotope directs a beam at a member and an X ray photographic plate is held against the back face. Gamma radiation attenuates when passing through a building component. The density and thickness of the materials of the building component will determine the degree of attenuation. Photographic film records are usually made, which could be analyzed.	It can be used for field measurements, simple to operate, relatively inexpensive compared to X ray radiography and is applicable to a variety of materials.	In many cases the method is unusable because it is difficult to place the photographic films in a suitable position. There are also the problems of health and safety.
Impact-echo	It is based on using a short-duration mechanical impact to generate low frequency stress waves (2 to 20 kHz, typically) that propagate into the structure and are reflected by flaws and external surfaces. The impact can be produced by tapping a steel ball against the concrete surface or by hitting the surface by using a hammer.	When properly used, the impact-echo method has achieved unparalleled success in locating flaws and defects in highway pavements, bridges, buildings, tunnels, dams, piers, sea walls and many other types of structures. Accuracy of 3 percent or better.	All stress wave energy is reflected at air boundaries, and no information can be obtained on materials beyond an initial void or delamination. Limited localized information, requiring a series of point-by-point measurements to map larger regions.
Electrical resistivity	The resistivity of concrete is related to its moisture content and to a lesser degree to its chloride content. Resistivity is measured by inserting electrodes into small holes on the surface and passing an alternating current through them. The difference in potential is then measured.	The equipment is inexpensive, simple to operate and many measurements can be rapidly made. It is very useful when used in conjunction with other methods of testing, e.g. half-cell potential.	It is not reliable at high moisture contents. It needs calibration and precise results are not usually obtained. The electrodes require good contact and nearby bars can affect readings.

## 1.4 Modeling needs

Computers have had significant impact on the modeling of NDT phenomena. In numerical modeling a physical phenomenon under investigation is represented by a mathematical system which can be solved numerically. The results obtained from the mathematical investigation of such a model are then interpreted in terms of the original phenomenon and serve to develop an understanding of the physical processes involved. The most important task in NDT modeling is the prediction of faults or inclusions in the physical parameters characterizing the region under test.

NDT modeling involves calculating a physical magnitude i.e. electromagnetic field, force, radiation, in a model defined by a postulated distribution of parameters in the medium under study, together with the exciting source. This can be done by solving finite-difference and finite-element equations. Concerning this work, the fundamental mathematical model is represented by Maxwell's equations, which prescribes the analytical relationship in the form of a system of first order vector equations between the components of electric and magnetic fields and the parameters of the medium under test.

The design of radar systems has been subjected to fundamental changes. Electronic devices are no longer designed on a simple desk using tables and calculators with inevitable design errors. Today, the design is computer aided, and both highly complex radars and complete electronic systems are simulated immediately. Design errors are excluded by a great deal by simulation. In reality, no designer and no simulation is perfect, so failures will still be detected on prototypes. However, the number of redesigns at the prototype stage has dropped to a reasonable level.

Traditionally NDT modeling seeks to improve the systems' sensors design and provide data for imaging. Imaging of defects in concrete structures plays an important role in NDT. They are usually applied to pulse-echo data carried out by either acoustic, elastic or electromagnetic waves.

However, the numerical modeling of the NDT approach still has all the limitations associated with the assumptions made to derive the equations in the first place, aside from the additional errors relating to the numerical techniques employed.

This chapter contextualized the use of NDT techniques for the assessment of concrete structures. The operating principles, advantages and limitations of the most commonly used techniques for this research purpose were outlined. It can be seen that no single technique or method has proven to give a complete answer for the NDT of concrete. The possible solutions to solve this problem are the use of techniques in combination and the improvement/optimization of a single technique. In this context, numerical modeling of the NDT assessment plays an important role for the development of best suited sensors and interpretation techniques for a given application.

---



## Chapter 2

# Numerical modeling

The systematic study of electromagnetic fields began in the late 1600 when *William Gilbert* published his book called *De Magnete* in which he described experiments in electricity and magnetism and introduced the word electricity. However, mathematical analysis of electromagnetic phenomena began only in the XVII century when *Charles-Augustin Coulomb* presented his three reports on electricity and magnetism explaining the laws of attraction and repulsion between electric charges.

However, significant changes in the interpretation of the electromagnetic phenomenon were proposed by *Michael Faraday*. Between 1821 and 1848 he created and studied a large number of experiments concluding that the phenomenon created by electric charges or magnetic dipoles could be represented by models based on field lines.

In 1864, *James Clerk Maxwell* presented his most important contribution extending and formulating mathematically the early work of *Michael Faraday*, *André-Marie Ampère*, and others into a linked set of differential equations. The mathematical consequence of these equations was that the electromagnetic waves propagate at the speed of light. Maxwell (1865) wrote:

*"This velocity is so nearly that of light, that it seems we have strong reason to conclude that light itself (including radiant heat, and other radiations if any) is an electromagnetic disturbance in the form of waves propagated through the electromagnetic field according to electromagnetic laws."*

In 1887, *Heinrich Rudolf Hertz* experimented with radio waves in his laboratory proving the theories of Maxwell and Faraday.

Today, 120 years later, engineers and scientists all around the world use computers in many configurations to study electromagnetic waves by solving Maxwell's equations with different numerical techniques. The impact of these researches in the society can be observed in many disciplines.

The interest in the modeling of NDT can be explained by the fact that radar system design follows an iterative procedure, requiring the construction and evaluation of many prototype models. Unfortunately, the construction and evaluation of prototypes can be labor intensive, time consuming, and expensive. At this juncture, the electronics industry has been under pressure from the marketplace to design better, less expensive products, in less time. Some segments have responded with some success, by developing software tools and techniques that assist designers in their work. It appears that for radar system designers to be able to keep pace with the rest of industry, such tools and techniques will need to be developed to assist in the task of radar design.

As an alternative to the construction of real prototype models, this research considers the development of specific tools that will build and evaluate mathematical models of prototypes on a given computer system. Naturally, in performing an evaluation, such a tool should yield data that any radar designer would have interest in. Such data might include the estimation of the scattering field from a buried target in a concrete structure.

For this research, FDTD, FEM, MoM and TLM techniques were selected to perform the required electromagnetic evaluation. Since both the construction of a model for the radar assessment of concrete structure as well as the technique itself are extremely computationally intensive, it was decided to use different techniques according to the objectives of simulation, interpretation and optimization of a radar assessment.

---

## 2.1 Basic electromagnetic equations

### 2.1.1 Maxwell's equations and constitutive relations

Consider a region of space that contains an electric current and charges, magnetic current and charges, and may have materials that absorb electric or magnetic field energy. Then using SI units, Maxwell's equations [54] are given in differential and integral form by

Faraday's Law:

$$\nabla \times \mathbf{E} = -\frac{\partial \mathbf{B}}{\partial t} - \mathbf{M}, \quad (2.1)$$

$$\oint_{ds} \mathbf{E} \cdot d\mathbf{l} = -\int_s \left( \frac{\partial \mathbf{B}}{\partial t} + \mathbf{M} \right) \cdot d\mathbf{s}, \quad (2.2)$$

Ampère's Law:

$$\nabla \times \mathbf{H} = \mathbf{J} + \frac{\partial \mathbf{D}}{\partial t}, \quad (2.3)$$

$$\oint_{ds} \mathbf{H} \cdot d\mathbf{l} = \int_s \left( \mathbf{J} + \frac{\partial \mathbf{D}}{\partial t} \right) \cdot d\mathbf{s} \quad (2.4)$$

Gauss' Law for the electric field:

$$\nabla \cdot \mathbf{D} = \rho_e, \quad (2.5)$$

$$\oint_{dv} \mathbf{D} \cdot d\mathbf{s} = \int_v \rho_e dv, \quad (2.6)$$

Gauss' Law for the magnetic field:

$$\nabla \cdot \mathbf{B} = \rho_m, \quad (2.7)$$

$$\oint_{dv} \mathbf{B} \cdot d\mathbf{s} = \int_v \rho_m dv, \quad (2.8)$$

In Eqs. 2.1-2.8, the following symbols (and their SI units) are defined:

- $\mathbf{E}$  : electric field (volts/meter),
- $\mathbf{D}$  : electric flux density (coulombs/meter<sup>2</sup>),
- $\mathbf{H}$  : magnetic field (amperes/meter),
- $\mathbf{B}$  : magnetic flux density (webers/meter<sup>2</sup>),
- $\mathbf{J}$  : electric current density (amperes/meter<sup>2</sup>),
- $\mathbf{M}$  : equivalent magnetic current density (volts/meter<sup>2</sup>),
- $\rho_e$  : electric charge density (coulombs/meter<sup>3</sup>),
- $\rho_m$  : magnetic charge current density (webers/meter<sup>3</sup>),

In linear, isotropic, nondispersive materials (materials having field-independent, direction-independent, and frequency-independent electric and magnetic properties) we can relate  $\mathbf{D}$  to  $\mathbf{E}$  and  $\mathbf{B}$  to  $\mathbf{H}$  using simple relations:

$$\mathbf{D} = \varepsilon \mathbf{E} = \varepsilon_0 \varepsilon_r \mathbf{E}, \quad (2.9)$$

$$\mathbf{B} = \mu \mathbf{H} = \mu_0 \mu_r \mathbf{H}, \quad (2.10)$$

where

---

- $\varepsilon$  : electrical permittivity (farads/meter),
- $\varepsilon_r$  : relative permittivity (dimensionless scalar),

being

$$\varepsilon_r = \varepsilon/\varepsilon_0 \quad (2.11)$$

- $\varepsilon_0$  : free space permittivity ( $\varepsilon_0 = 8,85 \times 10^{-12}$  farads/meter),
- $\mu$  : magnetic permeability (henry/meter),
- $\mu_r$  : relative permeability (dimensionless scalar),
- $\mu_0$  : free-space permeability ( $\mu_0 = 4\pi \times 10^{-7}$  henry/meter).

We also allow for materials with isotropic, nondispersive electric loss that attenuate  $\mathbf{E}$  fields via conversion to heat energy. This yields:

$$\mathbf{J} = \sigma \mathbf{E} \quad (2.12)$$

where  $\sigma$  is the electric conductivity (siemens/meter).

### Charge Conservation

Maxwell added the displacement current term to Ampere's law in order to guarantee charge conservation. Indeed, taking the divergence of both sides of Ampere's law and using Gauss's law  $\nabla \cdot \mathbf{D} = \rho_e$ , we get:

$$\nabla \cdot \nabla \times \mathbf{H} = \nabla \cdot \mathbf{J} + \frac{\partial}{\partial t} \nabla \cdot \mathbf{D} \quad (2.13)$$

Using the vector identity  $\nabla \cdot (\nabla \times \mathbf{H}) = 0$ , we obtain the differential form of the charge conservation law:

$$\nabla \cdot \mathbf{J} = -\frac{\partial}{\partial t} \rho_e. \quad (2.14)$$

In other words, charge does not disappear into (or get created out of) nothingness. Another consequence of this equation is that in good conductors, there cannot be any accumulated volume charge. Any such charge will quickly move to the conductor's surface and distribute itself such as to make the surface into an equipotential surface.

### 2.1.2 Interface Conditions

Maxwell's equations given above represented the fields in a given material. However, for a general case involving two different materials (Fig. 2.1), it is necessary to enforce field boundary conditions at the interface given by:

$$-\hat{n} \times (\mathbf{E}_1 - \mathbf{E}_2) = \mathbf{M}_s, \quad (2.15)$$

$$\hat{n} \times (\mathbf{H}_1 - \mathbf{H}_2) = \mathbf{J}_s, \quad (2.16)$$

$$\hat{n} \cdot (\mathbf{D}_1 - \mathbf{D}_2) = \rho_{e_s}, \quad (2.17)$$

$$\hat{n} \cdot (\mathbf{B}_1 - \mathbf{B}_2) = \rho_{m_s}, \quad (2.18)$$

where  $\mathbf{J}_s$  is the electric current density,  $\mathbf{M}_s$  is the magnetic current density,  $\rho_{e_s}$  is the surface electric charge density and  $\rho_{m_s}$  is the surface magnetic charge density. There are two special cases of interface conditions - those between a dielectric and a perfect conductor and between two dielectrics.

---

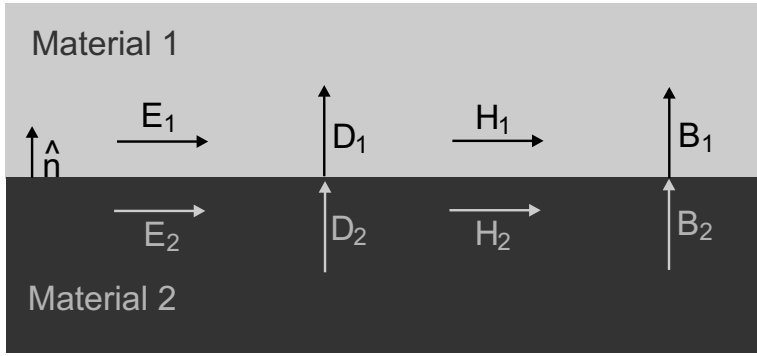


Figure 2.1: Interface between two materials.

### Perfect conductor interface

The special case frequently used when modeling antennas is defined when one material is a perfect conductor. In a perfect conductor there is no field inside the structure so the interface conditions are given by

$$\hat{n} \times \mathbf{E}_1 = 0, \quad (2.19)$$

$$\hat{n} \times \mathbf{H}_1 = \mathbf{J}_s, \quad (2.20)$$

$$\hat{n} \cdot \mathbf{D}_1 = \rho_{es}, \quad (2.21)$$

$$\hat{n} \cdot \mathbf{B}_1 = 0. \quad (2.22)$$

These equations show that there is no tangential electric fields in the conductor only normal electric fields. However there is a tangential magnetic field that generates a current in the surface of the conductor.

### Interface between two dielectrics

Consider now a region in the space with two dielectric materials. If there is no sources in the materials (density currents or charges) the interface conditions are given by:

$$\hat{n} \times \mathbf{E}_1 = \hat{n} \times \mathbf{E}_2, \quad (2.23)$$

$$\hat{n} \times \mathbf{H}_1 = \hat{n} \times \mathbf{H}_2, \quad (2.24)$$

$$\hat{n} \cdot \mathbf{D}_1 = \hat{n} \cdot \mathbf{D}_2, \quad (2.25)$$

$$\hat{n} \cdot \mathbf{B}_1 = \hat{n} \cdot \mathbf{B}_2. \quad (2.26)$$

These equations show that the tangential components of the fields are continuous just like the normal flux densities components in the interface.

### 2.1.3 Boundary conditions

Given domain of study there are many different functions that obey the Maxwell equations for the behaviour of the fields. However, only one solution is the real solution for an analyzed problem and to distinguish this solution it is necessary to impose special conditions on the problem. These conditions are known as boundary conditions. Some of them are discussed next.

#### Dirichlet conditions

The Dirichlet condition consists of imposing a value on the boundary of the problem. This condition is frequently applied when we know the value of a field, flux or charge in the region.

### Neumann conditions

This condition defines the behaviour of the normal component over the contour. It is frequently used to express symmetry conditions.

### Sommerfeld radiation condition

Scattering or radiation problems are considered "open-space problems" when the domain extends to the infinity. The solution of the problem requires the imposition of a boundary condition at infinity known as the Sommerfeld radiation condition.

### Absorbing boundary condition (ABC)

The Sommerfeld condition describes perfectly a physical phenomenon. However, this condition is imposed over the fields at the infinity and cannot be used in some numerical methods that require bounded domains. In this case, it is necessary to create a fictitious surface that limits the domain, originally open, to a closed domain. Here we need a boundary condition that permits all outward-propagating numerical waves to exit the domain as if the simulation were performed on a computational domain of infinite extent. In the process, the outer-boundary condition must suppress spurious reflections of the outgoing numerical waves to an acceptable level, especially after the reflected numerical waves return to the vicinity of the modeled structure.

## 2.1.4 Wave equation

Maxwell's equations describes coupled  $\mathbf{E}$  and  $\mathbf{H}$  fields. However, for some problems it is more convenient to work with decoupled equations. In this way, we can work with only the  $\mathbf{E}$  or  $\mathbf{H}$  field. However, this operation increases the differential order of Maxwell's equations. This new equation is defined as a wave equation. The advantage of working with a wave equation consists in solving the problem with only one unknown field (electric or magnetic). The wave equation for the electric field can be obtained by taking the curl of Faraday's equation and then replacing the magnetic flux term by Ampere's law. That results in:

$$\nabla \times \left\{ \frac{1}{\mu_r} \nabla \times \mathbf{E} \right\} - k_0^2 \varepsilon_c \mathbf{E} = -\nabla \times \left( \frac{\mathbf{M}}{\mu_r} \right) - j k_0 Z_0 \mathbf{J} \quad (2.27)$$

where  $\varepsilon_c$  is the complex-valued permittivity,  $k_0$  is the wavenumber in free space and  $Z_0$  is the intrinsic impedance of free space given by:

$$\varepsilon_c = \varepsilon_r - j\sigma / (\omega\varepsilon_0), \quad (2.28)$$

$$k_0 = \omega \sqrt{\mu\varepsilon_0}, \quad (2.29)$$

$$Z_0 = \sqrt{\mu/\varepsilon_0}. \quad (2.30)$$

## 2.2 Numerical techniques

For the study and understanding of the electromagnetic phenomena in any specific application, the solution of Maxwell's equations becomes necessary. There are two ways of solving the equations: analytical and/or numerical techniques.

Considering the EM problem of radar assessment the use of analytical methods fails due to: 1) the solution region is geometrically complex; 2) the boundary condition is time-dependent; 3) the medium is nonhomogeneous.

In the 1960s, electromagnetic modeling was done basically using analytical solutions. Many times the results were obtained through mechanical calculators. Later, the increase in availability of powerful computers and the development of powerful programming languages (FORTRAN, for example) allowed the use numerical techniques with increased precision.

In order to be efficient a numerical technique should ensure:

1. Precision,

2. Completeness,
3. Versatility,
4. Low computational cost.

However, no single numerical method or technique has been found to fulfill these four requirements. In decades, many different methods were developed. Some are based directly on the partial differential equations (PDE). Others tackle using integral representation.

These numerical methods have received considerable attention due to their theoretical rigour and precision of results. They are, in general, based on the solutions of the integral equations of Sommerfeld or on the solutions of Maxwell's equations in the time-domain. However, they maintain precision through increase in the cost and numerical complexity.

The most commonly used numerical methods include analyses of integral equations in the frequency-domain, analyses of integral equations in the time-domain and the approach of finite-differences in the time-domain.

However, no technique and/or method solves all types of problems. Some methods have been developed for solution of specific problems involving differential or integral equations.

### 2.2.1 Review on PDE based numerical methods

The numerical techniques based on the PDE, also known as domain methods, are efficient in the solution of problems in closed and open domains, filled with heterogeneous, nonlinear or anisotropic materials.

#### Finite-difference time-domain method

The finite-difference time-domain method (FDTD) is a technique to solve partial differential equations. This method has been applied to some problems in electromagnetism, including problems in open domain [55]. The finite-difference method is considered to be one of the oldest applied techniques in the solution of partial differential equations.

The FDTD is based on the replacement of differentiation by a simple approximation based on differences between points, divided by the distance between points [55]. In this way, it is possible to substitute a continuous equation, with an infinite number of degrees of freedom, with a discretized equation, with finite number of unknowns. Using this process, the original partial differential equation is transformed into a set of algebraic equations whose simultaneous solution supplies an approximate solution of the original equation of the problem [56].

The FDTD is of simple computational implementation. Moreover, it is capable of treating nonlinear and anisotropic problems, does not need a regular mesh, which allows good modeling of fields that vary quickly in space or the correct modeling of problems that possess curved surfaces. The cubic Yee's cell is shown in Fig. 2.2.

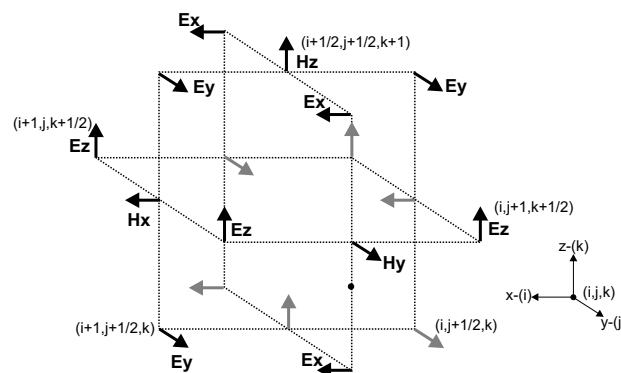


Figure 2.2: Yee's cell.

Rather than defining all electric and magnetic fields at individual points in space, the Yee cell distributes electromagnetic field components in a manner that makes the application of the discrete form of Maxwell's equations rather simple. In the Yee cell, electric field components are distributed along the edges such that each edge is parallel to the assigned component. Magnetic field components are defined to be normal and in the center of the cell surfaces.

### Transmission-line matrix method

The transmission line matrix (TLM) method is based on the use of electric circuits for the solution of scattering problems replacing a continuous system by a network or an array of lumped circuits. The method is inspired by Huygen's principle of wave propagation in space and time. The principle of Huygens affirms that every point on a primary wavefront serves as the source of spherical secondary wavelets such that the primary wavefront at some later time is the envelope of these wavelets. The wavelets advance with a speed and frequency equal to that of the primary wave at each point in space. This new numerical method was called the TLM Method [57].

In a typical TML simulation, a mesh of Transverse Electromagnetic (TEM) transmission lines represents the propagation medium. Electric and magnetic fields are made equivalent to voltages and currents on the network. Figure 2.3 shows a TLM Symmetrical Condensed Node (SCN) topology cell. SCN was developed to improve the analysis of electromagnetic waves by the TLM. It is exactly the TLM technique, except that the unit cell is constructed to overcome asymmetry and asynchronous problems. This node has the advantage of condensing the field components to one point in space.

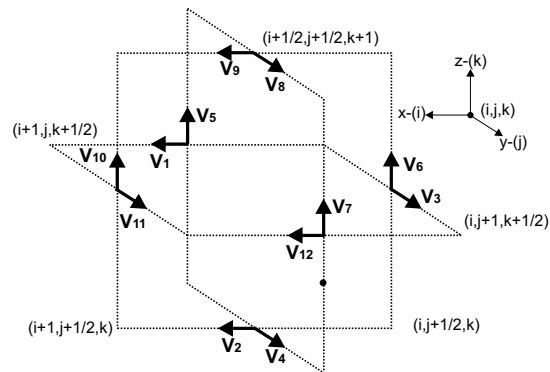


Figure 2.3: TLM 3D Symmetrical Condensed Node.

While the TLM is a physical model based on the principle of Huygens represented for interconnected transmission lines, the FDTD is a mathematical approach directly based on Maxwell's equations. In TLM, the magnetic and electric field components are located at the same position with respect to space and time whereas in the corresponding FDTD cell the magnetic field components are shifted by half an interval in space and time with respect to the electric field components.

However, the same FDTD simulation requires less of the half the time needed for an equivalent TLM simulation under the same conditions [58].

### Finite element method

The finite element method (FEM) is a numerical technique for solution of partial differential equations. This method started as a method of solving problems in structural mechanics but expanded quickly into other areas. In electromagnetism, FEM is associated with variational methods or residual methods. In the first case, the numerical procedure is established using a functional that must be minimized. The method does not work directly with the physical equation related to the problem, but with the corresponding functional.

On the other hand, residual methods are established directly from the physical equation to be solved. This is a considerable advantage compared with the variational methods since it is comparatively simpler

and easier to understand and apply. This is the main reason why most of the FEM work is performed using the residual method [59].

The principle of the finite element method consists of dividing the domain of the problem in small sub-domains, not necessarily with the same form and same dimensions. This procedure allows the FEM to vary the density of elements in accordance with the needs of the problem. In the interior of each element, the solution is represented by a polynomial function. Through the use of the method of weighted residuals or the 'variational' method, the partial differential equation is transformed into an algebraic system of equations whose matrix of coefficients is sparse and generally is also symmetrical.

The major advantage of finite element methods over other EM modeling techniques stems from the fact that the electric and geometric properties of each element can be defined independently. This permits the problem to be set up with a large number of small elements in regions of complex geometry and fewer, larger elements in relatively open regions. Thus it is possible to model configurations that have complicated geometries and many arbitrarily shaped dielectric regions in an efficient manner.

In addition, to take into account discontinuities at the interface between two media of different electromagnetic properties, Edge-based finite elements are useful due to their correct physical sense and accuracy. For three-dimensional problems, the tetrahedra generally used is depicted in Fig. 2.4 which shows that the edge function for the edges has a tangential component along a given edge and only normal components across the other edges.

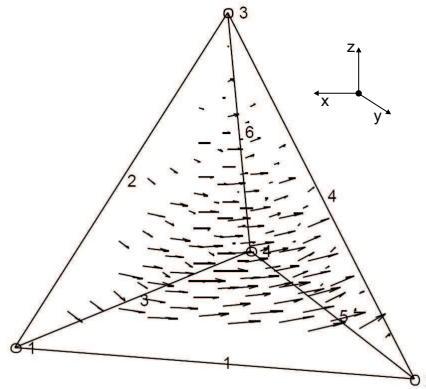


Figure 2.4: The field associated with edge 6.

Although the FDTD and the MoM are conceptually simpler and easier to program than the FEM, FEM is a more powerful and versatile numerical technique for handling problems involving complex geometries and nonhomogeneous media. However, for radar imaging and optimization purposes in time-domain the use of FEM becomes prohibitive due to the number of unknowns involved. One possible solution could be to switch to more advanced FEM strategies such as the Discontinuous Galerkin Method [60].

### 2.2.2 Review on integral formula based numerical methods

Numerical techniques based on integral representation are used to solve physical problems in terms of explicit integral equations. Due to the complexity in manipulating integral equations, these are recommended for problems whose domain is composed of linear, homogeneous and isotropic materials. The advantages of formulating an electromagnetic problem in terms of integral equations lies in the fact that this formulation incorporates the Sommerfeld radiation condition [59][61]. Amongst the techniques of solution applied to solve integral equations the boundary element method and the moment method are discussed here.

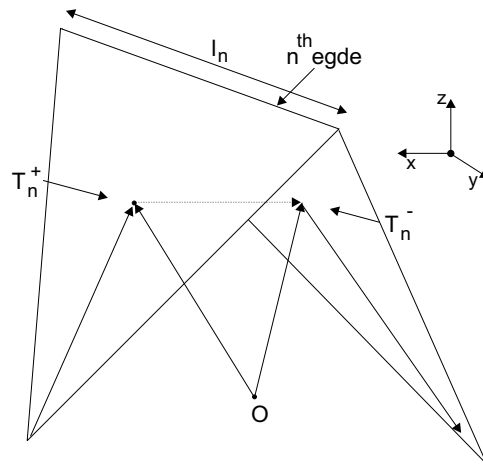


Figure 2.5: Triangle pair and geometrical parameters associated with interior edge.

### The method of moments

The method of moments (MoM), proposed by Harrington, transforms integral equations (generally Green's functions) into a system of algebraic equations through representation of the unknowns using base functions, which are multiplied by weight functions [59]. The equation solved by MoM is generally a form of the electric field integral equation (EFIE) or the magnetic field integral equation (MFIE). Both of them can be derived from Maxwell's equations by considering a field scattered by a perfect conductor. This method is mostly used to solve problems of antennas and scattering.

The general procedure of applying the MoM can be outlined as:

1. derivation of the appropriate integral equation,
2. conversion of the integral equation into a matrix equation using basis and weighting functions,
3. evaluation of the matrix elements, and
4. solution of the matrix equation and obtaining the parameters of interest.

In this work the antenna radiation and scattering were simulated for optimization purposes using the MoM with Rao-Wilton-Glisson (RWG) basis functions. First, the surface of a metal antenna under study is divided into separate triangles as shown in Fig. 2.5. Each pair of triangles, having a common edge, constitutes the corresponding RWG edge element [62]. Points in  $T_n^+$  may be designated by the position vector defined with respect to  $O$ . The plus or minus designation of the triangles is determined by the choice of a positive current reference direction for the  $n^{\text{th}}$  edge.

The surface electric current on the antenna surface (a vector) is a sum of the contributions over all edge elements, with unknown coefficients. These coefficients are found from the moment equations. The moment equations are a linear system of equations with the impedance matrix  $Z$  [63].

Once surface currents are known on the antenna surface, a radiated electromagnetic signal in free space can be found by a number of approaches. One method is to use the electric and magnetic field integral equations, with the observation point located somewhere outside the antenna surface.

### Boundary element method

The boundary element method (BEM) originated from studies of the finite element method and integral equations [61]. Therefore, the BEM can be considered as a modified version of the FEM that uses integral representation of the fields. Due to its origin, the BEM shares with the FEM the same weight functions for constructing the problem's solution [61].

The integral formulation has significant disadvantages. The more complex the geometry the more difficult is to represent the sources. In addition, in terms of the mechanics of solution, boundary integral

methods are rather inefficient: the integration process is often slow and expensive to solve. Therefore, the methods of 2.2.2 are used less often and in fewer applications than the methods introduced in 2.2.1, especially for NDT [64].

While the methods of 2.2.1 can easily deal with the structural complexity of the analyzed problems, the methods of 2.2.2 have the advantage of simplicity with boundary conditions of open problems, and reduction in the number of unknowns. Table 2.1 shows a brief comparison between the numerical methods discussed in this work.

The implementation of the methods described in 2.2.2 becomes complicated due to the strong analytical manipulations necessary for the formulation of the problem. Moreover, for applications involving nonhomogeneous materials, differential methods are more efficient.

In spite of using a larger number of elements, differential methods, show increasing use in the scientific community given its mathematical formulation and the fast growth of memory capacity of computers. In this research work most of the investigations are done using FDTD given its properties and the time-domain characteristics of the radar assessment of concrete. The TLM method was also implemented in order to provide some comparisons with the FDTD. In addition, the MoM was used in the optimization of bowtie antennas in a process that involves Genetic Algorithms (GA). Some FEM simulations were done when complex geometries were studied in a dispersive and nonhomogeneous medium. The main algorithm for the simulation in time-domain using FDTD will be described next.

## 2.3 FDTD algorithm

In engineering and particularly in electromagnetism, the problems are generally complex and nonlinear. Therefore, numerical methods such as the FDTD are very important for the understanding of complex phenomena such as: scattering, wave radiation and mutual coupling. The FDTD is one of the most widely used techniques in the solution of electromagnetic problems. This is due mainly to the simplicity of its implementation compared to methods, like the MoM or FEM and its better performance compared to the TLM.

However this method has important drawbacks that need to be discussed by the community. To the best knowledge of the candidate there is no proof of stability for lossy media using FDTD. The resulting matrix is not symmetric. Recently, it has been shown that the FDTD method, for lossless media, is stable [55]. When considering FDTD for applications in which staircaising cannot be used it is necessary to modify the main Yee algorithm in order to insert triangular elements. Each modification in the Yee algorithm makes the method more unstable especially in late time-steps.

In spite of the stability problem, the FDTD method has become the most common technique applied to the radar assessment since it:

- provides total field solution with direct implementation of Maxwell's equations in 3D,
- can be applied to both narrowband and (ultra-) broadband problems,
- can incorporate complex material properties without altering the basic mathematical structure of the scheme,
- can include arbitrary 3D geometries, complicated antenna structures, and complex material properties,
- suitable to both single and parallel processing,
- can be used with second order accuracy or higher,
- provides comprehensive temporal and spatial visualization of the electromagnetic fields.

It is important for the candidate to indicate that there is another technique whose performances (with respect to the radar assessment problem) is equal or better than the FDTD but it is still in development stages: The discontinuous Galerkin Time-Domain Method (DGTD). This method can be employed without loss for the radar problem since it provides some advantages over the FDTD such as

---

Table 2.1: Numerical techniques characteristics

Method	Principle	Advantages	Limitations
FDTD	Based on the solution of Maxwell's equations directly in the time-domain, where the physical geometry is divided into small cells that can be cubical, rectangular, but can be modified to model complex geometries. The time and spatial derivatives are handled with central finite differences. The electric and magnetic fields have different positions in time and space.	Simple and straightforward to formulate. Explicit update. Easily model problems with inhomogeneities.	For unbounded radiation problems, the mesh needs to be terminated by ABC's which adds to the modeling complexity raising the probability of instability. Approximations have to be made on the materials interface.
TLM	Uses a circuit equivalent model to represent electromagnetic waves based on Huygen's principle. A physical discretization of fields is done by an array of 3D lumped elements. The TLM requires replacing the field problem by the equivalent network and deriving analogy between the field and network quantities.	Shares the same advantages as FDTD. In addition, TLM is precise when modeling discontinuities and sources. The electric and magnetic fields are obtained in the same position.	For lossy structures the scattering matrix is $21 \times 18$ which results in a high computational effort. In the PML it becomes $24 \times 24$ . Moreover, changing the node geometry is a complicated task.
FEM	The FEM is associated with variational methods or residual methods. In the first case, the numerical procedure is established using a functional that has to be minimized and the method does not work directly with the physical equation related to the problem, but with the corresponding functional.	It has a correct physical sense. Can model complex geometries and material inhomogeneities. Strong mathematical background for proving their correctness.	The matrix inversion is a time consuming task since it works with complex and symmetric matrices. FEM is not a simple algorithm - it requires data preparation, which is basically element generation; therefore special mesh generators have been developed for this purpose.
MoM	Based on solving the Green's functions by reducing them to a system of linear equations. The equation solved by MoM is generally a form of the electrical or magnetic field integral equation. Both can be derived from Maxwell's equations.	Robust integral technique. It is fast and very useful for antenna optimization. Can be used in time or frequency-domain. No special processing is needed for unbounded radiation problems.	MoM is not effective when dealing with arbitrary configurations such as complex geometries or inhomogeneous dielectrics.

explicit updating and straightforward parallelization, with the added advantage that it yields high-order accuracy when treating arbitrary shape of scatters by employing finite-element-type meshes. In addition, the DGTD avoids accuracy degeneracy of the FDTD due to its treatment of interfaces of inhomogeneous media [60].

### 2.3.1 FDTD for dispersive media

Subsurface materials have different dielectric and conductivity properties. Based on this, a significant number of researchers have extensively investigated the dielectric properties of earth materials. They have shown experimentally that for most materials which constitute the shallow sub-surface of the earth the attenuation of electromagnetic radiation rises with frequency and that at a given frequency wet materials exhibit higher loss than dry ones [65].

This statement can be generalized to concrete structures. Theoretically, the exposure of a dielectric (not a perfect conductor) to an EM field results in changing the arrangements of its microscopic electric dipoles composed of positive and negative charges whose centers do not quite coincide. These are not free charges, and they cannot contribute to the conduction process. Rather, they are bound in place by atomic and molecular forces and can only shift position slightly in response to external fields.

Free charges, on the other hand, are the ones that determine conductivity. Upon the exposure to EM fields, a shift in the relative positions of the internal bound positive and negative charges versus normal molecular and atomic forces results in a storage of an electric energy in what is known as polarization.

The latter is expressed by the complex dielectric properties (or constant) of the material. While the real dielectric constant reflects the amount of polarization of the material, the imaginary part reflects the losses caused by conductivity (controlled by free charges) and the relaxation of the water dipole. This is why a perfect dry dielectric (with no free charges) would have no imaginary part.

The possible polarization forms in concrete, at the radio wave frequencies, are caused by a combination of ionic, electronic, dipolar, and heterogeneous polarization. At the microwave frequencies, however, the contribution of dipolar polarization is much smaller, and heterogeneous polarization is absent. Yet, losses due to water relaxation (time until the water dipole fully orients itself) increases, while conductivity losses are dramatically reduced. Therefore, changes in concrete chemistry (change in the composition of cement and/or aggregate), water content and state, and/or ions' content (in pore water) would result in changing its complex dielectric properties.

Therefore when dealing with concrete structure there is also dispersion, i.e. variations with frequency. To represent this numerically, several dispersion models are available, e.g. Lorentz, Debye, Drude.

In order to solve this problem in time-domain computational electrodynamics, the modeling requires the electromagnetic characteristics of concrete are required which can be done using dielectric models such as the Discrete Grain Size model. This model takes into account the porosity of the concrete, the water's salinity and the temperature.

In FDTD, frequency dispersive materials need to be modeled using either recursive-convolution or auxiliary differential equation approaches. The limitations and advantages of both are shown in Table 2.2. The following presents the approaches used to allow the FDTD method to model dielectric materials exhibiting linear dispersion in order to more properly simulate concrete structures.

The FDTD method has been widely used to model dispersive media because it allows the treatment of broadband response in a single simulation run. When the media are frequency-dependent, especially for those encountered the applications involving earth, biological materials, artificial dielectrics and optical materials, this frequency dispersive property will significantly change the electromagnetic response in the media. In these cases, the original FDTD algorithm needs to be modified to account for the frequency dispersion of the media.

For media which are only electrically dispersive, an important issue in the frequency-dependent FDTD method is how to calculate efficiently the temporal convolution of the electric field with causal susceptibility in an explicit or implicit form. This is done using two major frequency-dependent FDTD methods: piecewise-linear recursive convolution (PLRC) and auxiliary differential equation (ADE).

In the PLRC approach, the convolution integral is discretized into a convolution summation which is then evaluated recursively. In the ADE method, either the frequency-domain constitutive relation between the electric flux density and the electric field or the time-domain convolution integral, is first

expressed by ordinary differential equations, which are then discretized using the finite-difference method [66].

### Piecewise-linear recursive convolution

In general, the electric flux is related to the electric field by a convolution represented by  $*$  in the time-domain:

$$\mathbf{D}(t) = \varepsilon_0 \varepsilon_\infty \mathbf{E}(t) + \varepsilon_0 \chi(t) * \mathbf{E}(t) = \varepsilon_0 \varepsilon_\infty \mathbf{E}(t) + \varepsilon_0 \int_{\tau=0}^t \mathbf{E}(t-\tau) \chi(\tau) d\tau. \quad (2.31)$$

The strategy is then to replace the exact field by a piecewise-linear approximation which is based on the approximate value of  $E^n$  of the electric field at each instant  $n\Delta t$ . Thus for  $t$  in the interval  $[n\Delta t, (n+1)\Delta t]$  the approximation is:

$$\mathbf{E}(t) = \mathbf{E}^n + \frac{(t - n\Delta t)}{\Delta t} (\mathbf{E}^{n+1} - \mathbf{E}^n). \quad (2.32)$$

Plugging 2.32 into 2.31 and manipulating the result, one obtains:

$$\mathbf{D}^n = \varepsilon_0 \varepsilon_\infty \mathbf{E}^n + \varepsilon_0 \sum_{m=0}^{n-1} [(\chi^m - \xi^m) \mathbf{E}^{n-m} + \xi^m \mathbf{E}^{n-m-1}], \quad (2.33)$$

where

$$\chi^m = \int_{\tau=m\Delta t}^{(m+1)\Delta t} \chi(\tau) d\tau, \quad (2.34)$$

and

$$\xi^m = \frac{1}{\Delta t} \int_{\tau=m\Delta t}^{(m+1)\Delta t} (\tau - m\Delta t) \chi(\tau) d\tau. \quad (2.35)$$

Ampere's Law in the discrete-time domain:

$$\frac{\mathbf{D}^{n+1} - \mathbf{D}^n}{\Delta t} = \nabla \times \mathbf{H}^{n+1/2}. \quad (2.36)$$

We substitute 2.33 into 2.36 to obtain

$$\mathbf{E}^{n+1} = \left( \frac{\varepsilon_\infty - \xi^0}{\varepsilon_\infty - \xi^0 + \chi^0} \right) \mathbf{E}^n + \left( \frac{\Delta t / \varepsilon_0}{\varepsilon_\infty - \xi^0 + \chi^0} \right) \nabla \times \mathbf{H}^{n+1/2} + \left( \frac{1}{\varepsilon_\infty - \xi^0 + \chi^0} \right) \Psi^n, \quad (2.37)$$

$$\Psi^n = \sum_{m=0}^{n-1} [(\Delta \chi^m - \Delta \xi^m) \mathbf{E}^{n-m} + \Delta \xi^m \mathbf{E}^{n-m-1}], \quad (2.38)$$

$$\Delta \chi^m = \chi^m - \chi^{m+1}, \quad (2.39)$$

$$\Delta \xi^m = \xi^m - \xi^{m+1}. \quad (2.40)$$

### Auxiliary differential equation

Using an equivalent current, the frequency-domain Ampere's law can be expressed as:

$$\nabla \times \hat{\mathbf{H}}(\omega) = j\omega \varepsilon_0 \varepsilon_\infty \hat{\mathbf{E}}(\omega) + \hat{\mathbf{J}}(\omega), \quad (2.41)$$

$$\hat{\mathbf{J}}(\omega) = j\omega \varepsilon_0 \hat{\chi}(\omega) \hat{\mathbf{E}}(\omega). \quad (2.42)$$

Considering a Debye medium, with  $\varepsilon_\infty$  being the permittivity at the high frequency limit, that we choose  $\hat{\chi}(\omega) = \hat{\chi}_D(\omega)$  where:

Table 2.2: FDTD implementations.

	PLRC	ADE
Accuracy	$2^{nd}$ order	$2^{nd}$ order
Auxiliary variables	Complex-number for Lorentz	Real-number
Absorber materials	Difficult	Easy to apply

$$\hat{\chi}_D(\omega) = \frac{\Delta\varepsilon_D}{1 + j\omega\tau_D}, \quad (2.43)$$

consequently

$$\hat{\mathbf{J}}(\omega) = \frac{\varepsilon_0\Delta\varepsilon_D}{1 + j\omega\tau_D} j\omega\hat{\mathbf{E}}(\omega) \quad (2.44)$$

where  $\Delta\varepsilon_D = \varepsilon_s - \varepsilon_\infty$ , with  $\varepsilon_s$  being the static, low frequency permittivity, and  $\tau_D$  is the relaxation time. The time-domain equations can be obtained by performing an inverse Fourier transformation:

$$\nabla \times \mathbf{H}(t) = \varepsilon_0\varepsilon_\infty \frac{\partial}{\partial t} \mathbf{E}(t) + \mathbf{J}(t), \quad (2.45)$$

$$\mathbf{J}(t) + \tau \frac{\partial}{\partial t} \mathbf{J}(t) = \varepsilon_0\Delta\varepsilon_D \frac{\partial}{\partial t} \mathbf{E}(t), \quad (2.46)$$

Using central differences, the update equation for the electric field can be expressed as:

$$\nabla \times \mathbf{H}^{n+1/2} = \varepsilon_0\varepsilon_\infty \frac{\mathbf{E}^{n+1} - \mathbf{E}^n}{\Delta t} + \frac{\mathbf{J}^{n+1} - \mathbf{J}^n}{2}. \quad (2.47)$$

and the discretization of 2.46 is implemented

$$\mathbf{J}_D^{n+1} = \left[ \frac{1 - \Delta t/2\tau_D}{1 + \Delta t/2\tau_D} \right] \mathbf{J}_D^n + \left[ \frac{\varepsilon_0\Delta\varepsilon_D/\tau_D}{1 + \Delta t/2\tau_D} \right] (\mathbf{E}^{n+1} - \mathbf{E}^n). \quad (2.48)$$

Substituting 2.48 into 2.47, the final update equation for the electric field is obtained

$$\mathbf{E}^{n+1} = \mathbf{E}^n + \left[ \frac{2}{C_\gamma + C_{D,\beta}} \right] \nabla \times \mathbf{H}^{n+1/2} - \left[ \frac{1 + C_{D,\alpha}}{C_\gamma + C_{D,\beta}} \right] \mathbf{J}^n \quad (2.49)$$

where

$$C_\gamma = \frac{2\varepsilon_0\varepsilon_\infty}{\Delta t}, \quad C_{D,\beta} = \left[ \frac{\varepsilon_0\Delta\varepsilon_D/\tau_D}{1 + \Delta t/2\tau_D} \right] \text{ and } C_{D,\alpha} = \left[ \frac{1 - \Delta t/2\tau_D}{1 + \Delta t/2\tau_D} \right].$$

### PML for dispersive media

One of the more important development in the FDTD method consisted in the introduction of the PML as an ABC to simulate open space on a finite computational grid. Apart from its numerical efficiency, one of the major advantages of the PML over the previously proposed ABC is that its absorption properties hold independently of the frequency of the incident wave. Also, most previously proposed ABC's are not suited for dispersive media because they require knowledge of the wave velocity near the grid boundary, a quantity that is not well defined in the time-domain for dispersive media.

However, the PML, as originally devised, also applies only to nondispersive media. In order to apply it for radar simulations in dispersive media, it is necessary to extend the PML to handle dispersive media [67], [55].

Considering the goals of this work (solving Maxwell's equations) two basic formulations are possible when implementing the PML: the split-field formulation and the Maxwellian formulation (the PML is represented in terms of an anisotropic material medium, with  $\varepsilon$  and  $\mu$ ). Some advantages of using the split-field formulation with the complex coordinate stretching approach for dispersive media can be listed as follows [67]:

1. There is no need to derive constitutive parameters for the PML medium. This is because, to achieve the perfect matching condition in this approach, the same constitutive parameters can be assumed *everywhere* (i.e., both in the physical and PML regions). The PML region is then simply defined as the region where the complex stretching is enforced.
2. Treatment of corner regions poses no special difficulty since it just corresponds to regions where simultaneous stretchings in different directions are enforced. Therefore, 2D and 3D simulations can be easily treated.
3. It is particularly suited to be combined with the dispersion modeling techniques based on recursive convolution, such as the PLRC, thus providing easier treatment of multiterm Lorentz or Debye models.
4. Since the same set of equations is used both inside the physical and PML regions (the physical region can be considered as a special case of a PML region with all complex stretching variables equal to unity), an easier parallelization of the code is made possible.

Considering these properties this work uses an implementation of the complex frequency-shifted (CFS) PML originally proposed by Gedney using an ADE formulation with a recursive-convolution technique [68]. This has since been referred to as the CPML formulation. The CPML is based on the stretch-coordinate form of the PML. An important feature of the CPML formulation is that it can be readily extended to anisotropic, dispersive, and nonlinear media. This is because, at its most basic level, CPML has nothing to do with the **D-E** and **B-H** constitutive relationships that normally characterize a material. Rather, CPML is applied as stretched coordinates on the curl operator, which is applied only to the field intensities. The derivation and implementation in FDTD is shown in Appendix A.

### Source excitation

If at all possible, the source should be implemented in such a way that it is not a function of frequency to avoid performing a convolution. For 3D problems, it is desirable to have pulses with no DC content. In FDTD the source can be implemented in one of two ways:

1. The electric or magnetic field can be specified as boundary conditions to represent the source,
2. A magnetic or electric current source can be specified in a certain grid position.

Considering the first option, the electric or magnetic field can be specified as boundary conditions to represent the source; this can be done by specifying the incident field solution as a function of time. The reflected field must be properly separated from the incident field and handled properly with a boundary condition.

In the second option the source is related to the fields by a time derivative. The fields very close to the current source may be wrong and the current source distribution must be known.

The source can differ considering the application. For steady state response the time variation is sinusoidal and the simulation is run until steady state is reached. This kind of simulation is efficient only for very narrowband problems and is more susceptible to errors in the outer boundary. It is seldom used for realistic problems. However no advantages are seen compared to frequency-domain methods.

For pulsed simulations a pulse is chosen based on the frequency content of the pulse. The simulation is run until the appropriate physics of interest is properly accounted for. Typical pulses that are used are the derivative of a Gaussian pulse, modulated Gaussian pulse and, single sine period pulse [55]. The pulse should be chosen based on the highest frequency of interest. The Fourier transform of the pulse provides the frequency content of the pulse. We assume the maximum frequency bandwidth to be between points at which the amplitude is  $\pm 5-10\%$  off the peak value. The choice of the grid spacing should be based on the maximum frequency.

Since the pulse must be zero for  $t < 0$  there may be a jump discontinuity for some pulses. This discontinuity has to be watched to avoid undesirable frequencies and to preserve the algorithm stability.

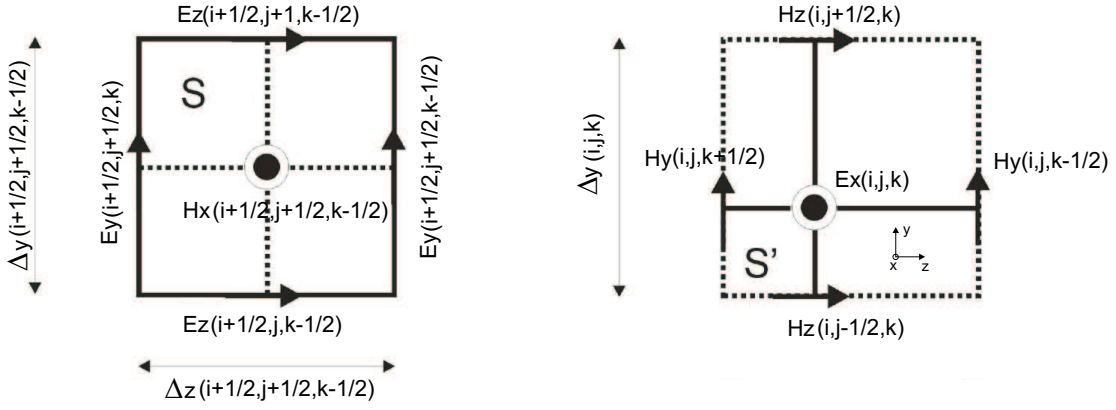


Figure 2.6: Nonuniform FDTD cell.

### Nonuniform orthogonal grids

The FDTD algorithm is second-order-accurate by nature of the central-difference approximations used to implement the first-order spatial and temporal derivatives. This leads to a discrete approximation for the fields based on a uniform orthogonal lattice. Unfortunately, structures with fine geometrical features cannot always conform to the edges of the uniform lattice. Further, it is often desirable to have a refined lattice in localized regions, such as the antenna in the radar problem or next to a target's interface.

Since such a high level of refinement is not needed in all regions (a good example for radar applications could be the air region above the antenna) this leads to unnecessary increase in the computational burden.

A quasi-nonuniform grid FDTD algorithm was introduced by Sheen [69]. This method is based on reducing the grid size by one-third of the global grid size (or other odd number). By choosing the subgrid to be one-third, the spatial derivatives of the fields at the interface between the two regions can be expressed using central-difference approximations, resulting in a second-order-accurate formulation.

The nonuniform FDTD algorithm for an isotropic medium can be easily derived from the integral form of Maxwell's equations. However, the derivation follows directly from Yee's original scheme. For a nonuniform mesh, as shown in Fig. 2.6, where the electric field components are located along the edges of the cells, and the magnetic field components are located on the faces of the cells, the discretized form of the equation for the  $\mathbf{E}$ , field component is

$$\begin{aligned} \epsilon \frac{E_x^{n+1}(i, j, k) - E_x^n(i, j, k)}{\Delta t} S_{(i, j, k)} &= H_z^{n+1/2}(i, j+1/2, k) \Delta z(i, j+1/2, k) - \\ &H_z^{n+1/2}(i, j-1/2, k) \Delta z(i, j-1/2, k) - \\ &H_y^{n+1/2}(i, j, k+1/2) \Delta y(i, j, k+1/2) + \\ &H_y^{n+1/2}(i, j, k-1/2) \Delta y(i, j, k-1/2) \end{aligned} \quad (2.50)$$

where  $S$  is the surface enclosed by the path of integration. Since the mesh is orthogonal,  $\Delta z(i, j-1/2, k) = \Delta z(i, j+1/2, k)$  and  $\Delta y(i, j, k-1/2) = \Delta y(i, j, k+1/2) = \Delta y(j)$ , and  $S_{(i, j, k)} = \Delta z(k) \Delta y(j)$ . Therefore, we can write

$$\begin{aligned} E_x^{n+1}(i, j, k) &= E_x^n(i, j, k) + \frac{\Delta t}{\epsilon} \\ &\left[ \frac{H_z(i, j+1/2, k) - H_z(i, j-1/2, k)}{\Delta y(j)} - \frac{H_y(i, j, k+1/2) - H_y(i, j, k-1/2)}{\Delta z(j)} \right]^{n+1/2}. \end{aligned} \quad (2.51)$$

For the validation of the algorithm implemented for the nonuniform grid a low-pass filter was used in which the substrate and air are assumed to be of infinite extent. The FDTD was used with global mesh parameters  $\Delta_x = 0.64mm$ ,  $\Delta_y = 0.635mm$  and  $\Delta_z = 0.1588mm$ , and secondary cells of dimensions  $\Delta_x = 0.4064mm$ ,  $\Delta_y = 0.4233mm$  and  $\Delta_z = 0.1588mm$  with  $\Delta t = 0.441ps$ . The mesh used and the scattering parameters of the filter are shown in Fig. 2.7.

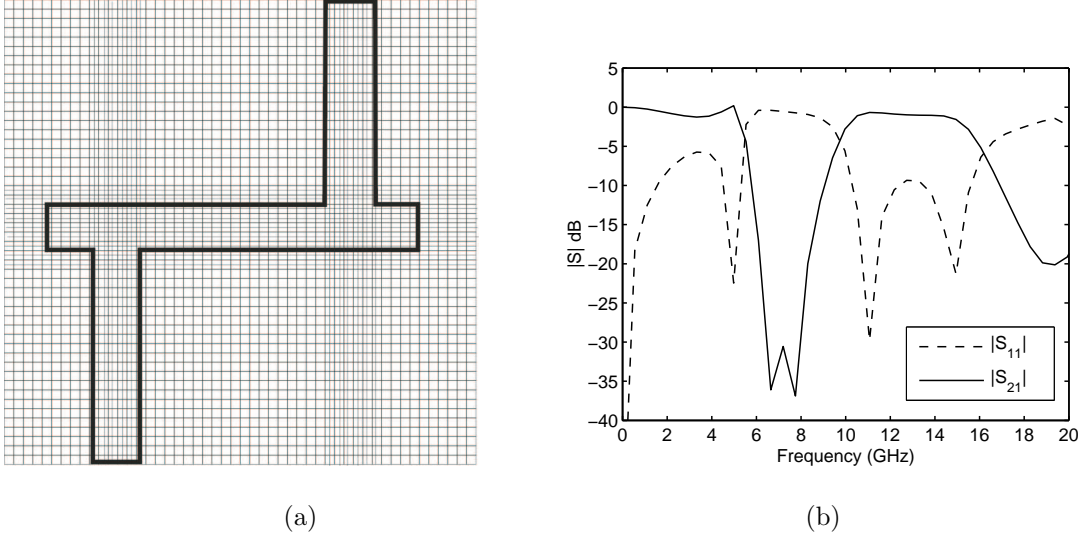


Figure 2.7: Low-pass filter simulation with nonuniform FDTD cell.

### Resistive Antennas

The impulse response of radar antennas is a critical factor, because the antenna must possess ultrawide bandwidth characteristics. A common problem encountered in the radar application of transient signals to antennas is late-time ringing, caused by reflections at the antenna open ends. One possible solution to eliminate open-end reflections is loading the antenna with passive elements. This can be done in different ways, among which, the one based on loading the antenna following the Wu-King resistive profile has been found to be very efficient. In this work, we implement the technique on the bowtie antenna, to obtain a low-cost, lightweight and efficient ultra-wideband antenna.

According to Wu-King theory [70], the resistance  $R$  per square meter of the thin sheet that forms the antenna should have a variation of the form:

$$R(p/L) = R_{1/2} \left[ \frac{p/L}{1 - p/L} \right] \quad 0 \leq p/L \leq 1 \quad (2.52)$$

where  $L$  is the length of the antenna wing, and  $p$  is the distance along the wing from the excitation point (antenna center). The total resistance of one wing is given by:

$$R_{TOT} = \sum_{i=0}^{r-1} \frac{R(p_i/L)}{N_i} \quad (2.53)$$

where  $r$  is the total number of rows (between the excitation point and the wing end),  $p_i$  is the distance from the antenna center to the  $i^{th}$  row,  $N_i$  is the number of parallel cells in the  $i^{th}$  row,  $L$  is the total length of the wing (excitation point to wing end), and  $R(p_i/L)$  is determined using Eq. 2.52. However, when  $p_i = L$ ,  $R(p_i/L) = \infty$ . To avoid this,  $p_i$  is normalized as follows:

$$p_i = p_{i+0.5} \quad \text{where } i = 0, 1, \dots, r - 1 \quad (2.54)$$

If we consider for example, an antenna with  $L = 4.18$  cm, and the wing divided into 3.8 mm cells resulting in 11 rows, the total resistance in one wing is:

$$R_{TOT} = \sum_{i=0}^{10} \frac{R(p_{(i+0.5)/11})}{N_i} = R_{1/2} \left\{ \sum_{i=0}^{10} \frac{p_{(i+0.5)/11}}{1 - p_{(i+0.5)/11}} \frac{1}{N_i} \right\} \quad (2.55)$$

The value of  $R_{1/2}$ , which is a scaling factor, is chosen so that the total wing resistance is approximately  $40\Omega$ , resulting in a total antenna resistance (both wings) of approximately  $80\Omega$ .

### Antenna loading

Another approach can be used to reduce the antenna ringing in the presence of a shield: the antenna can be resistively loaded by connecting its corners to the shield by resistors. For the simulation of the resistors, a lumped current density term  $\mathbf{J}$  is added to Maxwell's curl equation for the magnetic field [55].

Assuming a z-directed resistor  $R$  located in free space at the field component  $Ez_{i,j,k}$ , the field characteristic that describes its behaviour in a semi-implicit manner appropriate for stable operation of the FDTD field solver is:

$$Ez^{n+1}(i, j, k) = Ez^n(i, j, k) \left( \frac{1 - \frac{\Delta t \Delta z}{2R\epsilon_0 \Delta x \Delta y}}{1 - \frac{\Delta t \Delta z}{2R\epsilon_0 \Delta x \Delta y}} \right) + \left( \frac{\frac{\Delta t}{\epsilon_0}}{1 - \frac{\Delta t \Delta z}{2R\epsilon_0 \Delta x \Delta y}} \right) (\nabla \times H)_{i,j,k}^{n+1/2}. \quad (2.56)$$

### Simple feed model

The excitation of antennas using numerical methods is always a difficult task. This is due to the fact that the fields near the excitation are, in most cases, wrong. Therefore, in order to obtain good near fields values in the gap of the antenna and then calculating more exact impedance values feeding models are required. Generally in FDTD, it is better to model the feeding system i.e., coaxial cable or transmission line. To implement this without consuming memory, the one-dimensional FDTD grid shown in Fig. 2.8 is used to represent the transmission line attached to the bowtie antenna. The index  $k'$  locates a point within this grid. The top end of the transmission line is a point  $k'_{top}$  in the one-dimensional grid, and the feedpoint for the antenna (the center of the aperture in the coaxial line is the feed point of the antenna) in the three-dimensional lattice. The spatial step within the one-dimensional grid is the same as the spatial step for the z-coordinate in the three-dimensional lattice.

Under the assumption that the electromagnetic field within the coaxial line is TEM, the coaxial feed line can be replaced by a one-dimensional transmission line model that is simply connected to the antenna [71]. The voltage and current on the transmission line are updated in the standard FDTD fashion, i.e.,

$$I_{k'+1/2}^{n+1/2} = I_{k'+1/2}^{n-1/2} - \left( \frac{1}{Zline} \right) \left( \frac{\nu \Delta t}{\Delta z} \right) [V_{k'+1}^n - V_{k'}^n] \quad (2.57)$$

$$V_{k'+1}^n = V_{k'}^n - Zline \left( \frac{\nu \Delta t}{\Delta z} \right) [I_{k'+1/2}^{n+1/2} - I_{k'-1/2}^{n+1/2}] \quad (2.58)$$

where  $\nu$  is the phase velocity within the transmission line and  $Zline$  is the transmission line impedance.

This launches a TEM wave within the line only in the  $+z$  direction. The bottom of the coaxial line,  $k' = 0$ , is truncated with an absorbing boundary condition. The absorbing boundary condition is particularly simple when  $\Delta z/\nu \Delta t = \text{integer}$ ; for example with  $\Delta z/\nu \Delta t = 2$ , it is

$$V^{n+1}(0) = V^{n-1}(1). \quad (2.59)$$

The incident wave is introduced into the transmission line at the location  $k'_{source}$  by a "one-way" injector. This is an algorithm feature that launches a desired signal in the forward direction ( $+z$ ) while launching only a negligible, undesired signal in the backward direction ( $-z$ ).

### FDTD validation

Using the FDTD algorithm discussed above, the input characteristics of a rectangular microstrip patch antenna presented in [72] and shown in Fig. 2.9 was studied. The microstrip antenna is basically a transmission line characterized by a ground plane, a dielectric substrate and a conductor of arbitrary shape superposed in parallel layers.

The simulations were performed using a time step  $\Delta t = 0.441ps$  and spatial steps  $\Delta x = 0.389mm$ ,  $\Delta y = 0.400mm$ ,  $\Delta z = 0.265mm$ . In the microstrip antenna examined, the propagating waves are close to the TEM case. The time transient port voltage  $V$  can therefore be obtained from numerical integration of the electric field at the antenna terminals according to

$$V = \int_l E \cdot dl, \quad (2.60)$$

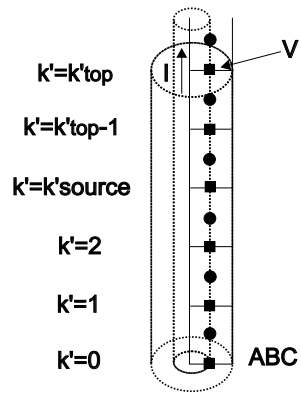


Figure 2.8: One-way injector.

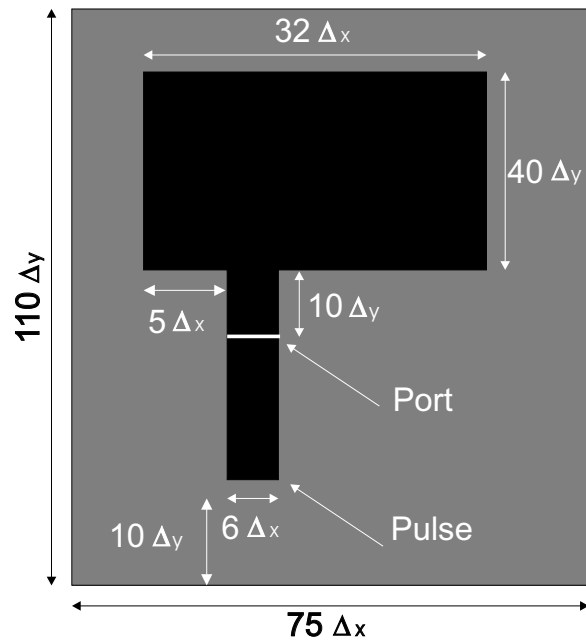


Figure 2.9: Rectangular microstrip patch antenna dimensions.

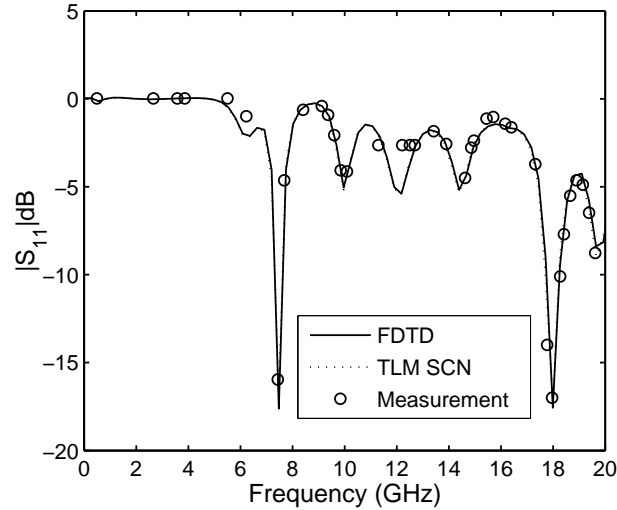


Figure 2.10: Return loss for the microstrip antenna simulated.

as the FDTD algorithm implemented is based on total field calculations, the resulting quantities are composed of reflected and incident waves and therefore cannot be directly used for the extraction of scattering parameters. To obtain the incident waveform, the simulation is performed only with the microstrip line, which will be simulated with an infinite extent. The resulting voltages (total and incident) recorded at every time step can now be used for extraction of the reflection waveform by subtracting the incident waveform from the total field. The return loss,  $S_{11}$  can then be obtained by simple Fourier transform of these transient waveforms as

$$S_{11} = \frac{V_{\text{ref}}(\omega)}{V_{\text{inc}}(\omega)}. \quad (2.61)$$

The results for the FDTD algorithm compared with the Symmetric Condensed Node (SCN) TLM (Full details about the PML implementation in TML is given in Appendix B) and the measured values published in [73] are shown in Fig. 2.10.

The full FDTD algorithm used in this research work is shown in Fig. 2.11.

### 2.3.2 Applications: Pulsed microwave confocal system

Significant progress has been made over the past decade towards the clinical realization of noninvasive nonionizing microwave imaging techniques employing large arrays of sensing antennas and sophisticated inversion algorithms. In particular, the ultrawideband (UWB) microwave technology has shown promise for early-stage breast cancer detection [55].

Often in biomedical applications, the goal of the antenna system is to radiate into the human body. These applications fall into three broad categories: diagnostic imaging, medical implants, and thermal therapy. The thermal therapy has been well developed for the Ampère laboratory in a recent work [74] using FEM in frequency-domain where annular phased arrays designed to heat deeply embedded cancer tumors<sup>1</sup> by controlling the phases and magnitudes of the excitations of the various radiating elements.

Based on the definition given by the American Cancer Society (ACS), cancer refers to "a group of diseases characterized by uncontrolled growth and spread of abnormal cells" [75]. Cancer is the second leading cause of death in the United States and the world after cardiovascular diseases (CVD). Cancer can develop almost anywhere in a human body, such as the skin, marrow, bone, brain, breast, colon, liver and lungs. Cancer can also strike people at any age. Among the various cancers, roughly 76% are

<sup>1</sup>Every year, roughly 7.1 million people die of cancer, accounting for 12.6% of all global mortalities.

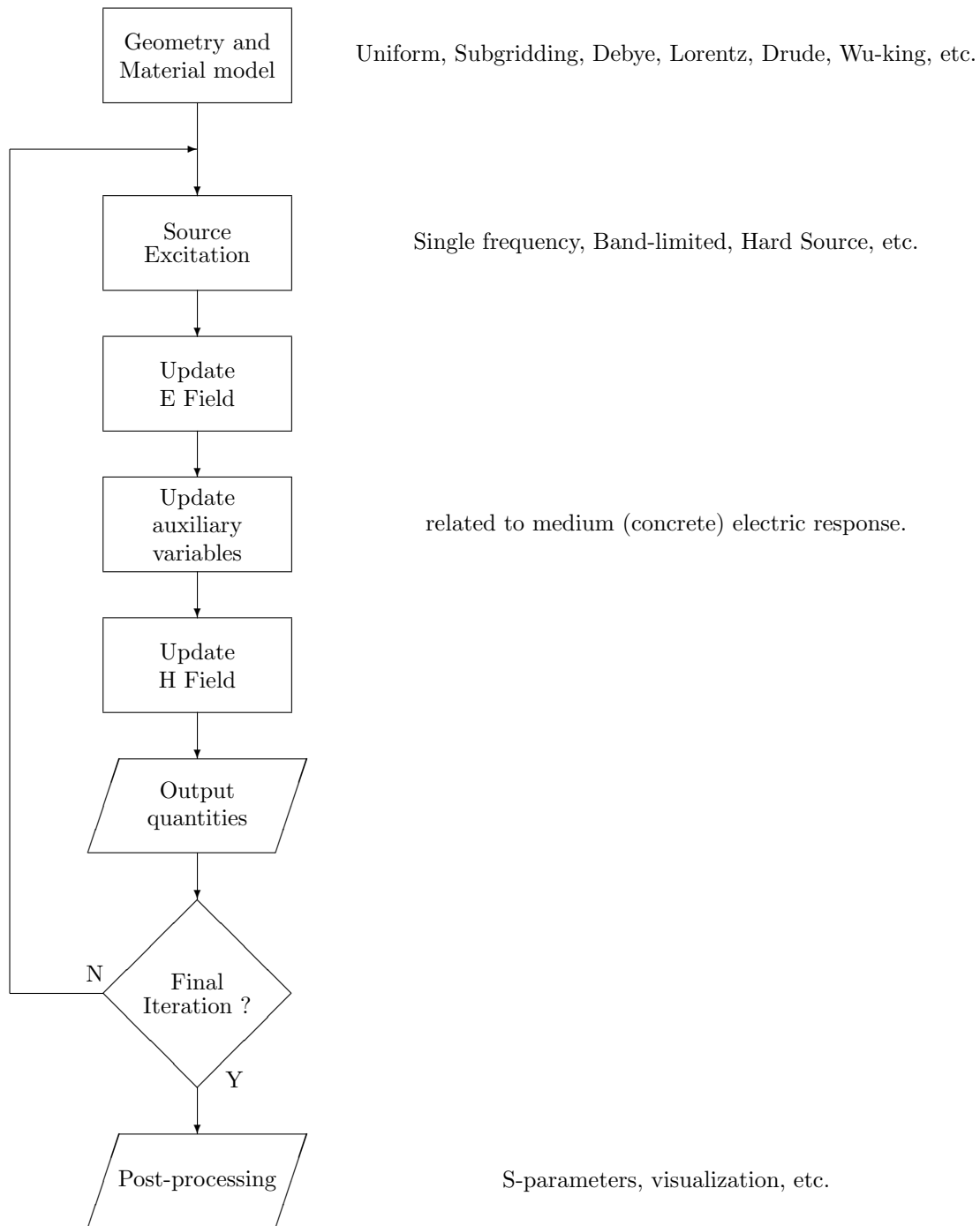


Figure 2.11: Flowchart of the FDTD Algorithm.

diagnosed in people over 55. However, in all of these cancer cases, only about 10% are genetically related and approximately 1/3 of the deaths can be completely avoided with appropriate diet and healthier living styles (such as not smoking and drinking). Studies on cell biology reveal important mechanisms for the development of cancer.

This work provides an alternative tool for studying the thermal therapy of cancer tumors in time-domain. The ability of FDTD to model essentially arbitrary configurations of inhomogeneous, lossy dielectric materials makes this method broadly applicable to this area.

It is desired to investigate the use of active confocal microwave technology to detect an image breast cancers under an obscuring layer of normal tissue. To this end, accurate and efficient modeling of electromagnetic waves in dispersive and nonlinear media is an important need for research in bioelectromagnetics. Here, the microwave sensor used to model this technology is again a bowtie antenna but now with  $h = 4$  cm and flare angle of  $53^\circ$  [76]. The slanted edges of the bowtie antenna are approximated using staircasing with a submillimeter spatial-grid resolution.

It is assumed that the antenna is placed directly on 1-mm-thick breast skin. The antenna is embedded within a large block of lossy dielectric material that matches the dielectric parameters of normal breast tissue (immersed in a bath of deionized water). Below the skin 3 centimetres of breast tissue at which depth a malignant tumor present. Excitation of the antenna is provided at its apex by a  $50 \Omega$  source which generates a 0.22 ns Gaussian-modulated carrier pulse [55]. The FDTD model uses the spatial discretization  $\Delta x = \Delta y = 0.5$ mm and  $\Delta z = 0.25$  and  $0.75$ mm. The following Debye dispersive material parameters are assumed for the various media in the FDTD model shown in Table 2.3.

Table 2.3: Dispersive materials for the microwave confocal simulation.

deionized water	$\varepsilon_\infty = 4.55$	$\varepsilon_s = 77.1$	$\sigma_s = 0.0002$	$\tau_D = 7.4$ ps
skin	$\varepsilon_\infty = 4$	$\varepsilon_s = 37$	$\sigma_s = 1.1$	$\tau_D = 7.23$ ps
breast tissue	$\varepsilon_\infty = 7$	$\varepsilon_s = 10$	$\sigma_s = 0.15$	$\tau_D = 7$ ps

It has been reported that detection of breast cancer in early stages is essential for reducing the breast cancer mortality rate [77]. There are several types of breast tumors. According to [76] the dielectric properties of malignant tumors vary in an approximate 10% range around  $\varepsilon = 50$  and  $\sigma = 7S/m$ . The 3D FDTD backscatter response for the tumor studied here with diameter of 5.8 mm, and depth of 3.1 cm depicted in Fig. 2.12 is seen to be -94.11 dB relative to signal without the tumor. Electric field snapshots are shown in Fig. 2.13.

It is important to indicate that given the main objective of this research work the geometries involved could be modelled using a staircasing approximation. However, due to the accuracy required in the application discussed above it is also important to consider the used of more complex cells involving triangular elements or the use of hybrid methods.

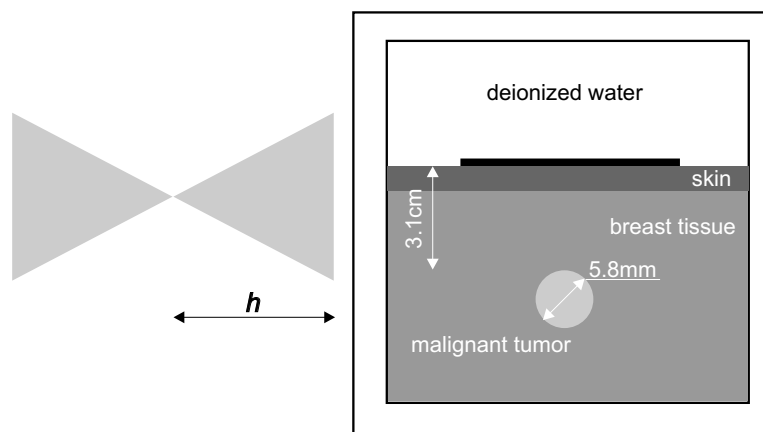


Figure 2.12: Problem description for breast cancer detection.

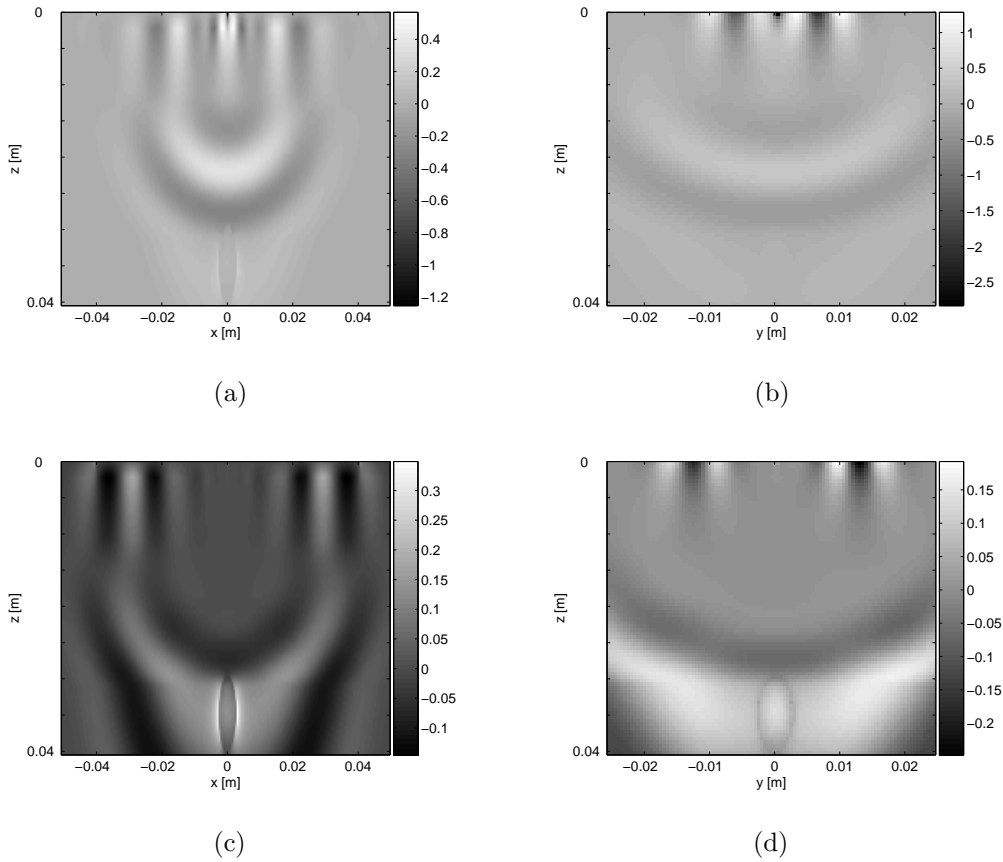


Figure 2.13: Snapshots of the Ex-field (V/m) in the breast cancer detection problem: (a) E-Plane  $t=0.83\text{ns}$  (b) H-Plane  $t=0.83\text{ns}$  (c) E-Plane  $t=1\text{ns}$  (d) H-Plane  $t=1\text{ns}$ .

### 2.3.3 Optimal configurations for PML

The PML is implemented from the physical absorption of the incident numerical wave by means of a lossy medium. This is devised using a novel split-field formulation of Maxwell's equations where each vector field component is split into two orthogonal components [78]. Unfortunately the PML requires a considerable amount of computational storage in contrast with analytical boundary conditions due to the storage of split-fields and the number of layers used to truncate the domain of study.

Reflections from the PML exist due to the FDTD discretization of the conductivity profile. Recent efforts have been made to reduce these reflections: in [79] a two-step conductivity profile was implemented using a micro-Genetic Algorithm (GA) to obtain the optimal values for each sub-layer, and in [80], a steady-state GA was used to optimize the conductivity profile by minimizing a function of the local error of a 2D FDTD code (both are mono-objective optimization).

In this research work, an alternative way to design PML boundaries that fulfill the requirements of realistic projects. This optimization process is composed of two stochastic procedures is presented. First, an MGA<sup>2</sup> is used to find a solution for the size of the PML which minimizes the reflection coefficient and the computational cost. Next, a GA is used to find a better conductivity profile in order to further reduce the reflectivity. A theoretical approach is utilized for the calculation of the reflection coefficient for the PML [81].

#### Reflection from the PML boundary

A numerical method was developed in [81] which computes an exact prediction of the reflection from PML absorbing layers without performing a FDTD simulation. This method considers the two mechanisms which govern the amount of reflection created by the PML boundary. These are: 1) reflections between PML/free-space and PML/PML interfaces, and 2) the amount of attenuation experienced as the incident wave travels through the PML medium [81].

This can be explained by the fact that the field components on the free-space side are calculated using the FDTD time-stepping equations, whereas, the fields within the PML region are calculated using the PML exponentially differenced time-stepping equations. When calculating  $E_y(i, 0)$  the FDTD equations require the magnitude of the  $H_x(i, k = 1/2)$  field component (Fig. 2.14). If there is no reflecting wave, then the FDTD equation will expect the magnitude of  $E_y$  to equal  $H_x/Z_x$ . Unfortunately, because the field  $H_x$  component is within the PML region, a small amount of decay has occurred to the traveling wave, and the magnitude of this component is less than what the FDTD equations would expect. This results in the generation of the reflected wave.

The variables necessary to obtain the reflection from the PML are: the normalized wavelength  $\lambda/\Delta$  (being  $\Delta$  the spatial discretization), the number of absorbing layers  $L$ , the incident angle  $\theta$ , and the conductivity  $\sigma$  which is gradually increased from zero to a maximum  $\sigma_m$  at the perfect electric-wall (Fig. 2.15) to avoid an abrupt transition between the discrete PML space and the discrete FDTD space. Several profiles have been suggested for grading  $\sigma$ . The most successful use a polynomial or geometric variation of PML loss with depth  $z$ . The spatial scale of the conductivity profile using a polynomial grading is given by:

$$\sigma(z) = \sigma_m \left(\frac{z}{d}\right)^n \quad (2.62)$$

where  $z$  is the depth within the PML region of total depth  $d$ , and  $n$  is the order of the conductivity's increase.

The design of an optimal PML is made difficult by the requirement to balance the level of reflection against the discretization error in using the variables  $\lambda/\Delta$ ,  $L$ ,  $\sigma_m$  and for a polynomial grading  $n$ . A large  $n$  yields a conductivity distribution that is relatively flat near the PML surface. However, deeper within the PML,  $\sigma(z)$  increases more rapidly than for small  $n$ . In this region, the field amplitudes are substantially attenuated and reflections due to the discretization error are reduced [55].

However, if  $\sigma_m$  is small, reflections from the PEC (perfect electric conductor) external boundary will dominate. If  $\sigma_m$  is large, reflections will be created by the abrupt changes in the inter-layers conductivities (discretization error). If the size of the PML is increased to lessen the inter-layers transition, the

---

<sup>2</sup>The MGA used in this work was implemented by Dr. Sérgio Avila. I would most sincerely like to thank him for his contribution to this work.

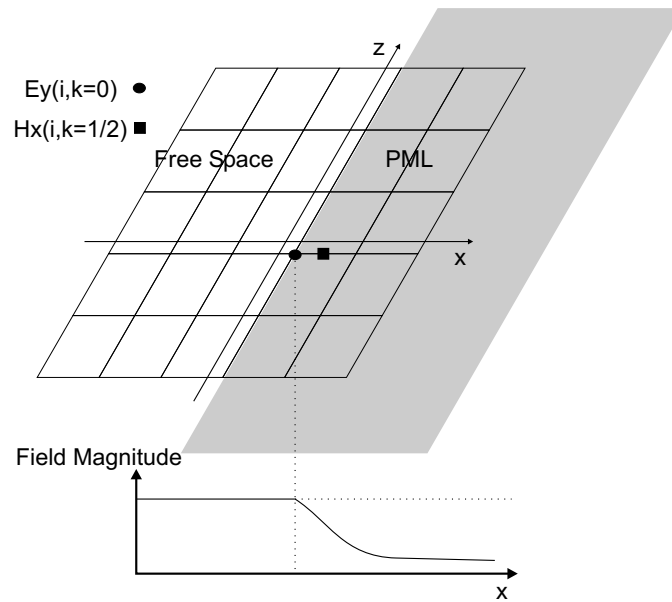


Figure 2.14: Field components near a PML/free-space boundary.

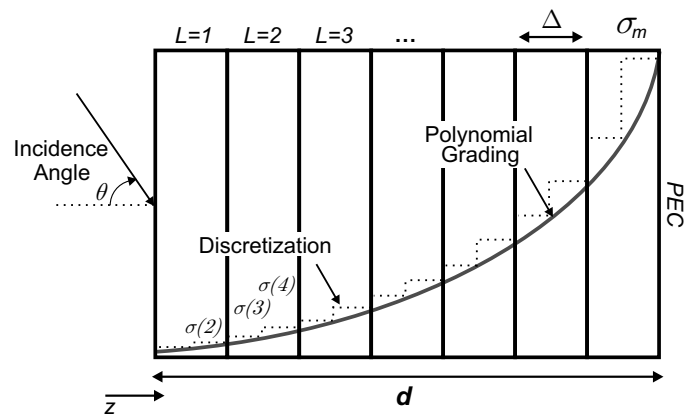


Figure 2.15: Schematic of a metal-backed PML.

computational time and memory requirement will be increased. To understand this balance, we use the MGA in order to facilitate the choice of the best variables.

### Genetic algorithms

In most optimization problems several goals must be satisfied simultaneously in order to obtain an optimal solution. As these objectives are usually conflicting, no single solution may exist that is best regarding all considered goals. This is what happens in PML design. We recognize that to reduce the reflection coefficient the computational effort must increase. It is important to know this balance to make an efficient FDTD model with low computational cost. Such a scenario requires a multi-objective optimization engine.

Multi-objective optimization seeks to optimize the components of a vector-valued cost function. Unlike single objective optimization, the solution to this problem is not a single point, but a family of efficient points called Pareto optimal front (POF). Each point on this surface is optimal in the sense that no improvement can be achieved in a cost vector component that does not lead to degradation in at least one of the remaining components. Each element in the efficient set constitutes a non-dominated (non-inferior or non-superior) solution to the multi-objective problem [82].

The main goal of the MGA is to find the efficient group of solutions. With this set of solutions it is possible to understand the dependence between objectives, which allows making efficient choices for the final solution decision. The MGA is derived from the GA, which is a stochastic procedure based on the concepts of natural selection in genetics [83]. Basically, the algorithm starts with a set of feasible solutions called population. The solutions provided by the population are used to form a new population. This is motivated by the hope that the new population will be better than the old one. The new solutions generated are selected according to their fitness (evaluation of objectives). This is repeated until some condition is satisfied, for example, the number of generations.

The general algorithm of the MGA is shown in Fig 2.16. The GA and MGA used in this work are described in [84].

### PML optimization

Theoretically, the PML interface is reflectionless in the continuum space [86]; this is not the case in the discretized space where there is local step-discontinuity of the conductivity. Since all numerical methods are carried out in the discretized space, one must exercise care to reduce the unwanted reflection due to the finite spatial sampling. A straightforward approach to reducing this unwanted reflection is to make the PML parameters change smoothly along the PML thickness so that the change from grid to grid is small. However, to do this we have to increase the size of the discretized grid which leads to an increase of the number of unknowns and the computational burden.

The design of an effective PML requires balancing the reflection error, the numerical discretization error and the computational cost associated with the number of the PML layers. Therefore, there is an issue of optimization in determining the PML parameters for best performance.

To address the issue of optimization, we considered the problem of a plane wave incident on a metal-backed PML obliquely at an angle  $\theta$  with the  $z$ -axis (see Fig. 2.15). The goal is to design a PML with the minimal thickness (or minimal computational cost) and maximal absorption quality (or minimal reflectivity for a given range of incidence angles) which are conflicting objectives and hence becomes a multi-objective optimization problem.

The MGA are then coded to find multiple non-dominant solutions (the Pareto-front) using a fixed conductivity profile given by Eq. 2.62. The PML parameters to adjust are:

$$P^g = \begin{bmatrix} L^{g,1} & n^{g,1} & \sigma_m^{g,1} \\ \vdots & \vdots & \vdots \\ L^{g,np} & n^{g,np} & \sigma_m^{g,np} \end{bmatrix} \quad (2.63)$$

where each line represents a feasible solution,  $g$  is the current generation and  $np$  is the population size.

The variables to be optimized are then the order of the conductivity increase, the maximal conductivity and the number of layers. They are adjusted to minimize the reflection coefficient for an incident wave

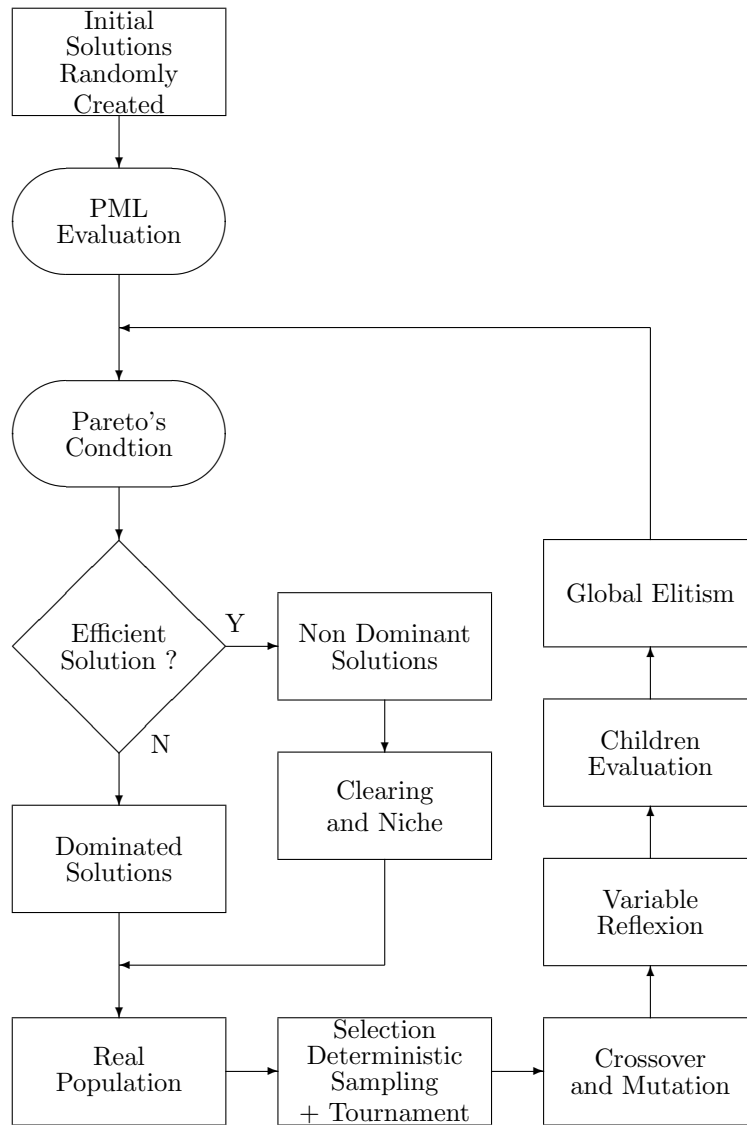


Figure 2.16: Flowchart of the multi-objective genetic algorithm [85].

Table 2.4: Solutions found by the MGA for  $0^\circ - 50^\circ$  absorption angle.

$L$	$\sigma_m^* \times \Delta z$	$n$	$ R _{max}$	$AO$
8	2634.629	3.812	2.94e-5	136496
10	2375.880	4.273	2.51e-6	142400
12	2184.965	4.266	5.30e-7	148016
14	2298.271	4.972	1.06e-7	153344
16	2525.573	5.342	1.96e-8	158384

range. This becomes the first objective function. The second objective function is to minimize the approximate operations associated to a domain surrounded by  $L$  PML layers.

In addition to the MGA procedure, we introduced a GA investigation to improve the conductivity profile given by Eq. 2.62. This investigation used some samples of the POF (set of best solutions found). The conductivity value of each layer is adjusted from a set of feasible solutions determined by a variation between +/- 10% of the value found by the MGA.

### Optimization results

In order to find the best configuration for the PML absorbing layers we implemented the MGA to work with two goals: to minimize the reflection coefficient and to minimize the computational cost associated with the number of layers [87]. For an  $M \times N$  computational space, and assuming  $\Delta x = \Delta z$ , the approximate operations (AO) count is given by:

$$AO = 20MN - 9(M - 2L)(N - 2L). \quad (2.64)$$

The parameters to be adjusted by the MGA are the variables necessary to obtain the reflection from the PML: the number of PML layers  $L$  [4 to 24], the order  $n$  of the conductivity profile Eq. 2.62 [0 to 10], the maximum normalized magnetic conductivity  $\sigma_m^* \times \Delta z$  [0 to 1e8]. A computational domain of  $M = N = 100$  cells was assumed with the normalized wavelength  $\lambda/\Delta = 20$ . The reason for this normalization is that the spatial discretization size can then be neglected as a factor which may affect the amount of reflection from a PML boundary. It is also useful to use the form, as this is also used as a criterion by which the FDTD-mesh discretization sizes are chosen [81].

The objective of the optimization procedure was to find a PML with the least reflection over a range of incident angles,  $\theta$  from  $\theta_1$  to  $\theta_2$ .

In this first procedure, efficient solutions are obtained using a population size 100; a crossover probability of 0.9 and a mutation probability of 0.025. Real-coded MGA are run for 50 generations. Several MGA executions had been carried out to guarantee the POF found. Some samples of the POF are shown in Table 2.4 for  $\theta_1 = 0^\circ$  and  $\theta_2 = 50^\circ$  at  $2^\circ$  increments.

In order to further improve these results, we decided to find an alternative conductivity profile based upon the results of the MGA analysis. To do this we selected some solutions found by the MGA and we performed a process of evolution of the conductivity profile.

Figure 2.17 shows the results for  $L = [8 \text{ and } 10]$ . Considering the simple polynomial grading of Eq. 2.62, it is clear that optimal values for the polynomial order and the maximum conductivity can be found to achieve suitable solutions with a reasonable number of layers (Table 2.4).

It can be seen in Fig. 2.18 that for the same number of layers the maximum reflection coefficient in the range is improved by modifying the behavior of the conductivity scaling.

The objective function to be minimized corresponds to the maximum reflection coefficient in the angle range specified. Convergence has been attained in about 100 generations with a population of 50 individuals in several GA executions. The crossover and mutation probabilities are set 0.9 and 0.05, respectively. Each generation took about 20s with a PC Pentium IV at 1GHz. The entire optimization process took about 45 minutes considering the limits described above.

The FDTD algorithm computes the electromagnetic fields at positions in space which are either on the boundaries of mesh cells or half way along. Hence for a PML of depth  $L$  there are actually  $2 \times L - 1$

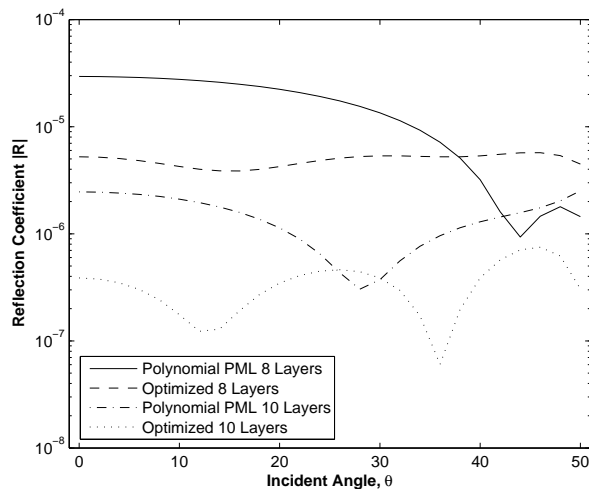


Figure 2.17: Reflection coefficient of an optimized PML for  $\theta$  from 0 to 50 degrees.

Table 2.5: Optimized ten-layer conductivity profile for  $0^\circ - 50^\circ$  angle absorption.

$\sigma_1^* = 0.006$	$\sigma_2^* = 0.13$	$\sigma_3^* = 0.715$	$\sigma_4^* = 2.41$
$\sigma_5^* = 6.218$	$\sigma_6^* = 13.53$	$\sigma_7^* = 26.16$	$\sigma_8^* = 46.32$
$\sigma_9^* = 76.67$	$\sigma_{10}^* = 120.27$	$\sigma_{11}^* = 180.6$	$\sigma_{12}^* = 261.9$
$\sigma_{13}^* = 368.6$	$\sigma_{14}^* = 506.2$	$\sigma_{15}^* = 680.1$	$\sigma_{16}^* = 895.0$
$\sigma_{17}^* = 1156$	$\sigma_{18}^* = 1482$	$\sigma_{19}^* = 1914$	

(the latest is a PEC wall) different conductivity values. Table 2.5 and Fig. 2.18 show the conductivity profile and the difference between the polynomial grading of Eq. 2.62 and the new profile found by the GA approach.

According with Fig. 2.18 the GA procedure made modifications all over the PML absorber. However, the modifications become almost constant inside the PML where reflections due to the discretization errors contribute less. These modifications lead to improvements of almost 16 dB for the maximal reflection error in the range.

Figure 2.19 shows the reflection from the optimized PML constructions as a function of the normalized wavelength. The observation that one can make is that the optimization procedure improved the reflection within a range of around 5 dB across most of the spectrum.

Next, we show another results obtained using our optimization methodology. Table 2.6 shows the

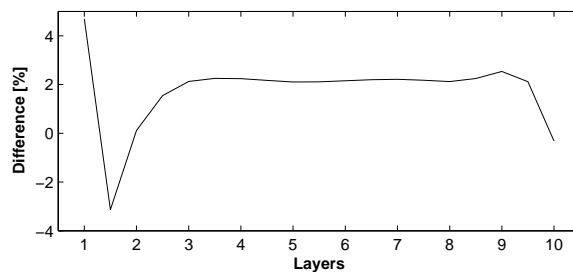


Figure 2.18: Difference between the conductivity profile given by Eq. 2.62 and the optimized solution for  $L = 10$ .

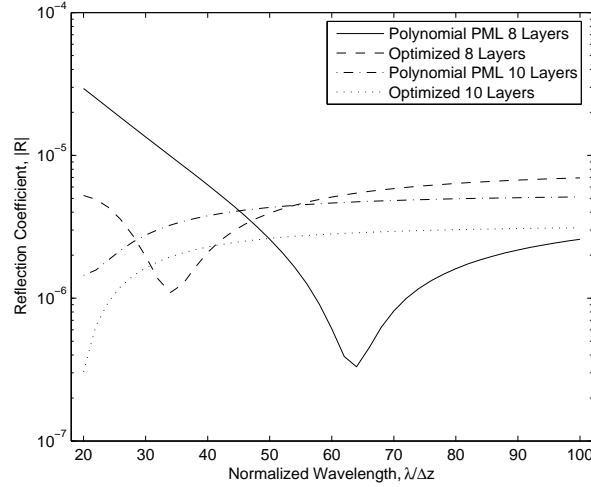


Figure 2.19: Reflection from the optimized PML constructions as a function of normalized wavelength with  $\theta = 0^\circ$ .

Table 2.6: Solutions found by the MGA for  $40^\circ - 70^\circ$  angle absorption

$L$	$\sigma_m^* \times \Delta z$	$n$	$ R _{max}$
8	3874.563	3.779	2.91e-5
10	3866.261	3.952	3.36e-6
12	4337.102	4.617	6.09e-7
14	4433.562	4.961	1.14e-7
16	4408.566	5.388	3.21e-8

Pareto-front obtained for  $\theta_1 = 40^\circ$  and  $\theta_2 = 70^\circ$ . In this case, the optimization process became more complex due to the proximity of the tangential incidence to the PML.

The MGA procedure had some difficulty to find better results in using the same parameters used in the last simulation due to the reflection coefficient found for  $70^\circ$ . In this case the largest discretization error is manifested at  $z = 0$ , the PML surface. The results for the conductivity profile in Eq. 2.62 and the optimized profile for this range are shown in Fig. 2.20.

Unlike the first range, the GA procedure performed changes with the objective to decrease the conductivity profile given by Eq. 2.62 of about 2.5%. Table 2.7 shows the optimized profile for 10 layers. The optimized results for others layers are tabulated in Table 2.8.

It is clear from the two first layers that in one single simulation run, the GA procedure is capable of finding a better conductivity profile.

However, when the number of layers increases (improving the discretization) the gain using this

Table 2.7: Optimized ten-layer conductivity profile for  $40^\circ - 70^\circ$  absorption angle.

$\sigma_1^* = 0.028$	$\sigma_2^* = 0.441$	$\sigma_3^* = 2.178$	$\sigma_4^* = 6.778$
$\sigma_5^* = 16.42$	$\sigma_6^* = 33.73$	$\sigma_7^* = 62.01$	$\sigma_8^* = 105.1$
$\sigma_9^* = 167.6$	$\sigma_{10}^* = 254.1$	$\sigma_{11}^* = 370.2$	$\sigma_{12}^* = 521.6$
$\sigma_{13}^* = 715.2$	$\sigma_{14}^* = 959.4$	$\sigma_{15}^* = 1261$	$\sigma_{16}^* = 1627$
$\sigma_{17}^* = 2075$	$\sigma_{18}^* = 2615$	$\sigma_{19}^* = 3184$	

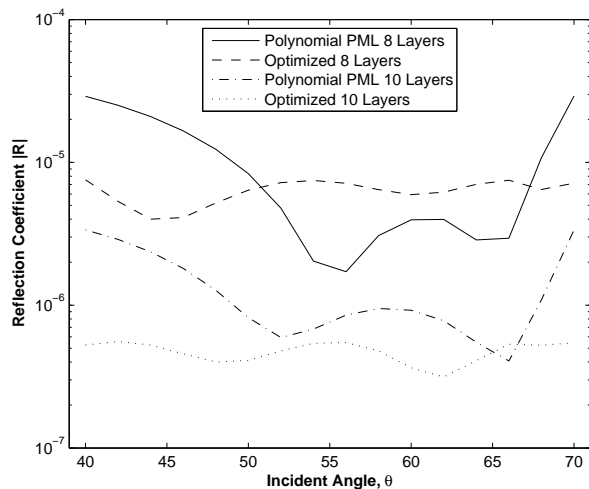


Figure 2.20: Reflection coefficient of an optimized PML for  $\theta$  from 40 to 70 degrees.

Table 2.8: Results of the optimized profile for  $40^\circ - 70^\circ$  absorption angle.

$L$	$Gain(dB)$	$ R _{max}$
8	11.73	7.54e-6
10	15.62	5.50e-7
12	6.96	2.70e-7
14	4.36	6.93e-8
16	2.19	2.57e-8

procedure becomes minimal.

In summary, these results show that Berenger's split-field PML can achieve better wide-angle performances in using multi-objective genetic algorithms to find better design parameters. In addition, the optimized PML require less memory for a desired reflectivity compared with the common design procedure.

This work demonstrated the application of the GA and MGA procedures in conjunction with a theoretical approach for computing the reflection coefficient to find an improved design configuration for the PML boundary layer. The objectives that were achieved were the minimization of the reflection coefficient and the computational cost of the electromagnetic analysis. This approach removes the burden of seeking adequate ABC absorption from the FDTD user.

Finally, it was demonstrated that the range of incident angles for which the polynomial-type PML boundaries are the most effective can be maximized by optimizing the conductivity grading.

This chapter presented a brief review of the governing equations to solve the radar problem and discussed the most common numerical techniques to model the EM fields in such an environment. It was argued that no single numerical method or technique has been found to provide a complete answer in the modeling and optimization of the radar evaluation. While promising, each technique has limitations and tradeoffs. Therefore, in order to investigate the different aspects of radar inspection of concrete, different techniques should be implemented according to the objectives.

The chapter also presented the FDTD method as an algorithm. Topics central to the FDTD method such as the FDTD mesh itself, the Yee Cell, stability and accuracy, and mesh boundary conditions were discussed. The form of the finite-difference equations used to perform the FDTD method in a dispersive medium was introduced. The actual finite difference equations used to implement the CPML in

FDTD methods are derived in appendix A. A discussion of PML optimization was presented along with a procedure to implement this special PML using genetic algorithms. Lastly, this chapter presented the FDTD method in the form of an algorithm, with a flowchart (Fig. 2.16) and a discussion of its complexity.

---

## Chapter 3

# Radar testing of concrete

Since the success of maintenance of a nation's infrastructure depends on the ability of government policy makers to strike a balance between available funds and the need for repair or replacement, radar inspection of concrete structures is increasingly being recognized as an effective way of maintenance. This is due to the fact that tools for detecting distress that results from deterioration have had undesirable limitations in the past and these same limitations extend to the detection of cracks and flaws. These limitations include requirements for prolonged structures and significant measurement uncertainty. Meanwhile, the life cycle cost of maintaining concrete structures increases when distress is not detected before it becomes too severe for effective repair or rehabilitation.

Despite the fact that radar can be used to investigate aspects of virtually any reinforced concrete structure, it has many drawbacks in currently available configurations. Before any investigation starts, the limitations imposed by reinforcement concentration, unit thickness and concrete condition must be considered. The strength of the reflected signal received by the antenna is dependent on the reflectivity of the boundaries between the elements of interest both within and surrounding the structure under investigation. The reflectivity is controlled primarily by the difference in the relative dielectric properties (reflection coefficient) of the elements and by the geometry of the boundaries. In addition, in these typical configurations, radar does not have fine enough resolution to detect small cracks.

For concrete structures, radar testing is used almost exclusively in the reflection mode, where by transmitting and receiving antennas at a small fixed distance apart traverse the inspected surface. The transmitting antenna sends a diverging beam of energy pulses into the structure and the receiving antenna collects the energy reflected from interfaces between materials of differing dielectric properties. A strong reflection will be received from the air/concrete interface at the surface, whilst other, generally weaker, reflections will occur wherever distinct boundaries occur beneath the surface.

Radar surveys on concrete structures tend to use electromagnetic waves in the nominal frequency range of 0.2 to 2 GHz. The frequency range of the pulse and depth of penetration are related, with higher frequency pulses achieving lower penetration, but better discrimination. Expert interpretation is generally required to recognize features in the data, since radar responses are dependent on the scattering of the radar pulses at dielectric material interfaces. Therefore, imaging algorithms may help an engineer to minimize the overall cost of an investigation and any subsequent works and to increase the likelihood of carrying out fully effective maintenance and repair.

The relative permittivity of air (1), concrete (typically around 6 to 10), and water (81) can be distinguished in the frequency range considered. Steel, as a conductor, is effectively a perfect reflector. Where the relative permittivity of an object is very close to that of the encapsulating material, or when the permittivity of two distinct materials is dominated by water, very low reflectivity values may be encountered, and no usable signals recovered [7].

The transmission loss is an important factor when designing a radar assessment. A balance must be struck between frequency, desired penetration, strength of reflection and size of target. Therefore the principal limitations of this technique are: the interpretation of results, the tradeoff between penetration and resolution, and the inability of penetrating steel or closely spaced reinforcements. Even considering all these limitations radar has proved to be the best technique for the assessment of concrete structures.

---

This technique can be designed to work with pulsed or time-harmonic sources. When operating in time-domain radar makes use of short transient pulses as the probing signals. In frequency-domain a frequency-hopping technique is used, in which narrow-band signals are transmitted sequentially over a period of time covering in total an ultra-wide frequency band [65].

The antenna requirements for pulsed radar are generally more stringent than for time-harmonic sources. For pulsed radar one should select the antennas which are able to transmit short pulses properly. For time-harmonic sources the antenna can be calibrated with the signal processing, which makes the antenna selection easier [88].

There is a compromise when choosing between time or frequency-domain. This decision will get in the way of all other parameters like the system design and the kind of antennas. Considering the nature of concrete structures, the numerical tools available and the computational cost associated with this kind of analysis, it was decided to work in the time-domain (the majority of commercially available radar systems use short pulses or impulses).

However, there are other factors that have to be considered like the size, type and shape of the target and the characteristics of the surface, for example. Figures 3.1 and 3.2 show 2D FDTD simulations of a radar assessment with different types, sizes and geometries of inclusions which show that void and crack detection is influenced by the size, depth, geometry, and whether air- or water-filled.

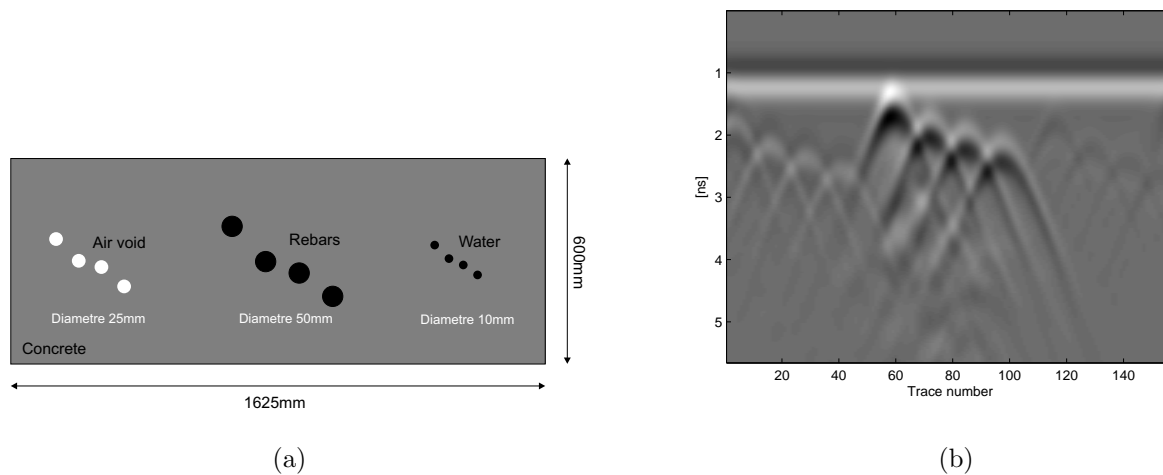


Figure 3.1: 2D simulation of a radar assessment (a) Description of the model problem (b) Reflected field computed by FDTD.

The specification of a particular type of system can be prepared by examining the various factors which influence detectivity and resolution of the system. The principal factors affecting the design of a radar testing system are discussed next.

### 3.1 System design

Radar has an enormously wide range of applications, ranging from planetary exploration to the military detection of buried mines. The selection of a range of operating frequency, modulation scheme, and the type of antenna depends on a number of factors, including the property of the host medium (physical and geometry characteristics), the characteristics of the target, including its size, shape and physical properties. The specification of a particular type of system can be prepared by examining the various factors which influence the detectivity and the resolution.

Various design options are shown in Fig. 3.3. The source can be an amplitude, frequency or phase modulated waveform or noise signal, and the selection of the bandwidth, repetition rate and mean power

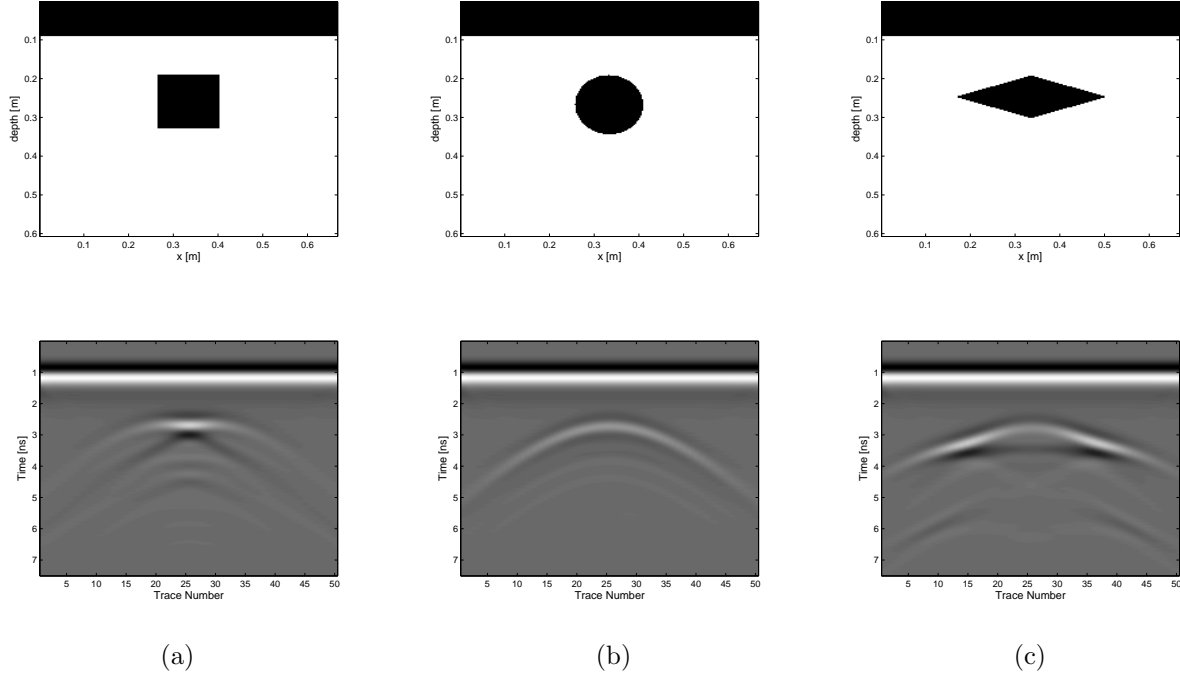


Figure 3.2: Reflected field from different target geometries. (a) Square (b) Circle (c) Losangle.

will depend upon the path loss and target dimensions. The transmit and receive antennas will be identical and will be selected to meet the characteristics of the generated waveform.

The receiver must be suitable for the type of modulation. The majority of radar systems uses amplitude modulation and an impulsive time-domain incident waveform and receive the reflected signal in a sampling receiver. In this research work, we are more interested in this type of modulation due to the numerical techniques used to simulate the radar assessment.

### 3.1.1 Range

The range of a radar is primarily governed by the total path loss, and the three main contributions to this are the material loss, the spreading loss and the target-reflection loss or scattering loss. The signal that is detected by the receiver undergoes various losses in its propagation path from the transmitter to the receiver. The total path loss for a particular distance is given as [65]

$$L_t = L_e + L_{t1} + L_{t2} + L_s + L_a + L_{sc} \quad (3.1)$$

where:

- $L_e$  = antenna efficiency loss,
- $L_{t1}$  = transmission loss from air to material,
- $L_{t2}$  = retransmission loss from material to air,
- $L_s$  = antenna spreading losses,
- $L_a$  = attenuation loss of material,
- $L_{sc}$  = target scattering loss.

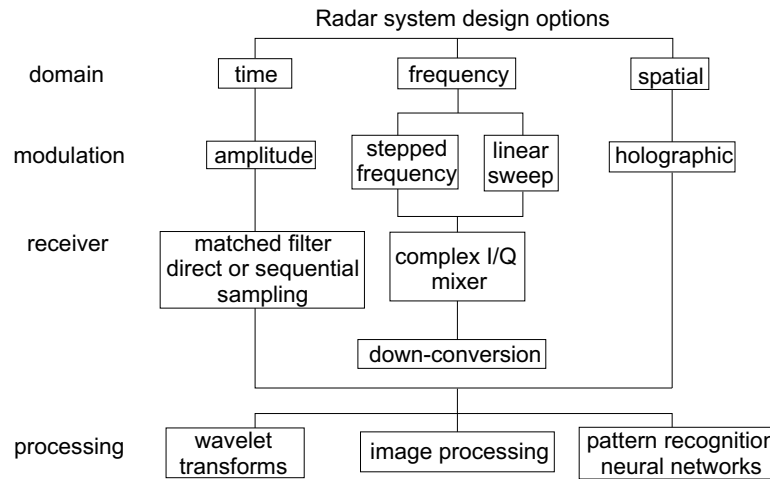


Figure 3.3: Radar system design options.

We can determine the depth range of a radar assessment using two methods: the radar equation or an estimation. A practical estimation can be obtained by using the following equation:

$$D = (35/\sigma) \text{ meters.} \quad (3.2)$$

Concluding, the attenuation is primarily determined by the ability of the material to conduct electrical currents. In simple uniform materials this is usually the dominant factor; thus a measurement of electrical conductivity (or resistivity) determines attenuation and therefore the radar depth range.

### 3.1.2 Clutter

The concrete structures in which cracks are to be detected are far from ideal. Reflective objects other than those of interest will undoubtedly be present, and the concrete structure in question will be far from homogenous. In addition, the surface of the specimen can be damaged. Clutter is a general term used to describe interference caused by coupling between the transmit and receive antennas, internal coupling and interference between the various RF components of the transceiver system, and multiple reflections between the antenna and concrete surface.

The clutter that affects the assessment can be defined as those signals that are unrelated to the target scattering characteristics but occur in the same sample-time window and have similar spectral characteristics to the scattered wave due to the target. Clutter will vary according to the type of antenna configuration. Reflections from targets in the sidelobes of the antenna, often above the ground surface, can be particularly difficult to handle. This problem can be overcome by careful antenna design and by incorporating an absorbing material in the antenna shield to attenuate the side- and back-lobe radiation from the antenna.

In general, clutter is more significant at short range times and reduces at longer times. It is possible to quantify the rate of change of the peak clutter signal level as a function of time, as in many cases this parameter sets a limit to the detection capability of the radar system.

### 3.1.3 Depth resolution

There are some applications of radar where the feature of interest is a single interface. Under such circumstances it is possible to determine the depth with sufficient accuracy by measuring the elapsed time between the leading edge of the received wavelet and a reference time such as the front-surface reflection provided that the propagation velocity is accurately known.

However, when a number of features may be present, such as in the detection of conducting bars and cracks, then a signal having a larger bandwidth is required to be able to distinguish between the various targets and to show the detailed structure of a target. In this context it is the bandwidth (B)

of the received signal which is important, as shown in Eq. 3.3, rather than that of the transmitted wavelet. However, it is important to consider that the concrete acts as a lowpass filter which modifies the transmitted spectrum in accordance with the electrical properties of the propagating medium. The depth resolution ( $\Delta r$ ) equation is:

$$\Delta r = \frac{c}{2 \cdot B \cdot \sqrt{\epsilon}}. \quad (3.3)$$

### 3.1.4 Plane resolution

The plane resolution of a radar system is important when localised targets that are sought and when there is a need to distinguish between more than one target at the same depth.

The plane resolution is defined by the characteristics of the antenna and the signal processing employed. In general, to achieve an acceptable plane resolution requires a high-gain antenna. This necessitates an antenna with a significant aperture at the lowest frequency transmitted. To achieve small antenna dimensions and high gain therefore requires the use of a high carrier frequency, which may not penetrate the material to a sufficient depth. When choosing equipment for a particular application it is necessary to compromise between the plane resolution, the size of the antenna, the scope for signal processing and the ability to penetrate the material.

### 3.1.5 Additional considerations

The majority of surface penetrating radars are based on the time-domain pulsed design where the antennas generally operate closely coupled to the object to be tested so that the polarisation of the transmitted and received signals are parallel. Alternative design options can be considered, and experimental versions of stepped frequency or synthesised impulse, as well as frequency modulated, noise or pseudo random coded, have been studied.

Time-domain pulsed radar systems are available commercially, and manufacturers usually offer a range of antennas and pulse lengths to suit the desired probing range. Some of them are shown in Fig. 3.4. For example, depths of greater than 30m require pulse lengths in the order of 40 ns, and very short range precision probing may use pulse lengths of the order of or less than 1.0 ns.

Although alternative modulation methods to the impulse radar have been used, few frequency modulated radar systems are available commercially. In order to design a radar system it is first necessary to obtain the concrete's electrical characteristics - permittivity and conductivity. In real problems, a concrete structure can be defined as an heterogeneous material. However, an approximation can be made by using dielectric models to represent the concrete mixture as an homogeneous material. The approach implemented in this research work is described in the next section.

## 3.2 Concrete properties

For over a hundred and fifty years, concrete, which is a mixture of cement, water and aggregate, has been the most commonly used building material because it is durable, cheap, and readily available and can be cast into almost any shape. The main components of concrete are the hydrated cement paste, aggregates, water, and the transition zone.

The main constituent of concrete is cement, which is made up of calcium, silica, alumina, and iron oxide. The aggregates occupy 60 to 80% of the concrete's volume. They are usually stronger than cement and therefore play a role as a filler [89].

Concrete has many voids that are usually filled with water. The water can be classified depending on the type of void and degree of firmness with which the water is held in these voids. The water, which is responsible for the electrical conductivity of concrete, is called free water and is present in voids greater than 50 nm in size.

The transition zone, the region that exists between the hydrated cement paste and the aggregate, is very thin, with a thickness on the order of 10 to 50  $\mu\text{m}$ . The transition zone is important in that it is the weakest zone in the concrete and thus influences its stiffness and durability.



Figure 3.4: Manufactures of radar systems.

As concrete is a porous and heterogeneous material, with pores filled with water, it can be expected that the relative permittivity is frequency-dependent. In order to simulate a more realistic concrete structure dielectric models are used to represent its frequency-dependent characteristics.

### 3.2.1 Theoretical models of the complex permittivity of concrete

Dielectric models attempt to determine the effective dielectric properties of a heterogeneous mixture of two or more substances of known permittivities. Factors influencing the effective permittivity of a mixture include the permittivities of the individual substances, their volume fractions, spatial distribution and shapes of the constituents and their orientation relative to the electric field vector of the incident electromagnetic wave. The substance having the highest volume fraction is generally regarded as the host medium, with the other substances being inclusions.

Many types of dielectric models have been developed for a wide variety of circumstances (not related to concrete) and several comprehensive reviews of the topic have been presented in the literature [90, 91].

In concrete, the most significant constituents are the coarse aggregate, fine aggregate, cement paste, air and water. The coarse and fine aggregates typically have a dielectric constant in the range of 4 to 7. The porosity of many concrete aggregates is low and is therefore discounted as an appreciable influence upon the effective permittivity of concrete.

However, it must also be recognised that aggregates can potentially have much larger porosities. Neville [92] reports porosities in some aggregates as high as 40%. Since aggregates may represent up to about three-quarters of the volume of concrete, it is clear that in some instances the porosity of the aggregate might materially contribute to the overall porosity of the concrete.

The porosity of cement paste varies between about 0 and 40%, depending upon the water-cement ratio and the degree of hydration achieved. Pores vary widely in their dimensions, being greatly influenced by the nature of the concrete constituents, the water-cement ratio and the presence of admixtures. Capillary pores are in the order of 1 micrometer in diameter. At high water-cement ratios (0.7) capillary porosity may introduce about 15% porosity into the concrete. More porosity in the concrete can represent more water retained in the structure which raises the conductivity making the radar assessment of the specimen more difficult.

#### Effect of water and salinity on permittivity of porous materials

Most earth and construction materials are mixtures of a bulk, or host material, air and water. In the absence of liquid water the real part of the relative permittivity rarely exceeds 7 or 8 in the frequency range utilised by subsurface radar systems. The dielectric loss factor or the imaginary part of the relative permittivity rarely exceeds 1, and, commonly, is less than 0.2 in dry materials [93].

In contrast the relative permittivity of water is in the order of 81. The dielectric loss factor for water is typically an order of magnitude larger than that of dry materials. Accordingly the dielectric properties of the host material will be dominated by the characteristics of water. The dielectric properties of dry material solids and air typically exhibit relatively little change with frequency compared to the influence arising from the presence of moisture and associated effects.

The presence of salt in solution, from minerals like sodium chloride, increases the conductivity of water and the associated dielectric losses. Salinity is defined as the mass of salt per kg of water and is denoted by  $S$ .

The frequency dependence of the dielectric permittivity of saline water  $\epsilon_{sw}$  is given by [94] the Debye equation. The velocity of propagation in pure and saline water is essentially constant above about 500 MHz, unless salinity is extremely high. Thus, concrete can be visualized as a three-phase mixture consisting of solid particles and air which have a real dielectric constant and saline water which has a complex dielectric permittivity. Two mixture models which are applicable to concrete are presented next.

#### Complex refractive index model (CRIM)

This model assumes that the solid grains and the air molecules in the concrete mixture are spherical in shape and have a continuous size distribution. This model has been derived by Feng and Sen [95]

---

who proposed a geometrical three-phase model based on the Effective Medium Theory to model partially saturated rocks. The refractive index  $\eta_t$  for a medium is defined as

$$\eta_i = c\sqrt{\mu_r \varepsilon_r}. \quad (3.4)$$

The CRIM model asserts that the effective complex refractive index for the mixture is given by the volume average of the complex refractive indices of the constituents

$$\sqrt{\varepsilon^*} = (1 - Sw)\phi\sqrt{\varepsilon_a} + \phi Sw\sqrt{\varepsilon_{sw}} \quad (3.5)$$

where:

- $Sw$  is the water saturation,
- $\phi$  is the void ratio (porosity),
- $\varepsilon_a$  is the dielectric permittivity of air,
- $\varepsilon_{sw}$  is the relative complex dielectric permittivity of water.

The CRIM model has been widely used for soils, rocks and concrete because of its simplicity, however, the method has no theoretical basis. It is generally considered to be inaccurate for high salinity or low frequencies. Sometimes, CRIM is used as real mixture law to predict the real part of  $\varepsilon^*$  by considering only the real part of the dielectric permittivity of water  $\varepsilon_{sw}$  and ignoring the imaginary part.

### Discrete grain size distribution model (DGSDM)

To simulate a more realistic model, Halabe [96] proposed the use of a discrete model. This model deals with complex conductivities instead of complex dielectric constants. Halabe suggested that the three constituents of concrete have to be added in a step by step manner. Water is considered as the smallest particle, is added first and becomes the host material.

The complex conductivity is expressed as

$$\sigma_N = \sigma_{N-1} - \sum_{i=1}^K \frac{3(\sigma_{N-1} - \sigma_i)\nu_i\sigma_N}{\sigma_i + 2\sigma_N} \quad (3.6)$$

where

- $\sigma_N$  is the complex conductivity of the mixture up to  $N^{th}$  step,
- $\sigma_{N-1}$  is the complex conductivity of the mixture up to  $(N - 1)^{th}$  step,
- $\sigma_i$  is the complex conductivity of the  $i^{th}$  inclusion,
- $\nu_i$  is the volume fraction of the  $i^{th}$  inclusion,
- $K$  number of inclusions at each step.

Equation 3.6 is a quadratic equation in  $\sigma_N$  which can be solved iteratively or using the direct closed form solution at each step to obtain the two roots for  $\sigma_N$ . If there is only one inclusion at each step then  $K = 1$ . Among the two mixture models presented, CRIM is the simplest but has no theoretical foundation. The discrete model is more robust, representing better the physics of concrete structures. A comparison between the two methods for retrieving concrete characteristics is shown next.

---

## Numerical study

The various input parameters in these models for dielectric properties of concrete are temperature, frequency, porosity and degree of saturation in concrete, salinity of the pore water and dielectric properties of concrete solids. In the case of the discrete grain size distribution model, a more detailed volumetric proportions of the concrete constituents is also required.

Temperatures of 20° and 5° have been considered in this study. The former represents conditions during fairly warm summer days while the latter is more typical of winter months in the northern hemisphere. The radar antennas typically used for concrete transmit energy in a narrow bandwidth of about 0.2 to 2 GHz and a central frequency of 1 GHz. The porosity of newly cast concrete is usually of the order of 0.1 but disintegration due to freeze cycles can cause concrete to have a higher porosity of about 0.15, and even up to 0.2 in some extreme cases. For the purpose of this study, porosities of 0.10 and 0.15 have been considered. The degree of saturation of concrete varies between 40 or 50% in warm summer months to 75% in cold winter months. The inner portion of concrete usually retains a higher degree of saturation, fluctuating between 70% and 95% round the year. This numerical study presents results for the entire range of 0 to 100%, but more emphasis has been placed on the 50% to 100% range.

No direct measurement of the salinity of water present in the pores of concrete exposed to natural environment has been found in the literature. One exception to this is the case of concrete exposed to marine environment, which is not the area of application considered in this work.

Usually the salinity of concrete is 21 ppt (parts per trillion). Such a small amount of salinity is inherent in concrete because of impurities in mixing water. Sometimes, salt is added to concrete during the mixing process to reduce the setting time. For the purpose of this numerical study, salinity values ranging between 12 and 150 ppt have been considered. This range represents the salinity of a typical deck during its entire service life.

The remaining parameters are the dielectric constant of air and the dielectric constant for concrete solids, which is taken as 5.0. Typical values for granite, sandstones and limestones usually range between 4.0 and 7.0.

The discrete grain size distribution model requires more detailed volumetric proportions of the concrete constituents. The amount of water in the mix, and the remaining void volume is filled with air. About two-thirds of this air volume is in the form of fine pores of size less than 100 nm and the remaining one-third constitutes coarse pores of approximate size 0.05 mm. The fine pores are the result of moisture evaporation during the setting process. The entrained air helps in reducing damage of the exposed concrete. The fine aggregates usually consists of particles with sizes less than 0.125 mm. The coarse aggregates in a typical concrete mix usually have a size range of 12 to 38 mm and a volumetric content of about 50%. The remaining half of the volume consists of fine aggregates and pores filled with air and water.

Figure 3.5 presents the results predicted by the two complex mixture models for some values of porosity, salinity and degree of saturation at the 1 GHz frequency. The discrete model could not predict any value for  $S=0.0$  because for this case the volume fraction of the inclusions happen to exceed the critical value of 67% due to absence of water [96]. It is possible to avoid this problem by replacing water by air to start with when  $S = 0.0$ , which was not done here.

It can be seen from Fig. 3.5 that the real part of the dielectric permittivity of concrete predicted by the two models are very close for the cases with low degree of saturation. Field measurements on actual bridge decks have indicated that dielectric permittivity is about 9.0 for deteriorated concrete. The 50% to 100% range of saturation shows a significant difference between the two models. It can be noted also that for winter temperatures the permittivity and conductivity of the mixture are greater than in summer.

The use of the DSGM for modeling of concrete structures is not perfect since it transforms all the heterogeneity of the concrete into a homogeneous material. Considering the electromagnetic theory, where the geometry of a scatterer is important, this can be view as a limitation. However, to the best knowledge of the candidate it would be very difficult to model all the inclusions (pores and solid phases) of a concrete mixture using the modeling techniques currently available.

---

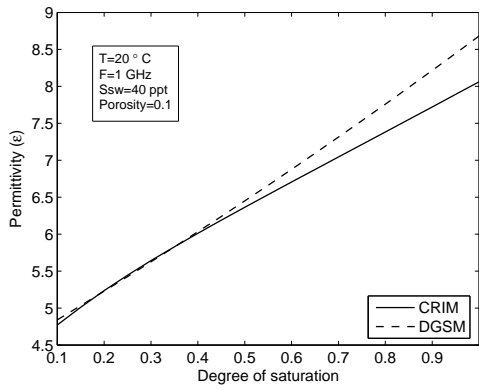
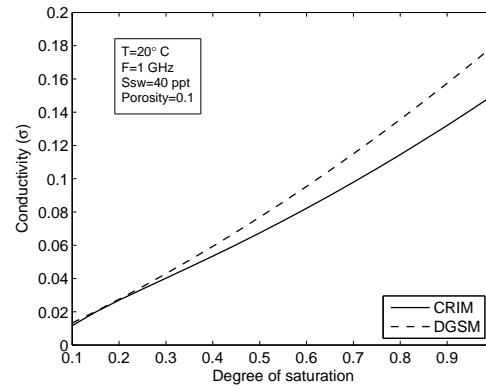
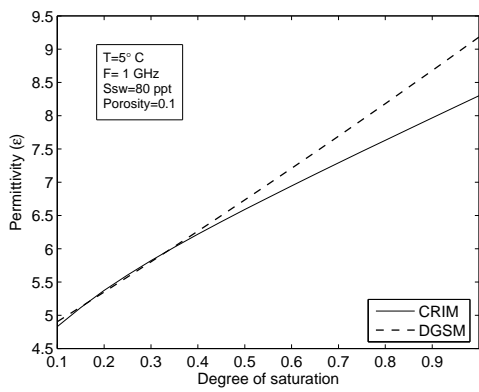
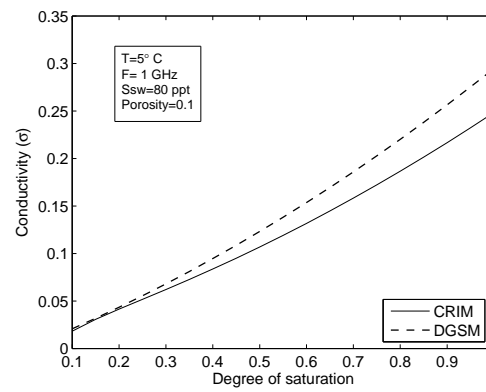
(a) Permittivity for  $T=20^\circ$ (b) Conductivity for  $T=20^\circ$ (c) Permittivity for  $T=5^\circ$ (d) Conductivity for  $T=5^\circ$ 

Figure 3.5: Comparison of the two mixture models.

### 3.3 Antennas

An antenna is defined by the *IEEE Standard Definitions of Terms for Antennas* [97] as a means for radiating or receiving radio waves. In other words the antenna is the transitional structure between free-space and a guiding device.

Further considerations in the selection of a suitable type of antenna are the type of target and the type of radar system. Where the radar system is a time-domain system which applies an impulse to the antenna, the requirement for linear phase response means that only a limited number of types of antenna can be used. Where the radar system is frequency modulated or synthesised, the requirement for linear phase response from the antenna can be relaxed and log-periodic, horn or spiral antennas can be used as their complex frequency response can be corrected if necessary by system calibration.

The antennas used in concrete inspection are, for reasons of portability, usually electrically small and consequently exhibit low gain. This has an important effect on the performance of the overall system and is probably the only example of a radar system where antenna gain is, in general, very low. However, the bandwidth of the antennas is much greater than that normally used in conventional radar systems, and radar systems generally demonstrate high range resolution. The choice of antenna is generally straightforward. The resistively loaded dipole, bowtie and TEM travelling-wave antenna have been primarily used for the impulse-based radar. These antennas can also be used in synthesised and frequency-modulated continuous-wave radars.

A typical antenna used in an impulse-radar system would be required to operate over a frequency range of a minimum of an octave and ideally at least a decade. The input-voltage driving function to the terminals of the antenna in an impulse radar is typically a Gaussian pulse and this requires the impulse response of the antenna to be extremely short. The main reason for requiring the impulse response to be short is that it is important that the antenna does not distort the input function and generate time sidelobes.

In general, radar antennas should meet specific requirements dictated by the radar's specifications, which strongly depend on the aimed purpose and application. For instance, a sophisticated radar capable of performing target identification usually imposes much more strict requirements on antennas in comparison with a radar for merely target detection. The former should be able to measure the amplitude of radar returns accurately, while the latter should only discriminate target echoes from noise and clutter.

The general requirements for antennas of pulsed subsurface radar and conventional radar are principally different due to the differences between subsurface radar and conventional radar systems as mentioned previously. For pulsed subsurface radar antennas one should consider the following aspects [88].

1. Because a subsurface radar antenna must be able to transmit in ultra-wide bandwidth, it may produce the so-called late-time ringing. The late-time ringing is oscillations that follow the transmitted pulse and occur after 2 or 3 times the pulse duration. These oscillations are caused by internal reflections in the antenna, as low-frequency components are not radiated efficiently. Such oscillations could obscure the signals reflected from the targets, rendering detection impossible. To transmit the pulse without the late-time ringing, the antenna should be ultra-wideband.
2. Because a subsurface radar antenna is usually operated near a ground (or surface) it must transmit electromagnetic fields across the air-ground interface effectively. This implies that the antenna should have good coupling to the ground for transferring more energy into the ground and less radiation into the air. However, when the antenna is situated near the ground, the antenna-ground interaction may have considerable impact on the antenna input impedance.

The above mentioned aspects limit the choice of antennas suitable for radar assessment for concrete structures. To design antennas for radar assessment one has to take into account of its characteristics when the antenna is located close to the specimen. This region is called the near-field region of the antenna. In order to explain better the concept of near-field region of an antenna and its behaviour when placed next to a dielectric specimen some antenna basic concepts are explained next.

---

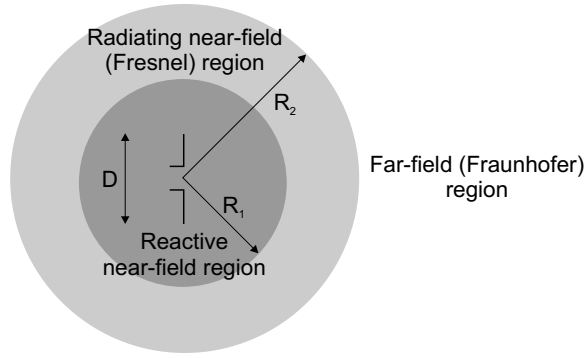


Figure 3.6: Field regions of an antenna.

### 3.3.1 Basic antenna concepts

The radiation field from a transmitting antenna is characterized by the complex Poynting vector  $\mathbf{E} \times \mathbf{H}$ . Close to the antenna, the Poynting vector is imaginary (reactive) and the electric and magnetic fields decay more rapidly than  $1/r$ , while further away it is real (radiating) and the fields decay as  $1/r$ . These two types of fields dominate in different regions in the space around the antenna. In general, the source of radiation of an antenna can be described as:

- 1 - A collection of electrical charges establishing a potential in space.

$$V(R) = \frac{1}{4\pi\epsilon} \int_V \frac{\rho e^{-jkR}}{R} dv \quad (3.7)$$

- 2 - A transport of charges resulting in time varying charge density, i.e. electrical currents.

$$\nabla \cdot \mathbf{J} = -\frac{\partial \rho}{\partial t} \Leftrightarrow \oint_S \mathbf{J} ds = - \int_V \frac{\partial \rho}{\partial t} dv \quad (3.8)$$

- 3 - Electrical currents inducing a magnetic vector potential in space. Charges can also be moved by applying magnetic vector potential.

$$\bar{\mathbf{A}} = \frac{1}{4\pi} \int_V \frac{\bar{\mathbf{J}} e^{-jk|R-R'|}}{|R-R'|} dv' \quad (3.9)$$

- 4 - A magnetic vector potential sustaining a magnetic field.

$$\bar{\mathbf{H}} = \nabla \times \bar{\mathbf{A}} \quad (3.10)$$

- 5 - A time-varying magnetic field inducing a time-varying electrical field.

$$\nabla \times \bar{\mathbf{E}} = -\frac{\partial (\mu \bar{\mathbf{H}})}{\partial t} \quad (3.11)$$

- 6 - A time-varying electrical field subsequently inducing a time varying magnetic field. Repeating the process in 5 and 6 generates radiation. Based on the characterization of the Poynting vector, we can identify three major regions as shown in Fig. 3.6.

$$\nabla \times \bar{\mathbf{H}} = \frac{\partial (\epsilon \bar{\mathbf{E}})}{\partial t} \quad (3.12)$$

#### *Reactive Near Field*

This region is the space immediately surrounding the antenna. The extent of this region is  $0 < R_1 < 0.62\sqrt{D^3/\lambda}$ , where  $\lambda$  is the wavelength and  $D$  is the largest dimension of the antenna [97]. In this space the Poynting vector is predominantly reactive, and all three components of this vector in spherical coordinates  $(r, \theta, \phi)$  decay more rapidly than  $1/r$ .

#### *Radiating Near Field*

Beyond the immediate neighbourhood of the reactive field, the radiating field begins to dominate. The extent of this region is  $0.62\sqrt{D^3/\lambda} \leq R_2 < 2D^2/\lambda$ . In this region radiation fields prevail and the angular field distribution is dependant on the distance from the antenna. This region is often referred to as the Fresnel zone [97].

#### *Radiating Far Field*

Beyond the radiating near-field region  $R > 2D^2/\lambda$  the Poynting vector is real (only radiating fields) and has only two components in spherical coordinates  $(\theta, \phi)$  [97]. The fields decay as  $1/r$ , and the radiation pattern is independent of  $r$ . This region is often referred to as the Fraunhofer zone, a term also borrowed from optics. In the far field region the radiating field can be approximated as a plane wave.

### Antenna medium interaction

In the radar assessment of concrete the antenna is used to detect a target embedded in another medium. In general, the antenna characteristics are profoundly influenced by this medium. This is particularly evident in the input resistance. When the antenna is located at a height that is small compared to the skin depth of the conducting material, the input resistance may even be greater than its free-space values [97]. This leads to antennas with very low efficiencies. Because the analytical formulation for the input impedance is complex, it will not be presented here. However, other analytical procedures are implemented to examine the field ratio ground/air and the radiation pattern when illuminated by an infinitesimal dipole located at a distance  $h$  from the surface.

According to the Fig. 3.7 we can calculate the direct air wave as:

$$E_{direct}^{air} = E_0 \frac{h}{h + \sqrt{\epsilon_r}d} e^{-jk_0(\sqrt{\epsilon_r}d)} \quad (3.13)$$

and the reflected air wave as

$$E_{reflect}^{air} = \Gamma E_0 \frac{h}{h + (h + \sqrt{\epsilon_r}d)} e^{-jk_0(2h + \sqrt{\epsilon_r}d)} \quad (3.14)$$

so that the total air wave is given by  $E^{air} = E_{direct}^{air} + E_{reflect}^{air}$  and the ground transmitted wave is given by

$$E^{ground} = T E_0 \frac{h'}{h' + d} e^{-jk_r d}. \quad (3.15)$$

In this way, considering the ground/air field ratio in Fig. 3.8 it can be concluded that one can transmit, for a point source, more energy into the material under test when  $h = 0$ . However, other aspects must be considered when dealing with radar antennas.

In the radar assessment, antennas are used on different air-dielectric interfaces that modify the spectrum, pulse shape, and directivity function. Many efforts have been made to study and predict antenna behavior over a given half-space. The radiation of dipole antennas over an homogeneous half-space have been studied by many authors [98, 99], and analytical solutions have been found, but the integral expressions of the fields still cannot be evaluated exactly. Approximate far-field solutions have been developed, and these are a useful tool for a physical understanding of the problem [100, 101].

Far-field solutions offer interesting insights into the physical meaning of the directivity function of a dipole over a half-space. Following the approach presented in [102] the far-field electric components of an electric dipole at height  $h$  over a half-space can be expressed in the  $\mathbf{H}$  and  $\mathbf{E}$  planes, respectively, as

$$E_{1\theta}(\theta) = \omega^2 \mu_0 k_{12} p |\cos \theta| e^{-jk_2 h \sqrt{1 - k_{12}^2 \sin^2 \theta}} \cdot T_{\parallel}(k_{12}) \frac{e^{-jk_1 r}}{4\pi r} \quad (3.16)$$

$$E_{1\phi}(\theta) = \omega^2 \mu_0 k_{12} p |\cos \theta| e^{-jk_2 h \sqrt{1 - k_{12}^2 \sin^2 \theta}} \cdot T_{\perp}(k_{12}) \frac{e^{-jk_1 r}}{4\pi r} \sqrt{1 - k_{12}^2 \sin^2 \theta} \quad (3.17)$$

where  $k_1$  and  $k_2$  are the wavenumbers in the dielectric and in air, respectively,  $k_{12} = (1/k_{21})$ ,  $T_{\perp}(k_{12})$  is the TE dielectric-air transmission coefficient

$$T_{\perp}(k_{12}) = \frac{2\sqrt{k_{21}^2 - \sin^2 \theta}}{|\cos \theta| + \sqrt{k_{21}^2 - \sin^2 \theta}} \quad (3.18)$$

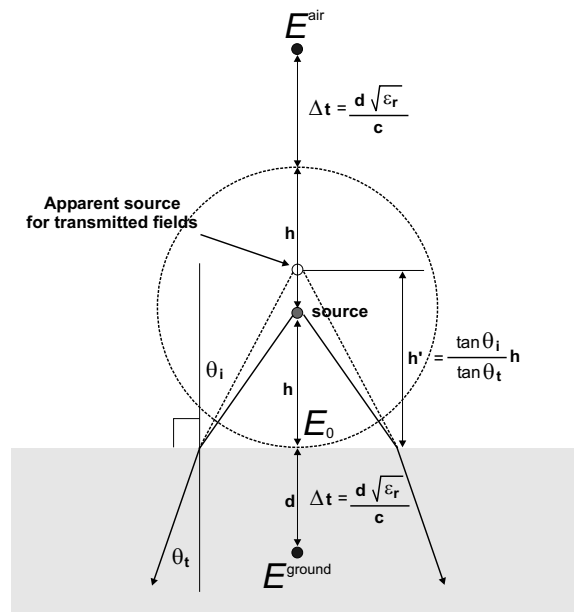


Figure 3.7: Problem description for ground/air field ratio calculation.

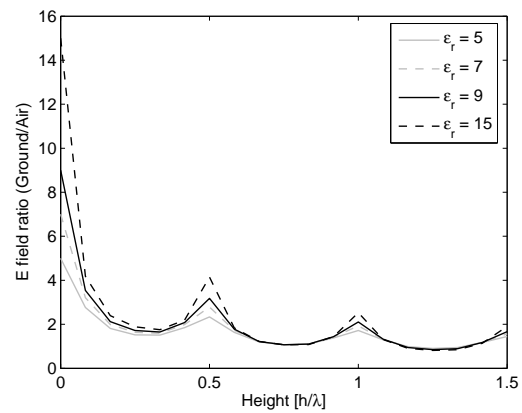


Figure 3.8: Ground/air field ratio.

$$T_{\parallel}(k_{12}) = \frac{2k_{21}\sqrt{k_{21}^2 - \sin^2\theta}}{k_{21}^2 |\cos\theta| + \sqrt{k_{21}^2 - \sin^2\theta}} \quad (3.19)$$

Figure 3.9 shows the radiation pattern of an infinitesimal dipole over a lossless dielectric medium with  $\varepsilon_r = 9$  at various heights where we can see that when the source interface space is increased, the antenna field patterns are modified by a reduction in the effect of the reactive field. Concluding, when the antenna is close to the specimen more energy is lost in the sidelobes reducing the ground/air ratio. When the antenna is far from the object the ground/air ratio is improved. However, clutter, noise and crosscoupling increase. Therefore, in order to get the target signature the better option is to place the antenna close to the object under test.

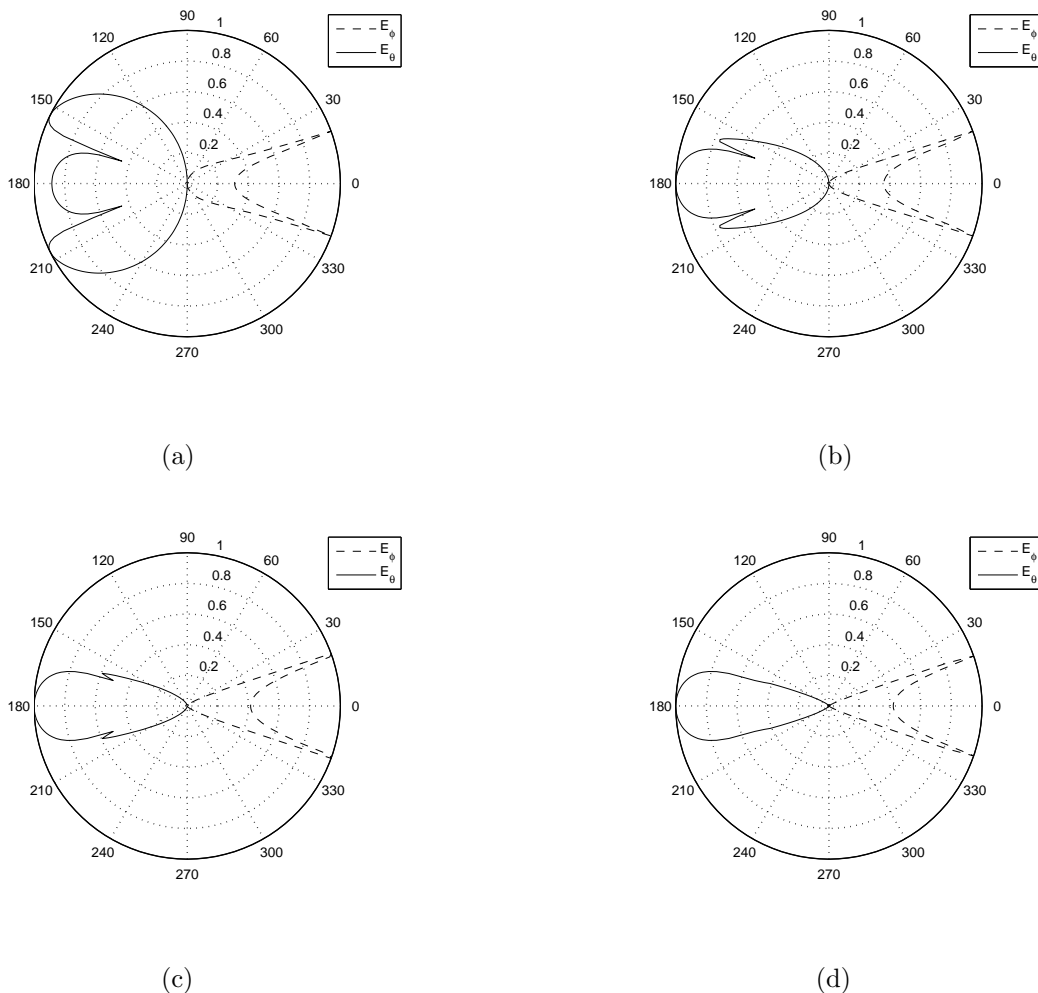


Figure 3.9: Far-field **H**-plane ( $E_{\phi}$ ) and **E**-plane ( $E_{\theta}$ ) patterns for dipoles above the interface between lossless dielectric media with  $\varepsilon_r = 9$  (a)  $h/\lambda_0 = 0$ , (b)  $h/\lambda_0 = 0.1$  (c)  $h/\lambda_0 = 0.2$  and (d)  $h/\lambda_0 = 0.35$  (normalized to 1).

### Polarization effects

When detecting linear targets (pipes, rebar, etc.), antenna orientation relative to the target becomes important. Antenna dipoles (transmitter and receiver) are predominantly sensitive to metal targets that

are parallel to them. However, if the intention is to see below the target, for instance to measure the slab thickness, then it is better to turn the antenna 90 degrees to decrease its sensitivity to the transverse targets.

Polarization effects are opposite for non-conductive targets such as PVC conduits or air-filled voids. Best results are obtained when the antenna is moved with the dipoles perpendicular to the targets.

### 3.3.2 Types of antennas

Choosing a radar antenna is a difficult matter given that the antenna picked should:

- Deliver the pulse very quickly to keep the energy in a spatially narrow band;
- Be perfectly matched with the object under test to avoid signal distortion;
- Have a progressive linear resistance in order to avoid late-time ringing;
- Have a shield that improves its radiation pattern but that does not change the other characteristics.

Considering this, for the radar assessment of concrete there are four main types of antennas: dipole, TEM horn, bowtie and spiral. These antennas will be discussed in the following.

#### Dipole

A dipole is the simplest antenna that is still frequently used for radar assessment mainly because of its simplicity. The main drawback of a dipole for this application is its inherent narrowband nature. In most of ultrawideband applications this drawback is dealt with by means of resistive loading, which can improve the dipole's bandwidth considerably by suppressing reflections from the dipole ends.

The dipole can be modified to provide good matching characteristics. One simple geometry that can achieve this is a folded wire which forms a very thin rectangular loop. This antenna is known as a folded dipole.

#### Bowtie

Bowtie antennas are simply the most commonly used antennas for radar assessment of concrete structures being employed in most of commercial radar systems. They not only have comparatively broadband characteristics but also are easy to make because of their planar surface structure and they thus have the advantage of being easily miniaturized because of their small volume as compared with horn antennas or biconical antennas. The popularity of bowtie antennas is due to their simplicity and relatively large bandwidth, which can be substantially improved by resistive loading.

#### TEM horn

Horn antennas have found most use with Frequency Modulated Continuous Wave (FMCW) radar where the generally higher frequency of operation and relaxation of the requirement for linear phase response permit the use of this class of antenna. The design of a horn antenna can provide useful gain over a decade bandwidth using a logarithmic characteristic curve for the ridges. Although horn antennas have been mostly used with FMCW systems, it can also radiate pulses.

#### Spiral

The spiral antenna is referred as frequency independent because its geometry is specified by angles. Since a curve along its surface extends to infinity, it is necessary to designate the length of the arm to specify a finite size antenna. The lowest frequency of operation occurs when the total arm length is comparable to the wavelength [97]. For all frequencies above this, the pattern and impedance characteristics are frequency independent. The main potential advantage of the planar equiangular spiral is the radiation of circular polarisation. Where the target, such as a pipe or cable, displays significant polarisation attributes, circular polarisation can be a means of preferential detection.

---

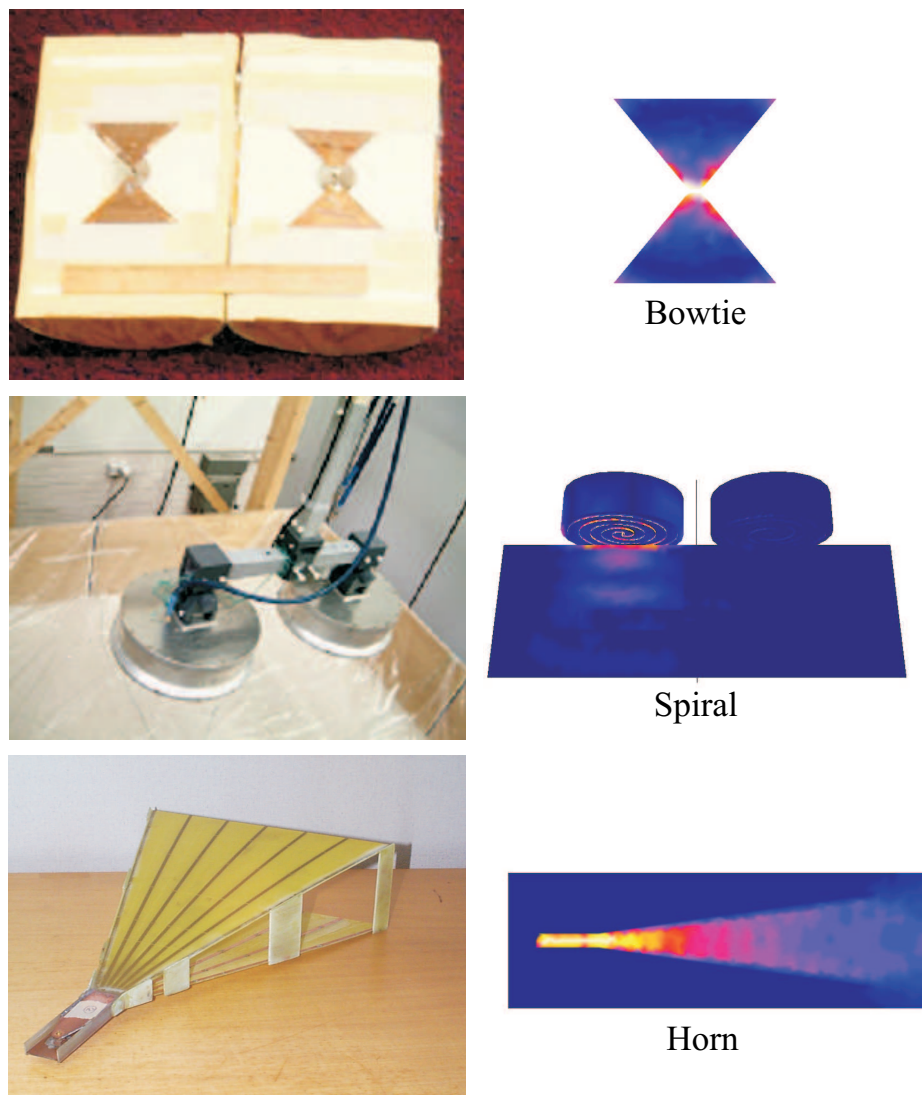


Figure 3.10: Radar antennas with FEM simulations.

In this research work the bowtie antenna and the dipole will be used based on the two facts: these antennas are the most commonly used by manufacturers of radar systems and, for amplitude modulation, these antennas are the best suited for the application. In addition, the computational effort needed for simulating antennas with a bigger conductor area such as a horn or with a complex geometry such as a spiral influenced this decision after performing FEM numerical simulations. Some of the of FEM simulations are shown in Fig. 3.10 with realistic antennas.

### 3.3.3 Bowtie antenna optimization

Antennas are one of the most critical parts in radar assessment. They substantially determine the quality of the obtained raw data.

For work on concrete two main types of antennas are used, generally described as either dipoles that operate in close proximity to the material to be surveyed or TEM horns that operate at least one wavelength from the material. Most commercial GPR antennas are bowtie dipoles given their low weight, low cost and broadband characteristics.

However bowtie antenna provides a dipole-like omni-directional pattern with broad main beams perpendicular to the plane of the antenna. Consequently, the image created by a radar assessment could not correspond to the actual target, and closely-spaced objects cannot be detected.

Antenna design is a topic of great importance to electromagnetics. It involves the selection of antenna physical dimensions to achieve optimal gain, pattern performance, voltage standing-wave ratio, bandwidth, and so on, subject to some specified constraints.

A trial and error process is typically used for antenna design and consequently the designer is required to have considerable experience and intuition.

In the last decade, several investigators have reported encouraging results from the coupling of gradient-free optimization methods with the method of moments. The combination of various optimization methods and numerical techniques further enables the optimization of planar antennas such as a bowtie shape using gradient or gradient-free optimization methods.

Gradient-free methods, or direct-search methods, are generally robust and particularly effective for problems with a large number of design variables, but require fast objective function evaluations for their practical implementation. They are largely independent of the initial design and solution domain. Therefore, global optima are more likely to be found. As is generally understood, gradient-free methods work very well when many local optima exist, whereas gradient-based methods break down in these cases.

In this work, an alternative way to design more efficient bowtie dipole antennas using multi-objective optimization process is presented.

Bowtie antennas are not isotropic radiators or receivers, and so they exhibit directionality of wave-fields. High directivity adversely affects wide angle surveys used to determine velocity and other physical attributes.

In addition, directivity becomes even more important for imaging applications used to accurately determine the shape, location, and size of subsurface targets and becomes essential when inverting GPR data to extract physical properties of targets.

The design of an effective planar bowtie antennas requires balancing the antenna length, the flare angle and the radiation pattern produced. Therefore, there is an issue of optimization in determining the antenna parameters for best performance. To address the issue of optimization, the location of the antenna in free-space was considered and evaluated in the far-field region.

Most antenna characteristics that are relevant to GPR applications such as the wave polarization, radiation field pattern and beam width are commonly defined in the far-field region of an antenna.

Notwithstanding the complexity of the electromagnetic radiation in the near-field region, most civil engineering applications using surface contact antennas are concerned with radar measurements in the near-field region [103].

Considering this complexity, edge finite elements (FEM) are used to investigate the behaviour of the optimized antenna in the near-field region of a concrete GPR assessment at the location of reinforced bars.

The goal in the optimized design of this antenna is to reduce the metal area (and consequently obtain minimal length and weight) and to improve the gain in the plane perpendicular to the antenna. The MGA are then coded to find multiple non-dominating solutions (the Pareto-front) using a fixed frequency of 1 GHz. The antenna parameters to adjust are:

$$P^g = \begin{bmatrix} L^{g,1} & \alpha^{g,1} & E^{g,1} \\ \vdots & \vdots & \vdots \\ L^{g,np} & \alpha^{g,np} & E^{g,np} \end{bmatrix} \quad (3.20)$$

where each line represents a feasible solution,  $g$  is the current generation and  $np$  is the population size. The variables to be optimized are then the antenna length  $L$ , the flare angle  $\alpha$  and the percentage of antenna elements  $E$  that can be erased. They are adjusted to minimize the metal area of the antenna. This becomes the first objective function. The second objective function is to maximize the gain in the direction perpendicular to the antenna plane.

In order to find the antenna configuration with a higher directivity and a smaller metal area we implemented an MGA to accomplish two conflicting objectives with the limits shown in Table 3.1. The solution chosen was the one with a maximal gain in the direction perpendicular to the antenna plane.

Table 3.1: Input data for the MGA optimization.

Limits		Optimization Variables		
		Antenna Length	Flare Angle	Erased Elements
Pareto	min	$0.1\lambda$	$30^\circ$	0%
	max	$1\lambda$	$120^\circ$	20%
Solution choosen		$0.87\lambda$	$79^\circ$	11%

First, the antenna is generated with 256 metal elements and then a percentage of this total between 0 and 20% is replaced with air according to the objectives. The feed region is obviously protected to avoid numerical errors. Figures 3.11(a) and 3.11(b) show, respectively, the pareto-front and the modifications applied to a given solution in order to improve the radiation pattern. The optimized antenna proposed by the algorithm with a maximal gain has  $\alpha=79^\circ$  and  $L=26\text{cm}$  with 11% of the elements erased.

The radiation pattern shown in Fig. 3.11(c) presents the gain obtained in the plane perpendicular to the antenna. The gain obtained was 6.37 dB versus 3.40 dB of a common structure with improvement of the half-power beam width from  $57.6^\circ$  to  $43.2^\circ$ . In this case, the area shown is maximum. Other solutions can be found according to the designer's needs.

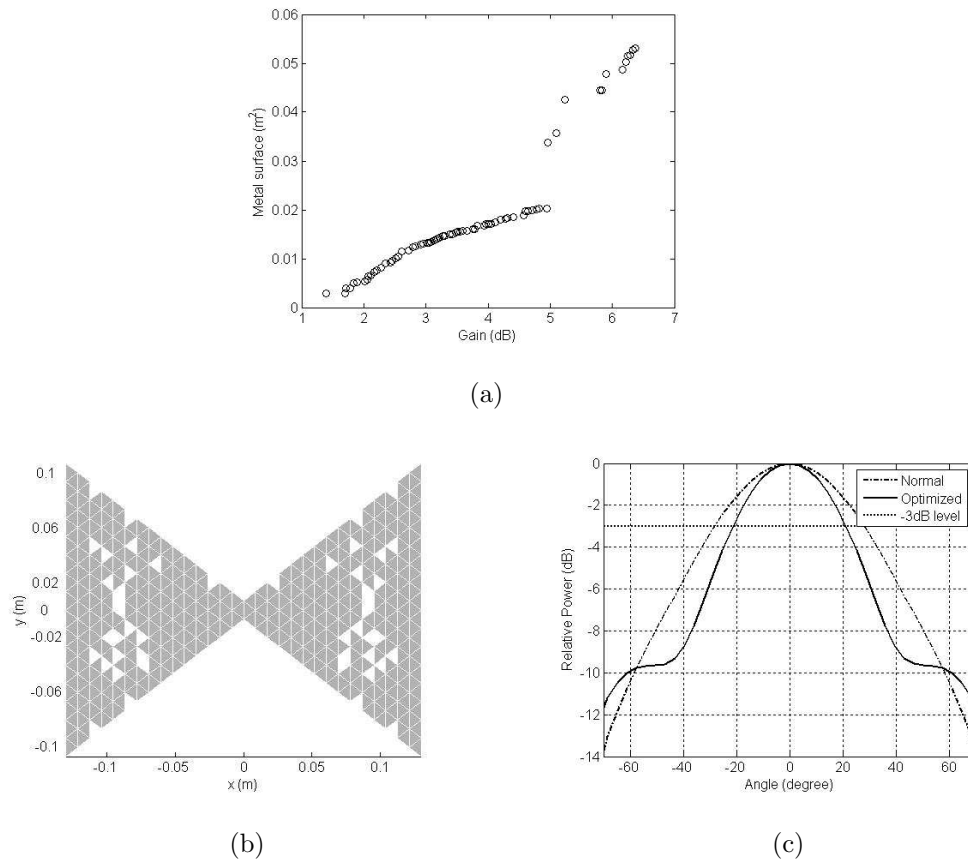


Figure 3.11: Planar bowtie (a) Pareto-front (b) Optimized antenna (c) Radiation pattern

The convergence has been attained in about 50 generations with a population of 50 individuals in several GA executions. The crossover and mutation probabilities were set to 0.9 and 0.05 respectively.

To take into account the coupling effects of the antenna on a dielectric interface, FEM are useful due to their correct physical sense and accuracy. One of the advantages of working with FEM is that this method

Table 3.2: Data for the concrete problem.

Porosity of concrete	0.15
Degree of saturation	0.7
Salt content	52 ppt
Temperature	20°C

can deal with complex geometries without additional modifications in the formulation. Considering this, the electromagnetic propagation of a more realistic model of concrete structure was implemented using FEM.

For the electrical properties of concrete, the discrete model proposed by Halabe [96] was used. This model deals with complex conductivities instead of complex dielectric constants. The discrete model is then used to compute the complex permittivity for each frequency component.

The electrical properties used are shown in Table 3.2. In addition, a conductor shield was added to the antenna to improve its directivity. For 1 GHz the concrete slab was simulated with  $\epsilon_r = 8.37$  and  $\sigma = 0.23\text{S/m}$ . First order boundary conditions were used to truncate the domain of study. The simulation was performed in about 15 min for a domain of 25000 nodes.

The scattered near field shown in Fig. 3.12(a) illustrates a non-destructive assessment to detect the presence of a conducting bar buried 15 cm in the concrete and located parallel to the antenna's direction.

Figure 3.12(b) shows the modifications in the antenna's input impedance for three different scenarios. In the case where the bar is perpendicular to the antenna, and consequentially, located in the more illuminated region, the input impedance is more affected indicating its presence.

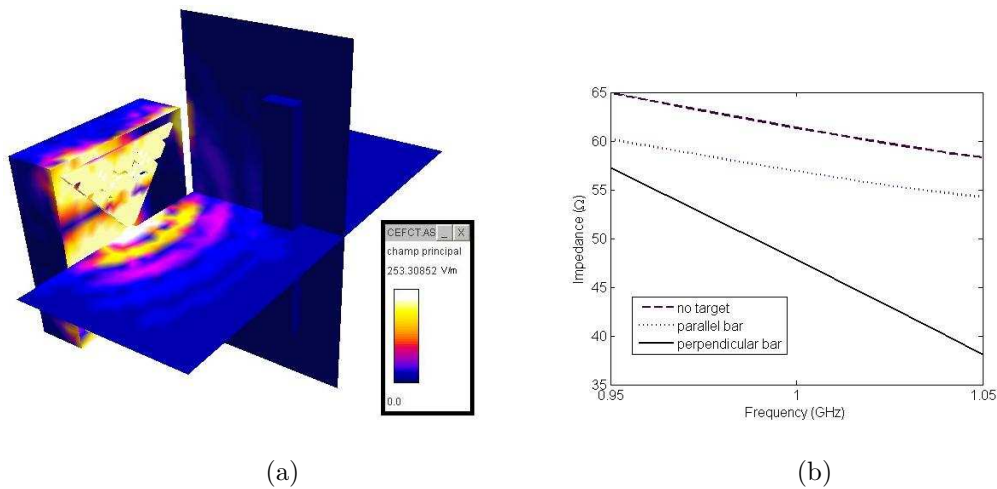


Figure 3.12: Near field results: (a) FEM simulation (b) Antenna's input impedance.

In order to improve the results, the angle between the bowtie wings was added to the problem as a new variable. The pareto-front for the V-shaped bowtie antenna is shown in Fig. 3.13 with the geometry of the solution with a maximum gain. At this time, a new constraint was imposed on the problem: the return loss of the antenna.

Antennas with a return loss greater than -10 dB fed with a 200 Ohm transmission line were penalized in the optimization process. The gain obtained was 8.77 dB with a return loss of -13.5 dB for 1 GHz. The angle between the bowtie wings found was 97.88°. In this case, the same antenna without the holes would not fulfill the impedance criteria.

The significance of this antenna pattern optimization approach is in the resolution that can be achieved by improving the antenna design. The results show that a better field pattern can be obtained with the optimized antenna which leads to a better signal penetration and more realistic GPR images of lossy

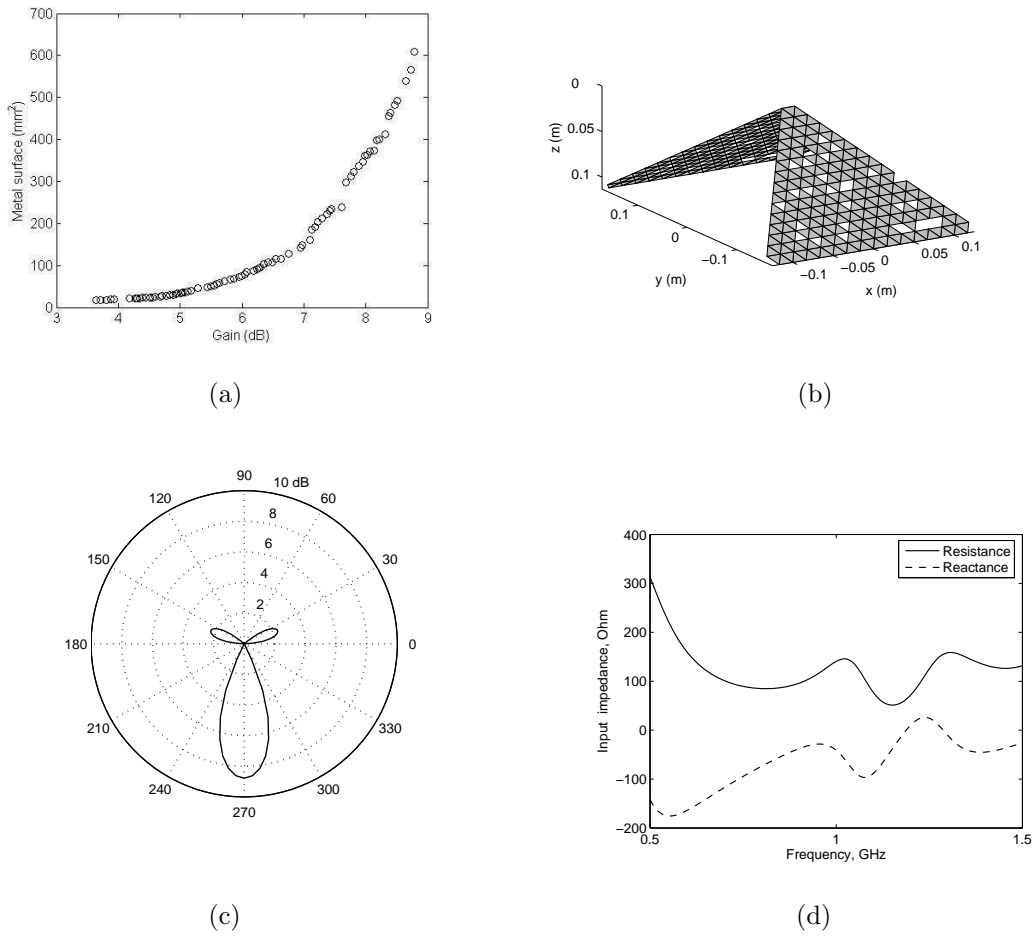


Figure 3.13: V-shaped antenna: (a) Pareto-front (b) Optimized antenna (c) Radiation pattern (d) Input impedance.

concrete structures.

### 3.4 Time-domain analysis

Deterioration and distress mechanisms in the concrete infrastructure are active under the surface and cannot be accurately assessed by visual inspection. Hence, periodic condition assessment of the concrete infrastructure results in better preventive and/or corrective planning, which will preserve its integrity and reduce its life-cycle costs. The radar method is applied as a very effective technique for investigating the integrity of concrete structures thanks to technological advancements over the past decade [65].

However, radar measurements in structures which are only accessible from one side have some limitations and the method must be optimized to detect a specific target considering the physical characteristics of concrete by selecting the appropriate antenna type, antenna frequency and antenna configuration. Therefore, the complex design of radar assessment can be aided by using numerical simulation techniques that provide the electromagnetic field behaviour when the antenna interacts with a concrete slab.

Three-dimensional FDTD simulations of the assessment of lossless and lossy soils are reported in [104] and [105], respectively. The influence of heterogeneity on GPR measurements is examined in [106]. This section presents the methodology and results from three-dimensional (3D) FDTD modeling of key system aspects relating to the bowtie antenna-element design, the propagation and scattering of the electromagnetic pulse radiated by this element within a heterogeneous and/or dispersive model of the concrete, and the backscatter response of air/water filled ducts and buried conductors.

#### 3.4.1 Summary of concrete dielectric properties

The concrete may be treated as a complex dielectric composed of inorganic material in the dry state with internal free water. The selection of a water/cement (w/c) ratio gives the engineer control over the final properties of the concrete. It is an important decision because it is a tradeoff between two desirable properties: strength and workability. As explained previously, the complex permittivity of water changes widely in the frequency bands used in the radar evaluation. Consequently, the mechanical and electric characteristics of the mixture are greatly affected by its water content.

In order to obtain the dielectric properties of concrete, dielectric models are necessary to determine the effective dielectric properties of a heterogeneous mixture of two or more substances of known permittivities. Factors influencing the effective permittivity of a mixture include the permittivities of the individual substances, their volume fractions, spatial distributions and the shapes of the constituents and their orientation relative to the electric field vector of the incident electromagnetic wave. To simulate a more realistic concrete model, we use two different approaches:

1. The model proposed by Halabe [96] that deals with complex conductivities instead of complex permittivities (homogenous model);
2. Randomly created subsurface heterogeneities.

#### 3.4.2 Homogeneous model

Simulations were performed with two types of concrete; the first is a high-performance concrete and the second is a concrete characterized by bad curing. This high-performance concrete is characterized by a low w/c ratio and use of additives and admixtures together with aggregates to obtain low porosity. But even if the composition is optimal and the compaction is well done something can go wrong through improper curing, which can determine the concrete's quality. Table 3.3 shows the properties of the two types of concrete mentioned above.

According to the discrete grain size model the permittivities of the two types of concrete can be described using the Debye parameters (shown in Table 3.4) considering the conductivity at the central frequency of 1.5 GHz. Where  $\epsilon_\infty$  is the permittivity at the high frequency limit and  $\epsilon_s$  is the static, low frequency permittivity.

The frequency behaviour of the two permittivities is shown in Fig. 3.14. Considering the simplified depth range and resolution equations (with  $\sigma$  in mS/m) the conclusion that can be made is that it is

Table 3.3: Characteristics of concrete.

Concrete	Type 1	Type 2
Degree of saturation	0.2	0.35
Salt content of water (ppm)	60	65
Temperature ( $^{\circ}C$ )	20	20
Porosity of mixture	0.08	0.2

Table 3.4: Electrical characteristics of concrete.

Concrete	$\varepsilon_{\infty}$	$\varepsilon_s$	$\tau_D$ (ns)	$\sigma$ (S/m)
Type 1	3.857	5.113	0.525	0.031
Type 2	3.981	6.398	0.033	0.182

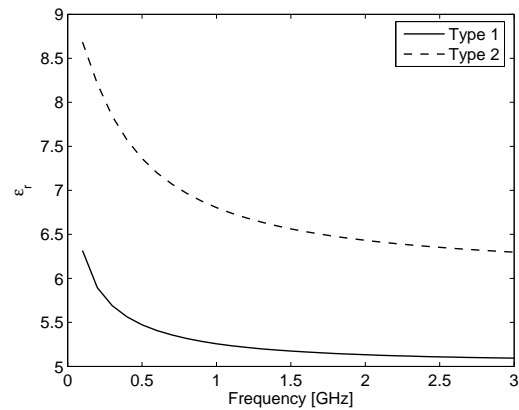


Figure 3.14: Permittivities for concrete of type 1 and 2.

more difficult to find any kind of inclusions in concrete structures affected by bad curing due to its higher conductivity and permittivity. The material loss will also affect the depth range of the assessment. Using these equations, a transmitted bandwidth ( $B$ ) of 2.5 GHz, the speed of light, and considering targets with high loss, the depth range for concrete of type 1 and 2 are  $D_1 = 1.10\text{m}$  and  $D_2 = 0.19\text{m}$  respectively. The resulting depth resolution is accurate to 2.4 cm for concrete of type 2.

Time-domain numerical simulations are performed next to verify the dispersion effects in the detection of buried targets.

### Results for the homogeneous model

In the following, we consider a bowtie antenna shielded with a metal casing. In the FDTD analysis, the slanted edges of the bowtie antenna are approximated using staircasing with a  $\lambda_{cf}/95$  ( $\lambda_{cf}$  is the central frequency wavelength in air) spatial-grid resolution.

The transmitting and receiving antennas based on the Geophysical Survey Systems Inc. (GSSI) model described in [107] are placed side-by-side immediately above the concrete. The antenna is fed by a  $80\Omega$  transmission line attached to the antenna terminals injecting a differentiated Gaussian voltage pulse with 2.5 GHz bandwidth and central frequency of 1.5 GHz. The targets to be detected are a reinforcement bar and air/water filled voids and fractures.

The design process of the antenna was the same as described in the previous section using MGA. However, at this time, no holes were inserted in the antenna. The antenna found has the following characteristics: base length 5cm, flare angle  $85.3^\circ$ , additional guide of 1.25cm and return loss of -10 dB for a feed impedance of  $80\Omega$  and is shown in Fig. 3.16.

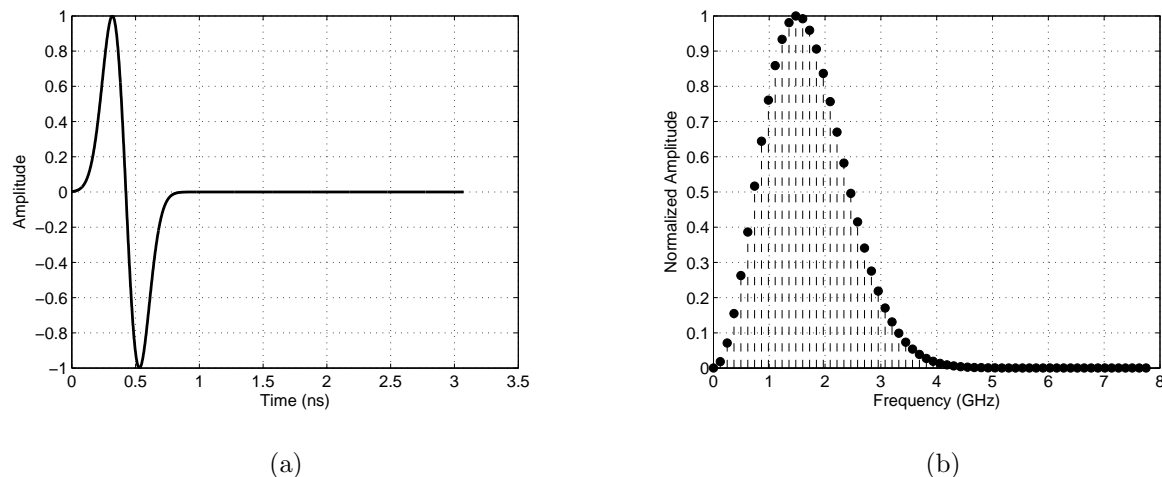


Figure 3.15: (a) Differentiated gaussian pulse with a center frequency of 1.5 GHz (b) Fourier transform of the pulse.

Pronounced effects on the radiation patterns are observed when the shielding box is filled with absorbing dielectric material [108]. In order to improve the energy delivered by the antenna the shield was filled with absorbing material with relative permittivities 3 and 20. Using a dielectric material in conjunction with the conducting shield helps improve the energy radiated below the antenna. This can be seen in Fig. 3.17 where horizontal cross section of the electric field below the antenna for the three cases are depicted. One can conclude that filling the shield with lossless dielectric material results in higher maximum radiation levels transmitted into the halfspace below the antenna than those transmitted by conductor shielded antennas. If the permittivity of the material in the shielding is lower than that of the dielectric, the conductivity of the filling material has a strong effect on the radiation patterns.

In the two cases studied with the lower permittivity (half that of the dielectric above) and with a permittivity much higher than the dielectric two facts must be considered: when the absorbing material's

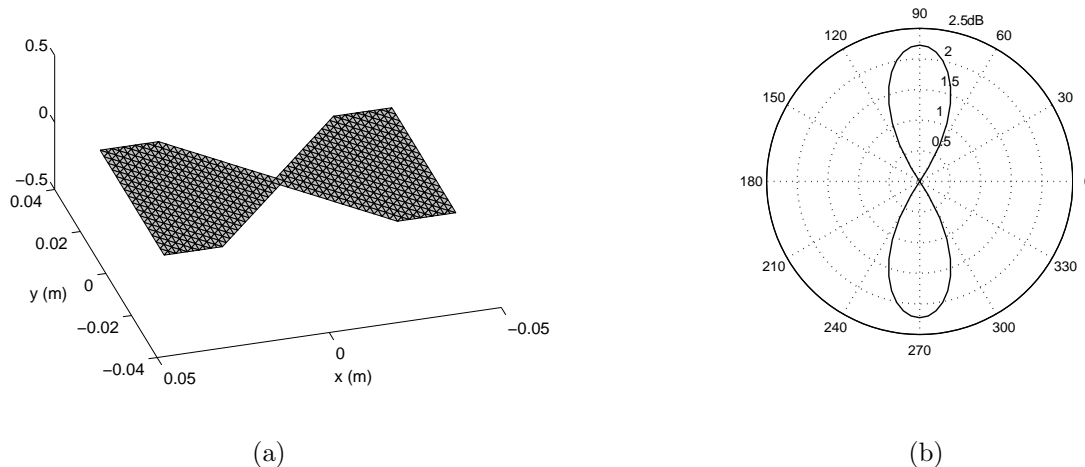


Figure 3.16: (a) Antenna geometry (b) Radiation pattern at 1.5 GHz.

permittivity is smaller than that of concrete the interactions between the antenna and the medium are small. However the clutter (first reflection from the concrete) is higher. When the permittivity of the absorbing material is higher, the inverse happens producing distortions for longer time.

Even though the energy delivered below the antenna is better for the conductor shielded antenna, the goal in this study is to analyse only the effects caused by the different models of concrete. For this reason, conducting shield without absorbers was used.

Materials having static conductivity are a serious problem for impedance matched absorbers. Past experience has shown that a classically constructed PML cannot attenuate evanescent modes. Considering the characteristics of the concrete structures analysed in this work a PML with coordinate stretching [67, 68] was used. Figure 3.18 shows the FDTD scenario of the simulation. The depth  $d$  of the reinforcement bar is 15cm with radius  $r = 1.25$ cm spaced a distance  $s = 5$ cm. The simulation was performed with the goal of studying the detection of the reinforcement bars, air and water filled ducts in different types of concrete. The 3D domain used had  $150 \times 150 \times 120$  cells with  $\Delta = 2.1$ mm and  $\Delta t = 4$ ps. Non-orthogonal grid was used to produce a fine mesh in the antenna.

Figure 3.19 shows the reflected signal from different inclusions in concrete of type 1 and 2. In type 1, it is possible to distinguish reflections from different locations. The type 2 concrete produced a reflected wave that normally cannot be detected by measurements.

This result can be explained by the fact that the radar equation doesn't account for the dispersion effects of the specimen. Figure 3.19(b) shows that even applying a time varying gain in the A-scan it would be difficult to distinguish between the reflected waves from different target positions. In spite of the relative ease of obtaining the reflected signal from the target the interpretation of the raw-data is a difficult issue. The study confirmed that the w/c ratio does have a dramatic effect on the flow properties within concrete samples which, in turn, has an effect on the durability of the concrete and the use of radar to access its condition.

### 3.4.3 Heterogeneous model

The influence of heterogeneity on radar measurements is examined in this section, looking at its influence on spatial dispersion of the signal, and defining the response from a range of standard deviations in the various distributions of physical properties. The physical properties in the near surface are never perfectly homogeneous. This heterogeneity is due to different moisture levels, grain packing, and types of material.

Physical properties play a critical role in radar measurements as important as antenna patterns, or velocity dispersion caused by complex permittivity does. Most of the studies concentrated on homogeneous blocks of material and not on heterogeneous material and its influence on spatial dispersion

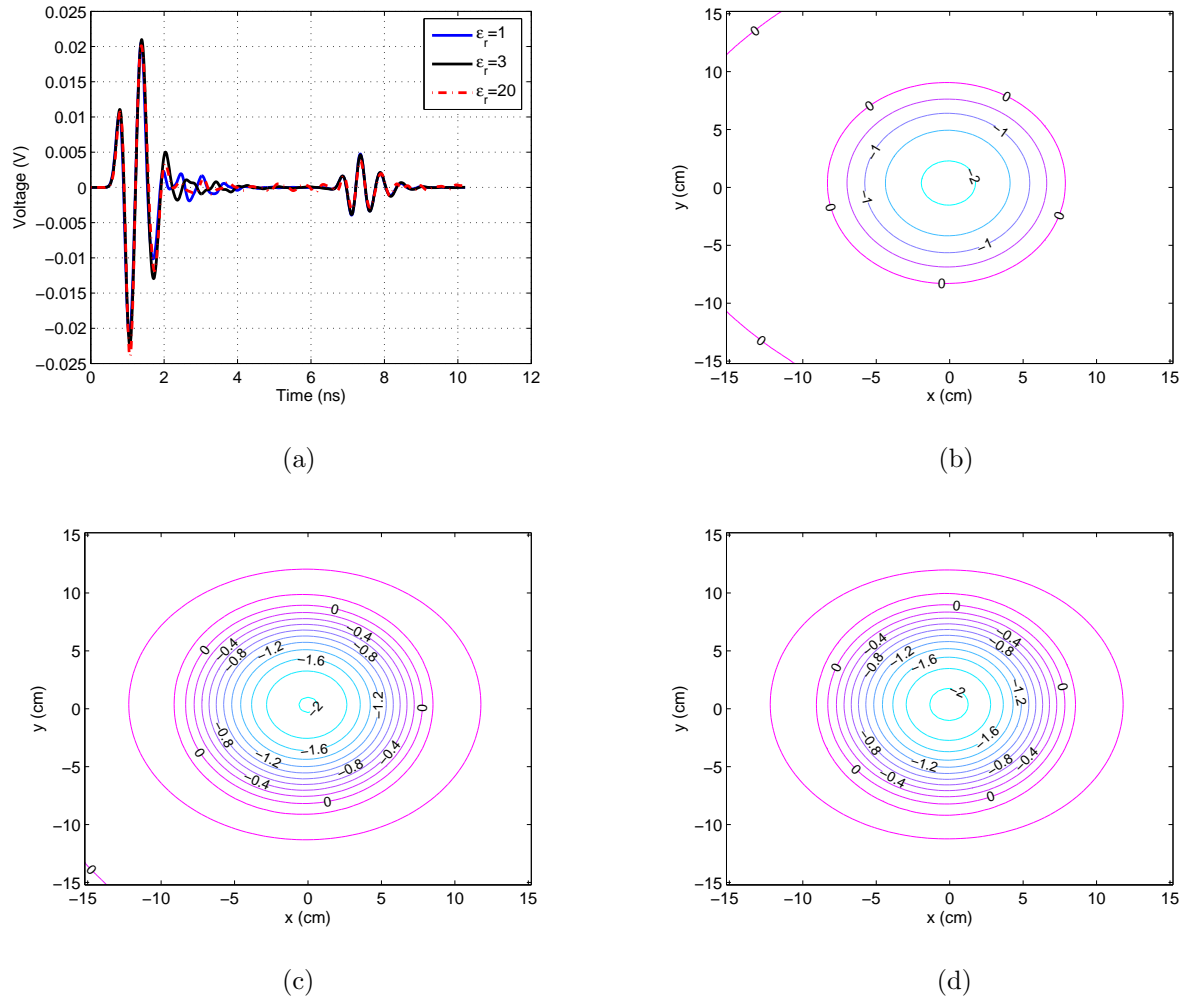


Figure 3.17: Adding permittivity in the shield (a) Received waveform (b) Horizontal cross section of the electric field for  $\epsilon_r = 1$  (c) Horizontal cross section of the electric field for  $\epsilon_r = 3$  (d) Horizontal cross section of the electric field for  $\epsilon_r = 20$ .

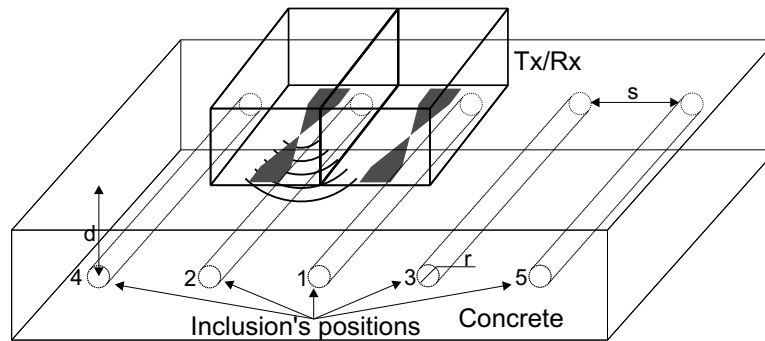


Figure 3.18: Concrete assessment problem description.

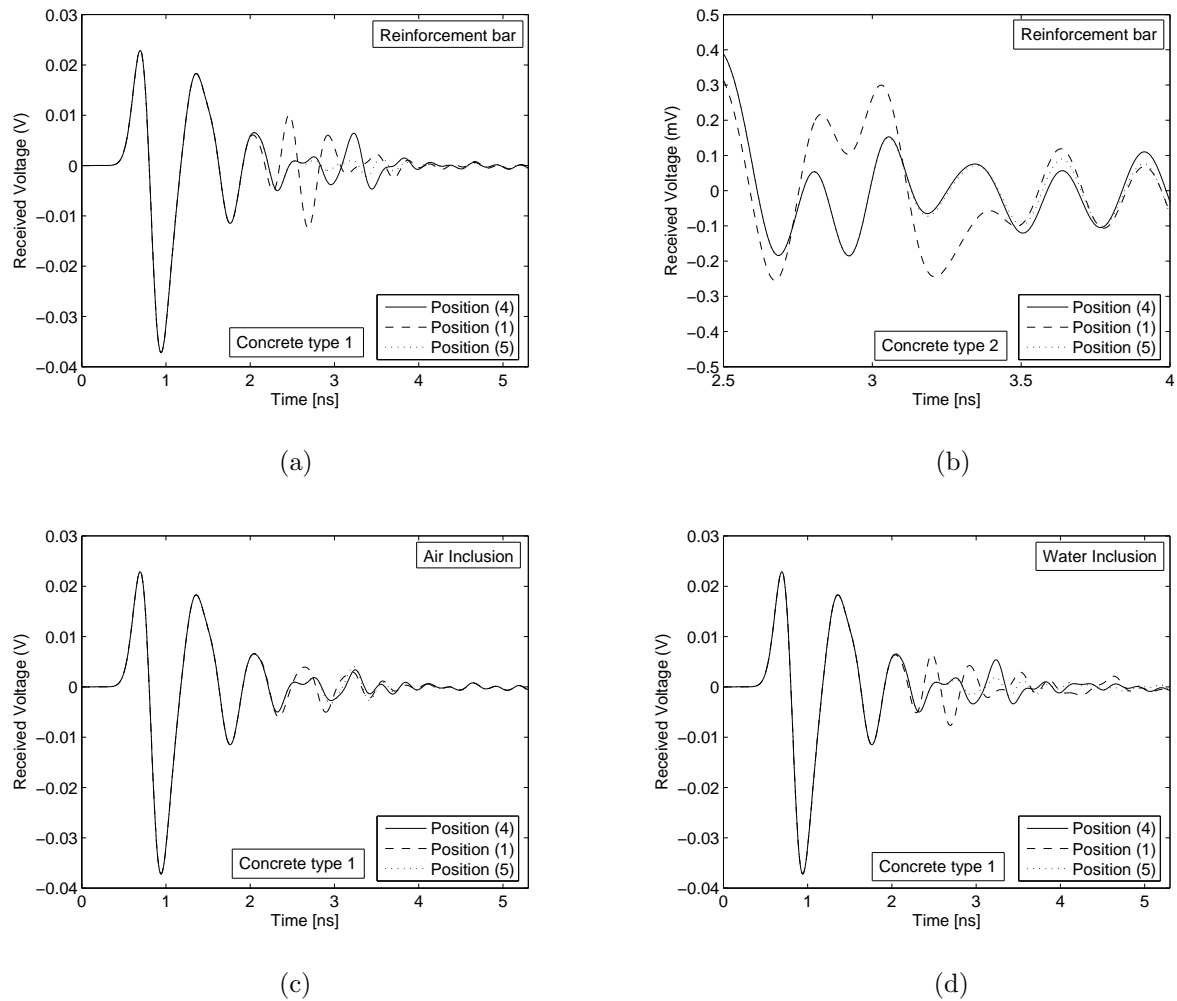


Figure 3.19: Received signal from: (a) rebar in Type 1 concrete: visual detection in positions (1) and (4); (b) rebar in Type 2 concrete: coincident signals; (c) air filled fracture in Type 1 concrete: weak reflected field; (d) water filled fracture in Type 1 concrete: strong reflected field.

of radar waves. This section investigates models that approximate the real world by incorporating the heterogeneous nature of the subsurface in lossless and lossy medium.

Physical properties of materials in the near surface are generally variable, and this heterogeneity increases as the sample size increases. Traditional geophysical models have not incorporated heterogeneity or modeled dispersive influences of geologic clutter and noise. The forward modeling results presented here incorporate heterogeneity by replacing the traditional homogenous spatial regions with a statistical distribution of physical properties.

### Model definition

The 3D model used in this section was a half space with a grid 0.4m square with a square cell size of 3.8 mm ( $\approx \lambda/10$  for the maximum frequency of 3 GHz and  $\epsilon_r = 7$ ). The center frequency of the differentiated gaussian pulse wavelet was 1.5 GHz (Fig. 3.15), the central frequency of the bowtie antenna. The ground/air interface was located 11.4 cm from the top of the grid. The relative permittivity of the half space was 6. The code was set up to run for 10 ns. The time step was 6.33 ps.

The homogeneous half space was used as the base case model. To understand where the response is coming from, the properties are changed in only one plane at a time. All of the following cases are artificial in that the heterogeneity is assumed to be totally random. This type of model was used to show the influence of random background noise in lossless and lossy media.

For this study, trends in the voltage traces and in the Ex component of the electrical field in the cross sections were examined. Random variables were used to generate distributions of physical properties. A random distribution of physical properties is a simple way to simulate a heterogeneous background media. Gaussian random variables were generated in MATLAB 7.0.1 using the randn function that creates random entries, chosen from a normal distribution with mean zero, variance one and standard deviation one.

A mean electrical permittivity value of 6 was used and standard deviations ranging from 0.05 to 0.25 were applied. Each distribution is then modified by three different standard deviations. The chosen standard deviation values were: 25%, 15% and 5% of  $\epsilon_r = 6$ .

The same random numbers were applied to modify the properties in the X direction, the Y direction, then the Z direction to simulate one dimensional changes in properties (see Fig. 3.20). A set of numbers modified the properties in the X and Y directions, the X and Z directions, then the Y and Z directions to simulate changes in permittivity simultaneously in two directions (see Fig. 3.21). A set of numbers modified the properties in X, Y, and Z directions to simulate changes in permittivity simultaneously in three directions.

The data generated by the FDTD model were examined to determine the influences of the scale change in the reflected wave received by a bowtie antenna. Starting with the individual voltage traces, the maximum amplitude and the amplitude of the reflection from a conducting plate were examined.

The cross sections of the Ex component of the electrical field were examined to determine the spatial influences of heterogeneity on a propagating wave. These data are presented in two different two dimensional cross sections and it is necessary to consider the spatial aspect of the data.

The domain of study was simulated with  $106 \times 106 \times 136$  cells with an eight cell-thick PML. Therefore the dielectric medium had the dimensions of the cube with a side of 40.28 cm. The objective is to verify the effect of the heterogeneity in the detection of a buried conductor plate at the far-end of the domain.

### Distribution change in one, two and three directions

To modify the homogeneous half space for random variations in the 1, 2 and 3 dimensions, the Matlab function randn was used to generate a list of random numbers with a Gaussian distribution centered around zero with a standard deviation of one. The random numbers that were used in the X direction were rotated 90 degrees to modify the homogeneous half space for random variation in the Y direction. To modify the homogeneous half space for random variation in the Z direction, the same numbers used for the X and Y cases were turned to create horizontal layers. Figures 3.20-3.22 show the modified permittivity for a standard deviation of 0.15 in all three cases.

The electric field is recorded in the horizontal cross-section 0.15m away from the dipole for comparisons. The sampling times and distances were chosen so that there would be data in the near field of the

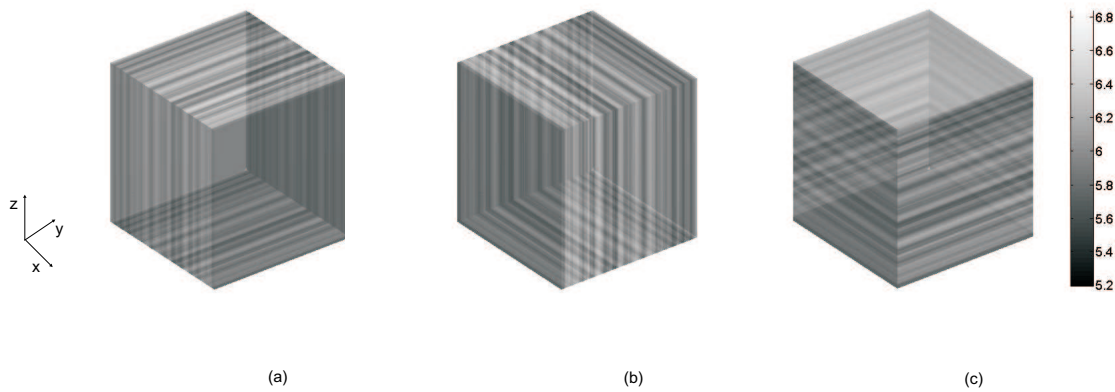


Figure 3.20: Variation of the relative permittivity with  $sd=0.15$  in the a) X direction, b) Y direction, and c) Z direction.

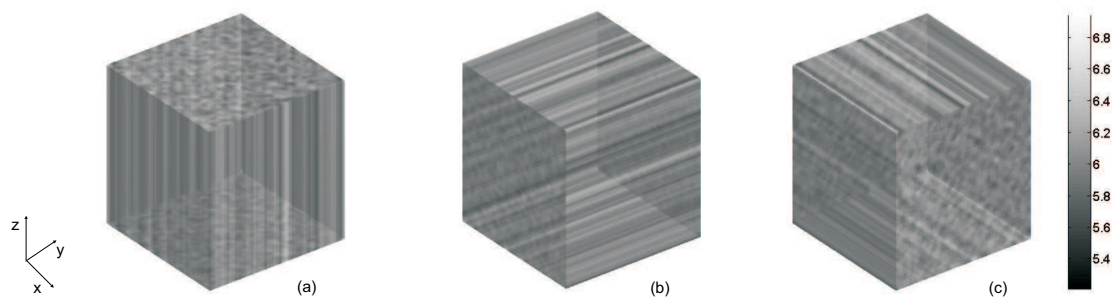


Figure 3.21: Variation of the relative permittivity with  $sd=0.15$  in the a) XY plane, b) XZ plane, and c) YZ plane.

electromagnetic wave. The near field is the region where the wave front is complex and is used in most cases for testing in civil engineering.

The random numbers were used to generate standard deviations of the relative permittivity of 6. The numbers were then added to the background permittivity to create noise. In the first case (Fig. 3.20(a)), vertical layers are used to establish change in the X direction. In the second case (Fig. 3.20(b)) vertical layers are used to establish change in the Y direction. In the third case (Fig. 3.20(c)) the change is only in the Z direction so there are horizontal layers.

#### Standard deviation 0.05

The vertical cross section in Fig. 3.23 and Fig. 3.24 were recorded at 0.15m below the surface at 3.6ns. These cases use a small standard deviation of 5% of the electrical permittivity (6) for the lossless medium and a conductivity (0.01S/m) for the lossy media. Little variation was expected between the homogeneous case and the other cases where the distribution of properties was changed in one direction.

In Fig. 3.23 and Fig. 3.24, the voltage traces illustrate that there is little visible difference from the homogeneous case. For variations in one direction the voltage plots show that the most change occurs when the thin layers are horizontal. This is expected because most of the energy is radiated below the antenna. There is also some difference when the layers are vertical. However, this difference does not affect the detection of the conducting plate in both lossless and lossy media.

There are visible reflections from the thin layers causing the spatial dispersion when the vertical layers are perpendicular to the cross sectional plane. The reflections from the thin layers can also be seen when the layers are horizontal.

The field maintains its symmetry when there are horizontal layers. However, as the interference of

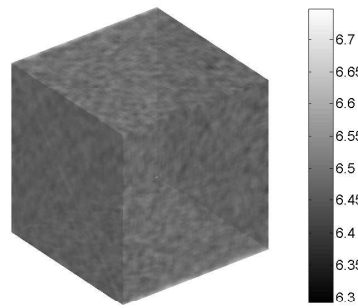


Figure 3.22: Variation of the relative permittivity with  $sd=0.15$  in the  $xyz$ .

the down going and up going waves increased, different widths of the symmetric rings occurred compared to the homogeneous case.

The most critical case in the received waveform occurred for the changes in the  $xz$  direction in which clutter is high compared with the amplitude of the reflected wave from the target. In the three directions, little visible differences from the homogeneous case are found.

#### Standard deviation 0.15

This set of runs has a standard deviation of 0.15 for the electrical permittivity and conductivity for the lossy media. Some visible difference was expected in these cases. In Fig. 3.23, the voltage traces illustrate that there are important differences from the homogeneous case when the properties vary in the  $Z$  direction.

This is expected because most of the energy is radiated below the antenna. There is also some delay in the received wavefield for the modifications in three dimensions.

#### Standard deviation 0.25

The next set of cases in this section is the high end member highlighted in this work. The voltage traces shown that there is some visible differences from the homogeneous case in all the cases for all media.

The reflected wavefield is attenuated even in lossless medium and the reflections between layers become as high as the reflected wave itself. Difficulties to find the exact location of the plate were found in all modifications.

In the lossy media, the reflections between layers become higher than the reflected wave. The location of the plate could not be obtained.

Concluding, for changes in one direction it can be seen that small changes in the relative permittivity can cause visible changes in the voltage response and the electrical field, see Fig. 3.23 and Fig. 3.24. When the layers are vertical there is a steady decline in the maximum voltage as the standard deviation gets larger. When the layers are horizontal, there is almost no change in the maximum voltage. The reflection between layers is shown for changes in  $Z$  direction. The changes in two directions show that these variations can still influence the data, especially in the  $XZ$  case. In both cases where the layers are vertical and horizontal there is no increase in the maximum voltage as the standard deviation gets larger.

These half space models show that when there are changes in the electrical permittivity, vertically and horizontally, there is dispersion in the electrical field. In addition, most of the change occurs in the near field of the antenna. The change in three directions shows that variation can still influence the data, though not as much as the thin layers. Therefore even small variations in the permittivity can have an influence on the electrical field.

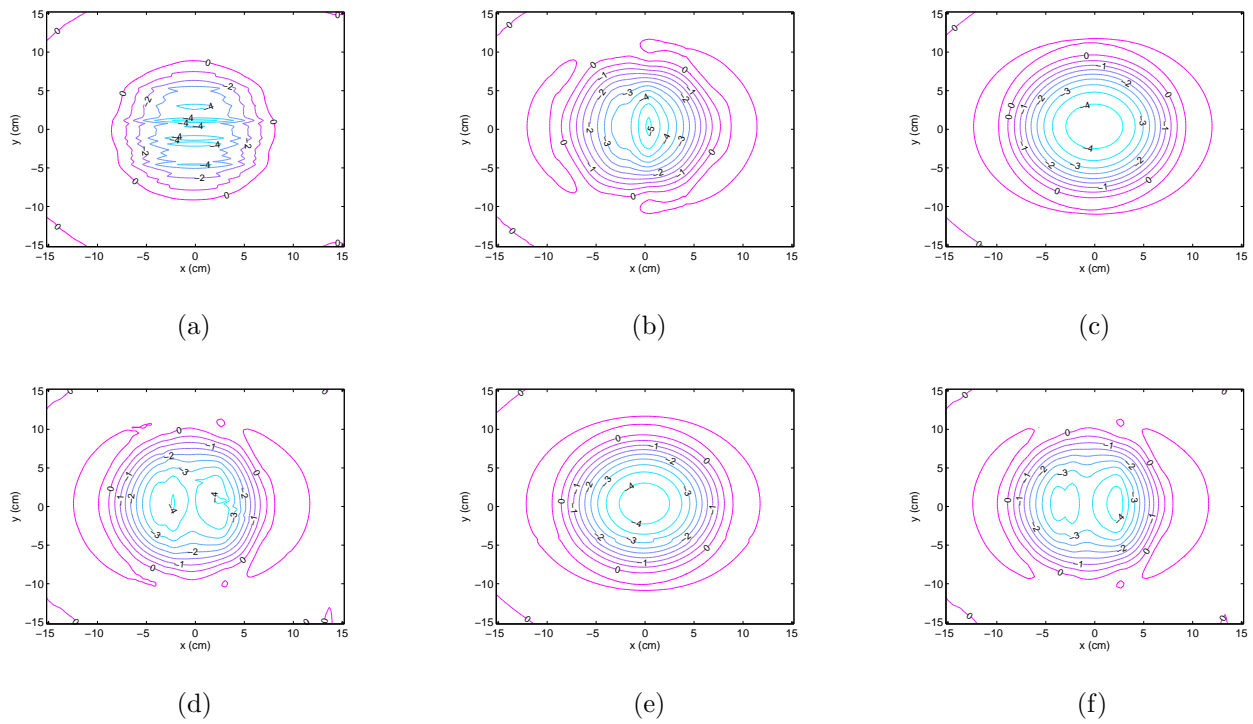


Figure 3.23: Representation of  $\mathbf{E}_x$  at 0.15 m for lossless medium with standard deviation 0.15 - Change in X direction (a), change in Y direction (b), change in Z direction (c), change in XY plane (d), change in XZ plane (e), change in YZ plane (f).

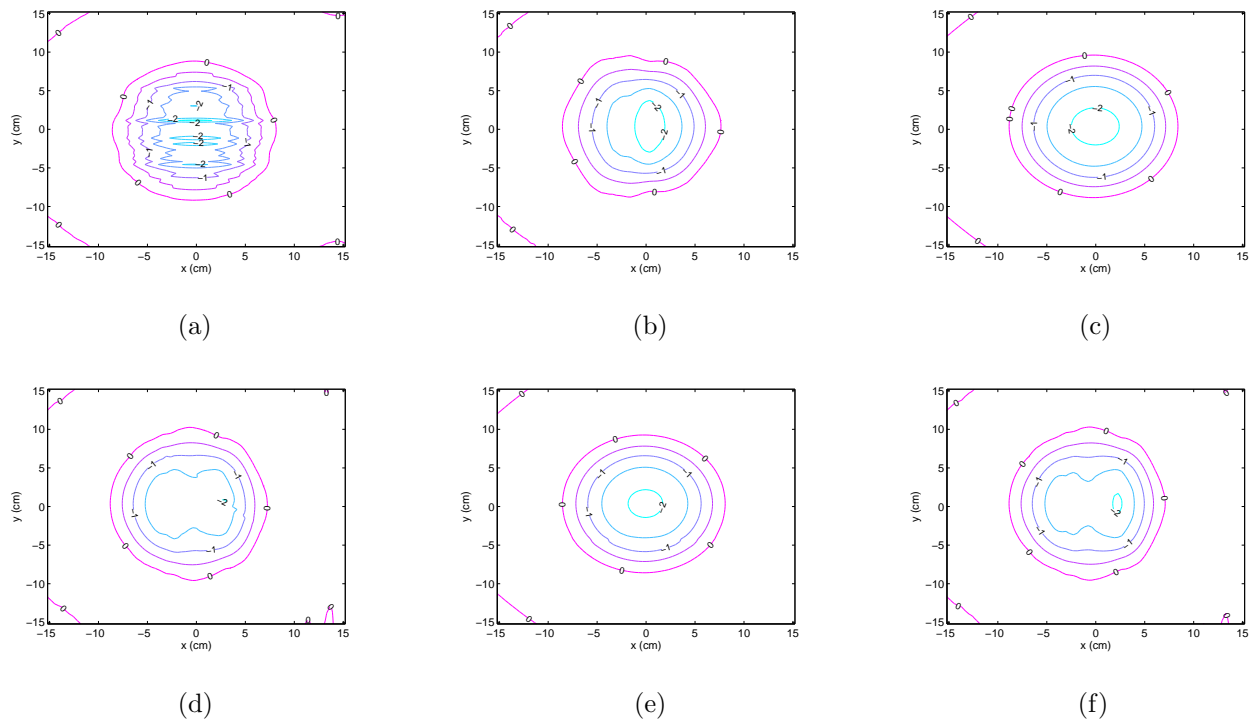


Figure 3.24: Representation of  $\mathbf{E}_x$  at 0.15 m for lossy medium with standard deviation 0.15 - Change in X direction (a), change in Y direction (b), change in Z direction (c), change in XY plane (d), change in XZ plane (e), change in YZ plane (f).

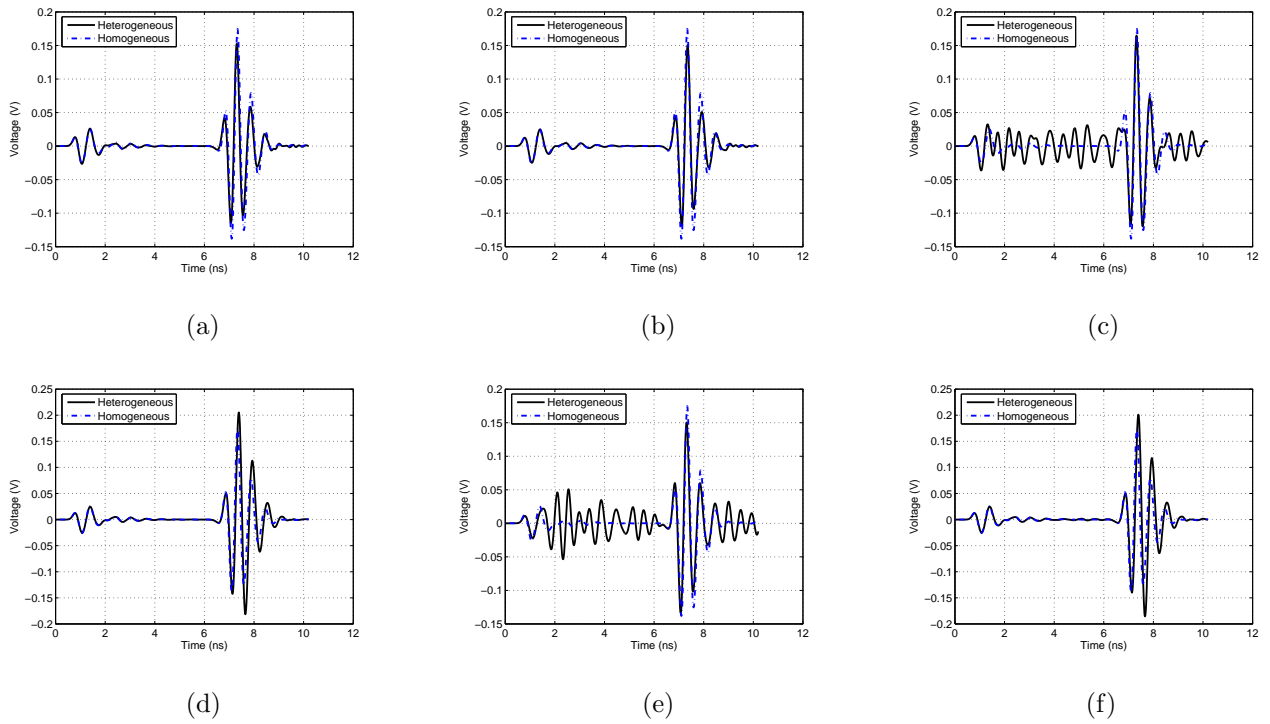


Figure 3.25: Received voltage in the antenna for lossless medium with standard deviation 0.15 - Change in X direction (a), change in Y direction (b), change in Z direction (c), change in XY plane (d), change in XZ plane (e), change in YZ plane (f).

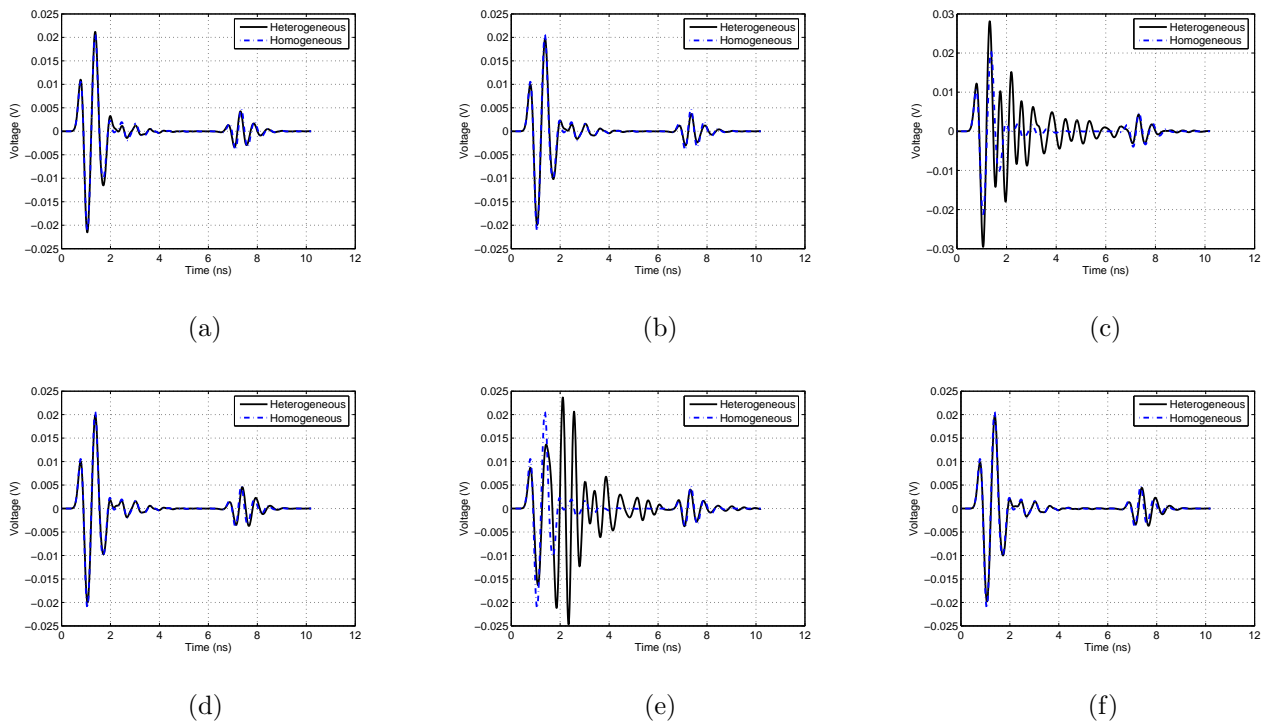


Figure 3.26: Received voltage in the antenna for lossy medium with standard deviation 0.15 - Change in X direction (a), change in Y direction (b), change in Z direction (c), change in XY plane (d), change in XZ plane (e), change in YZ plane (f).

## 3.5 Signal processing

The general objective of signal processing applied to radar assessment is to present an image that can readily be interpreted by the operator. Interpretation procedures separate and classify the reflections into different target categories and then map the relevant reflections to produce interpreted planes, sections or other diagrams. The image of a buried target generated by a radar will not correspond to its geometrical representation. The fundamental reasons for this are related to the ratio of the wavelength of the radiation and the physical dimensions of the target [65].

Significant benefits can be gained from an appropriate signal processing but past experience [65] has shown that techniques imported from image processing may cause artifacts that lead to incorrect interpretation. The general procedure when processing data is to store the data in the appropriate dimensional format and then apply appropriate algorithms.

Some of the signal processing algorithms that can be applied are: horizontal and vertical, high and low pass filters, deconvolution, migration and Hilbert transforms. Great care has to be taken so that the filters do not remove useful information.

In general most published radar data have been processed and presented in A, B or C-scan form as illustrated in Fig. 3.27. A radar trace consists of measurement noise, specular reflection from ground surface, clutter, and possibly object reflected signals. Measurement noise comes from imperfections of the hardware, approximation in analog to digital conversion, and human error. Specular reflection is the electromagnetic waves which have bounced off the air-ground interface.

There is no unique scheme for data processing, because required processing depends on: the radar system itself, the purpose of the measurement, the data acquisition scheme and the measurement conditions. One of the biggest challenges in radar assessment of concrete is to remove all the imperfections that come with the target reflected field. The area of signal processing is so extensive that only a basic view will be shown in this work.

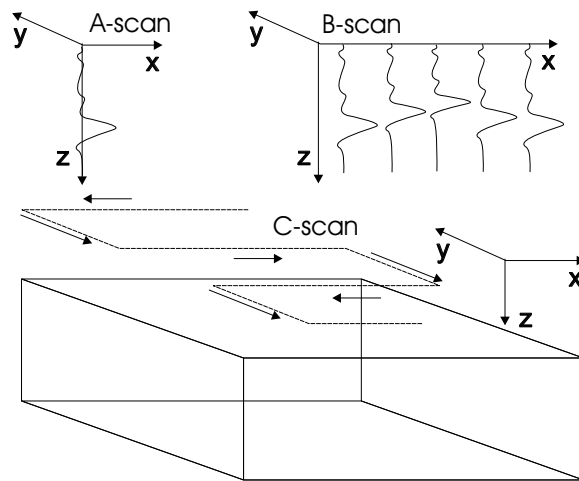


Figure 3.27: Co-ordinate system for scan description

### 3.5.1 A-scan processing

The received time waveform can be described as the convolution of a number of time functions each representing the impulse response of some component of the radar system in addition to noise contributions from various sources - hence the received time waveform [65] takes the form:

$$f_r = f_s(t) * f_{a1}(t) * f_c(t) * f_{gf}(t) * f_t(t) * f_{gr}(t) * f_{a2}(t) + n(t) \quad (3.21)$$

where

- $f_s(t)$  is the signal applied to the antenna,
- $f_{an}(t)$  is the antenna impulse response,
- $f_c(t)$  is the antenna crosscoupling response,
- $f_{gd}(t)$  is the ground impulse response ( $d$  denotes direction),
- $f_t(t)$  is the impulse response of the target,
- $n(t)$  is the noise.

The received signal is a complex response where the contributions come from all parts of the radar assessment. First, the signal applied to the antenna may be transmitted without loss in its bandwidth. In most cases the antennas used have a low frequency response that filters the signal. This is what happens with wire dipoles.

The antenna cross-coupling response  $f_c$  is composed of a fixed contribution  $f_{c'}$  due to antenna cross-coupling or reflection and a variable contribution  $f_{c''}$  due to the effect of the object. The ground impulse response  $f_g$  can be determined from its attenuation and dielectric constant across the frequency range of interest [65]. The following describes some simple processing methods.

### Zero offset removal

An important process operation is to ensure that the mean value of the A-scan is close to zero. This assumes that the amplitude probability distribution of the A-scan is symmetric about the mean value and that the short time mean value is constant over the time duration of the A-scan [65].

### Noise reduction

An other important processing technique is noise reduction and can be achieved by either averaging each individual sample of the A-scan or storing and averaging repeated A-scans. The general effect is to reduce the variance of the noise and gives an improvement in signal to noise ratio [65].

### Clutter reduction

Clutter reduction can be achieved by subtracting from each A-scan an averaged value of an ensemble of A-scans or B-scans taken over the area of interest. This method works well for situations where the number of targets is limited and they are physically well separated. Evidently, the summation of the average value will include contributions from all targets, and the greater the number of targets the lower will the difference be [65].

In addition, signal to noise ratio can be enhanced by using bandpass filtering including: Wiener filter, inverse filter, deconvolution of system transfer functions, wavelet decomposition and pulse compression. Object detection can be improved using waveform correlation and feature extraction using Multiple Signal Classification (MUSIC).

## 3.5.2 B-scan processing

The B-scan can be considered as many A-scans in one axis direction. If we consider an ensemble set of time samples comprising a B-scan, there are a number of approaches to process the signal that may be considered. Regarding topographic correction or suppression of polluted data we can cite background removal, hyperbola detection and determination of the EM wave velocity in the ground, horizontal filters and 2D migration as the most common.

---

### 3.5.3 C-scan processing

Even though many of the processes described can be applied to C-scans the principal problem when correcting C-scan data is the compensation of forward-backward movement of the radar system and positioning errors. It is important to focus the data, otherwise spurious features will appear at depths below the target. To solve this problems many techniques can be used, some of which are: ellipse detection and determination of EM wave in the ground, background removal, 3D migration and object and edge detection.

### 3.5.4 Image processing

In the assessment of concrete structures the most dominant component in the radar inspection is the specular reflection from the surface. Because this reflection does not suffer attenuation as the object scattered signals do, the specular reflection always has a large amplitude and makes the object scattered signals difficult to detect. However, the object signals can be enhanced by image processing methods. The general method of image processing is normally applied as a convolution of a two-dimensional mask filter whose coefficients are set to those of the image of the target (for which analysis is required) with the data. Alternatively, a three-dimensional data set is recorded for subsequent processing and two-dimensional data images in any orthogonal plane are produced.

Image-processing techniques involve filtering operations which require fast execution of two-dimensional convolution algorithms. These can be divided into four categories [65]:

1. lowpass,
2. highpass,
3. edge detection,
4. template matching.

All four types are commonly implemented by convolving the input data with a two-dimensional array of filter coefficients called the kernel. Each type performs a different function in the image-enhancement-restoration process and multiple types can be used to improve the image visibility. The most common convolution kernels are  $3 \times 3$  and  $5 \times 5$  and sets of commonly used kernels are listed below.

- $3 \times 3$  highpass

Highpass filter (divisor = 1)

$$\begin{array}{ccc} -1 & -1 & -1 \\ -1 & -9 & -1 \\ -1 & -1 & -1 \end{array}$$

- $3 \times 3$  lowpass

Lowpass filter (divisor = 9)

$$\begin{array}{ccc} 1 & 1 & 1 \\ 1 & 1 & 1 \\ 1 & 1 & 1 \end{array}$$

- $3 \times 3$  laplacian

Laplacian filter (divisor = 1)

$$\begin{array}{ccc} -1 & -1 & -1 \\ -1 & 8 & -1 \\ -1 & -1 & -1 \end{array}$$

- $3 \times 3$  vertical line enhancement

Vertical line enhancement (divisor = 1)

$$\begin{array}{ccc} -1 & 2 & -1 \\ -1 & 2 & -1 \\ -1 & 2 & -1 \end{array}$$

- $3 \times 3$  horizontal line enhancement  
Horizontal line enhancement (divisor = 1)

$$\begin{array}{ccc} -1 & -1 & -1 \\ 2 & 2 & 2 \\ -1 & -1 & -1 \end{array}$$

The operation called correlation is closely related to convolution. In correlation, the value of an output pixel is also computed as a weighted sum of neighboring pixels. The difference is that the matrix of weights, in this case called the correlation kernel, is not rotated during the computation. The following figure shows how to compute the (2,3) output pixel, whose initial value is 11, of the correlation of A, assuming that h is a correlation kernel instead of a convolution kernel.

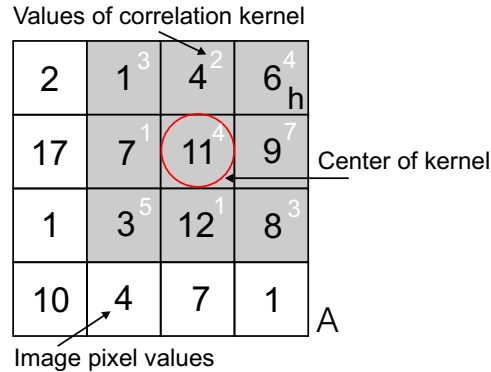


Figure 3.28: Computing the (2,3) output of correlation

$$1 \cdot 3 + 4 \cdot 2 + 6 \cdot 4 + 7 \cdot 1 + 11 \cdot 4 + 9 \cdot 7 + 3 \cdot 5 + 12 \cdot 1 + 8 \cdot 3 = 200 \quad (3.22)$$

Lowpass filtering smooths an image so that large objects are transformed into homogeneous zones and small objects are reduced in intensity and/or merged into the larger regions. In the process, edges are reduced in intensity so that the details of an object are lost and objects in close proximity to each other are combined.

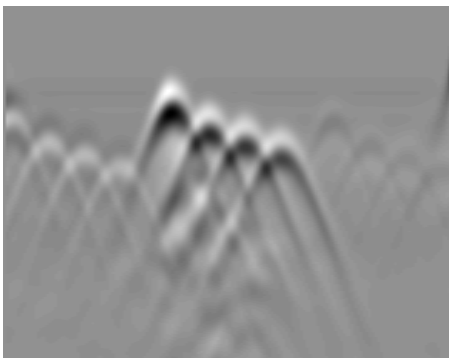
Highpass filtering performs the opposite function. Here, fine details that might be missed in the original image are increased in intensity. Note that the same mathematical operation as that for the lowpass filter is performed here; only the coefficients in the kernel have been changed.

Edge detection (or extraction) amplifies abrupt changes in intensity of an image and removes all other information. The three kinds of edge detection are the Laplacian, the Prewitt, and the Sobel operators. The Sobel and Prewitt operators have the advantage of providing edge-direction information. However, they require two or more passes, one for each edge direction. On the other hand, the Laplacian operator is isotropic, i.e. it extracts the image edges from all directions. Edge detectors provide the same type of information as highpass filters, but are more amenable to post filtering; small changes in intensity can be eliminated from further processing by comparing the output of the edge detector with a threshold value and discarding pixel values below the threshold.

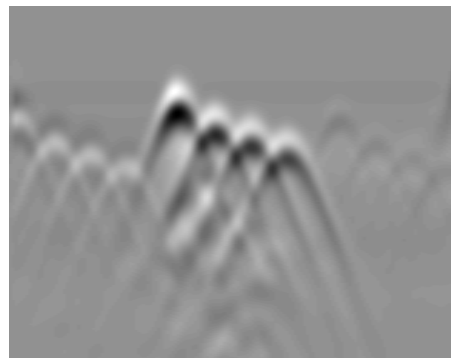
Template matching, or matched filtering, convolves the image with a kernel that contains a pattern to be detected in the data. Template matching is also often used in texture and pattern recognition to determine which parts of an image are most likely to contain targets. One example of image processing is shown in Fig. 3.29 for the problem shown previously.

### Contrast stretch with median filter

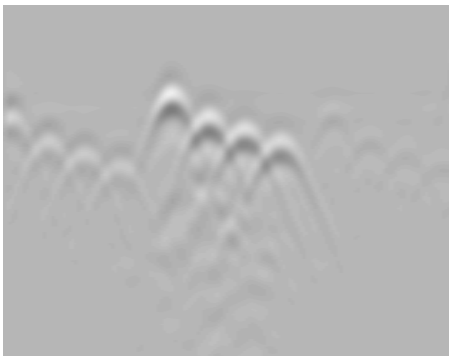
In radar image enhancement, histogram modeling techniques modify the radar image so that its histogram has a desired shape. For examples, in most cases, we would like to enhance the low-contrast part of the



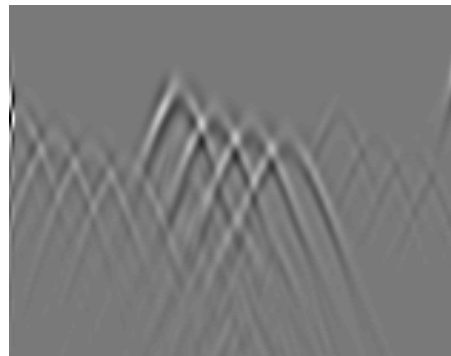
(a)



(b)



(c)



(d)

Figure 3.29: Image processing (a) Original image with clutter reduction (b) Lowpass filter (c) Vertical enhancement (d) Horizontal enhancement.

image which contains the target reflected signals. Histogram modeling techniques fall into three categories: contrast stretch, histogram modification, and histogram specification, respectively. In this section the contrast stretch was used to obtain better radar images in order to improve detection of voids. The contrast stretch increases the contrast of mid-region pixel values of an image. Mathematically, contrast stretch changes the contrast of an image  $I$  as [109]:

$$CS = \begin{cases} aI & 0 < I < a \\ b(I - a) + c & a \leq I < b \\ \gamma(I - b) + d & b \leq I \end{cases} \quad (3.23)$$

where  $a$  and  $b$  are the lower and upper boundaries defining the mid-region. Pixel whose contrast values falls into  $[a, b)$  will be given a large region, making them more observable. Pixels whose contrast values are less than  $a$  or greater than  $b$ , are given a smaller range of contrast.  $\gamma$  is a variable that controls the saturation of low and high intensities of  $I$ . The boundaries were set to zero and 255 to enhance the void reflection signal only, which falls into the mid-region. For the detection of buried voids, we note that simple background subtraction does not always produce satisfactory results. On the other hand, using contrast stretch, we can enhance the buried reflected signal and then background subtraction will be more constructive.

In this procedure, to enhance the buried reflected signals, we use contrast stretch to increase the contrast of the GPR image. After the contrast stretch, background removal is carried out by subtracting the ensemble average of the equalized image and a median filter is applied to remove any speckle point in the image. The whole process is iterated to give better results before it diverges. The median filter is taken over a window of  $3 \times 3$ . For a received GPR image  $R(m, n)$  of size  $M \times N$ , the mean subtraction is carried out as

$$Z(:, n) = R(:, n) - \bar{R}, \quad n = 1, \dots, N \quad (3.24)$$

where  $\bar{R} = 1/N \sum_{n=1}^N R(:, n)$  is the ensemble average of  $R$  along the column direction. The median filter is defined as

$$Z(m, n) = \text{median} \{R(m - k, n - l), (k, l) \in W\} \quad (3.25)$$

where  $W$  is a pre-chosen filter window, usually of size  $3 \times 3$ ,  $5 \times 5$ , or  $7 \times 7$ . The median filter is able to remove a single very unrepresentative pixel in the filter window. The algorithm for median filtering requires arranging the pixel values in the filter window in ascending or descending order and picking the middle value. Figure 3.30 shows image processing using contrast stretch for an image obtained by FDTD.

This chapter presented a review of radar systems for the detection of subsurface inclusions. The main focus was on understanding the design process of pulsed-radar and the conception of sensors for this application. In addition, dielectric models were implemented in order to represent concrete characteristics such as porosity, temperature, water and salt content in a time-domain simulation tool. An optimization procedure was implemented using MoM and MGA to detect closely spaced targets with less metal area in the antenna.

Time-domain analyses were performed for different problems and image processing techniques were described to improve the quality of data coming from these simulations. However, when attempting to estimate the depth, thickness, width and dielectric constant of subsurface inclusions from measured or simulated data image processing is not sufficient. In the past, the solution was to catalogue the curve obtained by numerical methods or scaled physical models.

The measured data were then interpreted by matching observed and predicted data. This procedure has the same limitation as the NDT method of visual inspection: misinterpretation by humans. To avoid this problem it is desirable to solve an inverse scattering problem. As is well known, inverse problems are often intractable, and therefore one has to make maximum use of the information that can be obtained from study of the direct scattering problem.

The next chapter presents three algorithms to treat inverse problems for the detection and characterization of buried inclusions in concrete structures.

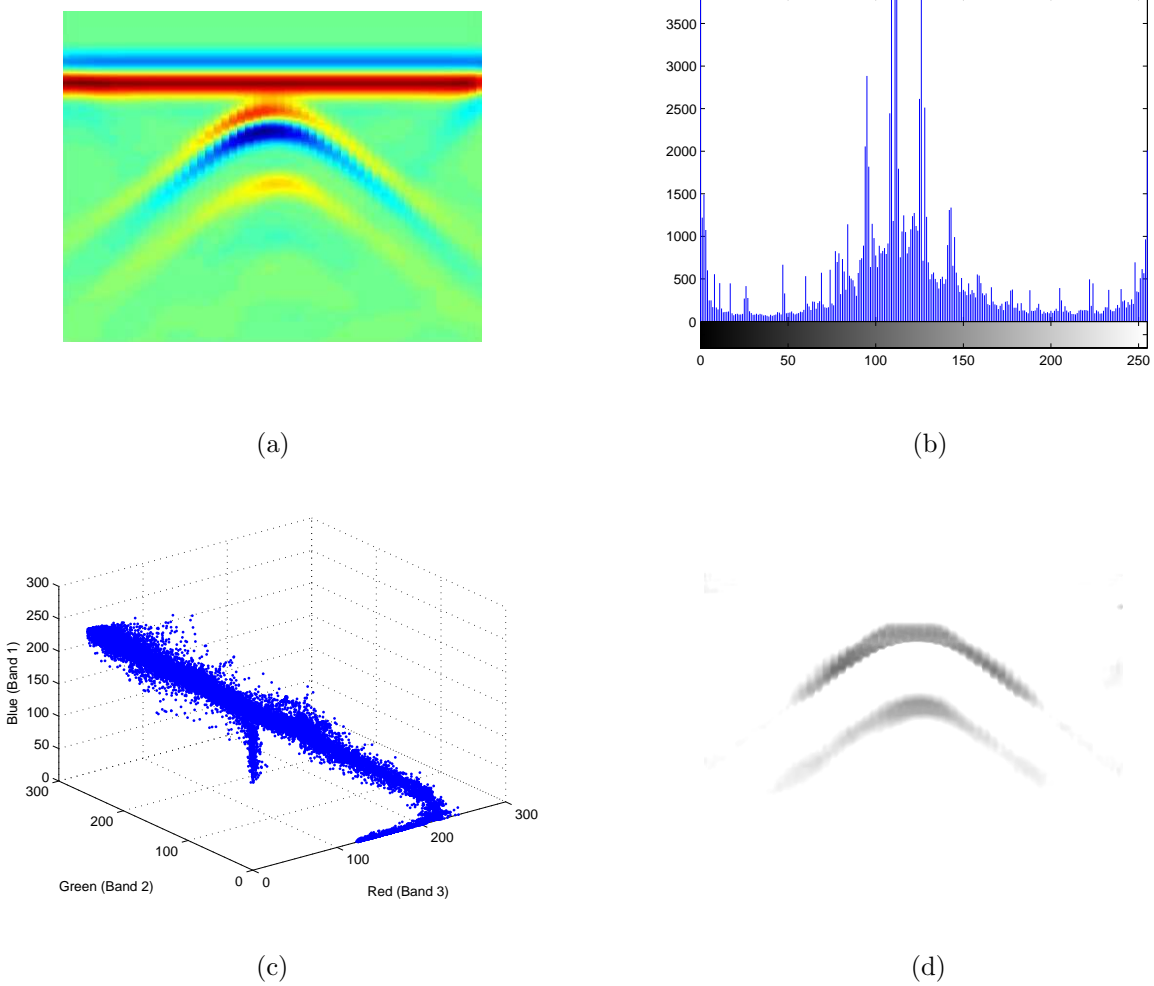


Figure 3.30: Contrast stretch example. (a) Original GPR image. (b) Histogram of the original image. (c) Scatterplot of the visible bands. (d) Final image.



## Chapter 4

# Imaging algorithms

Image classification is a commonly pursued areas in diverse fields such as military, security systems, health monitoring and biomedical engineering. This is due to the fact that it is necessary to eliminate the risk of human misinterpretation by using a machine. The main idea is to obtain information by processing data obtained from sensors. Such machines can substantially reduce the time employed for interpretation and improve accuracy of making decisions by humans operators.

The major technical problem when working with imaging algorithms is the large variation in the inspected target signature due to environmental conditions, geometric variations, noise, and sensors' characteristics. Therefore this can be considered as a multidisciplinary problem requiring contributions from diverse technologies.

Notwithstanding the importance of the above-mentioned applications, the NDT of concrete requires reliable measurement methods. Pulsed radars are attractive as environment measurement methods for various applications including the examples above. The waveform data is obtained by scanning an omnidirectional antenna. The use of this waveform for estimating target characteristics is known as an ill-posed inverse problems.

Physical problems are conventionally classified as direct or inverse problems according to the following rule. Considering a process in a physical system subject to external sources, the properties of the system are supposed to be known. Then the problem of describing the process is referred to as the forward problem. However, suppose that the information about the process is known but not about the system parameters or sources. Recovering these parameters is called an inverse problem.

In the past, various imaging or inversion techniques have been developed to refocus the scattered signals back to their true spatial location. Most of them were based on the numerical inversion of the integral equations. All these techniques are characterized by a high level of complexity and, even if the accuracy of the solution is good they require a significant computational burden. Consequently, the imaging of typical field data may be difficult due to problems like limited coverage, noisy data or nonlinear relations between observed quantities and physical parameters to be reconstructed.

Therefore, it has become necessary to use more efficient analysis for the raw-data interpretation. Such analysis requires algorithms by which problems having complex scattering properties can be solved as accurately and as fast as possible. This specification is difficult to achieve when dealing with iteratively solved algorithms characterized by a forward solver as part of the loop, which often makes the solution process computationally prohibitive for large problems. An alternative approach is the use of model-free methods based on example data. This category is represented by Artificial Neural Networks (ANN).

In this chapter, three imaging methods are investigated. First, a reverse-time migration algorithm is implemented to refocus the target to its true spatial location. Also, a model fitting technique was used to classify the target using Particle Swarm Optimization. Finally, buried inclusions characteristics considering a nonhomogenous host medium were found by using ANN. They are examined with respect to complexity and the ability to reproduce the characteristic of the underground targets considering the host medium as a concrete structure.

---

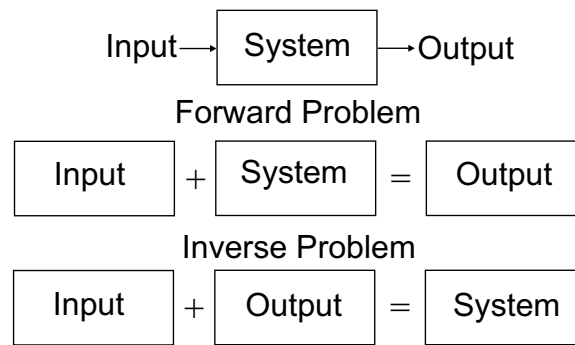


Figure 4.1: Forward and Inverse problems.

## 4.1 Inverse problems

To predict the result of a measurement requires a model of the system under investigation, and a physical theory linking the parameters of the model to the parameters being measured. This prediction of observations, given the values of the parameters defining the model constitutes the forward problem depicted in Fig. 4.1. The inverse problem consists in using the results of actual observations to infer the values of the parameters characterizing the system under investigation.

Estimating inclusions characteristics using measured signals obtained by scanning antennas is known as an ill-posed inverse problem. Electromagnetic wave propagation inverse problems are typically ill-posed, as opposed to the well-posed problems more typical when modeling physical situations where the model parameters or material properties are known. A problem is called an ill-posed problem if it satisfies one of the following three conditions.

1. Existence. There may be no model that exactly fits the data. This can occur in practice because our model of the system's physics is approximate or because the data contain noise.
2. Uniqueness. If exact solutions do exist, they may not be unique, even for an infinite number of exact data points. That is, there may be other solutions besides the one found that exactly satisfy the expected input.
3. Instability. The process of computing an inverse solution can be extremely unstable in that a small change in measurement can lead to an enormous change in the estimated model. The condition of stability is often violated for ill-posed problems.

The focus here is on the inverse problem of finding the characteristics of a target buried in a dielectric material given the reflected field measured by the antenna. In practice, the reflected signal is a collection of discrete observations in time. An important issue is that actual observations always contain some amount of noise. Two common ways that noise may arise are unmodeled influences on instrument readings or numerical round-off.

For the radar assessment of concrete, the objective is to determine a finite number of parameters. The parameters needed to characterize inclusions in a dielectric slab are found by identifying electrical (permittivity and conductivity) and geometrical (depth and radii) properties. Such a problem is called discrete inverse problem or parameter estimation problem. In general, this is a difficult problem because the obtained information is not sufficient for estimation, which requires some a priori information about the inclusions. On the other hand, a large number of data can bring the problem to instability.

One possible technique to overcome these problems is the use of parametric algorithms which are based on optimization algorithms. This kind of algorithms update the parameters iteratively to minimize (or maximize) a certain evaluation function. The computation of an approximate electric or magnetic field is done by the FDTD method as a forward solver.

The optimization process can be carried out by using many different algorithms such as the Newton method, conjugate gradient method or evolutionary algorithms. One major limitation of using parametric algorithms is the time of calculation that can be prohibitive for 3D problems.

Nonparametric algorithms can also be used. Usually they are complex to implement but they can solve inverse problems faster than parametric algorithms because it is not necessary to iteratively evaluate the function. Migration algorithms belong to nonparametric algorithms. Migration is an imaging technique commonly used for seismic prospecting. However, it can be applied for general media and targets. Considering the radar inspection of concrete structures a migration algorithm for vector waves was implemented with an idea of matched filter that is described next.

## 4.2 Reverse-time migration algorithm

The migration process essentially constructs the target reflector surface from the recorded surface. The migration technique has been much developed in acoustic, seismic and geophysical engineering and was originally developed in two-dimensional form by Hagedoorn (1954). Some reviews can be found in [110, 111, 112]. In [113] a pair of FDTD reverse-time migration algorithms was presented for radar data processing that use linear inverse scattering theory to develop a matched-filter response for the radar problem. These algorithms were developed for both bistatic and monostatic antenna configurations.

Spatial location and reflectivity are the typical information obtained from radar. Since most radars use broad beamwidth antennas, the energy reflected from a buried structure is recorded over a large lateral aperture in the image space. In the previous chapter, for example, a monostatic survey was used to collect the data over a discrete object, described as a pipe in which the diffraction appeared as a hyperbola in the space-time image. In this case, no further processing may be needed if the goal is simply to detect the pipe. However, imaging algorithms must be used to move the observed scattering events to their true spatial location and to estimate the target's reflectivity.

The algorithm developed in [113] is based on the notion of a matched filter, which is used extensively in radar applications. The matched filter concept can be explained as a correlation of the received signal with the expected or estimated signal from a specific target. If this correlation produces a large value, then it is likely that the target is present. The resulting algorithm can be directly related to reverse-time migration. Using this development, an image can be perceived as a backpropagated wave-field reconstruction of the dielectric contrast within the ground.

Mathematically, the matched filter transfer function  $H$  is expressed as the complex conjugate of the expected received waveform due to the target to which the filter is being matched. The output of the matched filter for  $N$  transmitters, located at the position vectors  $\mathbf{r}_n''$ , and an  $M$ -element receiver array, located at the position vectors  $\mathbf{r}_m''$  is expressed as [113]

$$S(\mathbf{r}) = \sum_{n=1}^N \int \sum_{m=1}^M H(\mathbf{r}_n'', \mathbf{r}', \mathbf{r}_m''; \omega) U_n(\mathbf{r}_m; \omega) d\omega \quad (4.1)$$

where  $U_n$  is the received waveform due to the  $n$ th transmitter as shown in the Fig. 4.2.

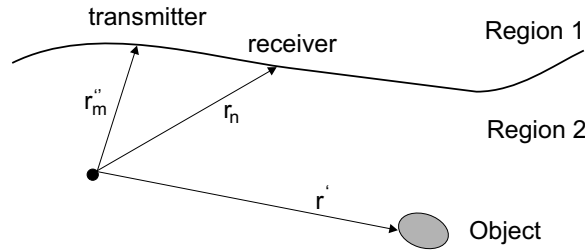


Figure 4.2: Radar problem geometry [113].

The problem geometry depicted in Fig. 4.2 consist of two half spaces where Region 1 corresponds to free space while an inhomogeneous ground, characterized by constitutive parameters  $\mu_0, \varepsilon_2(r)$ , is denoted as Region 2. Considering a weakly scattering object of finite size with constitutive parameters  $\mu_0, \varepsilon(r)$  located within the ground the matched filter will maximize the output power at  $t = 0$  if the complex conjugate of the matched filter is equal to the received signal.

The scattered electric field is expressed as

$$\mathbf{E}_{sca}(\mathbf{r}) = - \int \overline{\mathbf{G}}(\mathbf{r}, \mathbf{r}') \left[ k^2(\mathbf{r}') - k_b^2(\mathbf{r}') \right] \mathbf{E}(\mathbf{r}') d\mathbf{r} \quad (4.2)$$

where  $\overline{\mathbf{G}}(\mathbf{r}, \mathbf{r}')$  is the background dyadic Green's function, and  $k$  and  $k_b$  are the ordinary wavenumber and the Born-approximated wavenumber, respectively. If the scatterer is small enough, the following equation holds approximately

$$\mathbf{E}_{sca}(\mathbf{r}) = -\omega^2 \mu_0 \overline{\mathbf{G}}(\mathbf{r}, \mathbf{r}') \mathbf{E}_{inc}(\mathbf{r}') \quad (4.3)$$

where  $E_{inc}$  indicates the incident field. By using this approximation, the matched filter  $H$  can be written as

$$H(\mathbf{r}, \mathbf{r}', \mathbf{r}'') = \mathbf{u}_r^* \left\{ -\omega^2 \mu_0 \overline{\mathbf{G}}(\mathbf{r}, \mathbf{r}') j\omega \mu_0 \overline{\mathbf{G}}(\mathbf{r}', \mathbf{r}'') T \mathbf{u}_t \right\} \quad (4.4)$$

where  $*$  denotes the complex conjugate, and  $\mathbf{u}_t$  is the receive antenna effective length. The final image is then expressed by applying the complex conjugate of measured data to the filter

$$S(\mathbf{r}') = \left\{ j\omega \mu_0 \overline{\mathbf{G}}(\mathbf{r}', \mathbf{r}) [-j\omega R \mathbf{u}_r]^* \right\} \left\{ j\omega \mu_0 \overline{\mathbf{G}}(\mathbf{r}', \mathbf{r}'') T \mathbf{u}_t \right\}. \quad (4.5)$$

Equation (4.5) gives the migrated data as a function of frequency and the transmit and receive antenna locations. The first term is the electric field generated by a current source  $[-j\omega R \mathbf{u}_r]^*$ . If the time dependency of the received signal is introduced, this source is expressed as a derivative and time reversal  $[-j\omega R \mathbf{u}_r]^* \Rightarrow R'(-t) \mathbf{u}_r$ . The field generated by this source will be referred to as the backpropagated electric field  $\mathbf{E}_{bp}$ . The second term is simply the incident field  $\mathbf{E}_{inc}$ . Reintroducing the frequency dependencies and referring to Eq. (4.1), a complete expression for the migrated data is now shown as

$$S(\mathbf{r}') = \sum_{n=1}^N \int \sum_{m=1}^M \mathbf{E}_{mn,bp}(\mathbf{r}'; \omega) \mathbf{E}_{n,inc}(\mathbf{r}'; \omega) d\omega \quad (4.6)$$

$$\mathbf{E}_{mn,bp}(\mathbf{r}'; \omega) = j\omega \mu_0 \overline{\mathbf{G}}(\mathbf{r}_m, \mathbf{r}'; \omega) [-j\omega R_n(\omega) \mathbf{u}_r]^* \quad (4.7)$$

$$\mathbf{E}_{n,inc}(\mathbf{r}'; \omega) = j\omega \mu_0 \overline{\mathbf{G}}(\mathbf{r}', \mathbf{r}_n''; \omega) T(\omega) \mathbf{u}_t \quad (4.8)$$

where the subscripts  $m$  and  $n$  denote the field or signal due to the  $n$ th transmitter and  $m$ th receiver.

These equations are now applied to bistatic surveys using the FDTD technique.

#### 4.2.1 Bistatic configuration

In the bistatic mode, data are collected from  $N$  transmitter and  $M$  receiver locations. Equation (4.6) indicates that  $S(\mathbf{r}')$  is polarization dependent and therefore multivalued with respect to different combinations of  $(\mathbf{u}_r, \mathbf{u}_t)$  and the definition of the pixel profile  $O(\mathbf{r})$ . A physical explanation of migrated data is obtained by recalling that the value of the pixel  $O(\mathbf{r})$  was set equal to one in the previous section. Using this definition the currents induced in the object by the incident field are  $-j\omega O(\mathbf{r}) \mathbf{E}_{inc}(\mathbf{r})$ , while the scattered field is a direct result of these induced currents. Similarly, the collected data represent the currents induced on the receiving antenna by the scattered fields. In Eq. (4.7), these currents, associated with the  $[-j\omega R \mathbf{u}_r]^*$  term, are reintroduced at the received antenna locations and propagated through the object space via the same Green's function that described the propagation of the scattered field from the object to the receiving antenna during the collection process.

The final migrated data may be represented in the time domain as the convolution of the incident electric field with the backpropagated electric field evaluated at time zero

$$S(\mathbf{r}') = \sum_{n=1}^N \sum_{m=1}^M \mathbf{E}_{mn,bp}(\mathbf{r}') \otimes \mathbf{E}_{inc}(\mathbf{r}') |_{t=0}. \quad (4.9)$$

This expression is physically interpreted as the intersection of the backpropagated field with the incident field and consequently has strong ties to the reflector mapping formula used in seismic migration [114]. In fact, if the incident field is perceived to excite induced currents within the ground, this expression can be directly related to the excitation-time imaging condition [115].

Using the FDTD algorithm the image is expressed as a running sum of the product or intersection of the incident field propagating in reverse and simultaneously propagating the other field forward to save memory in the convolution process. Specifically, the incident field is propagated forward in time while recording the fields for every time step at the absorbing boundaries and the entire field at the last time step. In this work the generalized perfectly matched layers (GPML) [116] was used with 8 cells in length. This field can then be propagated in reverse by using a negative time step in FDTD and reintroducing the fields recorded at the GPML boundaries.

One example of the bistatic algorithm is shown in Fig. 4.3. In the first example, bistatic data were simulated for four localized objects, PVC pipes with 10 cm diameter buried in dry sand with  $\epsilon_r = 3.5$ . All pipes were oriented along the  $y$ -axis simplifying the experiment into a two-dimensional (2D) space in the  $x - z$  plane. An impulsive waveform with a bandwidth and center frequency of about 900 MHz was used. A sampling interval of 20 ps was chosen to meet the stability criteria of the FDTD, while 1500 samples were collected for each trace corresponding to a time interval of 30 ns. These values were used in [113] and are repeated here to validate the code. In order to prevent an invalid inversion - a different mesh was used to simulate the raw data used in the migration algorithm.

The raw data, collected at 31 receiver locations separated by 7.2 cm with the transmitter located above one of the two targets, are shown in Fig. 4.3. The three traces near the transmitter were zeroed out since the receiving and transmitting antennas were in too close proximity. The final image occur where the incident field intersects the backpropagated field. The result of the convolution is shown in Fig. 4.3(d).

In the second example shown in Fig. 4.4 a lossy environment was introduced with  $\sigma = 0.001\text{S/m}$ . In order to simulate a more realistic problem the measured signal was added to a white Gaussian noise with a signal to noise ratio of 10 dB. The simulated received signal added to a white Gaussian pulse is shown in Fig. 4.4(a).

The third example seeks to find the exact location of the targets in heterogeneous media. The FDTD scenario simulated, depicted in Fig. 4.5(a), consisted of four 12 cm diameter air filled pipes buried in concrete that was modeled with a mean electrical permittivity value of  $\epsilon_r = 6$  and conductivity  $1\text{mS/m}$  and standard deviation 0.25. Figure 4.5 shows the FDTD scenario and the final image obtained at  $t = 0$  that can be interpreted as the intersection of the back propagated field with the incident field providing a more exact location of the hollow tubes.

Finally, this process improves the final images provided by the radar inspection data. In addition its implementation is very simple. The MATLAB pseudo code is depicted in Fig. 4.6. However, this algorithm (Fig. 4.6) assumes that the background medium is known - a common assumption in many commercial softwares for the interpretation of GPR data [117]. In addition, in this simulation line sources were used which can create a problem when the objective is to find targets in close proximity. In real problems, this algorithm can be used for locating conductors and buried pipes but it can not find the exact characteristics of the inclusions.

### 4.3 Model fitting

Model fitting method is one of the parametric imaging algorithms which utilize the evaluation function and optimization algorithms. In the model fitting method, target characteristics and location are expressed as parameters. The parameters are updated iteratively to minimize the difference between the observed data and the estimated data.

An incident wave and a scattered wave can be used to characterize the scattering object. Usually, in real world problems, the incident and scattered waves are known and it is desired to identify the scattering object. This problem can be written as an optimization problem involving the scattered wave of the unknown object  $\mathbf{E}(\theta_0)$ , the reference object, and the scattered wave of a test object  $\mathbf{E}(\theta)$ . Thus,  $\theta^*$ , the optimum  $\theta$ , is the argument that minimizes the error of the reference object scattered wave  $\mathbf{E}(\theta_0)$  relative to the test object scattered wave  $\mathbf{E}(\theta)$ . Mathematically:

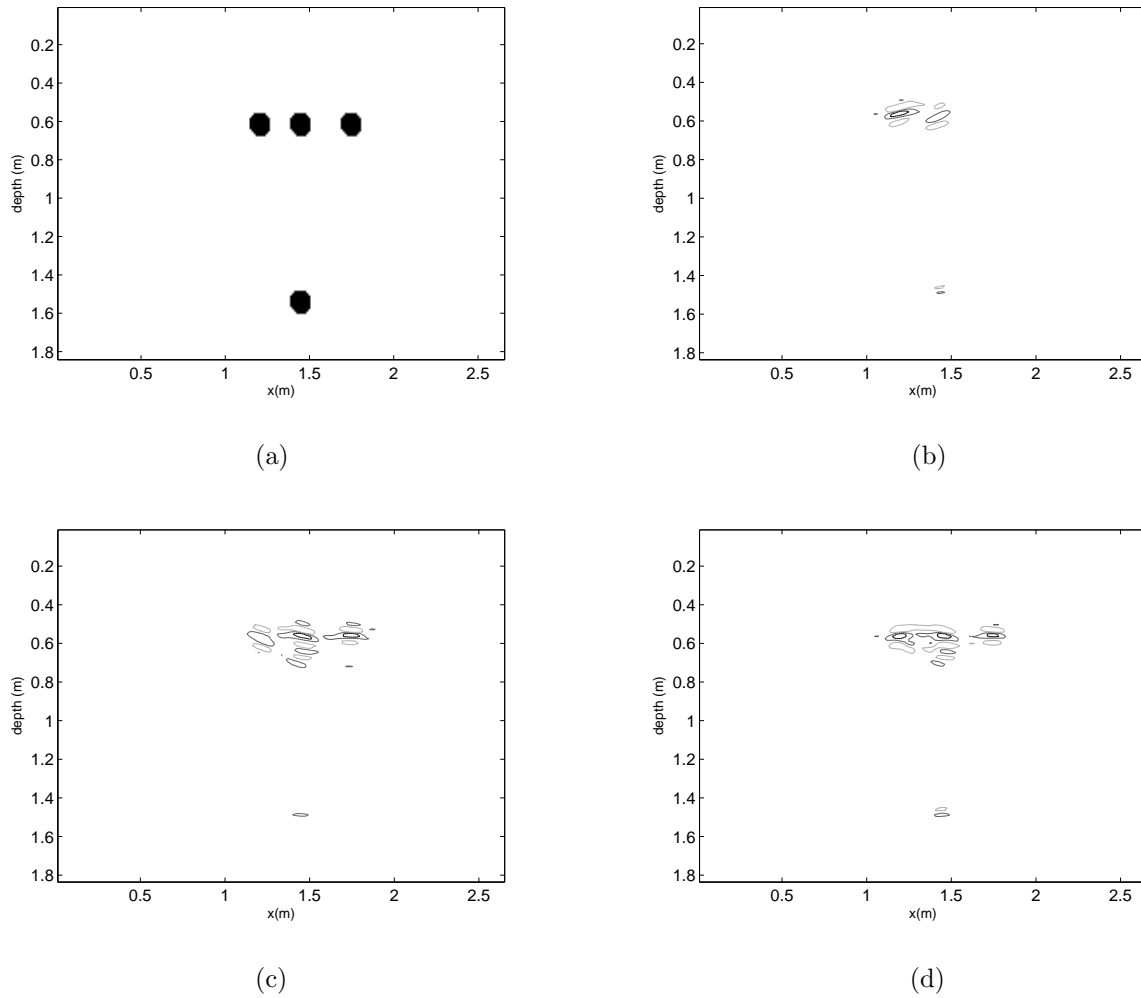


Figure 4.3: Bistatic results for the first example. (a) Problem geometry. (b) FDTD reverse-time migrated for the transmitter at location 7. (c) FDTD reverse-time migrated for transmitter at location 23. (d) FDTD reverse-time migrated using the two common-shot data sets.

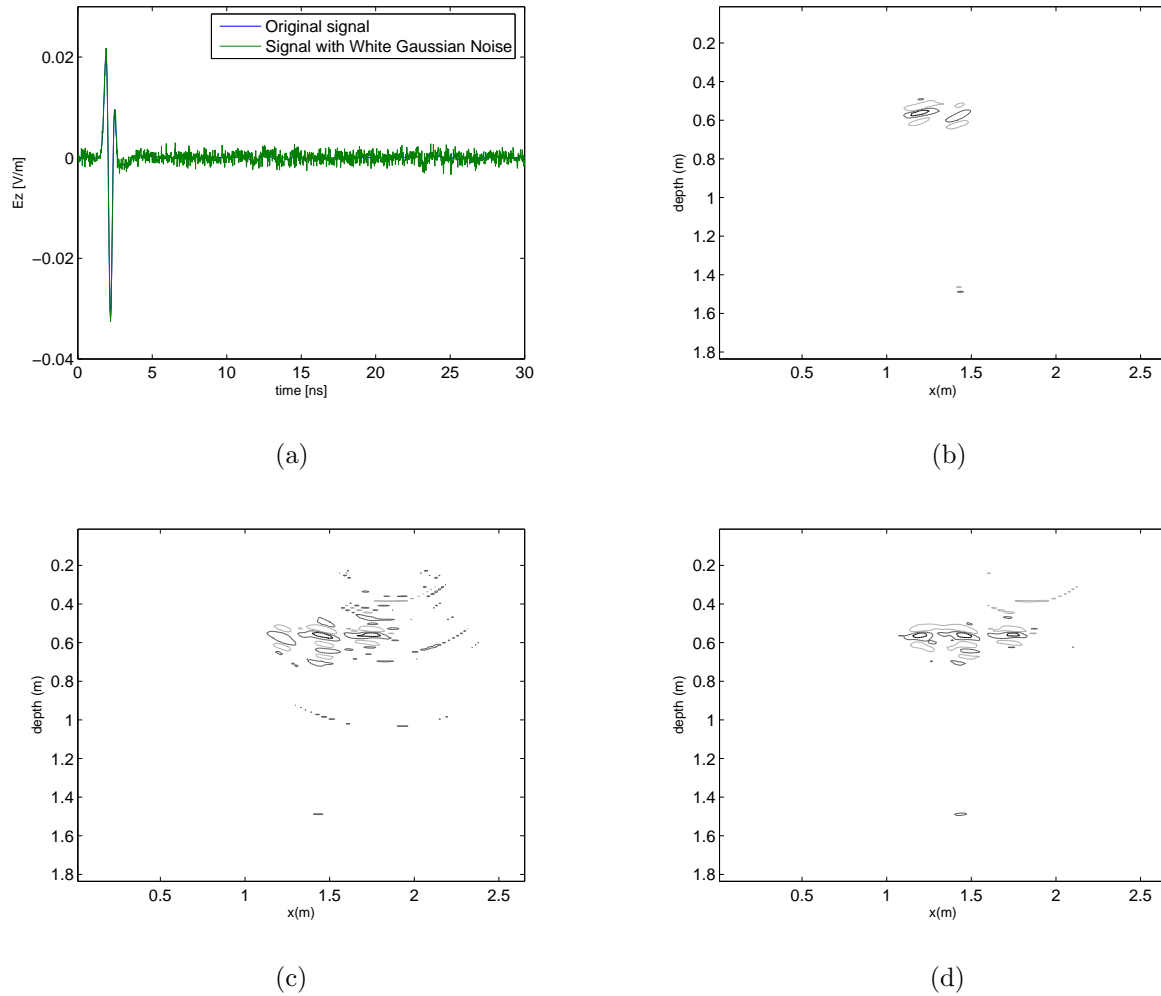


Figure 4.4: Bistatic results for the second example. (a) Measured signal with white Gaussian noise. (b) FDTD reverse-time migrated for the transmitter at location 7. (c) FDTD reverse-time migrated for transmitter at location 23. (d) FDTD reverse-time migrated using the two common-shot data sets.

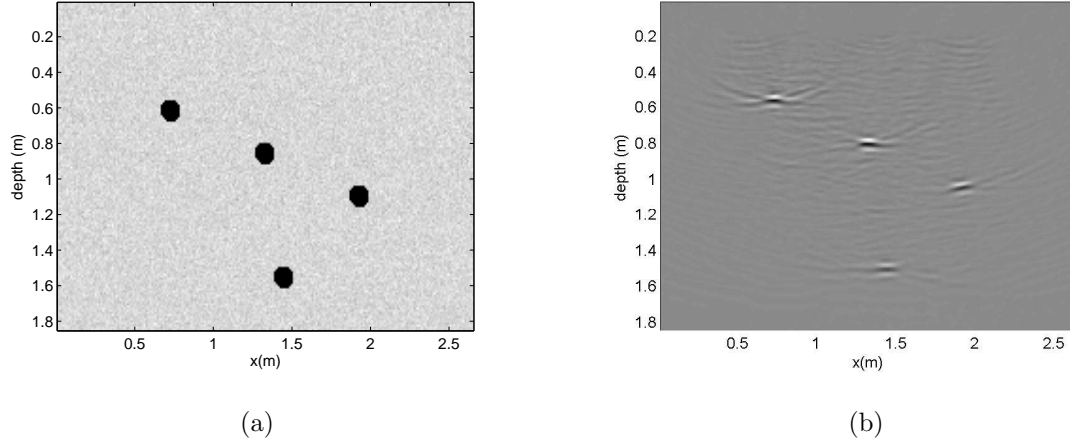


Figure 4.5: Third example using a heterogeneous dielectric (a) Problem description (b) Final migrated data.

$$\theta^* = \arg \min f(\theta) = \sum_{i=1}^{ns} (\mathbf{E}(\theta_0) - \mathbf{E}(\theta))^2 \quad (4.10)$$

where  $ns$  is the number of sample points where the scattered wave is measured. Note that  $\mathbf{E}(\theta_0)$  is known even though  $\theta_0$  is unknown. The scattered field  $\mathbf{E}(\theta)$  is then generated assuming one tests  $\theta$ , and the optimization procedure aims at minimizing the error between  $\mathbf{E}(\theta_0)$  and  $\mathbf{E}(\theta)$  in such a way as to identify the scatter object  $\theta_0$ .

This section studies a  $2D$  inverse scattering problem with non homogenous media trying to identify the standard deviation of the permittivity,  $sd$ , the depth of the inclusion and the inclusion radii. This problem was solved using the Particle Swarm Optimization, and is described next. The Particle Swarm Optimization (PSO) is a stochastic evolutionary technique dating to 1995 from the papers [118, 119].

PSO is one of the latest evolutionary optimization methods inspired by nature that includes evolutionary strategy (ES), evolutionary programming (EP), genetic algorithm (GA), and genetic programming (GP). PSO is based on the metaphor of social interaction and communication such as bird flocking and fish schooling. PSO is distinctly different from other evolutionary-type methods in a way that it does not use the filtering operation (such as crossover and/or mutation), and the members of the entire population are maintained through the search procedure so that information is socially shared among individuals to direct the search towards the best position in the search space.

The original intention was to graphically simulate the beautiful and unpredictable choreography of a group of birds. In a certain moment of the model evolution it was noticed that the algorithm was in fact an optimizer. Using an empirical process many parameters were eliminated, the ones relevant to the social model but not to the optimization, resulting in a simple algorithm [120].

In a PSO algorithm, each member is called a particle, and each particle moves around in the multi-dimensional search space with a specific velocity. There exist two variants of the PSO algorithm: one PSO with a local neighborhood, and PSO with a global neighborhood. According to the global neighborhood, each particle moves towards its best previous position and towards the best particle in the whole swarm.

The PSO is similar to genetic algorithms (GAs) due to the random initialization. The first difference is that each potential solution is called particles, instead of individuals, and they "fly" on the search space. To each particle of the swarm during the iterations, the positions of the best solution found to a given particle, called pbest (particle best) is saved.

The best value found considering all the particle is also saved, and is called gbest (global best). At each iteration, the PSO is based on the change in the particle's velocity in the direction of its pbest and gbest, weighted by random terms. The velocity and position are calculated as following:

```

%*****
%      Update electric fields (EZ) in main grid <reverse>
%*****
ezxi(2:ie,2:je)=ezxi(2:ie,2:je)-dt.*ezx(2:ie,2:je);
ezyi(2:ie,2:je)=ezyi(2:ie,2:je)-dt.*ezy(2:ie,2:je);
ezx(2:ie,2:je)=daezx(2:ie,2:je).*ezx(2:ie,2:je)-dbezx(2:ie,2:je).*...
    ((hy(2:ie,2:je)-hy(1:ie-1,2:je)))+dcezx(2:ie,2:je).*ezxi(2:ie,2:je);
ezy(2:ie,2:je)=daezy(2:ie,2:je).*ezy(2:ie,2:je)+dbezy(2:ie,2:je).*...
    ((hx(2:ie,2:je)-hx(2:ie,1:je-1)))+dcezy(2:ie,2:je).*ezyi(2:ie,2:je);
ez(2:ie,2:je)=ezy(2:ie,2:je)+ezx(2:ie,2:je);
%*****
%      Update magnetic fields (HX and HY) in main grid <reverse>
%*****
hxi(2:ie,1:je)=hxi(2:ie,1:je)-dt.*hx(2:ie,1:je);
hx(2:ie,1:je)=dahx(2:ie,1:je).*hx(2:ie,1:je)+dbhx(2:ie,1:je)...
    *((ez(2:ie,2:je)-ez(2:ie,1:je)))+dchx(2:ie,1:je).*hxi(2:ie,1:je);
hyi(1:ie,2:je)=hyi(1:ie,2:je)-dt.*hy(1:ie,2:je);
hy(1:ie,2:je)=dahy(1:ie,2:je).*hy(1:ie,2:je)-dbhy(1:ie,2:je)...
    *((ez(2:ie,2:je)-ez(1:ie,2:je)))+dchy(1:ie,2:je).*hyi(1:ie,2:je);
%*****
%      Update electric fields (EZ) in main grid <forward>
%*****
ezxif(2:ie,2:je)=ezxif(2:ie,2:je)+dt.*ezxf(2:ie,2:je);
ezyif(2:ie,2:je)=ezyif(2:ie,2:je)+dt.*ezyf(2:ie,2:je);
ezxf(2:ie,2:je)=daezx(2:ie,2:je).*ezxf(2:ie,2:je)+dbezxf(2:ie,2:je).*...
    ((hyf(2:ie,2:je)-hyf(1:ie-1,2:je)))-dcezx(2:ie,2:je).*ezxif(2:ie,2:je);
ezyf(2:ie,2:je)=daezy(2:ie,2:je).*ezyf(2:ie,2:je)-dbezyf(2:ie,2:je).*...
    ((hxf(2:ie,2:je)-hxf(2:ie,1:je-1)))-dcezy(2:ie,2:je).*ezyif(2:ie,2:je);
ezf(2:ie,2:je)=ezyf(2:ie,2:je)+ezxf(2:ie,2:je);
ezyf(irx:dc:irc,jconc+hc)=sandata(n,1:rc);
ezxf(irx:dc:irc,jconc+hc)=sandata(n,1:rc);
%*****
%      Update magnetic fields (HX and HY) in main grid <forward>
%*****
hxif(2:ie,1:je)=hxif(2:ie,1:je)+dt.*hxf(2:ie,1:je);
hxf(2:ie,1:je)=dahx(2:ie,1:je).*hxf(2:ie,1:je)-dbhxf(2:ie,1:je)...
    *((ezf(2:ie,2:je)-ezf(2:ie,1:je)))-dchx(2:ie,1:je).*hxif(2:ie,1:je);
hyif(1:ie,2:je)=hyif(1:ie,2:je)+dt.*hyf(1:ie,2:je);
hyf(1:ie,2:je)=dahy(1:ie,2:je).*hyf(1:ie,2:je)+dbhyf(1:ie,2:je)...
    *((ezf(2:ie,2:je)-ezf(1:ie,2:je)))-dchy(1:ie,2:je).*hyif(1:ie,2:je);
%*****
%      Convolution running
%*****
ezc=ezc+ez.*ezf;
hxc=hxc+hx.*hxf;
hyc=hyc+hy.*hyf;

```

Figure 4.6: RTM Matlab pseudo-code.

$$v = v + c_1 * \text{rand} * (\text{pbest} - x) + c_2 * \text{rand} * (\text{gbest} - x), \quad (4.11)$$

$$x = x + v. \quad (4.12)$$

Therefore, the PSO algorithm employed in this work can be described as:

```

Initialize parameters;
Initialize population;
Evaluate;
while until one stop criteria is achieved do
    Find the personal best;
    Find the global best;
    Update velocity;
    Update position;
    Evaluate;
end

```

**Algorithm 1:** PSO algorithm.

The velocity of each particle in each dimension is limited by a maximum velocity,  $V_{\max}$ . This parameter is important since it controls the local and global search. If it is made too big the particles will mainly perform global search, and, if it is too small the particles will mainly perform local search (they cannot move far away), since they do not have sufficient velocity to do it so. The MATLAB pseudo-code is depicted in Fig. 4.7.

The acceleration constants  $c_1$  and  $c_2$  used in Eq. 4.11, represent the trade-off between the search in the direction of  $\text{pbest}$  and  $\text{gbest}$ . Usual the values of  $c_1$  and  $c_2$  are equal to 2 and  $V_{\max}$  between 10% and 20% of the maximum value of each variable range.

In our radar problem, the unknown object was obtained by experiment at depth of the inclusion equal to 10 cm, the radius equal to 4.5 cm and the standard deviation of the nonhomogenous medium,  $sd$ , equal to 0.15. The target considered was water. The definition of the reference object as well as the range of the variables for the optimization process are summarized in Table 4.1.

Table 4.1: Inverse scattering problem definitions

	Depth	Radii
Min	5 cm	2.5 cm
Max	25 cm	10 cm
Ref. Object	10 cm	4.5 cm

The PSO was initialized using 50 particles over 50 iterations. The  $\text{gbest}$  evolution throughout the iterations is shown in Table 4.2. In the 50-th iteration, the algorithm was capable of finding a solution very close to the desired one. Nonetheless, good approximations were already available in the 5-th iteration, thus, if a very accurate outcome is not necessary the algorithm would need only about 5 iterations to converge. A new study has been started in order to mix the migration algorithm described in the previous section with the PSO in order to minimize the computational burden of this kind of investigation.

Table 4.2: PSO results		
Iteration	Depth	Radii
1	8.7 cm	3.2 cm
5	9.7 cm	4.4 cm
10	9.7 cm	4.7 cm
50	10 cm	4.44 cm
Ref. Object	10 cm	4.5 cm

```

%*****
% Functions initialization
%*****
funcao.tipo='Radar';
funcao=inicializa_funcoes(funcao);
%*****
% Population initialization
%*****
eNUVEM.parti=rand(pPSO.npart,funcao.num_var).*...
repmat(funcao.lmax-funcao.lmin,pPSO.npart,1)+repmat(funcao.lmin,pPSO.npart,1);
eNUVEM.velocidade=rand(pPSO.npart,funcao.num_var).*...
repmat((funcao.lmax-funcao.lmin)*pPSO.Vmax,pPSO.npart,1)...
-repmat((funcao.lmax-funcao.lmin)/2,pPSO.npart,1)*pPSO.Vmax;
%*****
i=1;
while i<=pPSO.niter
    fprintf('\n Iteration %i - ', i)
    fprintf('Processing - ')
    eNUVEM.Funcao=feval(funcao.tipo,eNUVEM.parti);
    fprintf('pbest - ')
    if i==1
        eNUVEM.pbestPart=eNUVEM.parti;
        eNUVEM.pbestFunc=eNUVEM.Funcao;
    else
        [posi]=find(eNUVEM.Funcao <= eNUVEM.pbestFunc);
        eNUVEM.pbestPart(posi,:)=eNUVEM.parti(posi,:);
        eNUVEM.pbestFunc(posi,:)=eNUVEM.Funcao(posi,:);
    end
    fprintf('gbest - ')
    [valor posi]= min(eNUVEM.pbestFunc);
    eNUVEM.gbestFunc(i)=valor;
    eNUVEM.gbestPart=eNUVEM.pbestPart(posi,:);
    gbest(i,:)=eNUVEM.gbestPart;
    eNUVEM.velocidade=pPSO.K*(pPSO.w(i)*eNUVEM.velocidade+pPSO.c1*...
    rand(pPSO.npart,funcao.num_var).*...
    (eNUVEM.pbestPart-eNUVEM.parti)+pPSO.c2*rand(pPSO.npart,funcao.num_var).*...
    (repmat(eNUVEM.gbestPart,pPSO.npart,1)-eNUVEM.parti));
    eNUVEM=limiteV(funcao,eNUVEM,pPSO);
    fprintf('Update particules ')
    eNUVEM.parti=eNUVEM.parti+eNUVEM.velocidade;
    eNUVEM=reflexao(funcao,eNUVEM,pPSO);
    eNUVEM.gbestPart(end,:)
    i=i+1;
end

```

Figure 4.7: PSO Matlab pseudo-code.

## 4.4 Neural networks

The brain can be viewed as a highly complex, nonlinear parallel computer that can compute in an entirely different way compared with a conventional computer. The brain is a complex network with approximately  $10^{10}$  neurons having over  $6 \cdot 10^{13}$  interconnections. Neural events occur at millisecond speeds whereas events in common computers occur in less than nanoseconds. However, the brain can compensate this slow speed through its massive number of neurons and interconnections. For example, the human brain can recognize a familiar face embedded in an unfamiliar scene in 100-200 ms, whereas a computer can take some hours.

Recognition of the brain's impressive power has led to interest in the development of Artificial Neural Network (ANN) technology. ANN are parallel computational models comprised of densely interconnected adaptive processing units. A very important feature of this technology is their adaptive nature, where the problem is solved by feeding the system with examples as in the human brain. This feature makes such computational models very appealing in application domains where one has little or incomplete understanding of the problem to be solved but where training data are readily available. Another key feature is the intrinsic parallel architecture that allows for fast computation of solutions.

ANN can be used in a wide range of applications including pattern classification, speech synthesis and recognition, adaptive interfaces between humans and complex physical systems, function approximation, image compression, associative memory, clustering, forecasting and prediction, combinatorial optimization, nonlinear system modeling, and control. In the context of this research work the ANN are used in Intelligent Signal Processing (ISP) which is characterized by the use of model free (intelligent) methods based on training data. In addition, ISP implies the ability to extract system information from the example data alone and be less dependent on a priori environmental and system information or simply, being less unstable.

A formal definition of an ANN according to [121] is: "A neural network is a massively parallel distributed processor that has a natural propensity for storing experiential knowledge and making it available for use. It resembles the brain in two respects:

1. Knowledge is acquired by the network through a learning process.
2. Interneuron connection strengths known as synaptic weights are used to store knowledge."

Neurons are the basic building blocks that make up the ANN. They are usually made to be all similar and can be interconnected in various ways to make a network. The ANN achieves its ability to learn and then recall that learning through the weighted interconnections of those neurons. The interconnection architecture can be very different for different types of networks. Architectures can vary through different types of feedforward to recurrent structures.

In the next section, a novel asynchronous model of the ANN arrangement is proposed which has outperformed the traditional approaches of using one ANN with two outputs and two parallel independent ANN as shown in the results.

## 4.5 Inclusion characterization

Over the past decade, various imaging or inversion techniques have been developed to refocus the scattered signals back to their true spatial location and then decrease the interpretation time for effective maintenance and/or repair. Among them the ANN has been proven to be a promising technique [122].

The use of ANN in the inverse scattering problem using parallel networks and networks with multiple outputs for an homogenous host medium was presented in [123] and [124]. In [124] it is shown that both configurations could deliver reasonable and very similar results.

In this section we considered the case when the host media is non-homogenous and, surprisingly, a network with multiple outputs and parallel networks were not adequate to estimate the *radii* of the inclusion. Thus, to increase the prediction accuracy, we propose the use of an asynchronous configuration for the neural networks. The training is then done in two steps: (i) training one network with the scattered wave to predict the *depth* of the inclusion, (ii) training one network with the scattered wave

---

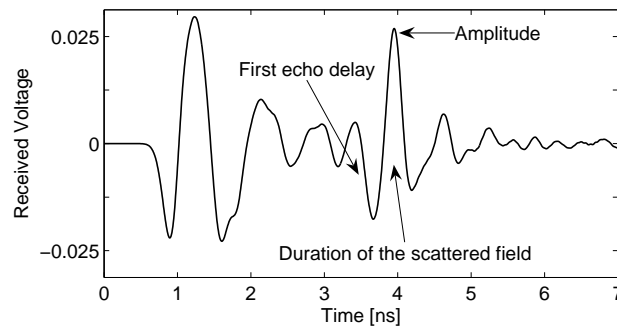


Figure 4.8: Reflected wavefield from a buried target.

and the predicted *depth* to define the inclusion *radii*. Even though it is a very simple modification in the training procedure a significant improvement in the predictions of the *radii* was observed.

The problem can be stated as the determination of the spatial map of the dielectric and/or conductive properties of a probed region embedded in the soil starting from the measurement of scattered field data gathered close to the air-soil interface. The purpose is to detect, locate and determine the extent of the buried objects [125].

From the scattered wave, following the recommendations of [124], the following input parameters were defined (see Fig. 4.8): 1) the peak amplitude of the reflected field ( $d_1$ ); 2) the delay of the first reflected echo, calculated with respect to the time of arrival, at the receiving point, of the direct field ( $d_2$ ); 3) a measure of the duration of the scattered field ( $d_3$ ).

These variables alone have proven sufficient for the homogenous inverse scattering problem but they were insufficient for the non-homogenous problem (in order to simulate a more realistic concrete model, we randomly created subsurface heterogeneities) treated in this research work.

### 4.5.1 Parallel layer perceptron

The Parallel Layer Perceptron (PLP) is a novel network that combines the advantages of both Multi-Layer Perceptrons (MLP) and Adaptive-Network-Based Fuzzy Inference System (ANFIS). The former has gained popularity in a vast range of applications due to its universal approximation characteristic. The latter has some advantage over MLP's due to the linear dependance of its output in relation of the result.

However the use of ANFIS is prohibitive for problems with several variables. Therefore the PLP tries to minimize those limitations by extending ANN to parallel environments. This section employs the PLP<sup>1</sup> illustrated in Fig. 4.9 [126, 127], but, MLP's and ANFIS have achieved similar results in our experiments.

In [124] two different configurations to solve this inverse problem were discussed, a network with multiple outputs, Fig. 4.10(a), and independent networks in parallel, Fig. 4.10(b). The network with multiple outputs, called here *C1*, calculates simultaneously the *depth* and *radii* given  $d_1$ ,  $d_2$  and  $d_3$ . The parallel networks, called here *C2*, calculate independently each output given the measured variables  $d_1$ ,  $d_2$  and  $d_3$ .

In our experiments it was noticed that having the information of the *depth*, the prediction of the *radii* was substantially improved. Considering this fact, we propose to use an asynchronous training as presented in Fig. 4.10(c). This configuration, called here *C3*, first calculates the depth using the measured variables  $d_1$ ,  $d_2$  and  $d_3$  and then calculates *radii* using  $d_1$ ,  $d_2$  and  $d_3$  and the predicted *depth*.

A typical two-dimensional radar data is simulated using two antennas located above the dielectric slab. The FDTD scenario used for the ANN training consisted of one buried inclusion in concrete that was modeled with a mean relative electrical permittivity value of 6 and  $sd=0.15$ . In particular, the

<sup>1</sup>The PLP used in this work was implemented by Dr. Douglas Vieira. I sincerely thank him for his contribution to this work.

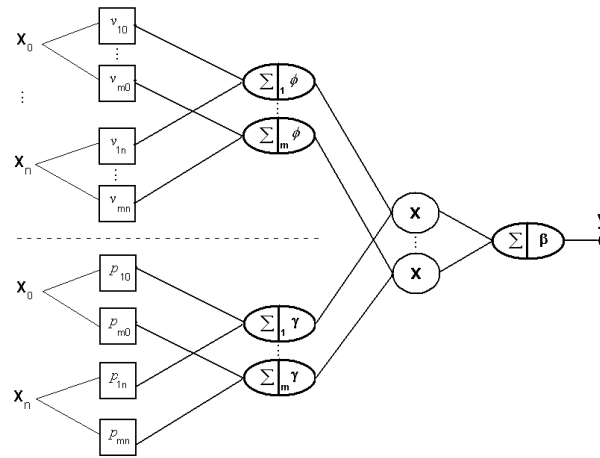


Figure 4.9: Parallel Layer Perceptron Architecture.

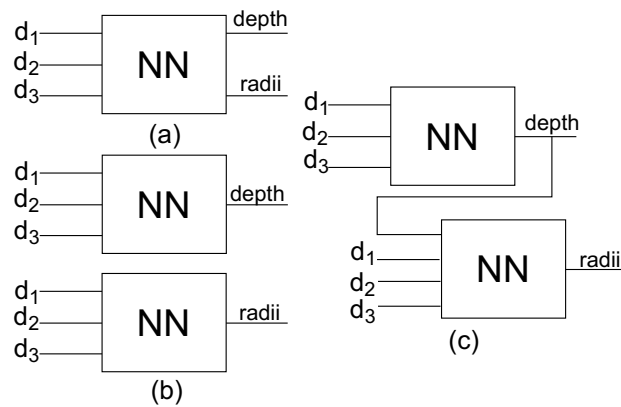


Figure 4.10: Three neural network configurations employed in this work. (a) One network used to calculate simultaneously the *depth* and *radii* given as  $d_1$ ,  $d_2$  and  $d_3$ , called here Configuration  $C1$ . (b) Two networks ( $C2$ ) applied in parallel to calculate independently the *depth* and *radii* given as  $d_1$ ,  $d_2$  and  $d_3$ . (c) The configuration proposed in this work ( $C3$ ) in which, the *depth* is calculated using  $d_1$ ,  $d_2$  and  $d_3$  and the *radii* are calculated in a second step (asynchronously) using also the calculated *depth*.

”experimental” data is generated with the same model adopted to train the ANN, an invalid inversion was avoided since different random numbers were used to create the heterogeneity for the two models.

The source type is a differentiated Gaussian pulse with a center frequency of  $f = 900$  MHz and significant energy between 0.3 and 2 GHz. In order to control the numerical dispersion and provide a good discretization for the inclusions the spatial steps were chosen as  $\Delta x = \Delta y = 6$ mm.

The ANN has been trained with a set of different inclusions examples, constructed by varying the *radii* in the range from 0.02 to 0.1 m according to the rule  $radii = 0.02 + i \times 0.001$ ,  $i = 0, \dots, 80$ , with  $\varepsilon_r$  in the range from 1 to 10, according to the rule  $\varepsilon_r = 1 + i \times 1$ ,  $i = 0, \dots, 9$ ,  $\sigma$  in the range from 0 to 4000 S/m according to the rule  $\sigma = 0 + i \times 500$ ,  $i = 0, \dots, 8$  and *depth* in the range from 0.05 to 0.25 m according to the rule  $depth = 0.05 + i \times 0.025$ ,  $i = 0, \dots, 9$  where 75% of these samples were used as a training set and 25% to validate the methodology.

The training of the ANN took only 2.9 s, while the processing of the entire test set took 17 ms.

To evaluate the performance of the techniques studied, the following error figure is used:

$$Err(p_r) = \frac{|p_t - p_r|}{p_r}, \quad (4.13)$$

where  $p$  is the unknown variable (*depth* or *radii*), the subscript  $t$  indicates the real value of the variable, and subscript  $r$  indicates the value reconstructed by the ANN.

The results for the configuration  $C1$ ,  $C2$  and  $C3$  are presented in Table 4.3. As all the techniques apply similar mechanism to reconstruct the *depth* their errors are also very similar, as indicated in the second column of Table 4.3. The main difference is in the reconstruction of the *radii* for which the technique proposed in this work has shown an improvement of at least 7.1% compared with  $C1$  and  $C2$ .

Table 4.3: Results for the three configurations of the ANN studied.

Configuration	$Err(depth)$	$Err(radii)$
$C1$	5.8%	12.9%
$C2$	5.7%	13.4%
$C3$	5.7%	5.8%

One problem arises when working with ANN: the training process may be difficult to treat when there are many variables. In the next section a new approach involving Principal Component Analysis and ANN is shown to compress the data for training the ANN.

## 4.6 Compressing data for ANN training

To train the ANN a set of different inclusion examples considering different *radii*, *depth*,  $\varepsilon_r$  and  $\sigma$  were generated. A uniform grid taking into account the range and the step size  $\delta$  of the above-mentioned variable is shown in Table 4.4, summing a total of 1640 examples. The corresponding scattered wave is thus calculated at each sample using FDTD.

Table 4.4: Inclusion data set settings.

Variable	Min	Max	$\delta$
<i>radii</i> (m)	0.02	0.1	0.01
<i>depth</i> (m)	0.02	0.25	0.025
$\varepsilon_r$	1	10	1
<i>sigma</i> (S/m)	0	4000	4000

The scattered wave is the only information available the real cases, therefore, it has to be used to characterize the inclusion. Here 1200 time steps were used, thus, a problem in  $\mathbb{R}^{1200}$  must be solved. ANNs suffer from a phenomenon called the curse of dimensionality, *i.e.*, the learning process becomes slower and less effective with increase in dimensionality. In the next section the curse of dimensionality will be addressed followed by the Principal Component Analysis (PCA) which was an effective way to reduce the dimensionality of this problem.

### 4.6.1 The curse of dimensionality

One phenomenon that takes place in high dimensional data space is the sparsity of the sample points [128]. Given a data set  $S$  with  $T$  data points uniformly distributed in a  $p$ -dimensional unit sphere centered at the origin, the median distance given from the origin to the closest sample is then given by:

$$d(p, T) = \left(1 - \frac{1^{1/T}}{2}\right)^{1/p}. \quad (4.14)$$

For a sample size of 1640 and 1200 dimensions,  $d(1200, 1640) = 0.9935$ , which means that the samples are closer to the boundary of the space than to any other data point.

Another phenomenon that takes place in high dimensional problems is the rise of the computational effort. Suppose that one wants to approximate the scattered wave for the 1640 samples. The numerous methods for modeling the nonlinear behavior are classically divided into three categories: physical, empirical and table-based ones. Some may be difficult to categorize in this way, however, and therefore

models are divided here simply into physical and empirical ones, and into black-box and circuit-level ones. A Volterra representation can be regarded either as a black-box (input-output) or a circuit-level description. Volterra series describe the output of a nonlinear system as the sum of the responses of a 1st order, 2nd order, 3rd order operator and so on. Consider the Volterra series [129] for a mapping  $x \in \mathbb{R}^p$  given by:

$$f(x) = a_0 + \sum_{i=1}^p a_i x_i + \sum_{i=1}^p \sum_{j=1}^p a_{ij} x_i x_j + \sum_{i=1}^p \sum_{j=1}^p \sum_{k=1}^p a_{ijk} x_i x_j x_k \dots \quad (4.15)$$

Given Eq. 4.15, the number of free parameters (the parameters  $a$ ), in a polynomial of order  $\tau$  is  $O(p, \tau) = \sum_{i=1}^{\tau} p^{i-1}$ . For instance, for a problem with 3 dimensions,  $p = 3$ , using a 3rd order series,  $\tau = 3$ , the number of free parameters will be  $O(3, 3) = 13$ . With  $p = 10$  and  $\tau = 10$ ,  $O(10, 10) > 1.1e + 9$ . In this case the computational cost becomes prohibitive.

For an ANFIS topology the number of rules  $R$  for a system with  $p$  inputs and  $P$  premises is  $R = P^p$ , hence it increases exponentially with the dimension  $p$ , which makes the learning slow [130]. The following section presents the Principal Component Analysis, which will be used for dimensional reduction.

### 4.6.2 Principal component analysis

In some situations, the dimension of the input vector is large, but the components of the vectors are highly correlated (redundant). Principal Component Analysis (PCA) is a way of identifying patterns in data, and expressing the data in such a way as to highlight their similarities and differences. The main advantage of PCA is that once you have found these patterns in the data, the data may be compressed, *i.e.* by reducing the number of dimensions, without much loss of information. This technique is mostly used in image compression.

This technique has three effects: it orthogonalizes the components of the input vectors (so that they are uncorrelated with each other), it orders the resulting orthogonal components (principal components) so that those with the largest variation come first, and it eliminates those components that contribute the least to the variation in the data set. The input vectors are first normalized so that they have zero mean and unity variance. For PCA to work properly, one has to subtract the mean from each of the data dimensions.

The PCA uses linear mapping of a given set of samples  $S_q = \{x_1, \dots, x_T | x_i \in \mathbb{R}^p\}$  to construct a new data set  $S_p = \{y_1, \dots, y_T | y_i \in \mathbb{R}^q\}$ , where  $q \leq p$ . Considering a  $p \times q$   $V_q$  matrix the PCA algorithm can be described as follows:

1. Subtract the mean from each data dimension,
2. Calculate the covariance matrix,
3. Calculate the eigenvectors and eigenvalues of the covariance matrix,
4. Choose components and form a feature vector,
5. Derive the new data set.

Another interpretation of the PCA is the constructions of directions that maximize the variance. The transformation  $V_q$  generates a projection space in which the covariance matrix is diagonal. The diagonal covariance matrix implies that the variance of a variable with itself is maximized but is minimized with any other variable. Thus, the  $q$  variables with higher variance in the new space should be kept. The principal components of a set of data in  $\mathbb{R}^p$  provide a sequence of best linear approximations to that data, of all ranks  $q \leq p$ .

The problem considered is initially in  $\mathbb{R}^{1200}$  but it can be projected in a  $\mathbb{R}^{286}$  without any loss of information, *i.e.*, 100% of the data variance was kept. Retaining 99.99% of the variance, the variables can be projected in  $\mathbb{R}^{139}$  and in  $\mathbb{R}^{51}$  when 99% of the original variance is kept. These are remarkable reductions that helps in reducing the curse of dimensionality.

### 4.6.3 The expected error

The model structure problem is given by choosing among a set of possible functions  $f(w, x)$ ,  $w_i \in R$ , the possible PLPs in the present case, the one that optimizes a given quality criterion. Mathematically

$$w^* = \arg \min_w R(f(w, x)) \quad (4.16)$$

where  $R(\cdot)$  is a pre-defined quality criterion. To apply the model structure selection, the best approximation of the desired output,  $d$ , must be defined, therefore, a measure of discrepancy,  $L(\cdot)$ , between the desired and obtained outputs should be employed. The expected risk (error) between the desired and the approximated outputs can be expressed [131] as:

$$R(f(w, x)) = \int L(d, f(w, x)) d\mathcal{F}(x, d). \quad (4.17)$$

The expected risk  $R(w)$  measures the expected test error for the neural network, *i.e.*, the ANN performance. The aim of the machine learning problem is to find  $f(w, x)$ ,  $w \in \Lambda$ , that minimizes the risk functional presented in Eq. 4.17. The integral cannot be directly evaluated since the distribution  $\mathcal{F}(x, d)$  is unknown and the only available information is the training set. The training set is composed of  $T$  random vectors  $z_i = (x_i, d_i)$ ,  $i = 1, \dots, T$ , independently and identically distributed (IID) according to some unknown but fixed probability distribution  $\mathcal{F}(z)$ . The training set  $S$  can be written as:

$$S = ((x_1, d_1), \dots, (x_T, d_T)). \quad (4.18)$$

The risk  $R(\cdot)$  defined in Eq. 4.17 can be asymptotically approximated, given some consistence conditions [131], when the number of training set samples  $T$  tends to infinity. Of course such an infinite size set is not available. To overcome this problem, resampling techniques can be used to approximated the expected risk.

The simplest resampling technique is the Hold Out (HO), also called external validation or validation. It consists of removing samples from the initial learning set, and using them for validation. This method was used in many works, dividing the set in training and test set. In this work we employed the  $k$ -fold cross-validation. For  $k$ -fold cross-validation, the training data  $S$  is divided into  $k$  sets of approximately the same size, in such a way that the learning takes place in  $k - 1$  sets and the model is independently validated in the remaining set. This is performed  $k$  times using all the  $k$  folds as validation set once. Figure 4.11 shows a 3-fold cross-validation. The estimate of a given parameter when resampling techniques are used is the statistical mean evaluated on each model over the corresponding test data. The  $k$ -fold cross-validation uses more effectively the data set and is employed in this work to evaluated the expected risk.

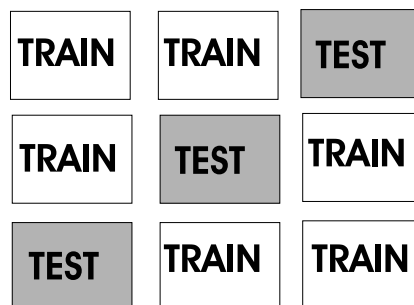


Figure 4.11: 3-fold cross-validation. The two sets labelled as train are used to train the neural network and the error is evaluated on the test set. After all the folders are used once as test set the expected risk is estimated as the average error of each set.

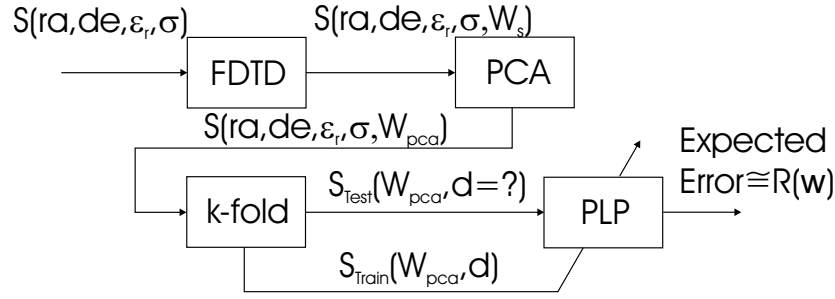


Figure 4.12: Overview of the detection system employed in this work. Firstly, given a set  $S$  of radii ( $ra$ ), depth ( $de$ ),  $\varepsilon_r$  and  $\sigma$  a scattered wave ( $W_s \in \mathbb{R}^p$ ) is calculated using FDTD. Then, given  $q < p$  a dimensional reduction is applied in  $W_s$  generating  $W_{pca} \in \mathbb{R}^q$ . Next, the  $W_{pca}$  is used in a  $k$ -fold system such that  $S_{test}$  is used to estimate the expected error, Eq. 4.17, and  $S_{train}$  are used to adapt the PLP network parameters. In this work a 10-fold cross-validation was employed.

#### 4.6.4 Results

For the concrete inclusion assessment the PLP network trained with the scattered wave calculated using FDTD (with Generalized Perfectly Matched Layers [116]) with dimensional reduction based on PCA is applied. This system is shown in Fig. 4.12.

To evaluate the performance of the techniques studied the following relative error (loss) figure is used:

$$L(d_r) = \frac{|d_t - d_r|}{d_r}, \quad (4.19)$$

where  $d$  is the unknown variable (*depth* or *radii*), the subscript  $t$  indicated the real value of the variable, and subscript  $r$  indicates the value reconstructed by the neural network. This measures the percentage deviation of the reconstructed object to the real one (desired object). The expected value of the test risk, Eq. 4.17, given the loss functional defined in Eq. 4.19 was calculated using the 10-fold cross-validation. Tables 4.5 and 4.6 show the mean deviation,  $\text{mean}(L)$ , the maximum deviation,  $\text{max}(L)$  and the train and test times considering the dimension reduction to  $q = 51, 139$  and  $286$ .

Table 4.5: Results of the Relative Error considering the *depth* prediction.

Configuration	$\text{mean}(L)$	$\text{max}(L)$	train(s)	test(s)
<i>PLP</i> (286)	0.001%	0.01%	8.44	0.016
<i>PLP</i> (139)	0.003%	0.15%	4.48	0.01
<i>PLP</i> (51)	1%	20%	6.2	0.011

Table 4.6: Results of the Relative Error considering the *radii* prediction.

Configuration	$\text{mean}(L)$	$\text{max}(L)$	train(s)	test(s)
<i>PLP</i> (286)	0.022%	0.94%	7.5	0.03
<i>PLP</i> (139)	1%	20%	11.1	0.018
<i>PLP</i> (51)	1%	22%	6.1	0.013

The results of Tables 4.5 and 4.6 show that the proposed system that combines a PCA pre-processor with a PLP is a very promising idea for assessment of inclusion in non-homogenous concrete structures.

Retaining only 286 of the initial 1200 points the information is still represented without any loss, thus, 100% of the data variance was kept.

The reduction to 139 and 51 dimensions resulted in 99.99% and 99% of the original variance respectively. It is clear from these results that it is harder to predict the *radii* than the *depth*. This can be physically understood by the fact that the antenna position is in front of the objects. The results presented in this work are superior to the results of [124].

Dimensional reduction was also considered in [124] but was done empirically using only three features, the peak amplitude of the reflected field; the delay of the first reflected echo, calculated with respect to the time of arrival (at the receiving point) of the direct field and a measure of the duration of the scattered field were considered. The average error of the best configuration in [124] was 1.46% for the depth reconstruction which is higher than the result shown here. However, while in an actual application framework a large number of uncertainties come into play (e.g. actual parameters of the investigated structure, dispersive behaviour of materials, noise on data, etc.), the assessment of the proposed tool against those uncertainties was not addressed and remains to be addressed of future work.

A number of important issues have been discussed in this chapter. First the definition of estimation schemes for microwave imaging was outlined. The concept of inverse problem was defined with respect to the image reconstruction. Three 2D reconstruction algorithms were implemented and new configurations were proposed including the use of Artificial Neural Networks. Forward field modeling in 2D algorithms were discussed including topics such as accuracy and efficiency. From comparison with other algorithms, the 2D FDTD method demonstrated promising advantages in modeling the transitory field in a lossy media compared with the FEM counterpart. Numerical simulations, with different types of inclusions were presented to assess the accuracy and efficiency of these algorithms for image reconstruction in real-world settings. For all cases, the targets were successfully reconstructed with the 2D algorithms and the convergence was assessed in terms of the relative field error.

In conclusion, significant algorithmic flexibilities utilizing 2D based algorithm were demonstrated in terms of accommodating various forms of inclusions in single and iterative reconstruction.



## Chapter 5

# Conclusions and scope for future research

In summary, the study presented in this work involved many different areas in engineering including: NDT, microwave theory, antennas, numerical modeling of the electromagnetic phenomenon, optimization and, inverse problems. The objective was the simulation, interpretation and optimization of the radar assessment of concrete structures.

The simulation of the electromagnetic "concrete-sensor" interaction shown to be the most difficult part of this work due to the complexity of the process itself and to the modeling of concrete materials and sensors as close to real situations as possible. The process of developing a tool capable of simulating this interaction took the form of implementing and validating time and frequency-domain numerical methods as FDTD and TLM or by using and modifying available tools as was done for FEM and MoM.

The choice of using FDTD is the result of a literature review and implementation of different numerical techniques that allowed the candidate to draw the advantages and the limitations of each technique considering the objectives. For the purpose of modeling radar EM propagation in a dispersive medium, a 3D FDTD code was written and implemented in a Cartesian coordinate system by using a CPML boundary wave absorber. The accuracy of the implemented code was first tested against published results. Thereafter, the code was used to simulate the EM responses from various settings. However, it was observed that for optimization purposes this technique was inappropriate and other techniques needed to be employed.

In addition, most of the research that has been applied to the nondestructive testing of concrete has focused on the ability and improvement of the method itself. As the applications of NDT methods become more complex it will be necessary for research to focus on the interactions of NDT techniques with the concrete. Taking into account this issue, this work implemented techniques for interpretation of the data coming from the radar assessment and the optimization of the antenna used for this purpose. The former is represented by an ill-posed inverse problem solved by parametric and nonparametric algorithms. The latter seeks to help the engineer in one of the most recurrent problems in his work: the design of sensors taking into account the tradeoff between efficiency and cost.

This research work began in October 2004. The time needed to achieve all the objectives was of 28 months. The first year was employed for the literature review and the implementation of numerical methods. In the second year it was possible to implement the first 3D FDTD algorithm using radar antennas. The implementation of imaging algorithms for the characterisation of inclusions also started in that period. In this context, it is important to cite the internship<sup>1</sup> realized at the University of Akron (April-November 2006). The writing process began in February 2007 together with teaching activities.

In conclusion, this thesis investigated different aspects of radar assessment of concrete structures. Signal processing techniques were explored by using optimization algorithms and by solving an inverse problem, which can be applied to real radar/EM simulation data. A useful simulation study was thus carried out in the context of NDT of concrete structures.

---

<sup>1</sup>This internship was financed by the EURODOC scholarship.

## 5.1 Future work

Scope for future work includes:

- Using the algorithm for the GPR Mars exploration including the design of optimized V-shaped bowtie antennas.
  - Optimization of the PML for general media. This includes the investigation of different conductivity profiles.
  - Conducting further investigation using varying ingredients with varying concrete mixture designs as well as varied exposure times to curing solutions and salt solutions.
  - Implementing discontinuous Galerkin method to introduce complicated geometries and to treat in a better way interfaces between different materials in the time-domain.
  - Extending the present 3D FDTD code to take into account a near to far field transformation to calculate far field patterns for antennas.
  - Future work can be done to parallelise the existing code. The FDTD algorithm is inherently parallel. This could be done using a parallel software library like Message Passing Interface (MPI). This could add efficiency and allow large scale simulations to be faster.
-

## Appendix A

# Implementation of CPML in FDTD

The classical tensor coefficients used in the Uniaxial PML can lead to large reflections errors for highly evanescent waves or for late-time, low-frequency interactions. One reason for the large reflection coefficient at low frequencies is that the tensor coefficient has a pole (is singular) at zero frequency. It was found that using the Complex Frequency-Shift (CFS) tensor coefficient with proper scaling can overcome these limitations [55]. An implementation of the CFS PML for FDTD was proposed by Gedney using an ADE formulation. However, a more efficient implementation was published by Roden and Gedney [68] based on a recursive-convolution technique. This has since been referred to as the CPML formulation. The CPML is based on the stretched-coordinate form of the PML. The CPML is more efficient and better suited for the application of domains with generalized materials.

### A.1 Derivation of the finite-difference expressions

First a complex coordinate space is defined. To this end, the following coordinate mapping is introduced:

$$\tilde{x} \rightarrow \int_0^x s_x(x') dx' ; \tilde{y} \rightarrow \int_0^y s_y(y') dy' ; \tilde{z} \rightarrow \int_0^z s_z(z') dz' ; \quad (\text{A.1})$$

In Eq. A.1, we assume that the PML parameters  $s_w$  are continuous functions along the axial directions. The partial derivatives in the stretched coordinate space are then

$$\frac{\partial}{\partial \tilde{x}} = \frac{1}{s_x} \frac{\partial}{\partial x} ; \frac{\partial}{\partial \tilde{y}} = \frac{1}{s_y} \frac{\partial}{\partial y} ; \frac{\partial}{\partial \tilde{z}} = \frac{1}{s_z} \frac{\partial}{\partial z} ; \quad (\text{A.2})$$

Thus, the  $\nabla$  operator in the mapped space is defined as

$$\tilde{\nabla} = \hat{\mathbf{x}} \frac{\partial}{\partial \tilde{x}} + \hat{\mathbf{y}} \frac{\partial}{\partial \tilde{y}} + \hat{\mathbf{z}} \frac{\partial}{\partial \tilde{z}} \quad (\text{A.3})$$

We first define the relation

$$\bar{s}_w = F^{-1} [1/s_w(\omega)], w = x, y, z \quad (\text{A.4})$$

where  $F^{-1}$  is the inverse Fourier transform operator and  $\{s_w\}$  are the CFS stretched-coordinate tensor coefficients defined by

$$s_w = \kappa_w + \frac{\sigma_w}{a_w + j\omega\varepsilon_0}. \quad (\text{A.5})$$

Then, with the stretched-coordinate form of the PML, we can express the time-dependent Ampere's law as

$$\begin{aligned} \frac{\partial \mathbf{D}}{\partial t} = & \hat{\mathbf{x}} \left( \bar{s}_y * \frac{\partial}{\partial y} H_z - \bar{s}_z * \frac{\partial}{\partial z} H_y \right) + \hat{\mathbf{y}} \left( \bar{s}_z * \frac{\partial}{\partial z} H_x - \bar{s}_x * \frac{\partial}{\partial x} H_z \right) \\ & + \hat{\mathbf{z}} \left( \bar{s}_x * \frac{\partial}{\partial x} H_y - \bar{s}_y * \frac{\partial}{\partial y} H_x \right). \end{aligned} \quad (\text{A.6})$$

In addition, Fourier transform theory yields

$$\bar{s}_w(t) = \frac{\delta(t)}{\kappa_w} - \frac{\sigma_w}{\varepsilon_0 \kappa_w^2} e^{-\left(\frac{\sigma_w}{\varepsilon_0 \kappa_w} + \frac{a_w}{\varepsilon_0}\right)t} u(t) \equiv \frac{\delta(t)}{\kappa_w} + \zeta_w(t), \quad \forall t \in \mathfrak{R}, \quad (\text{A.7})$$

where  $u(t)$  is the unit step function, and  $\delta(t)$  is the unit impulse function. Now, from Eq. A.7, Ampere's law in Eq. A.6 can be expressed more concisely as

$$\begin{aligned} \frac{\partial \mathbf{D}}{\partial t} = & \hat{\mathbf{x}} \left( \frac{1}{\kappa_y} \frac{\partial}{\partial y} H_z - \frac{1}{\kappa_z} \frac{\partial}{\partial z} H_y + \zeta_y * \frac{\partial}{\partial y} H_z - \zeta_z * \frac{\partial}{\partial z} H_y \right) \\ & \hat{\mathbf{y}} \left( \frac{1}{\kappa_z} \frac{\partial}{\partial z} H_x - \frac{1}{\kappa_x} \frac{\partial}{\partial x} H_z + \zeta_z * \frac{\partial}{\partial z} H_x - \zeta_x * \frac{\partial}{\partial x} H_z \right) \\ & \hat{\mathbf{z}} \left( \frac{1}{\kappa_x} \frac{\partial}{\partial x} H_y - \frac{1}{\kappa_y} \frac{\partial}{\partial y} H_x + \zeta_x * \frac{\partial}{\partial x} H_y - \zeta_y * \frac{\partial}{\partial y} H_x \right). \end{aligned} \quad (\text{A.8})$$

A dual expression can be derived for Faraday's law:

$$\begin{aligned} -\frac{\partial \mathbf{B}}{\partial t} = & \hat{\mathbf{x}} \left( \frac{1}{\kappa_y} \frac{\partial}{\partial y} E_z - \frac{1}{\kappa_z} \frac{\partial}{\partial z} E_y + \zeta_y * \frac{\partial}{\partial y} E_z - \zeta_z * \frac{\partial}{\partial z} E_y \right) \\ & \hat{\mathbf{y}} \left( \frac{1}{\kappa_z} \frac{\partial}{\partial z} E_x - \frac{1}{\kappa_x} \frac{\partial}{\partial x} E_z + \zeta_z * \frac{\partial}{\partial z} E_x - \zeta_x * \frac{\partial}{\partial x} E_z \right) \\ & \hat{\mathbf{z}} \left( \frac{1}{\kappa_x} \frac{\partial}{\partial x} H_y - \frac{1}{\kappa_y} \frac{\partial}{\partial y} H_x + \zeta_x * \frac{\partial}{\partial x} E_y - \zeta_y * \frac{\partial}{\partial y} E_x \right). \end{aligned} \quad (\text{A.9})$$

The objective now is to derive explicit updates for the electric fields from Eq. A.8 or the magnetic fields from Eq. A.9 in the context of an FDTD discretization. The challenge is to efficiently implement discrete convolutions arising from  $\zeta_w * (\partial H_v / \partial w)$ . If implemented naively, this could be prohibitively expensive in computer resources. However, given the form of  $\zeta_w(t)$ , excellent efficiency can be obtained by using the recursive-convolution (RC) technique.

The first step is to derive  $Z_w(m)$ , the discrete impulse response of  $\zeta_w(t)$ :

$$\begin{aligned} Z_w(m) &= \int_{m\Delta t}^{(m+1)\Delta t} \zeta_w(\tau) d\tau \\ &= -\frac{\sigma_w}{\varepsilon_0 \kappa_w^2} \int_{m\Delta t}^{(m+1)\Delta t} e^{-\left(\frac{\sigma_w}{\varepsilon_0 \kappa_w} + \frac{a_w}{\varepsilon_0}\right)\tau} d\tau = c_w e^{-\left(\frac{\sigma_w}{\varepsilon_0 \kappa_w} + \frac{a_w}{\varepsilon_0}\right)m\Delta t} \end{aligned} \quad (\text{A.10})$$

where

$$c_w = \frac{\sigma_w}{\sigma_w \kappa_w + \kappa_w^2 a_w} \left[ e^{-\left(\frac{\sigma_w}{\varepsilon_0 \kappa_w} + \frac{a_w}{\varepsilon_0}\right)\Delta t} - 1 \right]. \quad (\text{A.11})$$

Now, the convolution can be implemented in a discrete manner by using a piecewise-constant approximation for  $\zeta_w(t)$  and  $\partial H_v / \partial w$ :

$$\psi_{w,v}(n) = \zeta_w(t) * \frac{\partial}{\partial w} H_v(t) \Big|_{t=n\Delta t} \approx \sum_{m=0}^{n-1} Z_w(m) \frac{\partial}{\partial w} H_v(n-m). \quad (\text{A.12})$$

In this form, calculating the discrete convolution  $\psi$  at time  $n\Delta t$  requires order  $(n)$  floating-point operations. If implemented directly in an FDTD simulation, the computational burden would be intolerable. Instead, a recursive relationship that efficiently computes the time advancement of  $\psi$  can be derived. This is expressed as

$$\psi_{w,v}(n) = b_w \psi_{w,v}(n-1) + c_w \frac{\partial}{\partial w} H_v(n) \quad (\text{A.13})$$

where

$$b_w = e^{-\left(\frac{\sigma_w}{\varepsilon_0 \kappa_w} + \frac{a_w}{\varepsilon_0}\right)\Delta t} \quad (\text{A.14})$$

and  $c_w$  is given in Eq. A.11. In this form,  $\psi_{w,v}$  can be advanced in time with great efficiency using a simple time-marching procedure. By employing this recursive discrete convolution, an efficient FDTD formulation can be derived for Eq. A.8 and Eq. A.9. As an example, we consider the x-projection of Ampere's law in Eq. A.8, assuming for generality that the host medium has finite conductivity  $\sigma$ .

Applying the proper constitutive relationship between the electric flux density  $\mathbf{D}$  and the electric field intensity  $\mathbf{E}$ , we obtain:

$$\frac{\partial}{\partial t} (\varepsilon E_x) + \sigma E_x = \left( \frac{1}{\kappa_y} \frac{\partial}{\partial y} H_z - \frac{1}{\kappa_z} \frac{\partial}{\partial z} H_y \right) + \left( \zeta_y * \frac{\partial}{\partial y} H_z - \zeta_z * \frac{\partial}{\partial z} H_y \right). \quad (\text{A.15})$$

Using the discrete time and space approximations and the RC approximation of the convolution integrals Eq. A.16 is expressed in discrete form as

$$\begin{aligned} & \varepsilon_{i+1/2,j,k} \left( \frac{E_x \Big|_{i+1/2,j,k}^{n+1/2} - E_x \Big|_{i+1/2,j,k}^{n-1/2}}{\Delta t} \right) + \sigma_{i+1/2,j,k} \left( \frac{E_x \Big|_{i+1/2,j,k}^{n+1/2} - E_x \Big|_{i+1/2,j,k}^{n-1/2}}{2} \right) \\ &= \left( \frac{H_z \Big|_{i+1/2,j+1/2,k}^n - H_z \Big|_{i+1/2,j-1/2,k}^n}{\kappa_y \Delta y} - \frac{H_y \Big|_{i+1/2,j,k+1/2}^n - H_y \Big|_{i+1/2,j,k-1/2}^n}{\kappa_z \Delta z} \right) \\ & \quad + \psi_{E_{x,y}} \Big|_{i+1/2,j,k}^n - \psi_{E_{x,z}} \Big|_{i+1/2,j,k}^n \end{aligned} \quad (\text{A.16})$$

where  $\psi_{E_{x,y}}$  and  $\psi_{E_{x,z}}$  are discrete unknowns stored only in PML regions with  $y$ -normal and  $z$ -normal interface boundaries, respectively. These unknowns are updated as follows:

$$\psi_{E_{x,y}} \Big|_{i+1/2,j,k}^n = b_{y_j} \psi_{E_{x,y}} \Big|_{i+1/2,j,k}^{n-1} C_{y_j} \left( \frac{H_z \Big|_{i+1/2,j+1/2,k}^n - H_z \Big|_{i+1/2,j-1/2,k}^n}{\Delta y} \right), \quad (\text{A.17})$$

$$\psi_{E_{x,z}} \Big|_{i+1/2,j,k}^n = b_{z_k} \psi_{E_{x,z}} \Big|_{i+1/2,j,k}^{n-1} C_{z_k} \left( \frac{H_y \Big|_{i+1/2,j,k+1/2}^n - H_y \Big|_{i+1/2,j,k-1/2}^n}{\Delta z} \right). \quad (\text{A.18})$$

The discrete coefficients  $b_{y_j}$  and  $C_{y_j}$  are nonzero only in PML regions with  $y$ -normal interface boundaries. These coefficients are computed using A.14 and A.12, respectively, with the scaled tensor parameters  $\kappa_y$ ,  $\sigma_y$ , and  $a_y$  calculated at the discrete location  $j\Delta y$ , which is the  $y$ -coordinate of the discrete grid edge center  $(i+1/2, j, k)$ .

The explicit update for  $E_x$  is derived directly from A.10 and is given by

$$\begin{aligned} & E_x \Big|_{i+1/2,j,k}^{n+1/2} = C_a \Big|_{i+1/2,j,k} E_x \Big|_{i+1/2,j,k}^{n-1/2} \\ & + C_b \Big|_{i+1/2,j,k} \left( \frac{H_z \Big|_{i+1/2,j+1/2,k}^n - H_z \Big|_{i+1/2,j-1/2,k}^n}{\kappa_y \Delta y} - \frac{H_y \Big|_{i+1/2,j,k+1/2}^n - H_y \Big|_{i+1/2,j,k-1/2}^n}{\kappa_z \Delta z} \right) \\ & \quad + C_b \Big|_{i+1/2,j,k} \left( +\psi_{E_{x,y}} \Big|_{i+1/2,j,k}^n - \psi_{E_{x,z}} \Big|_{i+1/2,j,k}^n \right) \end{aligned} \quad (\text{A.19})$$

where

$$\begin{aligned} C_a \Big|_{i+1/2,j,k} &= \left( 1 - \frac{\sigma_{i+1/2,j,k} \Delta t}{2\varepsilon_{i+1/2,j,k}} \right) / \left( 1 + \frac{\sigma_{i+1/2,j,k} \Delta t}{2\varepsilon_{i+1/2,j,k}} \right) \\ C_b \Big|_{i+1/2,j,k} &= \left( \frac{\Delta t}{\varepsilon_{i+1/2,j,k}} \right) / \left( 1 + \frac{\sigma_{i+1/2,j,k} \Delta t}{2\varepsilon_{i+1/2,j,k}} \right). \end{aligned} \quad (\text{A.20})$$

Similar expressions are derived for  $E_y$  and  $E_z$  by simply permuting the  $(i, j, k)$  indices and  $(x, y, z)$ . The  $\mathbf{H}$  components can also be derived using Faraday's law.



## Appendix B

# Transmission line matrix method

The link between field theory and circuit theory, the major theories on which electrical engineering is based, has been exploited in developing numerical techniques to solve certain types of partial differential equations arising in field problems with the aid of equivalent electrical networks. Since the fundamental laws of circuit theory can be obtained from Maxwell's equations the Transmission-line modeling (TLM), otherwise known as the transmission-line-matrix method, is a numerical technique created for solving field problems using circuit equivalent. The TLM method is based on the discrete model of Huygen's principle. While Huygen's principle is an alternative form of Maxwell's equations, and the finite difference method is a discrete form of Maxwell's equations, one may conclude that the TLM method is similar to the finite difference method and can be derived directly from Maxwell's equations using differencing [132, 133, 134, 135, 136].

For instance, it has been shown that, in the case of the expanded TLM node model, the node equations can be reformulated as the finite difference equations used in [132], [137]. In the case of a uniform mesh and free space, [135], established the correspondences between the electric variables in the TLM method and the field variables in Maxwell's equations, demonstrated that the 3D TLM symmetrical condensed node can be rewritten as a new finite difference scheme for Maxwell's equations.

Next, the direct derivation of the perfectly matched layer symmetrical condensed node (PML SCN) proposed for the implementation of the Berenger's PML's using centered differencing and averaging will be described. The principal steps of this procedure have been introduced in [138]. A direct correspondence between the TLM and the finite difference method is established. The node scattering matrix and field expressions are presented for the general case with a graded mesh and anisotropic materials, including both electric and magnetic losses [139].

### B.1 PML derivation for the TLM SCN node

PML media are described by modifying Maxwell equations with the six electromagnetic field components split into 12 subcomponents and with anisotropic electric and magnetic conductivities. For example, in a normal medium with isotropic electric conductivity  $\sigma$ , the first Maxwell's equation can be written as follows:

$$\varepsilon_0 \varepsilon_r \frac{\partial e_x}{\partial t} + \sigma e_x = \frac{\partial h_z}{\partial y} - \frac{\partial h_y}{\partial z}. \quad (\text{B.1})$$

In Berenger's PML medium, each electromagnetic field is split into two subcomponents

$$e_x = e_{xy} + e_{xz} \quad h_y = h_{yx} + h_{yz} \quad h_z = h_{zx} + h_{zy} \quad (\text{B.2})$$

and B.1 is replaced by

$$\begin{aligned}\varepsilon_0\varepsilon_r\frac{\partial e_{xy}}{\partial t} + \sigma_y e_{xy} &= \frac{\partial(h_{zx} + h_{zy})}{\partial y} \\ \varepsilon_0\varepsilon_r\frac{\partial e_{xz}}{\partial t} + \sigma_z e_{xz} &= -\frac{\partial(h_{yx} + h_{yz})}{\partial z}\end{aligned}\quad (\text{B.3})$$

where  $\sigma_y$  and  $\sigma_z$  are the electric conductivities along the  $y$ - and  $z$ -axes. Equation B.3 can be rewritten in the following forms:

$$\begin{aligned}\varepsilon_0\varepsilon_r\frac{\partial(e_x - e_{xz})}{\partial t} + \sigma_y e_{xy} &= \frac{\partial h_z}{\partial y} \\ \varepsilon_0\varepsilon_r\frac{\partial(e_x - e_{xy})}{\partial t} + \sigma_z e_{xz} &= -\frac{\partial h_y}{\partial z}\end{aligned}\quad (\text{B.4})$$

or

$$\begin{aligned}\frac{Y_x + 4}{2}\frac{\partial E_x}{\partial T} &= \frac{\partial H_z}{\partial Y} + \frac{Y_x + 4}{2}\frac{\partial E_{xz}}{\partial T} - G_{xy}E_{xy} \\ \frac{Y_x + 4}{2}\frac{\partial E_x}{\partial T} &= \frac{\partial H_y}{\partial Z} + \frac{Y_x + 4}{2}\frac{\partial E_{xy}}{\partial T} - G_{xz}E_{xz}\end{aligned}\quad (\text{B.5})$$

using

$$\begin{aligned}X &= \frac{x}{u} \\ Y &= \frac{y}{v} \\ Z &= \frac{z}{w} \\ T &= \frac{t}{\Delta t} \\ E_x &= e_x u \\ E_{xy} &= e_{xy} u \\ E_{xz} &= e_{xz} u \\ H_y &= h_y v Z_0 \\ H_z &= h_z w Z_0 \\ Y_x &= 4\left(\varepsilon_r \frac{vw}{u\Delta l} - 1\right) \\ G_{xy} &= \sigma_y \frac{vw}{u} Z_0 \\ G_{xz} &= \sigma_z \frac{vw}{u} Z_0\end{aligned}\quad (\text{B.6})$$

where  $u$ ,  $v$ , and  $w$  are the sizes of the TLM SCN shown in Fig. B.1. The node is located in the TLM network by indexes  $(i, j, k)$ .  $\Delta l$  is the smallest cell size over the network and the time step is set as  $\Delta t \leq \Delta l/2c$ .  $Z_0$  and  $c$  are the characteristic impedance and the wave velocity of free space, respectively. As described by Jin et al., Eq. B.5 is reformulated as

$$\frac{1}{2}\left\{\frac{\partial(E_x - H_z)}{\partial A_y} - \frac{\partial(E_x + H_z)}{\partial B_y}\right\} = \frac{\partial E_{xz}}{\partial T} - \frac{Y_x + 2}{2}\frac{\partial E_{xy}}{\partial T}\quad (\text{B.7})$$

$$\frac{1}{2}\left\{\frac{\partial(E_x - H_z)}{\partial A_y} - \frac{\partial(E_x + H_z)}{\partial B_y}\right\} = \frac{\partial E_{xz}}{\partial T} - \frac{Y_x + 2}{2}\frac{\partial E_{xy}}{\partial T} - G_{xy}E_{xy}\quad (\text{B.8})$$

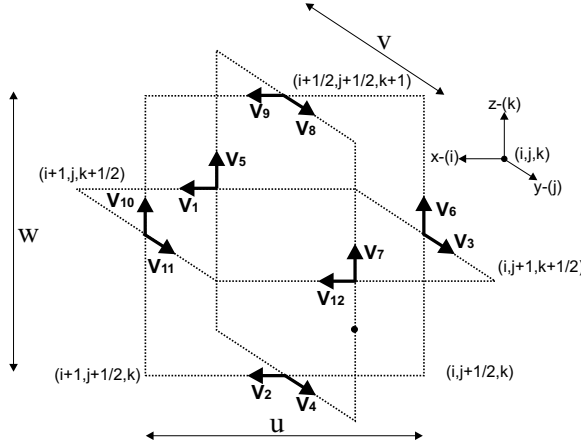


Figure B.1: A unit cell and field sampling points.

using the following new coordinate system where time and space are mixed:

$$\begin{aligned}
 A_x &= X + T \\
 A_y &= Y + T \\
 A_z &= Z + T \\
 B_x &= X - T \\
 B_y &= Y - T \\
 B_z &= Z - T
 \end{aligned}
 \tag{B.9}$$

A set of finite-difference equations can be obtained from B.7 and B.8 by using centered differencing at point  $(i, j, k)$  and time  $n\Delta t$  in the new coordinate system B.9. For example, B.7 gives

$$\begin{aligned}
 & \frac{1}{2} \left[ E_x \left( n + \frac{1}{2}, i, j + \frac{1}{2}, k \right) - H_z \left( n + \frac{1}{2}, i, j + \frac{1}{2}, k \right) \right] \\
 & - \frac{1}{2} \left[ E_x \left( n - \frac{1}{2}, i, j - \frac{1}{2}, k \right) - H_z \left( n - \frac{1}{2}, i, j - \frac{1}{2}, k \right) \right] \\
 & - \frac{1}{2} \left[ E_x \left( n - \frac{1}{2}, i, j + \frac{1}{2}, k \right) + H_z \left( n - \frac{1}{2}, i, j + \frac{1}{2}, k \right) \right] \\
 & + \frac{1}{2} \left[ E_x \left( n + \frac{1}{2}, i, j - \frac{1}{2}, k \right) + H_z \left( n + \frac{1}{2}, i, j - \frac{1}{2}, k \right) \right] \\
 & + \frac{Y_x + 2}{2} \left[ E_{xy} \left( n + \frac{1}{2}, i, j, k \right) - E_{xy} \left( n - \frac{1}{2}, i, j, k \right) \right] \\
 & - \left[ E_{xz} \left( n + \frac{1}{2}, i, j, k \right) - E_{xz} \left( n - \frac{1}{2}, i, j, k \right) \right] \\
 & + G_{xy} E_{xy} (n, i, j, k) = 0.
 \end{aligned}
 \tag{B.10}$$

In the TLM formulation, each elementary plane waves penetrating into the cell along the  $x$ -,  $y$ , and  $z$  directions of space is associated with a voltage impulse travelling toward the center of the cell through one of the 12 transmission lines linking the node to its six neighbors. For example, an  $x$  polarized plane wave propagating in the  $+y$  direction is related to the incident voltage impulse  ${}_n V_1^i$  on port number 1 at the cell boundary  $(i, j - 1/2, k)$  and time step  $(n - 1/2)\Delta t$  as follows:

$$E_x \left( n - \frac{1}{2}, i, j - \frac{1}{2}, k \right) - H_z \left( n - \frac{1}{2}, i, j - \frac{1}{2}, k \right) = 2 {}_n V_1^i
 \tag{B.11}$$

According to the Huygens' principle these incident voltage impulses are scattered at the center of the node and at time step  $n\Delta t$  into reflected voltage impulses associated with outgoing plane waves. For

example, for an  $x$  polarized outgoing wave propagating in the  $+y$  direction, the relation between the  $E_x$ - and  $H_z$ - field components and the reflected voltage impulse  ${}_nV_{12}^r$  on port number 12 at the cell boundary  $(i, j + 1/2, k)$  and time step  $(n + 1/2)\Delta t$  is

$$E_x \left( n + \frac{1}{2}, i, j + \frac{1}{2}, k \right) - H_z \left( n + \frac{1}{2}, i, j + \frac{1}{2}, k \right) = 2{}_nV_{12}^r \quad (\text{B.12})$$

Open and short stubs connected at the center of the node allow modeling of permittivity and permeability of various materials. In the case of  $x$  polarized waves, for example, it is necessary to add two open stubs with normalized characteristic admittance  $Y_x$  (numbered 13 and 14), to take into account the two subcomponents  $E_{xy}$  and  $E_{xz}$  as follows:

$$E_{xy} \left( n - \frac{1}{2}, i, j, k \right) = 2{}_nV_{13}^i \quad (\text{B.13})$$

$$E_{xz} \left( n - \frac{1}{2}, i, j, k \right) = 2{}_nV_{14}^i \quad (\text{B.14})$$

$$E_{xy} \left( n + \frac{1}{2}, i, j, k \right) = 2{}_nV_{13}^r \quad (\text{B.15})$$

$$E_{xz} \left( n + \frac{1}{2}, i, j, k \right) = 2{}_nV_{14}^r \quad (\text{B.16})$$

Using B.11-(B.16), B.10 can be reduced to

$$\begin{aligned} & {}_nV_1^r + {}_nV_{12}^r - {}_nV_1^i - {}_nV_{12}^i + (Y_x + 2) ({}_nV_{13}^r - {}_nV_{13}^i) \\ & - 2 ({}_nV_{14}^r - {}_nV_{14}^i) + G_{xy}E_{xy} (n, i, j, k) = 0 \end{aligned} \quad (\text{B.17})$$

Another set of finite-difference equations can be obtained from B.3, which can be rewritten using B.2 and B.6 as

$$\frac{Y_x + 4}{2} \frac{\partial E_{xy}}{\partial T} = \frac{\partial H_z}{\partial Y} - G_{xy}E_{xy} \quad (\text{B.18})$$

$$\frac{Y_x + 4}{2} \frac{\partial E_{xz}}{\partial T} = \frac{\partial H_y}{\partial Z} - G_{xz}E_{xz} \quad (\text{B.19})$$

By using centered differencing and averaging at point  $(i, j, k)$  and time step  $(n + 1/2)\Delta t$  in the coordinate system B.6, and by using B.11-B.16, for example B.18, gives

$$\begin{aligned} & \frac{Y_x + G_{xy} + 4}{2} [E_{xy} (n + 1, i, j, k) - E_{xy} (n, i, j, k)] \\ & = {}_{n+1}V_1^i + {}_{n+1}V_{12}^i - {}_nV_1^r - {}_nV_{12}^r - G_{xy}E_{xy} (n, i, j, k) \end{aligned} \quad (\text{B.20})$$

Substituting B.17 into B.20, we obtain finally

$$E_{xy} (n, i, j, k) = \frac{2 [{}_nV_1^i + {}_nV_{12}^i + (Y_x + 2) {}_nV_{13}^i - 2{}_nV_{14}^i]}{Y_x + G_{xy} + 4} \quad (\text{B.21})$$

Performing the same procedure for the other 11 modified Maxwell equations provide the following expressions:

$$E_{xz} (n, i, j, k) = \frac{2 [{}_nV_2^i + {}_nV_9^i + (Y_x + 2) {}_nV_{14}^i - 2{}_nV_{13}^i]}{Y_x + G_{xz} + 4} \quad (\text{B.22})$$

$$E_{yx} (n, i, j, k) = \frac{2 [{}_nV_3^i + {}_nV_{11}^i + (Y_y + 2) {}_nV_{15}^i - 2{}_nV_{16}^i]}{Y_y + G_{yx} + 4} \quad (\text{B.23})$$

$$E_{yz}(n, i, j, k) = \frac{2[nV_4^i + nV_8^i + (Y_y + 2)nV_{16}^i - 2nV_{15}^i]}{Y_y + G_{yz} + 4} \quad (\text{B.24})$$

$$E_{zx}(n, i, j, k) = \frac{2[nV_6^i + nV_{10}^i + (Y_y + 2)nV_{17}^i - 2nV_{18}^i]}{Y_z + G_{zx} + 4} \quad (\text{B.25})$$

$$E_{zy}(n, i, j, k) = \frac{2[nV_5^i + nV_7^i + (Y_z + 2)nV_{18}^i - 2nV_{17}^i]}{Y_z + G_{zy} + 4} \quad (\text{B.26})$$

$$H_{xy}(n, i, j, k) = \frac{2\left[nV_5^i - nV_7^i + \left(1 + \frac{2}{Z_x}\right)nV_{19}^i - \frac{2}{Z_x}nV_{20}^i\right]}{Z_x + R_{xy} + 4} \quad (\text{B.27})$$

$$H_{xz}(n, i, j, k) = \frac{2\left[nV_8^i - nV_4^i + \left(1 + \frac{2}{Z_x}\right)nV_{20}^i - \frac{2}{Z_x}nV_{19}^i\right]}{Z_x + R_{xz} + 4} \quad (\text{B.28})$$

$$H_{yx}(n, i, j, k) = \frac{2\left[nV_{10}^i - nV_6^i + \left(1 + \frac{2}{Z_y}\right)nV_{21}^i - \frac{2}{Z_y}nV_{22}^i\right]}{Z_y + R_{yx} + 4} \quad (\text{B.29})$$

$$H_{yz}(n, i, j, k) = \frac{2\left[nV_2^i - nV_9^i + \left(1 + \frac{2}{Z_y}\right)nV_{22}^i - \frac{2}{Z_y}nV_{21}^i\right]}{Z_y + R_{yz} + 4} \quad (\text{B.30})$$

$$H_{zx}(n, i, j, k) = \frac{2\left[nV_3^i - nV_{11}^i + \left(1 + \frac{2}{Z_z}\right)nV_{23}^i - \frac{2}{Z_z}nV_{24}^i\right]}{Z_z + R_{zx} + 4} \quad (\text{B.31})$$

$$H_{zy}(n, i, j, k) = \frac{2\left[nV_{12}^i - nV_1^i + \left(1 + \frac{2}{Z_z}\right)nV_{24}^i - \frac{2}{Z_z}nV_{23}^i\right]}{Z_z + R_{zy} + 4} \quad (\text{B.32})$$

where

$$\begin{aligned}
Y_x &= 4 \left( \varepsilon_r \frac{vw}{u\Delta l} - 1 \right) \\
Y_y &= 4 \left( \varepsilon_r \frac{uw}{v\Delta l} - 1 \right) \\
Y_z &= 4 \left( \varepsilon_r \frac{uv}{w\Delta l} - 1 \right) \\
Z_x &= 4 \left( \mu_r \frac{vw}{u\Delta l} - 1 \right) \\
Z_y &= 4 \left( \mu_r \frac{uw}{v\Delta l} - 1 \right) \\
Z_z &= 4 \left( \mu_r \frac{uv}{w\Delta l} - 1 \right) \\
G_{xy} &= \sigma_y Z_0 \frac{vw}{u} \\
G_{yz} &= \sigma_z Z_0 \frac{uw}{v} \\
G_{zx} &= \sigma_x Z_0 \frac{uv}{w} \\
G_{xz} &= \sigma_z Z_0 \frac{vw}{u} \\
G_{yx} &= \sigma_x Z_0 \frac{uw}{v} \\
G_{zy} &= \sigma_y Z_0 \frac{uv}{w} \\
R_{xy} &= \sigma_y^* Z_0^{-1} \frac{vw}{u} \\
R_{yz} &= \sigma_z^* Z_0^{-1} \frac{uw}{v} \\
R_{zx} &= \sigma_x^* Z_0^{-1} \frac{uv}{w} \\
R_{xz} &= \sigma_z^* Z_0^{-1} \frac{vw}{u} \\
R_{yx} &= \sigma_x^* Z_0^{-1} \frac{uw}{v} \\
R_{zy} &= \sigma_y^* Z_0^{-1} \frac{uv}{w}.
\end{aligned} \tag{B.33}$$

In B.33,  $\sigma_x^*$ ,  $\sigma_y^*$ , and  $\sigma_z^*$  are the magnetic conductivities along the  $x$ ,  $y$ , and  $z$  axes. Note that, to prevent the term in  $1/Z$  to go to infinity in B.27-B.32 when  $u = v = w = \Delta l$  and  $\mu_r = 1$ , it is necessary to make  $\Delta t$  slightly lower than the maximum time step  $\Delta l/2c$ . Futhermore, in the case of normal media with isotropic electric and magnetic conductivities  $\sigma$  and  $\sigma^*$ , B.21 and B.22 can be reduced to

$$\begin{aligned}
E_x &= E_{xy} + E_{xz} \\
&= \frac{2 \left[ {}_n V_1^i + {}_n V_{12}^i + {}_n V_2^i + {}_n V_9^i + Y_x ({}_n V_{13}^i + {}_n V_{14}^i) \right]}{Y_x + G_x + 4}
\end{aligned} \tag{B.34}$$

where  $G_x = G_{xy} = G_{xz}$ . Equation B.34 is the  $E_{x-}$  field expression for the standard SCN. This new PML SCN can then simulate at once PML layers and normal media such as vacuum or conductive media. It can be used in all the computational domain leading to a uniform algorithm. As described in [138], the scattering process can finally be obtained by using averaging in space-time coordinate system B.9 from field expressions  $E_a \pm H_b$ , where superscript  $a$  and  $b$  are  $x, y$ , or  $z$ . The  $24 \times 24$  scattering matrix of this

new PML SCN has been given in [137] and can be formulated for practical computation as follows:

$$\begin{aligned}
{}_nV_1^r &= [E_{xy}(n, i, j, k) + E_{xz}(n, i, j, k)] + [H_{zx}(n, i, j, k) + H_{zy}(n, i, j, k)] - {}_nV_{12}^i \\
{}_nV_2^r &= [E_{xy}(n, i, j, k) + E_{xz}(n, i, j, k)] - [H_{yx}(n, i, j, k) + H_{yz}(n, i, j, k)] - {}_nV_9^i \\
{}_nV_3^r &= [E_{yx}(n, i, j, k) + E_{yz}(n, i, j, k)] - [H_{zx}(n, i, j, k) + H_{zy}(n, i, j, k)] - {}_nV_{11}^i \\
{}_nV_4^r &= [E_{yx}(n, i, j, k) + E_{yz}(n, i, j, k)] + [H_{xy}(n, i, j, k) + H_{xz}(n, i, j, k)] - {}_nV_8^i \\
{}_nV_5^r &= [E_{zx}(n, i, j, k) + E_{zy}(n, i, j, k)] - [H_{xy}(n, i, j, k) + H_{xz}(n, i, j, k)] - {}_nV_7^i \\
{}_nV_6^r &= [E_{zx}(n, i, j, k) + E_{zy}(n, i, j, k)] + [H_{yx}(n, i, j, k) + H_{yz}(n, i, j, k)] - {}_nV_{10}^i \\
{}_nV_7^r &= [E_{zx}(n, i, j, k) + E_{zy}(n, i, j, k)] + [H_{xy}(n, i, j, k) + H_{xz}(n, i, j, k)] - {}_nV_5^i \\
{}_nV_8^r &= [E_{yx}(n, i, j, k) + E_{yz}(n, i, j, k)] - [H_{xy}(n, i, j, k) + H_{xz}(n, i, j, k)] - {}_nV_4^i \\
{}_nV_9^r &= [E_{xy}(n, i, j, k) + E_{xz}(n, i, j, k)] + [H_{yx}(n, i, j, k) + H_{yz}(n, i, j, k)] - {}_nV_2^i \\
{}_nV_{10}^r &= [E_{zx}(n, i, j, k) + E_{zy}(n, i, j, k)] - [H_{yx}(n, i, j, k) + H_{yz}(n, i, j, k)] - {}_nV_6^i \\
{}_nV_{11}^r &= [E_{yx}(n, i, j, k) + E_{yz}(n, i, j, k)] + [H_{zx}(n, i, j, k) + H_{zy}(n, i, j, k)] - {}_nV_3^i \\
{}_nV_{12}^r &= [E_{xy}(n, i, j, k) + E_{xz}(n, i, j, k)] - [H_{zx}(n, i, j, k) + H_{zy}(n, i, j, k)] - {}_nV_1^i \\
{}_nV_{13}^r &= E_{xy}(n, i, j, k) - {}_nV_{13}^i \\
{}_nV_{14}^r &= E_{xz}(n, i, j, k) - {}_nV_{14}^i \\
{}_nV_{15}^r &= E_{yx}(n, i, j, k) - {}_nV_{15}^i \\
{}_nV_{16}^r &= E_{yz}(n, i, j, k) - {}_nV_{16}^i \\
{}_nV_{17}^r &= E_{zx}(n, i, j, k) - {}_nV_{17}^i \\
{}_nV_{18}^r &= E_{zy}(n, i, j, k) - {}_nV_{18}^i \\
{}_nV_{19}^r &= {}_nV_{19}^i - Z_x H_{xy}(n, i, j, k) \\
{}_nV_{20}^r &= {}_nV_{20}^i - Z_x H_{xz}(n, i, j, k) \\
{}_nV_{21}^r &= {}_nV_{21}^i - Z_y H_{yx}(n, i, j, k) \\
{}_nV_{22}^r &= {}_nV_{22}^i - Z_y H_{yz}(n, i, j, k) \\
{}_nV_{23}^r &= {}_nV_{23}^i - Z_z H_{zx}(n, i, j, k) \\
{}_nV_{24}^r &= {}_nV_{24}^i - Z_z H_{zy}(n, i, j, k)
\end{aligned} \tag{B.35}$$

Then, scattering with the PML SCN requires 108 additions/subtractions, 42 multiplications, and 12 divisions in place of 54 additions/subtractions and 12 multiplications with the standard SCN. This higher computational cost may be prohibitive. Thus, it is recommended to use the standard SCN in the domain of interest and the PML SCN in the PML layers. This can be done without difficulties. Since the 12-link lines are the same for the two nodes, they can be directly connected together at the interface vacuum/PML medium.

There are some techniques that can be used to reduce and to optimize the computational burden of the TLM simulation such as alternating (ATLM), rotated (RTLTM), and alternating rotated transmission line matrix (ARTLM) schemes. However, this work used the simplest implementation of the TLM for validation purposes. The full algorithm of the TLM code implemented is depicted in Fig. B.2.

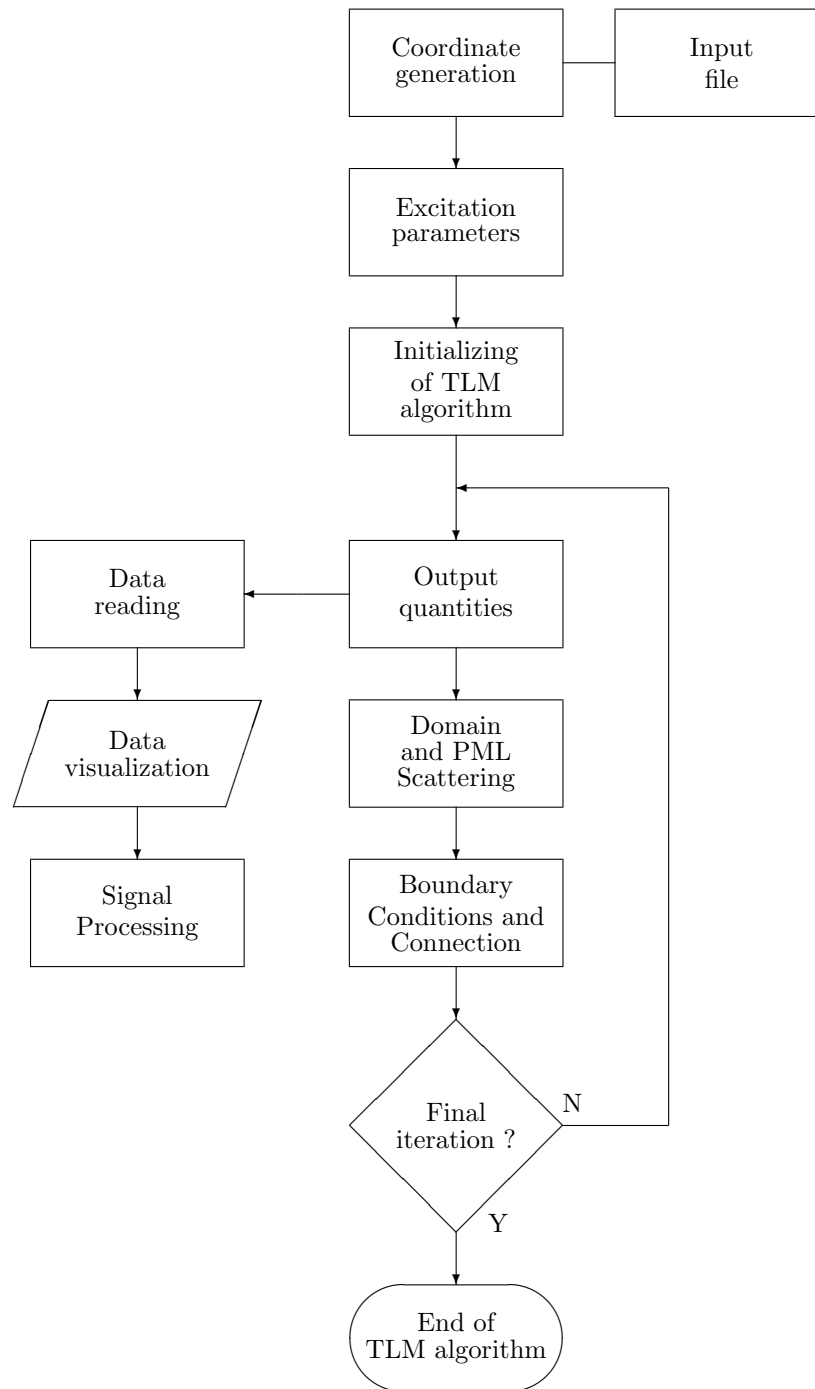


Figure B.2: TLM algorithm.

---

# Bibliography

- [1] “Annuaire de l’industrie nucléaire française,” tech. rep. <http://www.giin.fr>.
  - [2] <http://www.edf.fr>.
  - [3] L. Travassos, S. L. Avila, D. Prescott, A. Nicolas, and L. Krähenbühl, “Optimal Configurations for Perfectly Matched Layers in FDTD Simulations,” *IEEE Trans on Magnetics*, vol. 42, pp. 563–566, 2006.
  - [4] L. Travassos, N. Ida, C. Vollaire, and A. Nicolas, “Solution of Maxwell’s Equations for the Simulation and Optimization of the Radar Assessment of Concrete Structures,” *accepted for publication in Research in Nondestructive Evaluation Journal*.
  - [5] L. Travassos, D. A. G. Vieira, N. Ida, C. Vollaire, and A. Nicolas, “Concrete Inclusion Assessment using Principal Component Analysis and Neural Networks,” *in writing process*.
  - [6] C. Hellier, *Handbook of Nondestructive Evaluation*. Blacklick. OH, USA: McGraw-Hill Professional Publishing, 2001.
  - [7] C. Society, “Guidance on Radar Testing of Concrete Structures,” tech. rep., The Concrete Society, 1997. <http://www.concrete.org.uk>.
  - [8] “Development priorities for non-destructive examination of concrete structures in nuclear plant,” tech. rep., Nuclear Energy Agency Committee on the Safety of Nuclear Installations, 1998.
  - [9] D. McCann and M. Forde, “Review of *NDT* methods in the assessment of concrete and masonry structures,” *NDTE International*, vol. 34, pp. 71–84, 2001.
  - [10] “Bridge inspection manual,” tech. rep., Texas Department of Transportation, 2001.
  - [11] S. Millard, “Corrosion rate measurement of in-situ reinforced concrete structures,” *Proceedings of the Institution of Civil Engineers*, vol. 99, pp. 84–88, 1993.
  - [12] N. Carino and M. Sansalone, “Pulse-echo method for flaw detection in concrete,” tech. rep., US National Bureau of Standards Technical, 1984. Note 1199.
  - [13] J. Martin, M. S. A. Hardy, A. S. Usmani, and M. C. Forde, “Accuracy of *NDE* in bridge assessment,” *NDTE International*, vol. 20(11), pp. 979–984, 1998.
  - [14] M. P. Schuller, “Nondestructive testing and damage assessment of masonry structures,” *Prog. Struct. Engng Mater.*, vol. 5, pp. 239–251, 2003.
  - [15] M. Ohtsu, “A review of acoustic emission in civil engineering with emphasis on concrete,” *Journal of Acoustic Emission*, vol. 8, pp. 93–98, 1989.
  - [16] T. Okamoto, “Discrimination of cracking pattern developed in reinforced concrete structures by acoustic emission,” *4th World Meeting on Acoustic Emission*, 1991.
  - [17] D. Reddy, “Acoustic emission as a nde tool - certain laboratory and field investigations,” *Proc. Conf. Nondestructive Evaluation of Materials and Structures Using Vibration and Acoustic Techniques*, 1989.
-

- 
- [18] C. Sklarczyk, "Detection of cracks in concrete by acoustic emission," *Testing During Concrete Construction*, 1990.
- [19] L. Rogers and L. Phillips, "Acoustic emission and ultrasonic testing of concrete structures," *Structural Integrity Assessment*, 1992.
- [20] P. Shull, *Nondestructive Evaluation: Theory, Techniques, and Applications*. New York, NY, USA: Marcel Dekker Incorporated, 2002.
- [21] Y. Kharrat, J. Rhazi, G. Ballivy, and P. Cote, "Auscultation of concrete hydraulic structures using sonic tomography," *Canadian Journal of Civil Engineering*, vol. 22, pp. 1072–1083, 1995.
- [22] K. Heiskanen, H. C. Rhim, and P. J. M. Monteiro, "Computer simulations of limited angle tomography of reinforced concrete," *Cement and Concrete Research*, vol. 21, pp. 625–634, 1991.
- [23] F. Jalinoos, L. D. Olson, M. F. Aouad, and A. H. Balch, "Acoustic tomography for qualitative nondestructive evaluation (qnde) of structural concrete using a new ultrasonic scanner source," *Review of Progress in Quantitative Nondestructive Evaluation*, vol. 14, 1994.
- [24] R. Haskins and A. Alexander, "Computer interpretation of ultrasonic pulse-echo signs for concrete dams," *Nondestructive Evaluation of Ageing Structures and Dams*, vol. 2457, pp. 182–194, 1995.
- [25] D. Andrews, "Future prospects for ultrasonic inspection of concrete," *Proc. Institution of Civil Engineers, Structures and Buildings*, vol. 99, pp. 71–73, 1993.
- [26] A. Kovalev, "Ultrasonic testing of the structurally inhomogeneous materials by one-sided access," *Proceedings of the 13th World Conference on Non-Destructive Testing*, vol. 2, pp. 911–913, 1992.
- [27] G. Weil, *CRC Handbook on Nondestructive Testing of Concrete*. New York: CRC Press, 1991.
- [28] X. Maldague, *Theory and practice of infrared thermography for nondestructive evaluation*. OH, USA: New York: Wiley, 2001.
- [29] F. J. Madruga, "Application of infrared thermography to the fabrication process of nuclear fuel containers," *NDTE International*, vol. 38, pp. 397–401, 2005.
- [30] J. Milne, "Thermodynamic inspection of concrete using a controlled heat source," *Infrared Technology and Applications*, vol. 1320, pp. 227–241, 1990.
- [31] N. J. Carino, "Characterisation of electromagnetic covermeters," *Non-Destructive Testing in Civil Engineering*, vol. 2, pp. 753–765, 1993.
- [32] J. Alldred, "An improved method for measuring reinforcing bars of unknown diameter in concrete using a cover meter," *Non-Destructive Testing in Civil Engineering*, vol. 2, pp. 767–788, 1993.
- [33] S. Millard, J. A. Harrison, and A. J. Edwards, "Measurement of the electrical resistivity of reinforced concrete structures for the assessment of corrosion risk," *British Journal of Non-Destructive Testing*, vol. 31, pp. 617–662, 1989.
- [34] K. Saravanan, S. Srinivasan, and R. H. S. Bapu, "Electrochemical non-destructive testing of reinforcement corrosion in existing concrete structures," *Bulletin of Electrochemistry*, vol. 6, pp. 385–386, 1990.
- [35] K. R. Gowers, S. G. Millard, and J. H. Bungey, "The influence of environmental conditions upon the measurement of concrete resistivity for the assessment of corrosion durability," *Non-Destructive Testing in Civil Engineering*, vol. 2, pp. 633–659, 1993.
- [36] P. K. Mehta, *Concrete Technology - Past, Present and Future*. Detroit, MI, USA: American Concrete Institute, 1994.
-

- 
- [37] A. Davis, K. L. Malcolm, and C. G. Petersen, "Rapid and economical evaluation of concrete tunnel linings with impulse response and impulse radar non-destructive methods," *NDTE International*, 2004.
- [38] B. Euram, "Subsurface radar as a tool for non-destructive testing and assessment in the construction and building industries," tech. rep.
- [39] A. P. Anman, "GPR -history, trends, and future developments," *Subsurface Sensing Technologies and Applications*, vol. 3, pp. 253–270, 2002.
- [40] G. Clemena, "Nondestructive Inspection of Overlaid Bridge Decks with Ground Penetrating Radar," tech. rep., Transportation Research Board, 1983.
- [41] G. Smith and W. Scott, "A scale model for studying ground penetrating radars," *IEEE Transactions on Geoscience and Remote Sensing*, vol. 27, pp. 358–363, 1989.
- [42] M. Sayers, "The International Road Roughness Experiment: Establishing Correlation and a Calibration Standard for measurements," tech. rep., Transportation Research Board, 1992.
- [43] J. Bungey, "The influence of reinforcing steel on radar surveys of concrete structures," *Construction and Building Materials*, vol. 8, pp. 119–126, 1994.
- [44] J. Bungey and S. Millard, "Radar inspection of structures," *Proc. Institution of Civil Engineers (Structures and Buildings)*, vol. 99, pp. 173–186, 1993.
- [45] M. Forde, "Evaluating structures using impulse radar and sonic techniques," *Decommissioning and Demolition 1992*, 1992.
- [46] S. G. Millard, "The assessment of concrete quality using pulsed radar reflection and transmission techniques," *Non-destructive Testing in Civil Engineering*, vol. 1, pp. 161–185, 1993.
- [47] J. Warhus, "Advanced ground penetrating radar," *Advanced Microwave and Millimetre-Wave Detectors.*, vol. 2275, pp. 177–185, 1994.
- [48] P. Okamoto and A. Ciolko, "High resolution impulse radar imaging- civil engineering applications," *Nondestructive Testing and Evaluation for Manufacturing and Construction*, 1990.
- [49] S. Nelson, "EM modelling for GPIR using 3d FDTD modelling codes," *Advanced Microwave and Millimetre-Wave Detectors*, vol. 2275, pp. 186–195, 1994.
- [50] C. Flohrer and B. Bernhardt, "Detection of prestressed steel tendons behind reinforcement bars, detection of voids in concrete structures - a suitable application for radar systems," *Nondestructive Testing in Civil Engineerings*, 1993.
- [51] R. Zoughi and G. Cone, "Microwave non-destructive detection of rebars in concrete slabs," *Materials Evaluation*, vol. 49, pp. 1385–1388, 1991.
- [52] J. Broomfield, "The assessment of corrosion of reinforcing steel on highway bridges," *Advanced Microwave and Millimetre-Wave Detectors*, vol. 2, pp. 551–566, 1993.
- [53] K. Lim and D. Gress, "Detecting areas of high chloride concentration in bridge decks," *Non-Destructive Testing in Civil Engineering*, 1988.
- [54] T. W. Barrett, H. F. Harmuth, and B. Meffert, *Modified Maxwell Equations in Quantum Electrodynamics*. World Scientific, 2001.
- [55] A. Taflove and S. Hagness, *Computational Electrodynamics: The finite-difference time-domain method*. Norwood, MA: Artech House, 2000.
- [56] M. V. K. Chari and P. P. Silvestre, *Finite Element in Electrical and Magnetic Field Problems*. John Wiley and Sons Inc., 1980.
-

- 
- [57] P. B. Johns and R. L. Beurle, "Numerical solution of 2-dimensional scattering problems using a transmission-line matrix," *Proceedings of the IEEE*, vol. 118, pp. 1203–1208, 1971.
- [58] M. N. O. Sadiku and C. N. Obiozor, "A comparison of finite difference time-domain (*FDTD*) and transmission-line modeling (*TLM*) methods," *Proceedings of the IEEE*, 2000.
- [59] N. Ida and J. P. A. Bastos, *Electromagnetics and Calculation of Fields*. Springer Verlag, 1992.
- [60] F. Bassi and S. Rebay, "Extracting sensitivity information of electromagnetic devices models from a modified anfs topology," *J. Comput. Phys.*, vol. 131, pp. 267–279, 1997.
- [61] J. Jin, *The Finite Element Method in Electromagnetics*. Wiley-IEEE Press, 2002.
- [62] S. Rao, D. Wilton, and A. Glisson, "Electromagnetic scattering by surfaces of arbitrary shape," *IEEE Transactions of antennas and propagation*, vol. 3, pp. 409–418, 1982.
- [63] S. Makarov, "MoM antenna simulations, with matlab: RWG basis functions," *IEEE Antennas and Propagation Magazine*, vol. 43, pp. 100–107, 2001.
- [64] N. Ida, *Numerical Modeling for Electromagnetic Non-Destructive Evaluation*. London: Chapman and Hall, 1995.
- [65] D. J. Daniels, *Ground Penetrating Radar*. United Kingdom: IEE Radar, Sonar and Navigation, 2004.
- [66] R. Lee and F. L. Teixeira, "Finite difference time domain model for GPR applications," *GPR 2006 Conference Short Course Notes*, 2006.
- [67] F. L. Teixeira, C. Chew, M. Straka, M. L. Oristaglio, and T. Wang, "Finite-difference time-domain simulation of ground penetrating radar on dispersive, inhomogeneous, and conductive soils," *IEEE Transactions on Geoscience and remote sensing*, vol. 36, pp. 1928–1937, 1998.
- [68] J. A. Roden and S. D. Gedney, "Convolutional PML (*CPML*): An efficient *FDTD* implementation of the *CFS-PML* for arbitrary media," *Microwave Optical Tech. Lett.*, vol. 27, pp. 334–339, 2000.
- [69] D. Sheen, *Numerical Modeling of Microstrip Circuits and Antennas*. PhD thesis, MIT, Cambridge, MA, 1991.
- [70] K. L. Shlager, G. S. Smith, and J. G. Maloney, "Optimization of bow-tie antennas for pulse radiation," *IEEE Transactions on Antennas and Propagation*, vol. 42, pp. 975–982, 1994.
- [71] J. G. Maloney, K. L. Shlager, and G. S. Smith, "A simple *FDTD* model for transient excitation of antennas by transmission lines," *IEEE Transactions on Antennas and Propagation*, vol. 42, pp. 289–292, 1994.
- [72] D. M. Sheen, "Application of the three-dimensional finite-difference time-domain method to the analysis of planar microstrip circuits," *IEEE Trans. On Microwave Theory and Techniques*, vol. 38, pp. 849–857, 1990.
- [73] R. C. Benson, R. A. Glaccum, and M. R. Noel, "Geophysical techniques for sensing buried wastes and waste migration (ntis pb84-198449) .," tech. rep., Prepared for U.S. EPA Environmental Monitoring Systems Laboratory, 1984.
- [74] N. Siauve, L. Nicolas, C. Vollaire, and C. Marchal, "3D modelling of electromagnetic fields in local hyperthermia," *Eur. Phys. Journal AP.*, vol. 21, pp. 243–250, 2003.
- [75] "Cancer facts and figures 2004," tech. rep., American Cancer Society, 2004.
- [76] S. C. Hagness, A. Taflove, and J. E. Bridges, "Three-dimensional *FDTD* analysis of a pulsed microwave confocal system for breast cancer detection: Design of an antenna-array element," *IEEE Transactions on Antennas and Propagation*, vol. 47, pp. 783–791, 1999.
-

- 
- [77] J. R. Harris, M. E. Lippman, U. Veronesi, and W. Willett, "Medical progress: Breast cancer," *New Eng. J. Med.*, vol. 327, pp. 319–328, 1992.
- [78] J. P. Berenger, "A perfectly matched layer for the *FDTD* solution of wave-structure interaction problems," *IEEE Trans. Antennas and Propagation*, vol. 51, pp. 110–117, 1996.
- [79] S. Kim and J. Choi, "Optimal design of *PML* absorbing boundary condition for improving wide-angle reflection performance," *Electronics Letters*, vol. 40, pp. 104–106, 2004.
- [80] C. L. Li, C. W. Liu, and S. H. Chen, "Optimization of *PML* absorber's conductivity profile using *FDTD*," *Microwave and Optical Technology Letters*, vol. 37, pp. 380–383, 2003.
- [81] D. T. Prescott and V. Shuley, "Reflection analysis of *FDTD* boundary conditions - part ii: Berenger's *PML* absorbing layers," *Microwave Theory and Techniques*, vol. 45, pp. 1171–1178, 1997.
- [82] K. Deb, *Multi-Objective Optimization Using Evolutionary Algorithms*. John Wiley & Sons, 2002.
- [83] D. E. Goldberg, *Genetic Algorithms in search, optimization and machine learning*. New York: Addison Wesley, 1989.
- [84] S. L. Avila, L. Travassos, W. P. Carpes, and L. Krähenbühl, "An educational tool for teaching optimization in engineering," in *Record of the 15TH Compumag Conference*, June 2005.
- [85] S. L. Avila and L. Krähenbühl, "A multi-niching multi-objective genetic algorithm for solving complex multimodal problems," *OIPE 2006, The 9th Workshop on Optimization and Inverse Problems in Electromagnetics*, 2006.
- [86] W. C. Chew and J. M. Jin, "Perfectly matched layers in the discretized space: An analysis and optimization," *Electromagnetics*, vol. 16, pp. 325–340, 1996.
- [87] J. Schneider and O. M. Ramahi, "A comparison and evaluation of the *PML* and *COM* mesh truncation techniques for *FDTD* simulation," *IEEE Antennas and Propagation*, vol. 3, pp. 1904–1907, 1997.
- [88] A. A. Lestari, *Antennas for improved ground penetrating radar*. PhD thesis, Technische Universiteit Delft, Netherlands, 2003.
- [89] P. K. Mehta, *Concrete: Structure, Properties and Materials*. Englewood Cliffs, NJ: Prentice Hall, 1986.
- [90] G. P. De Loor, "Dielectric properties of heterogeneous mixtures," *Applied Science Research*, pp. 310–320, 1964.
- [91] L. K. H. Van Beek, "Dielectric behaviour of heterogeneous mixtures," *Progress in Dielectrics*, vol. 7, pp. 69–114, 1967.
- [92] A. M. Neville, *Properties of Concrete*, vol. 3. Pitman Publishing Ltd., 1981.
- [93] F. Tsui, "Analytical modelling of the dielectric properties of concrete for subsurface radar applications," *The British Library*.
- [94] F. T. Ulaby, *Microwave Remote Sensing*, vol. 3. MA: Artech House Inc, 1986.
- [95] S. Feng and P. N. Sen, "Geometrical model of conductive and dielectric properties of partially saturated rocks," *J. Appl. Phys.*, vol. 58, pp. 3236–3243, 1985.
- [96] U. B. Halabe, *Condition assessment of reinforced concrete structures using electromagnetic waves*. PhD thesis, Massachusetts Institute of Technology, USA, 1990.
- [97] C. A. Balanis, *Antenna Theory*. Third Edition, New Jersey: Wiley, 2005.
- [98] J. R. Wait, "Electromagnetic surface waves," *Advances in Radio Research*, vol. 1, pp. 157–217, 1964.
-

- 
- [99] A. Banos, *Dipole radiation in the presence of a conducting half-space*. New York: Pergamon, 1966.
- [100] A. P. Annan, "Radio interfering depth sounding. part I: Theoretical discussion," *Geophysics*, vol. 38, pp. 557–580, 1973.
- [101] D. B. Rutledge and M. S. Muha, "Imaging antenna arrays," *IEEE Trans. Antennas Propagat.*, vol. 30, pp. 535–540, 1982.
- [102] G. S. Smith, "Directive properties of antenna for transmission into a material half-space," *IEEE Trans. Antennas Propagat.*, vol. 32, pp. 232–246, 1984.
- [103] S. G. Millard, A. Shaari, and J. H. Bungey, "Field pattern characteristics of GPR antennas," *NDTE International*, vol. 35, pp. 473–482, 2002.
- [104] D. Uduwawala, M. Norgren, P. Fuks, and A. W. Gunawardena, "A deep parametric study of resistor-loaded bow-tie antennas for ground-penetrating radar applications using FDTD," *IEEE Trans. on Geoscience and Remote Sensing*, vol. 51, pp. 732–742, 2004.
- [105] B. Lampe and K. Holliger, "Resistively loaded antennas for ground-penetrating radar: A modeling approach," *Geophysics*, vol. 70, pp. K23–K32, 2005.
- [106] J. Holt, *Finite Difference time domain modeling of dispersion from heterogeneous ground properties in ground penetrating radar*. PhD thesis, The Ohio State University, USA, 2004.
- [107] G. Klysz, G. Balayssac, J. P. Laurens, and S. Ferrieres, "Simulation of direct wave propagation by numerical FDTD for a GPR coupled antenna," *NDTE International*, vol. 39, pp. 338–347, 2006.
- [108] N. Izzat, G. H. Hilton, C. J. Railton, and S. Meade, "Use of resistive sheets in damping cavity resonance," *Electron. Lett.*, vol. 32, pp. 721–722, 1996.
- [109] C. H. Chen, *Frontiers of remote sensing information processing*. World scientific publishing, 2003.
- [110] J. Gazdag and P. Sguazzero, "Migration of seismic data," *Proc. IEEE*, vol. 72, pp. 1302–1315, 1984.
- [111] A. J. Berkhout, "Wave field extrapolation techniques in seismic migration-a tutorial," *Geophysics*, vol. 46, pp. 1638–1656, 1981.
- [112] A. J. Berkhout, *Seismic Migration-Imaging of Acoustic Energy by Wave Field Extrapolation-A. Theoretical Aspects*. New York: Elsevier, 1982.
- [113] C. J. Leuschen and R. G. Plumb, "A matched-filter-based reverse-time migration algorithm for ground-penetrating radar data," *IEEE Trans. Geoscience and Remote Sensing*, vol. 39, pp. 929–936, 2001.
- [114] J. F. Claerbout, "Toward a unified theory of reflector mapping," *Geophysics*, vol. 36, pp. 467–481, 1971.
- [115] W. F. Chang and G. A. McMechan, "Reverse-time migration of offset vertical seismic profiling data using the excitation-time imaging condition," *Geophysics*, vol. 51, pp. 67–84, 1986.
- [116] J. Fang and Z. Wu, "Generalized perfectly matched layer for the absorption of propagating and evanescent waves in lossless and lossy media," *IEEE Trans. on Microwave Theory and Techniques*, vol. 44, pp. 2216–2222, 1996.
- [117] *GSSI Handbook For Radar Testing of Concrete*. North Salem, NH: Published by Geophysical Survey Systems, Inc. 13, 2001.
- [118] R. C. Eberhart and J. Kennedy, "A new optimizer using particle swarm theory," *Proceedings of the Sixth International symposium on Micro Machine and Human Science*, pp. 39–43, 1995.
- [119] J. Kennedy and R. C. Eberhart, "Particle swarm optimization," *Proceedings of IEEE International Conference on Neural Networks*, vol. 4, pp. 1942–1948, 1995.
-

- 
- [120] R. C. Eberhart, P. K. Simpson, and R. W. Dobbins, *Computational Intelligence PC Tools*. Boston, MA: Academic Press Professional, 1996. Chapter 5.
- [121] S. Haykin, *Adaptive filter theory (3rd ed.)*. Upper Saddle River, NJ, USA: Prentice-Hall, Inc., 1996.
- [122] S. Hoole, "Artificial neural networks in the solution of inverse electromagnetic field problems," *IEEE Trans. on Magn.*, vol. 29, no. 2, pp. 1931–1934, 1993.
- [123] S. Caorsi and G. Cevini, "Neural networks trained by scattered electromagnetic data for gpr applications," in *2d International Workshop on Advanced GPR*, (The Netherlands), pp. 14–16, May 2003.
- [124] S. Caorsi and G. Cevini, "An electromagnetic approach based on neural networks for the gpr investigation of buried cylinders," *IEEE Geoscience and Remote Sensing Letters*, vol. 2, pp. 3–7, January 2005.
- [125] R. Persico and R. Bernini, "The role of the measurement configuration in inverse scattering from buried objects under the born approximation," *IEEE Trans. on Antennas and Propagation*, vol. 53, no. 6, pp. 1875–1887, 2005.
- [126] W. M. Caminhas, D. A. G. Vieira, and J. A. Vasconcelos, "Parallel layer perceptron," *Neurocomputing*, vol. 55, pp. 771–778, October 2003.
- [127] D. A. G. Vieira, W. M. Caminhas, and J. A. Vasconcelos, "Extracting sensitivity information of electromagnetic devices models from a modified anfis topology," *IEEE Trans. on Magn.*, vol. 40, no. 2, pp. 1180–1183, 2004.
- [128] T. Hastie, R. Tibshirani, and J. H. Friedman, *The Elements of Statistical Learning*. Springer, first ed., August 2001.
- [129] W. W. D. Gabor and R. Woodcock, "A universal nonlinear ite predictor and simulator which optimizes itself by a learning process.," *IEE Proceedings*, vol. 108B, pp. 422–438, 1961.
- [130] J. S. R. Jang, "Anfis: Adaptative-network-based fuzzy inference systems," *IEEE Transactions on Systems, Man and Cybernetics*, vol. 23, pp. 665–685, May 1993.
- [131] V. N. Vapnik, *Statistical Learning Theory*. New York: Wiley, 1998.
- [132] P. B. Johns, "On the relationship between *TLM* and finite difference methods for maxwell's equations," *IEEE Trans. Microwave Theory and Tech.*, vol. 35, pp. 60–61, 1987.
- [133] M. Celuch-Marcysiak and W. K. Gwarek, "Formal equivalence and efficiency comparison of the *FDTD*, *TLM* and sn methods in application to microwave cad programs," in *Proc. 21st European Microwave Conference*, 1991.
- [134] N. R. S. Simons and E. Bridges, "Equivalence of propagation characteristics for the transmission-line matrix and finite-difference time-domain methods in two dimensions," *IEEE Trans. Microwave Theory Tech.*, vol. 39, pp. 354–357, 1991.
- [135] Z. Chen, M. M. Ney, and W. J. R. Hofer, "A new finite-difference time-domain formulation and its equivalence with the *TLM* symmetrical condensed node," *IEEE Trans. Microwave Theory Tech.*, vol. 39, pp. 2160–2169, 1991.
- [136] J. LoVetri and N. R. S. Simons, "A class of symmetrical condensed node *TLM* methods derived directly from maxwell's equations," *IEEE Trans. Microwave Theory Tech.*, vol. 41, pp. 1419–1428, 1993.
- [137] A. Taflov and M. E. Brodwin, "Numerical solution of steady-state electromagnetic scattering problems using the time-dependent maxwell's equations," *IEEE Trans. Microwave Theory Tech.*, vol. 23, pp. 623–630, 1975.
-

- [138] H. Jin, V. Ruediger, and J. Huang, "Direct derivation of the *TLM* symmetrical condensed node from maxwell's equations using centered differencing and averaging," in *IEEE Int. Microwave Symp. Dig.*, 1994.
  - [139] H. Jin and R. Vahldieck, "Direct derivations of *TLM* symmetrical condensed node and hybrid symmetrical condensed node from maxwell's equations using centered differencing and averaging," *IEEE Trans. Microwmve Theory Tech.*, 1994.
-

# Vita

Lucas Travassos Jr was born March 1, 1978, in Santos, Brazil, to Marilena and Lucas Travassos. He graduated from the Federal Technical School of Sao Paulo in December 1996. He received his Electrical Engineer degree in December of 2002 from the Federal University of Santa Catarina in Florianopolis. While attending the engineer school full time, Lucas worked part time for different laboratories in the Department of Electrical Engineering with scholarships from the Brazilian Education Ministry, graduating with a high performance citation.

Lucas continued with his education, entering graduate school to pursue a Master of Electrical Engineering in the GRUCAD Group (Applied Research in the area of Electromagnetics for analysis, design, optimization and implementation of electromagnetic devices) of the Electrical Engineering Department in Mars 2003. After the graduation from the Federal University of Santa Catarina in Florianopolis with a Master of Engineering Lucas started his PhD in the Ecole Centrale de Lyon in October 2004 becoming a Temporary Professor/Researcher in December 2006.

## Publications

1. C. Quinteiro, L. Travassos, L. C. Albornoz and R. Garcia. *Unidade Eletro-Cirurgica de Alta Frequncia em Hospitais Publicos da Grande Florianopolis: Avaliacao de Utilizacao*. Brazilian Conference on Biomedical Engineering - CBEB 2000 (portuguese), August 2000, Florianopolis (Brazil).
2. L. Travassos, M B. Liz and A. Raizer. *Eletromagnetic Interference Created by Medical Equipments*. Brazilian Conference on Biomedical Engineering - CBEB 2002 (portuguese), August 2002, Sao Jose dos Campos (Brazil).
3. L. Travassos, M B. Liz and A. Raizer. *CEM Analisis of Medical Equipments*. 5th Brazilian Conference on Electromagnetism (portuguese), CBMAG 2002, November 2002, Gramado (Brazil).
4. L. Travassos, W. P. Carpes and E. J. Silva. *Comparison and Evaluation of Boundary Conditions to Calculate Input Parameters of a Microstrip Patch Antenna using FDTD*. 6th Brazilian Conference on Electromagnetism, CBMAG 2004, August 2004, Sao Paulo (Brazil).
5. L. Travassos, S. L. Avila, W. P. Carpes and E. J. Silva. *Optimal Configurations for ABC's in FDTD Simulations*. 11th International IGTE Symposium on Numerical Field Calculation in Electrical Engineering, IGTE 2004, September 2004, Graz (Austria).
6. L. Travassos, A. C. Lisboa, W. P. Carpes and E. J. Silva. *A Simple Tool for Modeling Microstrip Structures using the Finite-Difference Time-Domain Method*. XXI Brazilian Telecommunication Symposium - SBT'04, September 2004, Belem (Brazil).
7. L. Travassos, S. L. Avila, A. C. Lisboa, A. Nicolas. *A Simple Tool for Modeling Microstrip Structures using FDTD Method*. 15th Conference on the Computation of Electromagnetic Fields, COMPUMAG 2005, 26-30 June 2005, Shenyang (China).
8. S. L. Avila, L. Travassos and L. Krähenbühl. *An Educational Tool for Teaching Optimization in Engineering*. 15th Conference on the Computation of Electromagnetic Fields, COMPUMAG 2005, 26-30 June 2005, Shenyang (China).

9. L. Travassos, S. L. Avila, D. Prescott, A. Nicolas and L. Krähenbühl. *Optimal Configurations for Perfectly Matched Layers in FDTD Simulations*. 15th Conference on the Computation of Electromagnetic Fields, COMPUMAG 2005, 26-30 June 2005, Shenyang (China).
  10. L. Travassos, C. Vollaire, A. Nicolas. *FDTD Method Applied to Radar Testing of Concrete Structures*. Sixth International Conference on Computation in Electromagnetics - CEM 2006, 4 - 6 April 2006, Aachen (Germany).
  11. L. Travassos, S. L. Avila, A. C. Lisboa, C. Vollaire, A. Nicolas. *Multi-objective Optimization of Bow-tie Antennas for Radar Assessment of Concrete Structures*. The 12th biennial IEEE Conference on Electromagnetic Field Computation (CEFC 2006), April-May 2006, Miami (USA).
  12. L. Travassos, C. Vollaire, A. Nicolas. *Solution of Maxwell's Equations for GPR Simulation and Optimization*. The 11th International Conference on Ground-Penetrating Radar - GPR 2006, 19 - 22 June 2006, Columbus (USA).
  13. L. Travassos, L. Bernard, C. Vollaire, A. Nicolas. *The Reverse-time Migration Algorithm Applied to the Interpretation of Electromagnetic Subsurface Assessment of Concrete Structures*. 7th Brazilian Conference of Electromagnetism, CBMAG 2006, August 2006, Belo Horizonte (Brazil).
  14. L. Travassos, S. L. Avila, A. C. Lisboa, C. Vollaire, A. Nicolas. *Simulation and Optimization of GPR Antennas for the Assessment of Concrete Structures*. The first European Conference on Antennas and Propagation (EuCAP 2006), 6 - 10 November 2006, Nice (France).
  15. S. L. Avila, L. Travassos, L. Krähenbühl and J. R. Bergmann. *Contour Beam Shaped Reflector Antenna with Frequency Reuse*. The first European Conference on Antennas and Propagation (EuCAP 2006), 6 - 10 November 2006, Nice (France).
  16. L. Travassos, S. L. Avila, D. Prescott, A. Nicolas and L. Krähenbühl, "Optimal Configurations for Perfectly Matched Layers in FDTD Simulations", *IEEE Transactions on Magnetics*, Vol. 42, No. 4, pp. 563-566, April 2006.
  17. L. Travassos, S. L. Avila, N. Ida, C. Vollaire, A. Nicolas, "Design of Optimal GPR Antennas for Concrete Evaluation", *IEEE Multidisciplinary Engineering Education Magazine* Vol. 2, Iss. 2, pp. 1-4, June 2007.
  18. L. Travassos, N. Ida, C. Vollaire, and A. Nicolas, "Solution of Maxwell's Equations for the Simulation and Optimization of the Radar Assessment of Concrete Structures", accepted for publication in the *Research in Nondestructive Evaluation Journal*.
  19. L. Travassos, N. Ida, C. Vollaire, and A. Nicolas, "Time-Domain Modeling of Radar Assessment of Concrete: a Parametric Study", accepted to *16th COMPUMAG - IEEE Conference on the Computation of Electromagnetic Fields* - June 24-28, 2007, Aachen (Germany).
  20. L. Travassos, D. A. G. Vieira, N. Ida, C. Vollaire, and A. Nicolas, "Inverse Algorithms for the GPR Assessment of Concrete Structures", accepted to *16th COMPUMAG - IEEE Conference on the Computation of Electromagnetic Fields* - June 24-28, 2007, Aachen (Germany).
  21. L. Travassos, D. A. G. Vieira, N. Ida, C. Vollaire, and A. Nicolas, "Characterization of Inclusions in a non-homogeneous GPR Problem by Neural Networks", accepted to *16th COMPUMAG - IEEE Conference on the Computation of Electromagnetic Fields* - June 24-28, 2007, Aachen (Germany).
-



*dernière page de la thèse*

## **AUTORISATION DE SOUTENANCE**

Vu les dispositions de l'arrêté du 25 avril 2002,

Vu la demande du Directeur de Thèse

Monsieur A. NICOLAS

et les rapports de

Monsieur N. IDA

Professeur - The University of Akron - Nondestructive Testing and Applied Electromagnetics Lab - Rm 252, Auburn Science & Engineering Center - South Tower Akron - 44325-3904 - USA

Et de

Monsieur J-P-A. BASTOS

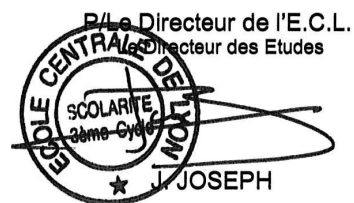
Professeur - Universidade Federal de Santa Catarina - Departamento de Engenharia Elétrica - CTC - Caixa Postal 476 - CEP 88040-970 - Florianópolis - Santa Catarina - Brésil

**Monsieur TRAVASSOS Lucas**

est autorisé à soutenir une thèse pour l'obtention du grade de **DOCTEUR**

**Ecole doctorale ELECTRONIQUE, ELECTROTECHNIQUE, AUTOMATIQUE (EEA)**

Fait à Ecully, le 14 juin 2007



**Modélisation numérique pour l'évaluation non destructive électromagnétique :  
Application au contrôle non destructif des structures en béton.**

**Résumé :**

Le béton est un des matériaux de construction principaux dans les grandes infrastructures telles les routes, les ponts et les centrales électriques. Pour évaluer l'évolution du béton dans ces structures, le contrôle non destructif est une des techniques les plus répandues. Elle fournit des informations non perceptibles à l'œil humain ce que ne permettent pas des techniques d'évaluation conventionnelles.

L'objectif principal de ce travail est la simulation numérique d'une technique particulière de contrôle non destructif : l'analyse radar. La modélisation numérique de cette analyse radar de structures en béton doit permettre de prévoir le comportement du système et sa capacité à détecter des défauts dans différentes configurations.

Nous proposons pour atteindre cet objectif, la mise en oeuvre de modèles de propagation des ondes électromagnétiques dans des structures en béton, en utilisant des techniques numériques diverses afin d'examiner les différents aspects de l'inspection radar. Tout d'abord, nous mettons en oeuvre la méthode des différences finies en 3D qui permet de prendre aisément en compte la modélisation des caractéristiques du béton comme la porosité, la présence de sel et le degré de saturation du mélange en utilisant des modèles de Debye. Ensuite, nous proposons un algorithme d'optimisation pour l'amélioration d'antennes papillon dans le cas de la détection de cibles spatialement proches, en utilisant des Algorithmes Génétiques et la Méthode des Moments. Finalement, nous mettons en oeuvre des algorithmes d'imagerie, qui accomplissent l'évaluation rapide et précise de la forme de la cible enfouie dans des milieux inhomogènes, en utilisant trois méthodes différentes. La performance des algorithmes proposés est confirmée par des simulations numériques.

**Mots-clés :** contrôle non destructif, électromagnétisme, radar.

---

**Numerical modeling for the electromagnetic non-destructive evaluation :  
Application to the non-destructive evaluation of concrete.**

**Abstract:** Concrete is the most common building material and accounts for a large part of the systems that are necessary for a country to operate smoothly including buildings, roads, and bridges. Nondestructive testing is one of the techniques that can be used to assess the structural condition. It provides nonperceptible information that conventional techniques of evaluation unable to do.

The main objective of this work is the numerical simulation of a particular technique of nondestructive testing: the radar. The numerical modeling of the radar assessment of concrete structures make it possible to envisage the behavior of the system and its capacity to detect defects in various configurations.

To achieve this objective, it was implemented electromagnetic wave propagation models in concrete structures, by using various numerical techniques to examine different aspects of the radar inspection. First of all, we implemented the finite-difference time-domain method in 3D which allows to take into account concrete characteristics such as porosity, salt content and the degree of saturation of the mixture by using Debye models. In addition, a procedure to improve the radiation pattern of bowtie antennas is presented. This approach involves the Moment Method in conjunction with the Multiobjective Genetic Algorithm. Finally, we implemented imaging algorithms which can perform fast and precise characterization of buried targets in inhomogenous medium by using three different methods. The performance of the proposed algorithms is confirmed by numerical simulations.

**Keywords:** nondestructive testing, electromagnetism, radar.

---

**Laboratoire :** Laboratoire AMPERE, UMR CNRS 5005. Ecole Centrale de Lyon, 69134 Ecully cedex.

**Contact :** lucas.travassos@ec-lyon.fr